INTRODUCTION TO THE PHYSICS OF THE EARTH'S INTERIOR
Edition 2

JEAN-PAUL POIRIER

Cambridge University Press

Introduction to the Physics of the Earth's Interior describes the structure, composition and temperature of the deep Earth in one comprehensive volume.

The book begins with a succinct review of the fundamentals of continuum mechanics and thermodynamics of solids, and presents the theory of lattice vibration in solids. The author then introduces the various equations of state, moving on to a discussion of melting laws and transport properties. The book closes with a discussion of current seismological, thermal and compositional models of the Earth. No special knowledge of geophysics or mineral physics is required, but a background in elementary physics is helpful. The new edition of this successful textbook has been enlarged and fully updated, taking into account the considerable experimental and theoretical progress recently made in understanding the physics of deep-Earth materials and the inner structure of the Earth.

Like the first edition, this will be a useful textbook for graduate and advanced undergraduate students in geophysics and mineralogy. It will also be of great value to researchers in Earth sciences, physics and materials sciences.

Jean-Paul Poirier is Professor of Geophysics at the Institut de Physique du Globe de Paris, and a corresponding member of the Académie des Sciences. He is the author of over one-hundred-and-thirty articles and six books on geophysics and mineral physics, including *Creep of Crystals* (Cambridge University Press, 1985) and *Crystalline Plasticity and Solid-state flow of Metamorphic Rocks* with A. Nicolas (Wiley, 1976).

This Page Intentionally Left Blank

INTRODUCTION TO THE PHYSICS OF THE EARTH'S INTERIOR

SECOND EDITION

JEAN-PAUL POIRIER
Institut de Physique du Globe de Paris

CAMBRIDGE
UNIVERSITY PRESS

PUBLISHED BY CAMBRIDGE UNIVERSITY PRESS (VIRTUAL PUBLISHING)
FOR AND ON BEHALF OF THE PRESS SYNDICATE OF THE UNIVERSITY OF CAMBRIDGE
The Pitt Building, Trumpington Street, Cambridge CB2 IRP
40 West 20th Street, New York, NY 10011-4211, USA
477 Williamstown Road, Port Melbourne, VIC 3207, Australia

http://www.cambridge.org

First published in printed format 1991
Second edition 2000

A catalogue record for the original printed book is available
from the British Library and from the Library of Congress
Original ISBN 0 521 66313 X hardback
Original ISBN 0 521 66392 X paperback

ISBN 0 511 01034 6 virtual (netLibrary Edition)

Contents

Preface to the first edition

Not so long ago, Geophysics was a part of Meteorology and there was no such thing as Physics of the Earth's interior. Then came Seismology and, with it, the realization that the elastic waves excited by earthquakes, refracted and reflected within the Earth, could be used to probe its depths and gather information on the elastic structure and eventually the physics and chemistry of inaccessible regions down to the center of the Earth.

The basic ingredients are the travel times of various phases, on seismograms recorded at stations all over the globe. Inversion of a considerable amount of data yields a seismological earth model, that is, essentially a set of values of the longitudinal and transverse elastic-wave velocities for all depths. It is well known that the velocities depend on the elastic moduli and the density of the medium in which the waves propagate; the elastic moduli and the density, in turn, depend on the crystal structure and chemical composition of the constitutive minerals, and on pressure and temperature. To extract from velocity profiles self-consistent information on the Earth's interior such as pressure, temperature, and composition as a function of depth, one needs to know, or at least estimate, the values of the physical parameters of the high-pressure and high-temperature phases of the candidate minerals, and relate them, in the framework of thermodynamics, to the Earth's parameters.

Physics of the Earth's interior has expanded from there to become a recognized discipline within solid earth geophysics, and an important part of the current geophysical literature can be found under such key words as "equation of state", "Grüneisen parameter", "adiabaticity", "melting curve", "electrical conductivity", and so on.

The problem, however, is that, although most geophysics textbooks devote a few paragraphs, or even a few chapters, to the basic concepts of the physics of solids and its applications, there still is no self-contained book

that offers the background information needed by the graduate student or the non-specialist geophysicist to understand an increasing portion of the literature as well as to assess the weight of physical arguments from various parties in current controversies about the structure, composition, or temperature of the deep Earth.

The present book has the, admittedly unreasonable, ambition to fulfill this role. Starting as a primer, and giving at length all the important demonstrations, it should lead the reader, step by step, to the most recent developments in the literature. The book is primarily intended for graduate or senior undergraduate students in physical earth sciences but it is hoped that it can also be useful to geophysicists interested in getting acquainted with the mineral physics foundations of the phenomena they study.

In the first part, the necessary background in thermodynamics of solids is succinctly given in the framework of linear relations between intensive and extensive quantities. Elementary solid-state theory of vibrations in solids serves as a basis to introduce Debye's theory of specific heat and anharmonicity. Many definitions of Grüneisen's parameter are given and compared.

The background is used to explain the origin of the various equations of state (Murnaghan, Birch–Murnaghan, etc.). Velocity–density systematics and Birch's law lead to seismic equations of state. Shock-wave equations of state are also briefly considered. Tables of recent values of thermodynamic and elastic parameters of the most important mantle minerals are given. The effect of pressure on melting is introduced in the framework of anharmonicity, and various melting laws (Lindemann, Kraut–Kennedy, etc.) are given and discussed. Transport properties of materials – diffusion and viscosity of solids and of liquid metals, electrical and thermal conductivity of solids – are important in understanding the workings of the Earth; a chapter is devoted to them.

The last chapter deals with the application of the previous ones to the determination of seismological, thermal, and compositional Earth models.

An abundant bibliography, including the original papers and the most recent contributions, experimental or theoretical, should help the reader to go further than the limited scope of the book.

It is a pleasure to thank all those who helped make this book come into being: First of all, Bob Liebermann, who persuaded me to write it and suggested improvements in the manuscript; Joël Dyon, who did a splendid job on the artwork; Claude Allègre, Vincent Courtillot, François Guyot,

Jean-Louis Le Mouël, and Jean-Paul Montagner, who read all or parts of the manuscript and provided invaluable comments and suggestions; and last but not least, Carol, for everything.

1991 *Jean-Paul Poirier*

Preface to the second edition

Almost ten years ago, I wrote in the introduction to the first edition of this book: 'It will also probably become clear that the simplicity of the inner Earth is only apparent; with the progress of laboratory experimental techniques as well as observational seismology, geochemistry and geomagnetism, we may perhaps expect that someday "Physics of the Inner Earth" will make as little sense as "Physics of the Crust" '. We are not there yet, but we have made significant steps in this direction in the last ten years. No geophysicist now would entertain the idea that the Earth is composed of homogeneous onion shells. The analysis of data provided by more and better seismographic nets has, not surprisingly, revealed the heterogeneous structure of the depths of the Earth and made clear that the apparent simplicity of the lower mantle was essentially due to its remoteness. We also know more about the core.

Mineral physics has become an essential part of geophysics and the progress of experimental high-pressure and high-temperature techniques has provided new results, solved old problems and created new ones. Samples of high-pressure phases prepared in laser-heated diamond-anvil cells or large-volume presses are now currently studied by X-ray diffraction, using synchrotron beams, and by transmission electron microscopy. In ten years, we have thus considerably increased our knowledge of the deep minerals, including iron at core pressures. We know more about their thermoelastic properties, their phase transitions and their melting curves. Concurrently, quantum mechanical *ab-initio* computer methods have made such progress as to be able to reproduce the values of physical quantities in the temperature- and pressure-ranges that can be experimentally reached, and therefore predict with confidence their values at deep-Earth conditions.

In this new edition, I have therefore expanded the chapters on equations

of state, on melting, and the last chapter on Earth models. Close to two-hundred-and-fifty new references have been added.

I thank Dr Brian Watts of CUP, my copy editor, for a most thorough review of the manuscript.

1999 *Jean-Paul Poirier*

Introduction to the first edition

> The interior of the Earth is a problem at once fascinating and baffling, as one may easily judge from the vast literature and the few established facts concerning it.
>
> *F. Birch, J. Geophys. Res., 57, 227 (1952)*

This book is about the inaccessible interior of the Earth. Indeed, it is because it is inaccessible, hence known only indirectly and with a low resolving power, that we can talk of the physics of the interior of the Earth. The Earth's crust has been investigated for many years by geologists and geophysicists of various persuasions; as a result, it is known with such a wealth of detail that it is almost meaningless to speak of the crust as if it were a homogeneous medium endowed with averaged physical properties, in a state defined by simple temperature and pressure distributions. We have the physics of earthquake sources, of sedimentation, of metamorphism, of magnetic minerals, and so forth, but no physics of the crust.

Below the crust, however, begins the realm of inner earth, less well known and apparently simpler: a world of successive homogeneous spherical shells, with a radially symmetrical distribution of density and under a predominantly hydrostatic pressure. To these vast regions, we can apply macroscopic phenomenologies such as thermodynamics or continuum mechanics, deal with energy transfers using the tools of physics, and obtain Earth models – seismological, thermal, or compositional. These models, such as they were until, say, about 1950, accounted for the gross features of the interior of the Earth: a silicate mantle whose density increased with depth as it was compressed, with a couple of seismological discontinuities inside, a liquid iron core where convection currents generated the Earth's magnetic field, and a small solid inner core.

The physics of the interior of the Earth arguably came of age in the 1950s,

when, following Bridgman's tracks, Birch at Harvard University and Ringwood at the Australian National University started investigating the high-pressure properties and transformations of the silicate minerals. Large-volume multi-anvil presses were developed in Japan (see Akimoto 1987) and diamond-anvil cells were developed in the United States (see Bassett 1977), allowing the synthesis of minerals at the static pressures of the lower mantle, while shock-wave techniques (see Ahrens 1980) produced high dynamic pressures. It turn out, fortunately, that the wealth of mineral architecture that we see in the crust and uppermost mantle reduces to a few close-packed structures at very high pressures.

It is now possible to use the arsenal of modern methods (e.g. spectroscopies from the infrared to the hard X-rays generated in synchrotrons) to investigate the physical properties of the materials of the Earth at very high pressures, thus giving a firm basis to the averaged physical properties of the inner regions of the Earth deduced from seismological or geomagnetic observations and allowing the setting of constraints on the energetics of the Earth.

It is the purpose of this book to introduce the groundwork of condensed matter physics, which has allowed, and still allows, the improvement of Earth models. Starting with the indispensable, if somewhat arid, phenomenological background of thermodynamics of solids and continuum mechanics, we will relate the macroscopic observables to crystalline physics; we will then deal with melting, phase transitions, and transport properties before trying to synthetically present the Earth models of today.

The role of laboratory experimentation cannot be overestimated. It is, however, beyond the scope of this book to present the experimental techniques, but references to review articles will be given.

In a book such as this one, which topic to include or reject is largely a matter of personal, hence debatable, choice. I give only a brief account of the phase transitions of minerals in a paragraph that some readers may well find somewhat skimpy; I chose to do so because this active field is in rapid expansion and I prefer outlining the important results and giving recent references to running the risk of confusing the reader. Also, little is known yet about the mineral reactions in the transition zone and the lower mantle, so I deal only with the polymorphic, isochemical transitions of the main mantle minerals, thus keeping well clear of the huge field of experimental petrology.

It is hoped that this book may help with the understanding of how condensed matter physics may be of use in improving Earth models. It will

also probably become clear that the simplicity of the inner Earth is only apparent; with the progress of laboratory experimental techniques as well as observational seismology, geochemistry, and geomagnetism, we may perhaps expect that someday "physics of the interior of the Earth" will make as little sense as "physics of the crust."

1

Background of thermodynamics of solids

1.1 Extensive and intensive conjugate quantities

The physical quantities used to define the state of a system can be scalar (e.g. volume, hydrostatic pressure, number of moles of constituent), vectorial (e.g. electric or magnetic field) or tensorial (e.g. stress or strain). In all cases, one may distinguish extensive and intensive quantities. The distinction is most obvious for scalar quantities: extensive quantities are size-dependent (e.g. volume, entropy) and intensive quantities are not (e.g. pressure, temperature).

Conjugate quantities are such that their product (scalar or contracted product for vectorial and tensorial quantities) has the dimension of energy (or energy per unit volume, depending on the definition of the extensive quantities), (Table 1.1). By analogy with the expression of mechanical work as the product of a force by a displacement, the intensive quantities are also called *generalized forces* and the extensive quantities, *generalized displacements*.

If the state of a single-phase system is defined by N extensive quantities e_k and N intensive quantities i_k, the differential increase in energy per unit volume of the system for a variation of e_k is:

$$dU = \sum_k i_k de_k \tag{1.1}$$

The intensive quantities can therefore be defined as partial derivatives of the energy with respect to their conjugate quantities:

$$i_k = \frac{\partial U}{\partial e_k} \tag{1.2}$$

For the extensive quantities, we have to introduce the Gibbs potential

Table 1.1. *Some examples of conjugate quantities*

Intensive quantities	i_k	Extensive quantities	e_k
Temperature	T	Entropy	S
Pressure	P	Volume	V
Chemical potential	μ	Number of moles	n
Electric field	$\mathscr{E}$	Displacement	$\mathbf{D}$
Magnetic field	$\mathbf{H}$	Induction	$\mathbf{B}$
Stress	σ	Strain	ε

(see below):

$$G = U - \sum_k i_k e_k \tag{1.3}$$

$$dG = \sum_k i_k de_k - d\sum_k i_k e_k = -\sum_k e_k di_k \tag{1.4}$$

and we have:

$$e_k = -\frac{\partial G}{\partial i_k} \tag{1.5}$$

Conjugate quantities are linked by *constitutive relations* that express the response of the system in terms of one quantity, when its conjugate is made to vary. The relations are usually taken to be linear and the proportionality coefficient is a *material constant* (e.g. elastic moduli in Hooke's law).

In general, starting from a given state of the system, if all the intensive quantities are arbitrarily varied, the extensive quantities will vary (and vice-versa). As a first approximation, the variations are taken to be linear and systems of linear equations are written (Zwikker, 1954):

$$di_k = K_{k1} de_1 + K_{k2} de_2 + \cdots + K_{kn} de_n \tag{1.6}$$

or

$$de_k = \kappa_{k1} di_1 + \kappa_{k2} di_2 + \cdots + \kappa_{kn} di_n \tag{1.7}$$

The constants:

$$\kappa_{kl} = \left(\frac{\partial e_k}{\partial i_l}\right)_{i1, \ldots, in, \, except \, il} \tag{1.8}$$

are called *compliances*, (e.g. compressibility), and the constants:

$$K_{lk} = \left(\frac{\partial i_l}{\partial e_k}\right)_{e1, \ldots, en, \text{ except } ek} \tag{1.9}$$

are called *stiffnesses* (e.g. bulk modulus).

Note that, in general,

$$K_{lk} \neq \frac{1}{\kappa_{kl}}$$

The linear approximation, however, holds only locally for small values of the variations about the reference state, and we will see that, in many instances, it cannot be used. This is in particular true for the relation between pressure and volume, deep inside the Earth: very high pressures create finite strains and the linear relation (Hooke's law) is not valid over such a wide range of pressure. One, then, has to use more sophisticated equations of state (see below).

1.2 Thermodynamic potentials

The energy of a thermodynamic system is a state function, i.e. its variation depends only on the initial and final states and not on the path from the one to the other. The energy can be expressed as various potentials according to which extensive or intensive quantities are chosen as independent variables. The most currently used are: the *internal energy* E, for the variables volume and entropy, the *enthalpy* H, for pressure and entropy, the *Helmholtz free energy* F, for volume and temperature and the *Gibbs free energy* G, for pressure and temperature:

$$E \tag{1.10}$$

$$H = E + PV \tag{1.11}$$

$$F = E - TS \tag{1.12}$$

$$G = H - TS \tag{1.13}$$

The differentials of these potentials are total exact differentials:

$$dE = TdS - PdV \tag{1.14}$$

$$dH = TdS + VdP \tag{1.15}$$

$$dF = -SdT - PdV \tag{1.16}$$

$$dG = -SdT + VdP \tag{1.17}$$

The extensive and intensive quantities can therefore be expressed as partial differentials according to (1.2) and (1.5):

$$T = \left(\frac{\partial E}{\partial S}\right)_V = \left(\frac{\partial H}{\partial S}\right)_P \tag{1.18}$$

$$S = -\left(\frac{\partial F}{\partial T}\right)_V = -\left(\frac{\partial G}{\partial T}\right)_P \tag{1.19}$$

$$P = -\left(\frac{\partial E}{\partial V}\right)_S = -\left(\frac{\partial F}{\partial V}\right)_T \tag{1.20}$$

$$V = \left(\frac{\partial H}{\partial P}\right)_S = \left(\frac{\partial G}{\partial P}\right)_T \tag{1.21}$$

In accordance with the usual convention, a subscript is used to identify the independent variable that stays fixed.

From the first principle of thermodynamics, the differential of internal energy dE of a closed system is the sum of a heat term $dQ = TdS$ and a mechanical work term $dW = -PdV$. The internal energy is therefore the most physically understandable thermodynamic potential; unfortunately, its differential is expressed in terms of the independent variables entropy and volume that are not the most convenient in many cases. The existence of the other potentials H, F and G has no justification other than being more convenient in specific cases. Their expression is not gratuitous, nor does it have some deep and hidden meaning. It is just the result of a mathematical transformation (Legendre's transformation), whereby a function of one or more variables can be expressed in terms of its partial derivatives, which become independent variables (see Callen, 1985).

The idea can be easily understood, using as an example a function y of a variable x: $y = f(x)$. The function is represented by a curve in the (x, y) plane (Fig. 1.1), and the slope of the tangent to the curve at point (x, y) is: $p = dy/dx$. The tangent cuts the y-axis at the point of coordinates $(0, \phi)$ and its equation is: $\phi = y - px$. This equation represents the curve defined as the envelope of its tangents, i.e. as a function of the derivative p of $y(x)$.

In our case, we deal with a surface that can be represented as the envelope of its tangent planes. Supposing we want to express $E(S, V)$ in terms of T and P, we write the equation of the tangent plane:

$$\phi = E - \left(\frac{\partial E}{\partial V}\right)_S V - \left(\frac{\partial E}{\partial S}\right)_V S = E + PV - TS = G$$

In geophysics, we are mostly interested in the variables T and P; we will therefore mostly use the Gibbs free energy.

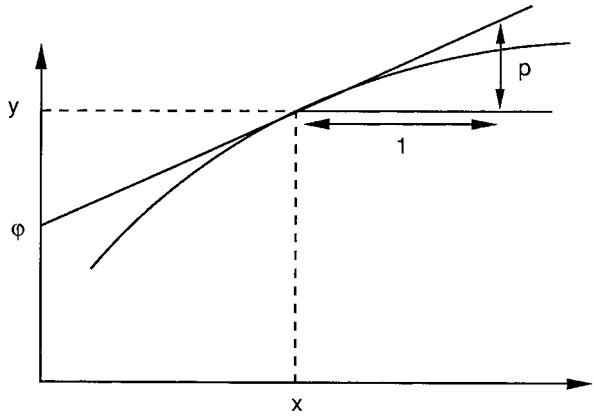

Figure 1.1 Legendre's transformation: the curve $y = f(x)$ is defined as the envelope of its tangents of equation $\phi = y - px$.

1.3 Maxwell's relations. Stiffnesses and compliances

The potentials are functions of state and their differentials are total exact differentials. The second derivatives of the potentials with respect to the independent variables do not depend on the order in which the successive derivatives are taken. Starting from equations (1.18)–(1.21), we therefore obtain *Maxwell's relations*:

$$-\left(\frac{\partial S}{\partial P}\right)_T = \left(\frac{\partial V}{\partial T}\right)_P \tag{1.22}$$

$$\left(\frac{\partial S}{\partial V}\right)_T = \left(\frac{\partial P}{\partial T}\right)_V \tag{1.23}$$

$$\left(\frac{\partial T}{\partial P}\right)_S = \left(\frac{\partial V}{\partial S}\right)_P \tag{1.24}$$

$$\left(\frac{\partial T}{\partial V}\right)_S = -\left(\frac{\partial P}{\partial S}\right)_V \tag{1.25}$$

Other relationships between the second partial derivatives can be obtained, using the chain rule for the partial derivatives of a function $f(x, y, z) = 0$:

$$\left(\frac{\partial x}{\partial y}\right)_z \cdot \left(\frac{\partial y}{\partial z}\right)_x \cdot \left(\frac{\partial z}{\partial x}\right)_y = -1 \tag{1.26}$$

For instance, assuming a relation $f(P, V, T) = 0$, we have:

Table 1.2. *Derivatives of extensive* (S, V) *and intensive* (T, P) *quantities*

$\left(\frac{\partial S}{\partial T}\right)_V = \frac{C_V}{T}$	$\left(\frac{\partial S}{\partial V}\right)_T = \alpha K_T$	$\left(\frac{\partial S}{\partial P}\right)_V = \frac{C_P}{\alpha K_S T}$
$\left(\frac{\partial S}{\partial T}\right)_P = \frac{C_P}{T}$	$\left(\frac{\partial S}{\partial V}\right)_P = \frac{C_P}{\alpha V T}$	$\left(\frac{\partial S}{\partial P}\right)_T = -\alpha V$
$\left(\frac{\partial T}{\partial S}\right)_V = \frac{T}{C_V}$	$\left(\frac{\partial T}{\partial V}\right)_S = -\frac{\alpha K_S T}{C_P}$	$\left(\frac{\partial T}{\partial P}\right)_V = \frac{1}{\beta P}$
$\left(\frac{\partial T}{\partial S}\right)_P = \frac{T}{C_P}$	$\left(\frac{\partial T}{\partial V}\right)_P = \frac{1}{\alpha V}$	$\left(\frac{\partial T}{\partial P}\right)_S = \frac{\alpha V T}{C_P}$
$\left(\frac{\partial P}{\partial T}\right)_V = \alpha K_T$	$\left(\frac{\partial P}{\partial V}\right)_S = -\frac{K_S}{V}$	$\left(\frac{\partial P}{\partial S}\right)_T = -\frac{1}{\alpha V}$
$\left(\frac{\partial P}{\partial T}\right)_S = \frac{C_P}{\alpha V T}$	$\left(\frac{\partial P}{\partial V}\right)_T = -\frac{K_T}{V}$	$\left(\frac{\partial P}{\partial S}\right)_V = \frac{\alpha K_S T}{C_P}$
$\left(\frac{\partial V}{\partial T}\right)_S = -\frac{C_P}{\alpha K_S T}$	$\left(\frac{\partial V}{\partial P}\right)_S = -\frac{V}{K_S}$	$\left(\frac{\partial V}{\partial S}\right)_T = \frac{1}{\alpha K_T}$
$\left(\frac{\partial V}{\partial T}\right)_P = \alpha V$	$\left(\frac{\partial V}{\partial P}\right)_T = -\frac{V}{K_T}$	$\left(\frac{\partial V}{\partial S}\right)_P = \frac{\alpha V T}{C_P}$

$$\left(\frac{\partial V}{\partial T}\right)_P = -\left(\frac{\partial V}{\partial P}\right)_T \cdot \left(\frac{\partial P}{\partial T}\right)_V \tag{1.27}$$

With Maxwell's relations, the chain rule yields relations between all derivatives of the intensive and extensive variables with respect to one another (Table 1.2). Second derivatives are given in Stacey (1995).

We must be aware that Maxwell's relations involved only conjugate quantities, but that by using the chain rule, we introduce derivatives of intensive or extensive quantities with respect to non-conjugate quantities. These will have a meaning only if we consider cross-couplings between

fields (e.g. thermoelastic coupling, see Section 2.3) and the material constants correspond to second-order effects (e.g. thermal expansion).

In Zwikker's notation, the second derivatives of the potentials are stiffnesses and compliances (Section 1.1):

$$K_{lk} = \frac{\partial i_l}{\partial e_k} = \frac{\partial^2 U}{\partial e_l \partial e_k} \tag{1.28}$$

$$\kappa_{kl} = \frac{\partial e_k}{\partial i_l} = \frac{\partial^2 G}{\partial i_k \partial i_l} \tag{1.29}$$

It follows, since the order of differentiations can be reversed, that:

$$K_{lk} = K_{kl} \tag{1.30}$$

$$\kappa_{kl} = \kappa_{lk} \tag{1.31}$$

Inspection of Table 1.2 shows that, depending on which variables are kept constant when the derivative is taken, we define isothermal, K_T, and adiabatic, K_S, bulk moduli and isobaric, C_P, and isochoric, C_V, specific heats. We must note here that the adiabatic bulk modulus is a stiffness, whereas the isothermal bulk modulus is the reciprocal of a compliance, hence they are not equal (Section 1.1); similarly, the isobaric specific heat is a compliance, whereas the isochoric specific heat is the reciprocal of a stiffness.

Table 1.2 contains extremely useful relations, involving the thermal and mechanical material constants, which we will use throughout this book. Note that, here and throughout the book, V is the specific volume. We will also use the specific mass ρ, with $V\rho = 1$. Often loosely called density, the specific mass is numerically equal to density only in unit systems in which the specific mass of water is equal to unity.

2

Elastic moduli

2.1 Background of linear elasticity

We will rapidly review here the most important results and formulas of linear (Hookean) elasticity. For a complete treatment of elasticity, the reader is referred to the classic books on the subject (Love, 1944; Brillouin, 1960; Nye, 1957). See also Means (1976) for a clear treatment of stress and strain at the beginner's level.

Let us start with the definition of infinitesimal strain (a general definition of finite strain will be given in Chapter 4). We define the tensor of infinitesimal strain ε_{ij}, $(i,j = 1,2,3)$, as the symmetrical part of the displacement gradient tensor $\partial u_i/\partial x_j$, where the u_is are the components of the displacement vector of a point of coordinates x_j, (Fig. 2.1):

$$\varepsilon_{ij} = \frac{1}{2}\left(\frac{\partial u_i}{\partial x_j} + \frac{\partial u_j}{\partial x_i}\right) \tag{2.1}$$

The trace of the strain tensor is the *dilatation* (positive or negative):

$$\mathrm{Tr}\varepsilon_{ij} = \sum_k \varepsilon_{kk} = \frac{\partial u_1}{\partial x_1} + \frac{\partial u_2}{\partial x_2} + \frac{\partial u_3}{\partial x_3} = \mathrm{div}\,\mathbf{u} \cong \frac{\Delta V}{V} \tag{2.2}$$

The components σ_{ij} of the stress tensor are defined in the following way: Let us consider a volume element around a point in a solid submitted to surface and/or body forces. If we cut the volume element by a plane normal to the coordinate axis i and remove the part of the solid on the side of the positive axis, its action on the volume element can be replaced by a force, whose components along the axis j is σ_{ij} (Fig. 2.2). In the absence of body torque, the stress tensor is symmetrical.

The trace of the stress tensor is equal to three times the *hydrostatic pressure*:

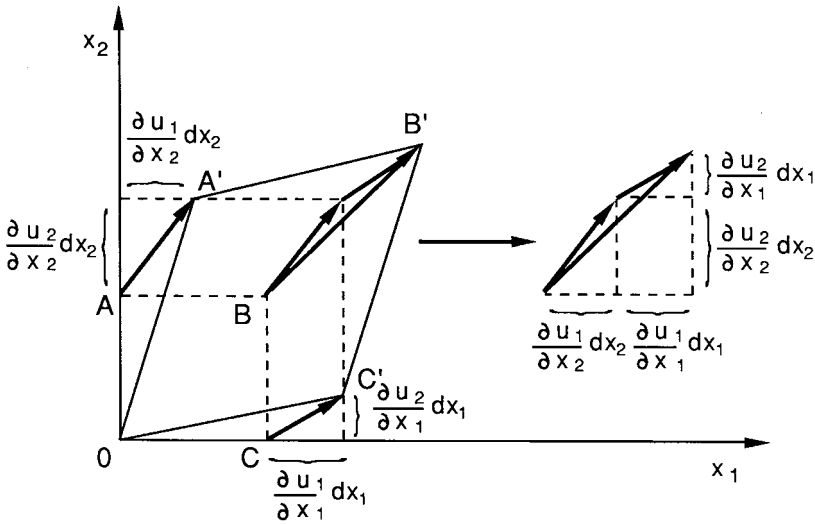

Figure 2.1 Components of the displacement gradient tensor in the case of infinitesimal plane strain. The components of the strain tensor are:

$$\varepsilon_{11} = \partial u_1/\partial x_1,\ \varepsilon_{22} = \partial u_2/\partial x_2,\ \varepsilon_{12} = \tfrac{1}{2}(\partial u_1/\partial x_2 + \partial u_2/\partial x_1) = \varepsilon_{21}$$

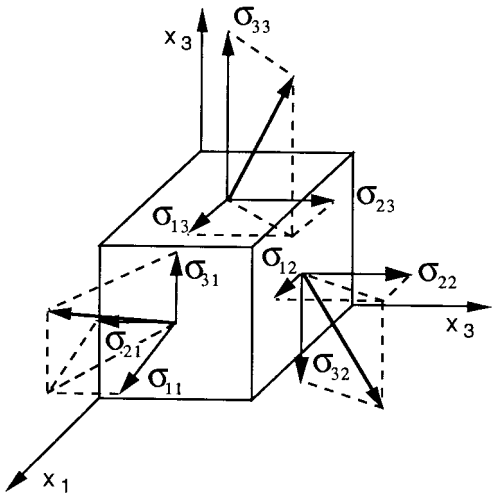

Figure 2.2 Components of the stress tensor σ_{ij}. The bold vectors represent the force per unit area exerted on the volume element by the (removed) part of the solid on the positive side of the normal to the corresponding plane.

$$\mathrm{Tr}\,\sigma_{ij} = \sigma_{11} + \sigma_{22} + \sigma_{33} = 3P \tag{2.3}$$

Hence the hydrostatic pressure is:

$$P = \frac{1}{3}\sum_k \sigma_{kk} \tag{2.4}$$

2.2 Elastic constants and moduli

For an isotropic, homogeneous solid and infinitesimal strains, there is a linear constitutive relation between the second order tensors of stress and strain, that expresses the response of an elastic solid to the application of stress or strain, starting from an initial, "natural", stress- and strain-free state

$$\sigma_{ij} = \sum_{kl} c_{ijkl}\varepsilon_{kl} \tag{2.5}$$

This is Hooke's law. The fourth-order symmetrical tensor c_{ijkl} is the *elastic constants* tensor. Due to the fact that the stress and strain tensors are symmetrical, the most general elastic constants tensor has only 21 non-zero independent components. For crystals, the number of independent elastic constants decreases as the symmetry of the crystalline system increases and it reduces to three for the cubic system *:

$$c_{1111} = c_{11},\ c_{1122} = c_{12},\ c_{2323} = c_{44}$$

* The elastic constants are usually expressed in contracted notation, pairs of indices being replaced by one index according to the correspondence rule:

$$11 \to 1,\ 22 \to 2,\ 33 \to 3,\ 23 = 32 \to 4,\ 13 = 31 \to 5,\ 12 = 21 \to 6.$$

In what follows, we will mostly give examples relative to cubic crystals, for the sake of simplicity and also because many of the most important minerals of the deep Earth are cubic (spinel, garnet, magnesiowüstite, ideal silicate perovskites).

For an isotropic system (e.g. an aggregate of crystals in various random orientations), the number of independent elastic constants reduces to two. Hooke's law is then conveniently expressed as:

$$\sigma_{ij} = \lambda\delta_{ij}\sum_k \varepsilon_{kk} + 2\mu\varepsilon_{ij} \tag{2.6}$$

where δ_{ij} is equal to 1 if $i = j$ and to zero if $i \neq j$, $\Sigma_k\varepsilon_{kk} = \Delta V/V$ is the trace of the strain tensor, λ and μ are the two independent *Lamé constants*, defined by:

$$\mu = c_{44} \text{ (the } \textit{shear modulus}\text{)}$$

and:

$$\lambda + 2\mu = c_{11}$$

hence:

$$\lambda = c_{12} = c_{11} - 2c_{44}$$

Note that c_{11}, c_{12} and c_{44} here are the three non-independent elastic constants of the isotropic aggregate, not the three independent constants of cubic crystals.

The elastic properties of an isotropic material can be described by *elastic moduli*, which consist of any two convenient functions of λ and μ.

The elastic moduli most currently used in solid earth geophysics are (see Weidner, 1987, for a review of the experimental methods of determination of the elastic moduli):

- The *shear modulus* μ.
- The *bulk modulus* or *incompressibility* K, defined (Table 1.2) by:

$$K = -V\frac{dP}{dV} = -\frac{dP}{d\ln V} \tag{2.7}$$

In linear elasticity, when a pressure P is applied to a solid in the natural state, the corresponding relative volume change is given by:

$$\frac{\Delta V}{V} = -\frac{P}{K} \tag{2.8}$$

Hence, from (2.6):

$$K = \frac{3\lambda + 2\mu}{3} \tag{2.9}$$

- *Poisson's ratio* ν, defined in a regime of uniaxial stress σ_{11}, as minus the ratio of the strain normal to the stress axis, $\varepsilon_{22} = \varepsilon_{33}$, to the strain along the stress axis, ε_{11} (i.e. ratio of thinning to elongation or thickening to contraction, if $\nu > 0$):

$$\nu = \frac{-\varepsilon_{22}}{\varepsilon_{11}} = \frac{-\varepsilon_{33}}{\varepsilon_{11}} \tag{2.10}$$

Poisson's ratio, being dimensionless, is not strictly speaking a modulus, but it is a combination of elastic moduli and it can be used,

together with any one modulus to completely define the elastic properties of a body. Indeed, using (2.6) and writing $\sigma_{22} = \sigma_{33} = 0$, we obtain:

$$\nu = \frac{\lambda}{2(\lambda + \mu)} \tag{2.11}$$

and, with (2.9):

$$\nu = \frac{3K - 2\mu}{2(3K + \mu)} = \frac{3(K/\mu) - 2}{2[3(K/\mu) + 1]} \tag{2.12}$$

In many cases, especially in the Earth's crust, it so happens that $\lambda = \mu$, i.e. there is only one independent elastic modulus (a Cauchy solid); then $\nu = 0.25$.

If the solid is incompressible ($K = \infty$), then, from (2.12), $\nu = 0.5$. The same result can of course be obtained with the definition of ν, by writing $\Delta V/V = \varepsilon_1 + 2\varepsilon_2 = 0$. Note that for a liquid $\mu = 0$, hence we also have $\nu = 0.5$, but that does not mean that the liquid is incompressible. Also, it is important to realize that Poisson's ratio results from a complicated combination of elastic constants and can take widely different values depending on the material. A value of ν close to 0.5 does not mean that there is some proportion of fluid present: solid gold, for instance, at room temperature, has a Poisson's ratio of about 0.42. Poisson's ratio can be negative, if cracks are present in the body. For an infinitely compressible solid ($K = 0$), we would have $\nu = -1$.

We therefore have the bounds on Poisson's ratio:

$$-1 < \nu < 0.5 \tag{2.13}$$

Poisson's ratio is especially interesting in geophysics, since it can be expressed as a function of the ratio v_P/v_S of the velocities of the longitudinal (P) and transverse (S) elastic waves only . We have:

$$v_P = \left(\frac{\lambda + 2\mu}{\rho}\right)^{1/2} = \left(\frac{K + \frac{4}{3}\mu}{\rho}\right)^{1/2} \tag{2.14}$$

$$v_S = \left(\frac{\mu}{\rho}\right)^{1/2} \tag{2.15}$$

hence:

$$\frac{v_P}{v_S} = \left(\frac{\lambda + 2\mu}{\mu}\right)^{1/2} \tag{2.16}$$

From (2.16) and (2.11), we have:

$$\nu = \frac{\left(\frac{v_P}{v_S}\right)^2 - 2}{2\left[\left(\frac{v_P}{v_S}\right)^2 - 1\right]} \tag{2.17}$$

The condition $\nu = 0.25$ corresponds to $v_P = v_S\sqrt{3}$, which is frequently obtained in the crust.

Let us remind the reader here that (2.14) and (2.15) can be derived from Newton's equation of motion of a unit volume element of a continuum medium:

$$\rho \frac{\partial^2 \mathbf{u}}{\partial t^2} = \mathbf{F} \tag{2.18}$$

where $\mathbf{u}$ is the displacement vector, ρ the specific mass and $\mathbf{F}$ the force that balances the stress on the volume element, given by:

$$F_i = \sum_j \frac{\partial \sigma_{ij}}{\partial x_j} \tag{2.19}$$

We will here write the equation of motion in the simple case of a longitudinal wave propagating in the x_1 direction ($u_1 = u$, $u_2 = u_3 = 0$, $\partial u_1/\partial x_1 = \partial u/\partial x$, $\partial u_1/\partial x_2 = \partial u_1/\partial x_3 = 0$) and a shear wave polarized along x_2 and propagating along x_1 ($u_1 = u$, $u_2 = u_3 = 0$, $\partial u_1/\partial x_2 = \partial u/\partial x$, $\partial u_1/\partial x_1 = \partial u_1/\partial x_3 = 0$).

From (2.1), (2.6), (2.18) and (2.19), we have for the longitudinal wave:

$$\sigma_{11} = (\lambda + 2\mu)\frac{\partial u_1}{\partial x_1}$$

and:

$$\rho \frac{\partial^2 u}{\partial t^2} = (\lambda + 2\mu)\frac{\partial^2 u}{\partial x^2} \tag{2.20}$$

and for the shear wave ($u_1 = u_3 = 0$, $u_2 = u$):

$$\sigma_{21} = \mu \frac{\partial u_2}{\partial x_1}$$

and:

$$\rho \frac{\partial^2 u}{\partial t^2} = \mu \frac{\partial^2 u}{\partial x^2} \tag{2.21}$$

The wave equations (2.20) and (2.21) correspond to waves propagating with velocities given by (2.14) and (2.15) respectively.

Here is a good opportunity to introduce the *seismic parameter* Φ, which we will frequently use later on:

$$\Phi = \frac{K}{\rho} \tag{2.22}$$

It is related to v_Φ, the propagation velocity of the hydrostatic part of the strain (dilatation), given by:

$$v_\Phi = \left(\frac{K}{\rho}\right)^{1/2} = \left(\frac{3\lambda + 2\mu}{3\rho}\right)^{1/2} \tag{2.23}$$

Hence:

$$\Phi = v_P^2 - \tfrac{4}{3}v_S^2 \tag{2.24}$$

Note that:

$v_\Phi < v_P$ in solids, for $\lambda + 2\mu/3 < \lambda + 2\mu$.
$v_\Phi = v_P$ in liquids, for $\mu = 0$ (the strain is purely dilatational)

We can find another useful expression for Φ from the definition of K, (2.7):

$$K = -\frac{dP}{d\ln V} = \frac{dP}{d\ln \rho} = \rho\frac{dP}{d\rho} \tag{2.25}$$

where $\rho = 1/V$ is the specific mass, hence:

$$\Phi = \frac{dP}{d\rho} \tag{2.26}$$

The bulk modulus K is, by definition, isotropic. The average bulk modulus of a single-phase aggregate of anisotropic crystals is therefore the same as the bulk modulus of the single crystals and it can easily be found from the experimentally determined elastic constants.

For cubic crystals:

$$K = \frac{c_{11} + 2c_{12}}{3} \tag{2.27}$$

The problem of calculating the effective shear moduli of an aggregate from the single-crystal elastic constants is, however, much more difficult and, indeed, it has no exact solution; all we know is that the aggregate value lies between two bounds (see Watt *et al.*, 1976): a lower bound calculated assuming that the stress is uniform in the aggregate and that the strain is the total sum of all the strains of the individual grains in series (*Reuss bound*), and an upper bound calculated assuming that the strain is uniform and that the stress is supported by the individual grains in parallel (*Voigt bound*). The arithmetic average of the two bounds is often used (*Voigt–Reuss–Hill average*).

Variational methods allow the calculation of the tighter *Hashin–Shtrikman bounds* (Watt *et al.*, 1976; Watt, 1988).

For cubic crystals, with elastic constants c_{11}, c_{12}, c_{44}, there are two shear moduli, c and c' corresponding to shear on the $\{100\}$ and $\{110\}$ planes respectively:

$$c = c_{44}$$
$$c' = \tfrac{1}{2}(c_{11} - c_{12})$$

The effective Reuss and Voigt shear moduli of a single-phase aggregate are:

$$\mu_R = \frac{15}{6/c' + 9/c} \tag{2.28a}$$

$$\mu_V = \frac{1}{5}(2c' + 3c) \tag{2.28b}$$

Expressions for the effective moduli of aggregates of crystals with lower symmetry can be found in Sumino and Anderson (1984).

The lower and upper Hashin–Shtrikman bounds are:

$$\mu_L = c' + \frac{3}{5}(2c - c' - 4\beta) \tag{2.29a}$$

$$\mu_U = c + \frac{2}{5}(c' - c - 6\beta') \tag{2.29b}$$

with:

$$\beta = \frac{3}{5}\frac{K + 2c'}{c'(3K + 4c')}$$

$$\beta' = \frac{3}{5}\frac{K + 2c}{c(3K + 4c)}$$

A compilation of elastic constants and averaged aggregate moduli for a number of mantle minerals as a function of temperature is given in Anderson and Isaak (1995). The single-crystal elastic constants and aggregate (Hashin–Shtrikman) moduli of San Carlos olivine were measured up to 1500 K (Isaak, 1992), and at room temperature, for pressures up to 17 GPa (Abramson *et al.*, 1997) and up to 32 GPa (Zha *et al.*, 1998a, see Fig. 2.3). The elastic moduli of forsterite Mg_2SiO_4 and its high-pressure polymorph, wadsleyite, were measured up to the pressures of the transition zone (Li *et*

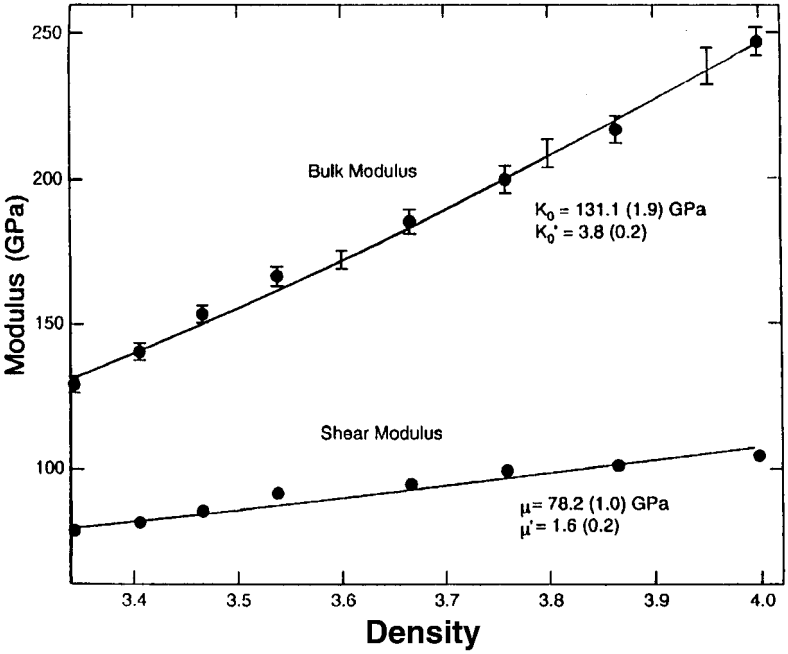

Figure 2.3 Aggregate bulk and shear moduli (Hashin–Shtrikman averages) of San Carlos olivine as a function of density. Experimental points are fitted to a third-order Birch–Murnaghan equation of state (after Zha *et al.*, 1998a).

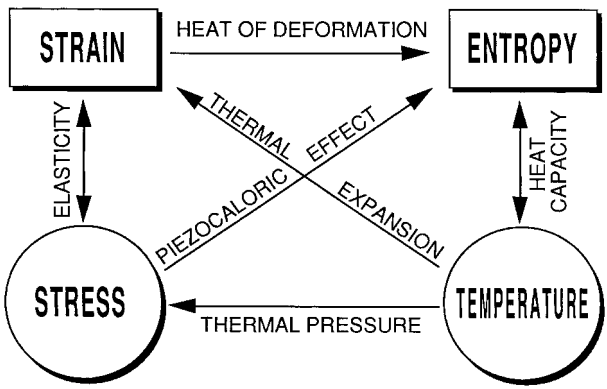

Figure 2.4 Schema of the coupling between thermal and mechanical variables (after Nye, 1957).

al., 1996; Zha *et al*., 1998b). Chen *et al*. (1998) measured the elastic constants of periclase (MgO) at simultaneous high temperature and pressure, up to 1600 K and 8 GPa.

2.3 Thermoelastic coupling

2.3.1 Generalities

All the extensive and intensive variables, conjugate or not, can be cross-coupled in many ways and the couplings are responsible for a variety of first- and second-order physical effects, e.g. thermoelastic or piezoelectric effects (see Nye, 1957).

We will deal here only with thermoelastic coupling (Fig. 2.4) and derive the expressions for the isothermal and adiabatic bulk moduli.

2.3.2 Isothermal and adiabatic moduli

Let us assume that the intensive variables σ_{ij} and T depend only on the two extensive variables ε_{kl} and S and that we can write the coupled equations for the differentials (Nye, 1957):

$$d\sigma_{ij} = \left(\frac{\partial \sigma_{ij}}{\partial \varepsilon_{kl}}\right)_S d\varepsilon_{kl} + \left(\frac{\partial \sigma_{ij}}{\partial S}\right)_\varepsilon dS \tag{2.30}$$

$$dT = \left(\frac{\partial T}{\partial \varepsilon_{kl}}\right)_S d\varepsilon_{kl} + \left(\frac{\partial T}{\partial S}\right)_\varepsilon dS \tag{2.31}$$

Let us consider only the simple scalar case (geophysically relevant) of hydrostatic pressure: $\sigma_{ij} = \delta_{ij} P$ and isotropic compression $\varepsilon = \Delta V/V$.

We can then write (2.30) and (2.31) as:

$$dP = \left(\frac{\partial P}{\partial \varepsilon}\right)_S d\varepsilon + \left(\frac{\partial P}{\partial S}\right)_\varepsilon dS \tag{2.32}$$

$$dT = \left(\frac{\partial T}{\partial \varepsilon}\right)_S d\varepsilon + \left(\frac{\partial T}{\partial S}\right)_\varepsilon dS \tag{2.33}$$

Dividing both sides of (2.32) by $d\varepsilon$:

$$\frac{dP}{d\varepsilon} = \left(\frac{\partial P}{\partial \varepsilon}\right)_S + \left(\frac{\partial P}{\partial S}\right)_\varepsilon \frac{dS}{d\varepsilon} \tag{2.34}$$

Let us consider the isothermal case, and assume $dT = 0$ in (2.33). We find:

$$\frac{dS}{d\varepsilon} = -\frac{\left(\frac{\partial T}{\partial \varepsilon}\right)_S}{\left(\frac{\partial T}{\partial S}\right)_\varepsilon} \tag{2.35}$$

Carrying (2.35) into (2.34), we get:

$$\left(\frac{dP}{d\varepsilon}\right)_T = \left(\frac{\partial P}{\partial \varepsilon}\right)_S - \left(\frac{\partial P}{\partial S}\right)_\varepsilon \left(\frac{\partial S}{\partial T}\right)_\varepsilon \left(\frac{\partial T}{\partial \varepsilon}\right)_S$$

$$\left(\frac{dP}{d\varepsilon}\right)_T = \left(\frac{\partial P}{\partial \varepsilon}\right)_S - \left(\frac{\partial P}{\partial T}\right)_\varepsilon \left(\frac{\partial T}{\partial \varepsilon}\right)_S \tag{2.36}$$

Now:

$$\left(\frac{\partial P}{\partial \varepsilon}\right)_T = K_T \quad \text{[isothermal bulk modulus]}$$

$$\left(\frac{\partial P}{\partial \varepsilon}\right)_S = K_S \quad \text{[adiabatic bulk modulus]}$$

and:

$$\left(\frac{\partial T}{\partial \varepsilon}\right)_S = -\left(\frac{\partial T}{\partial V}\right)_S V$$

Hence:

$$K_T - K_S = \left(\frac{\partial P}{\partial T}\right)_\varepsilon \left(\frac{\partial T}{\partial V}\right)_S V \tag{2.37}$$

We find in Table 1.2 that:

$$\left(\frac{\partial P}{\partial T}\right)_V = \left(\frac{\partial P}{\partial T}\right)_\varepsilon = \alpha K_T$$

$$\left(\frac{\partial T}{\partial V}\right)_S = -\frac{\alpha K_S T}{C_P}$$

hence:

$$K_S - K_T = \alpha K_T T\left(\frac{\alpha K_S V}{C_P}\right) \tag{2.38}$$

The dimensionless parameter in brackets is the *thermodynamic Grüneisen parameter* (see Chapter 3):

$$\gamma_{\text{th}} \equiv \frac{\alpha K_S V}{C_P} \tag{2.39}$$

Hence:

$$\frac{K_S}{K_T} = 1 + \gamma_{\text{th}} \alpha T \tag{2.40}$$

Now, from Table 1.2, we see that:

$$\left(\frac{\partial P}{\partial S}\right)_V = \frac{\alpha K_S T}{C_P} \tag{2.41}$$

We also see that:

$$\left(\frac{\partial P}{\partial T}\right)_V = \alpha K_T \tag{2.42}$$

and:

$$\left(\frac{\partial T}{\partial S}\right)_V = \frac{T}{C_V} \tag{2.43}$$

Hence, from (2.41), (2.42) and (2.43):

$$\left(\frac{\partial P}{\partial T}\right)_V \left(\frac{\partial T}{\partial S}\right)_V = \left(\frac{\partial P}{\partial S}\right)_V = \frac{\alpha K_T T}{C_V} = \frac{\alpha K_S T}{C_P} \tag{2.44}$$

and:

$$\frac{C_P}{C_V} = \frac{K_S}{K_T} = 1 + \gamma_{\text{th}} \alpha T \tag{2.45}$$

Incidentally, we note that:

$$\gamma_{\text{th}} = \frac{\alpha K_S V}{C_P} = \frac{\alpha K_T V}{C_V} \tag{2.46}$$

Zwikker (1954) gives a general formulation for calculating the difference between a stiffness and the reciprocal of a compliance. Starting from the linear equations (1.6) between intensive and extensive quantities:

$$di_1 = K_{11} de_1 + K_{12} de_2 \tag{2.47}$$

$$di_2 = K_{21} de_1 + K_{22} de_2 \tag{2.48}$$

and the definition:

$$K_{11} = \left(\frac{\partial i_1}{\partial e_1}\right)_{e_2} \tag{2.49}$$

we can calculate $1/\kappa_{11} = (\partial i_1/\partial e_1)_{i_2}$ by putting $di_2 = 0$ in (2.48), from which we obtain:

$$de_2 = -\frac{K_{21}}{K_{22}} de_1 \tag{2.50}$$

Substituting in (2.47):

$$di_1 = \left(K_{11} - \frac{K_{12}^2}{K_{22}}\right) de_1 \tag{2.51}$$

hence:

$$\left(\frac{\partial i_1}{\partial e_1}\right)_{i_2} = \frac{1}{\kappa_{11}} = K_{11} - \frac{K_{12}^2}{K_{22}} \tag{2.52}$$

or:

$$K_{11} - \frac{1}{\kappa_{11}} = \frac{K_{12}^2}{K_{22}} \tag{2.53}$$

For thermoelastic coupling, if subscript 1 corresponds to the elastic variables and subscript 2 to the thermal variables (i.e. $i_1 = P$, $i_2 = T$, $e_1 = \varepsilon$, $e_2 = S$):

$$K_{11} = K_S, \qquad \frac{1}{\kappa_{11}} = K_T, \qquad K_{12} = \left(\frac{\partial P}{\partial S}\right)_V, \qquad K_{22} = \left(\frac{\partial T}{\partial S}\right)_V$$

For unit volume, (2.53) is equivalent to (2.38) if we take (2.45) into account.

The difference between the bulk modulus at constant temperature and the bulk modulus at constant entropy (adiabatic) is not trivial since the elastic moduli measured in the laboratory by ultrasonic methods are adiabatic, as well as the ones derived from the seismic wave velocities (the transit time of the waves is too short to allow exchange of heat); on the other hand, the elastic moduli relevant to geodynamic processes on the scale of millions of years are evidently isothermal. However, for values of α and γ_{th} typical of Earth materials, the difference between K_T and K_S at room temperature is of the order of 1% only (Dewaele and Guyot, 1998).

It is interesting to remark that the adiabatic and isothermal shear moduli of an isotropic solid are identical to first order. The following hand-waving demonstra-

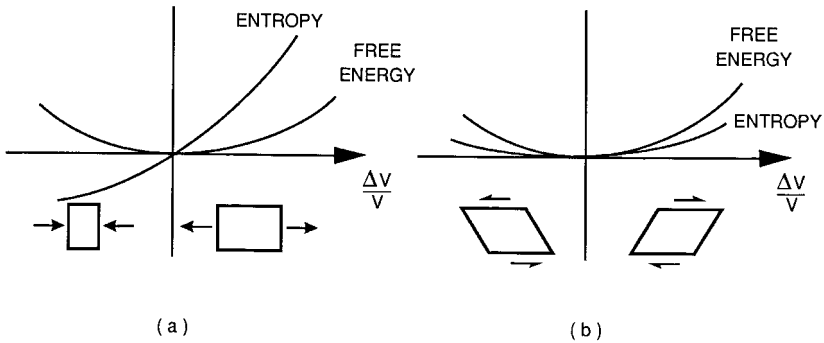

Figure 2.5 Variation of the entropy and free energy with elastic deformation: (a) extension–compression, and (b) shear (after Brillouin, 1940).

tion is borrowed from Brillouin (1940, p. 23).

Let us consider a solid of unit volume, at equilibrium. Its free energy is a minimum. Hence, if we impose a dilatation or a compression, the free energy increases in both cases. The free-energy curve has a horizontal tangent (Fig. 2.5(a)). However, due to thermoelastic coupling, the variation of entropy S is not symmetrical: dilatation ($\Delta V/V > 0$) absorbs heat ($\Delta S > 0$), whereas compression ($\Delta V/V < 0$) evolves heat ($\Delta S < 0$). If the entropy is kept constant, the temperature increases on compression and decreases on dilatation. The variation of pressure as a function of $\Delta V/V$ (bulk modulus) is therefore (as seen above) greater for constant entropy than for constant temperature.

Let us now turn to the case of shear strain. For symmetry reasons, at constant temperature, positive and negative shear are equivalent and correspond to an increase in entropy. Free energy and entropy are represented by curves with a minimum and a horizontal tangent (Fig. 2.5(b)). Hence, a shear isothermal transformation is also adiabatic to first order and $\mu_T \cong \mu_S$.

The variation of temperature with reversible adiabatic compression or dilatation is easily found by simple inspection of Table 1.2:

$$\left(\frac{\partial T}{\partial V}\right)_S = -\frac{\alpha K_S T}{C_P} = -\frac{\gamma_{\text{th}} T}{V} \tag{2.54}$$

$$\left(\frac{\partial \ln T}{\partial \ln V}\right)_S = -\gamma_{\text{th}} \tag{2.55}$$

or:

$$\left(\frac{\partial \ln T}{\partial \ln \rho}\right)_S = \gamma_{\text{th}} \tag{2.56}$$

We may note that for an adiabatic compression or decompression we have, from (2.55):

$$\left(\frac{T_2}{T_1}\right)_S = \left(\frac{V_1}{V_2}\right)^{\gamma_{th}} \tag{2.57}$$

This relation is known for perfect gases with $\gamma = C_P/C_V - 1$. For solids, we have from (2.45):

$$\gamma = \gamma_{th} = \frac{1}{\alpha T}\left(\frac{C_P}{C_V} - 1\right) \tag{2.58}$$

With the definition $K = dP/d\ln\rho$, we find a useful expression for the variation of temperature with pressure

$$\left(\frac{\partial T}{\partial P}\right)_S = \gamma_{th}\frac{T}{K_S} \tag{2.59}$$

which, of course, we could have found from Table 1.2 and the definition of γ_{th}.

2.3.3 Thermal pressure

Let us calculate the increase in internal pressure, ΔP_{th}, caused by heating a solid at constant volume (*thermal pressure*).

Table 1.2 gives:

$$\left(\frac{\partial P}{\partial T}\right)_V = \alpha K_T = \gamma_{th}\frac{C_V}{V} \tag{2.60}$$

Integrating at constant volume and supposing $\gamma_{th} = \text{const}$, we obtain:

$$\Delta P_{th} = P_2 - P_1 \cong \frac{\gamma_{th}}{V}\int_{T_1}^{T_2} C_V dT = \frac{\gamma_{th}}{V}(E_2 - E_1) = \gamma_{th}\frac{\Delta E}{V} \tag{2.61}$$

where E is the internal energy. Hence:

$$\Delta P_{th} = \gamma_{th}\frac{\Delta E}{V} \tag{2.62}$$

This is the *equation of state of Mie–Grüneisen*, to which we will return later. The Grüneisen parameter is defined here as the coefficient relating the thermal pressure to the thermal energy per unit volume:

$$\gamma_{th} = V\frac{\Delta P_{th}}{\Delta E} \tag{2.63}$$

Integration of (2.60) at constant volume also yields:

$$\Delta P_{\text{th}} = \int_{T_1}^{T_2} \alpha K_T dT \tag{2.64}$$

It is experimentally verified in many solids that αK_T is approximately independent of temperature (O. L. Anderson, 1995a). Equation (2.64) can then be written:

$$\Delta P_{\text{th}} = \alpha K_T \Delta T \tag{2.65}$$

or:

$$\frac{\Delta P_{\text{th}}}{K_T} = \frac{\Delta V}{V} = \alpha \Delta T \tag{2.66}$$

This is consistent with the definition of the thermal expansion coefficient. It could be said that thermal pressure causes thermal expansion when volume is not constrained to remain constant.

It is interesting to find the variation of αK_T with volume (Anderson *et al.*, 1995) and the conditions for which it is independent of volume, because in this case the thermal pressure depends only on temperature (O. L. Anderson, 1995b). The logarithmic derivative of αK_T:

$$\left(\frac{\partial \ln(\alpha K_T)}{\partial \ln V}\right)_T = \frac{\partial \ln \alpha}{\partial \ln V} + \frac{\partial \ln K_T}{\partial \ln V} \tag{2.67}$$

can be written:

$$\left(\frac{\partial \ln(\alpha K_T)}{\partial \ln V}\right)_T = \delta_T - K' \tag{2.68}$$

where:

$$\delta_T \equiv \frac{\partial \ln \alpha}{\partial \ln V} = -\frac{1}{\alpha}\left(\frac{\partial \ln K_T}{\partial T}\right)_P \tag{2.69}$$

is the Anderson–Grüneisen parameter (see Section 3.6), and:

$$K' \equiv \frac{\partial K_T}{\partial P} = -\frac{\partial \ln K_T}{\partial \ln V} \tag{2.70}$$

The condition $\delta_T - K' \approx 0$ is fulfilled for olivine between 300 K and 1500 K, and only above 1600 K for MgO (O. L. Anderson, 1995b).

3
Lattice vibrations

3.1 Generalities

In a crystal at temperatures above the absolute zero, atoms vibrate about their equilibrium positions. The crystal can therefore be considered as a collection of oscillators, whose global properties can be calculated. In particular, it will be interesting to determine:

(i) The normal modes of vibration of the crystal.
(ii) The dispersion relation, i.e. the relation $\omega = f(\mathbf{k})$ between the frequency ω and the wave vector $\mathbf{k}$.
(iii) The vibrational energy.

The vibrational approach is especially fruitful since it allows a synthesis between the thermal and elastic properties and gives a physical basis to thermoelastic coupling. This is due to the fact that the low-frequency, long-wavelength part of the vibrational spectrum corresponds to elastic waves, whereas the high-frequency part corresponds to thermal vibrations. In finite crystals, the lattice vibrations are quantized and behave as quasi-particles: the *phonons*.

In the following section, we will give the elementary basis of the calculations in the simple case of a monatomic lattice. This will be sufficient to introduce the concepts and formulas needed for our purpose. For a more complete and still elementary treatment, the reader is referred to the standard textbooks by Kittel (1967) and Ziman (1965).

3.2 Vibrations of a monatomic lattice

3.2.1 Dispersion curve of an infinite lattice

Let us consider an infinite crystalline lattice formed of only one kind of atoms. Furthermore, let us assume that the lattice is a very simple one and

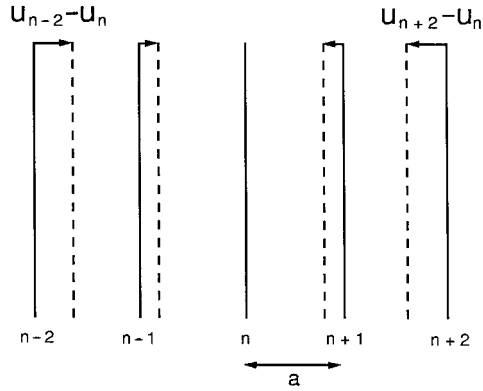

Figure 3.1 Parallel identical lattice planes of an infinite crystalline lattice. The displacement of plane $n + i$ with respect to plane n is $u_{n+i} - u_n$.

can be described as an infinite stacking of identical, equally spaced, lattice planes. Each atomic plane, of mass M, is labeled by an index n and is connected to all the other planes $n + p$ (p positive or negative can become infinite) by a symmetrical pair-interaction potential $V_{n,n+p}$ (Fig. 3.1).

Let us now consider a longitudinal planar wave propagating normal to the planes, (the reasoning would be the same for a shear wave). The displacements $u_{n\pm1}, \ldots, u_{n\pm p}$ are counted from an arbitrary origin taken at plane n and they are assumed to be infinitesimal.

Plane n is in the potential of all the other planes $\Sigma_p V_{n,n+p}$, that can be expanded to second order in powers of $(u_n - u_{n+p})$:

$$\sum_p V_{n,n+p} = \sum_p V^0 + \frac{1}{2}\sum_p \frac{\partial^2 V_{n,n+p}}{\partial u_n^2}(u_{n+p} - u_n)^2 + \cdots \tag{3.1}$$

The potential is assumed to be symmetrical; this is an important constraint that will be lifted later on.

The potential well corresponding to a symmetrical potential truncated after the second order is therefore parabolic. This is the *harmonic approximation*, the vibrations of the planes are harmonic, like those of a mass–spring system, as we will see presently.

Plane n is subjected to a force F_n given by:

$$F_n = -\frac{\partial}{\partial u_n}\left(\sum_p V_{n,n+p}\right) = \sum_p \frac{\partial^2 V_{n,n+p}}{\partial u_n^2}(u_{n+p} - u_n) \tag{3.2}$$

or:

$$F_n = \sum_p K_p(u_{n+p} - u_n) \tag{3.3}$$

with a force constant:

$$K_p = \frac{\partial^2 V_{n,n+p}}{\partial u_n^2} = V''_p \tag{3.4}$$

The force is linear in displacement as in the case of a harmonic mass–spring system with a force constant K.

If we had only a pair of planes of mass M, Newton's equation would give the equation for a harmonic oscillator:

$$M\frac{d^2u}{dt^2} + Ku = 0$$

with a restoring force: $F = -dE/du$, which corresponds to a parabolic potential well:

$$E = \frac{Ku^2}{2} + \text{const}$$

(i) Dispersion relations

Let us consider the motion of plane n of mass M in the potential of the other planes. The equation of motion is:

$$M\frac{d^2u_n}{dt^2} = \sum_p K_p(u_{n+p} - u_n) \tag{3.5}$$

Let us look for progressive plane wave solutions:

$$u_n = u^0 \exp i(n\mathbf{k}\cdot\mathbf{a} - \omega t) \tag{3.6}$$

where $\mathbf{a}$ is the interplanar distance at rest, i.e. the period of the lattice (Fig. 3.1).

Let us carry u_n into the equation of motion:

$$-\omega^2 M u^0 \exp i(n\mathbf{k}\cdot\mathbf{a} - \omega t) =$$
$$\sum_p K_p u^0[\exp i(n+p)\mathbf{k}\cdot\mathbf{a} - \exp in\mathbf{k}\cdot\mathbf{a}] \exp(-i\omega t)$$

or:

$$\omega^2 M = -\sum_p K_p \exp(ip\mathbf{k}\cdot\mathbf{a} - 1) \tag{3.7}$$

All planes being identical, we have $K_p = K_{-p}$ and we can write:

$$\omega^2 M = -\sum_{p>0} K_p[\exp(ip\mathbf{k}\cdot\mathbf{a}) + \exp(-ip\mathbf{k}\cdot\mathbf{a}) - 2] \tag{3.8}$$

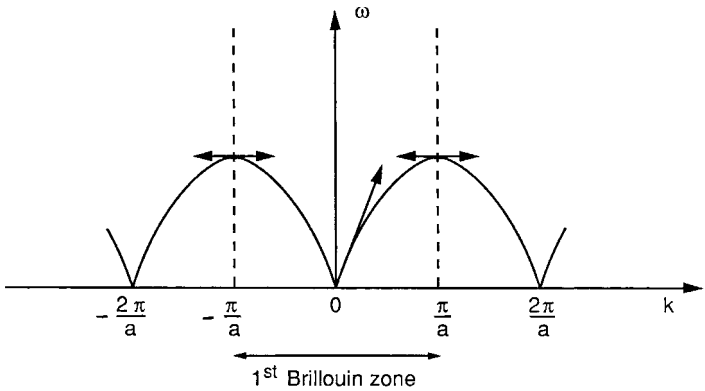

Figure 3.2 Dispersion curve of the lattice of Fig. 3.1. In the center of the Brillouin zone, for long wavelengths, the frequency ω is proportional to the wave number k, Hence, the group velocity of the lattice waves is equal to the phase velocity of sound. At the edge of the Brillouin zone, the group velocity is zero, that is, the waves do not propagate.

and remembering (3.4) that $K_p = V_p''$:

$$\omega^2 = \frac{2}{M} \sum_{p>0} V_p''(1 - \cos p\mathbf{k}\cdot\mathbf{a}) \tag{3.9}$$

This is the dispersion relation for the infinite crystal. We will discuss it, without loss of generality, in the simple case where the interaction is limited to the nearest-neighbor planes ($p = 1$). We have then:

$$\omega^2 = \frac{2}{M} V''(1 - \cos \mathbf{k}\cdot\mathbf{a}) = \frac{4}{M} V'' \sin^2\left(\frac{\mathbf{k}\cdot\mathbf{a}}{2}\right)$$

or:

$$\omega = 2\left(\frac{V''}{M}\right)^{1/2} \left|\sin\left(\frac{\mathbf{k}.\mathbf{a}}{2}\right)\right| \tag{3.10}$$

The dispersion curve is given in Fig. (3.2).

We can make the following observations:

(i) $\omega = f(\mathbf{k})$ is periodic with the period $|\mathbf{g}| = |2\pi/\mathbf{a}|$, equal by definition to the period of the reciprocal lattice. The interval $-\pi/a, +\pi/a$ defines the first *Brillouin zone*.

(ii) $\omega = f(\mathbf{k})$ is a symmetrical function. It is therefore sufficient to specify it in the interval $0, \pi/a$.

(iii) At the edge of the Brillouin zone, i.e. for $|\mathbf{k}| = (2n + 1)\pi/a =$

$(n + 1/2)|\mathbf{g}|$, the frequency is a maximum:

$$\omega = \omega_{\max} = 2\left(\frac{V''}{M}\right)^{1/2} \tag{3.11}$$

(The maximum atomic vibrational frequency is of the order of 10^{13} Hz.)

At the maximum, $d\omega/dk = 0$, which means that the group velocity of the waves vanishes. The only permissible wave is a stationary wave that does not propagate energy:

$$u_n = u^0 \exp i[(n + \tfrac{1}{2})\mathbf{k}\cdot\mathbf{a} - \omega t] = \pm u^0 \exp(-i\omega t) \tag{3.12}$$

The neighboring planes vibrate with opposite phases.

(iv) Near the origin, at very low frequencies and long wavelengths, i.e. for $\omega \ll \omega_{\max}$ (in practice, $\omega < 10^9$ Hz), we have: $\lambda \gg a$ and $|\mathbf{k}| \ll 1/a$.

The neighboring planes vibrate almost in phase and we can write:

$$\omega \cong ak\left(\frac{V''}{M}\right)^{1/2} \tag{3.13}$$

The frequency is proportional to the wave number. In other terms, in the long-wavelength limit, the group velocity $d\omega/dk$ is equal to the phase velocity: there is no dispersion. The phase velocity is equal to the velocity v_{P} of the longitudinal wave:

$$\frac{d\omega}{dk} = a\left(\frac{V''}{M}\right)^{1/2} = \frac{\omega}{k} = v_{\mathrm{P}} \tag{3.14}$$

Indeed, if the wave vector k is much smaller than the reciprocal lattice parameter, i.e. if the lattice parameter in real space is much smaller than the wavelength, it is reasonable to assimilate the lattice to an elastic continuum in which the wave equation for longitudinal waves is (2.20) and the velocity of the waves is given by (2.14):

$$v_{\mathrm{P}} = \left(\frac{\lambda + 2\mu}{\rho}\right)^{1/2}$$

The reasoning would, of course, be the same for transverse waves. Indeed, there are three dispersion curves, one for the P-waves and one for each polarization of the S-waves.

Comparing the classic expression (2.14) for the velocity of the P-waves with (3.14), we see that the relevant elastic modulus is proportional to the

second derivative of the potential energy with respect to strain. Therefore, the elastic constants, introduced as phenomenological material constants in the thermodynamic approach, can be physically interpreted in terms of interatomic potentials.

As an example, let us calculate the value of the bulk modulus K_0 at 0 K (no thermal energy), for a simple ionic crystal like NaCl (Kittel, 1967). The pair-interaction potential E_{ij} between neighboring ions of opposite charge consists of an attractive Coulombic part and a short-range repulsive part due to the ion cores:

$$E_{ij} = \frac{q_i q_j}{r_{ij}} + \frac{ZB}{r_{ij}^n} \tag{3.15}$$

Here q_i and q_j are the electric charges of ion i and its neighbor j, r_{ij} is the distance between the ions, Z is the coordination number and B and n are parameters of the repulsive part of the potential (Born potential).

The *cohesive energy* E_c of the crystal is obtained by summing the attractive parts of the potential (a somewhat complicated process) and assuming that the short-range repulsive part extends only to nearest neighbors:

$$E_c = N\left(-\frac{\alpha q^2}{R} + \frac{ZB}{R^n}\right) \tag{3.16}$$

where $\alpha \equiv \Sigma_j(\pm) R/r_{ij}$ is the *Madelung constant* ($\alpha \cong 1.75$ for the NaCl structure), R is the nearest-neighbor distance, $q = q_i = -q_j$ is the electric charge, and N is the total number of ions of one sign.

At equilibrium, the nearest-neighbor distance is R_0 given by: $(dE_c/dR)_{R=R_0} = 0$ and we have then:

$$R_0^{n-1} = \frac{nZB}{\alpha q^2} \tag{3.17}$$

Hence:

$$E_c = -\frac{N\alpha q^2}{R_0}\left[\frac{R_0}{R} - \frac{1}{n}\left(\frac{R_0}{R}\right)^n\right] \tag{3.18}$$

We can now calculate $K_0 = -V\left(\frac{dP}{dV}\right)_{R=R_0}$.

From $P = -\left(\frac{\partial E}{\partial V}\right)_S$, we get $\left(\frac{\partial P}{\partial V}\right)_S = -\left(\frac{\partial^2 E}{\partial V^2}\right)_S$ and $K_0 = V\frac{\partial^2 E}{\partial V^2}$.

For the NaCl structure, we have $N = 4$ formula units per face centered cubic unit cell, each occupying a volume $a^3/4$ ($a = 2R$ is the cell parameter), hence $V = 2NR^3$.

$$\frac{dE_c}{dV} = \frac{dE_c}{dR}\frac{dR}{dV} = \frac{dE}{dR}\frac{1}{6NR^2}$$

$$\frac{d^2E_c}{dV^2} = \frac{d^2E_c}{dR^2}\left(\frac{dR}{dV}\right)^2 + \frac{dE_c}{dR}\frac{d^2R}{dV^2}$$

At equilibrium, $dE/dR = 0$ and $R = R_0$, hence:

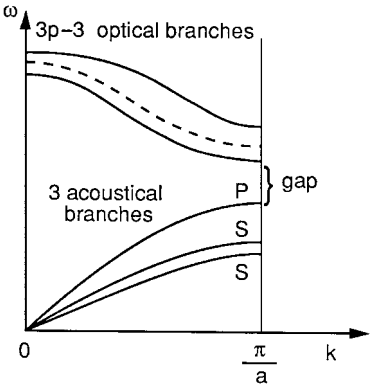

Figure 3.3 Dispersion curve (half of the first Brillouin zone) of an infinite lattice with p atoms per primitive unit cell. there are three acoustical modes (one P mode and two S modes polarized at right angles) and $3p - 3$ optical modes. There is a gap of forbidden energies at the edge of the Brillouin zone.

$$K_0 = V\left(\frac{1}{6NR^2}\right)^2 \left(\frac{d^2E_c}{dR^2}\right)_{R=R_0} = \frac{1}{18NR_0}\left(\frac{d^2E_c}{dR^2}\right)_{R=R_0} \tag{3.19}$$

From (3.16) , (3.17) and (3.19) we obtain:

$$K_0 = \frac{1}{R_0^3}\frac{\alpha q^2(n-1)}{18R_0} \tag{3.20}$$

In the general case of an infinite crystal, with p atoms per primitive unit cell (not necessarily of the same chemical nature), it can be shown (see Kittel, 1967) that for each value of the wave number k, there are $3p$ frequencies, each corresponding to one normal mode. There are:

Three acoustical modes corresponding to one longitudinal (P) mode and two transverse (S) modes, if they are pure. The modes are orthogonal to one another.

$3p - 3$ optical modes corresponding to out-of-phase vibrations of neighboring planes for small wave numbers. The optical modes often have frequencies in the range of that of infrared or visible light and can cause optical absorption, hence their name. Near the edge of the Brillouin zone, there is a forbidden gap (Fig. 3.3).

3.2.2 Density of states of a finite lattice

In the case of a finite lattice, the number of degrees of freedom, hence of possible normal modes, is finite and the vibrations are quantized: instead of

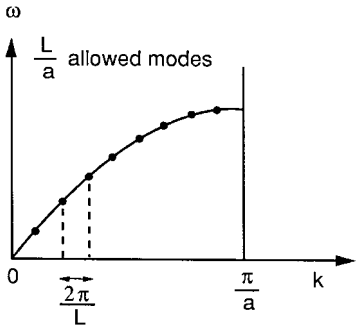

Figure 3.4 Dispersion "curve" of a finite unidimensional lattice of length L and period a; it consists of L/a discrete points, one for each allowed mode.

continuous dispersion curves, we have a succession of discrete points, one for every one of the allowed wave numbers (Fig. 3.4).

We also need boundary conditions: For a crystal large enough compared with the interatomic distance a, the boundary conditions chosen do not matter much as long as there are boundary conditions. The ones currently used are the Born–von Karman periodic boundary conditions: For N parallel planes in the crystal, we impose that the vibrational state of the N^{th} (last) plane be the same as that of the first, which amounts to ideally closing the crystal on itself (as a hypertorus in 4-D space), hence imposing a period N:

$$u_{n+N} = u_n$$

We have therefore:

$$u^0 \exp i(n\mathbf{k}\cdot\mathbf{a} - \omega t) = u^0 \exp i[(n+N)\mathbf{k}\cdot\mathbf{a} - \omega t]$$

hence:

$$\exp iN\mathbf{k}\cdot\mathbf{a} = 1$$

or:

$$N\mathbf{k}\cdot\mathbf{a} = 2m\pi$$

with m an integer (positive or negative).

The length of the crystal is $L = Na$. The allowed modes therefore have wave numbers given by:

$$k = 2m\pi/L \tag{3.21}$$

and the number of allowed wave numbers is:

Table 3.1. *Volume and mass of the various subunits in a polyatomic crystal*

Unit	Volume	Mass	Number of subunits
Mole	V	ρV	Unit cells: V/V_L Formulas: $VZ/V_L = N_A$ Atoms: $nN_A = VZn/V_L$
Unit cell	V_L	ρV_L	Formulas: Z Atoms: Zn
Formula ("molecule")	$V_L/Z = V/N_A$	$\rho V_L/Z = M$	Atoms: n
Atoms	V/nN_A	$M/n = \bar{M}$	

$$\frac{2\pi}{a}\left(\frac{2\pi}{L}\right)^{-1} = \frac{L}{a} = N \tag{3.22}$$

Let us now generalize this result to three-dimensional reciprocal space (k-space) and consider, for the sake of simplicity, the case of a crystal of volume V and primitive unit cell volume V_L, where subscript L stands for "lattice".

The volume of the Brillouin zone is: $(2\pi)^3/V_L$, and the volume per allowed wave number in k-space is: $(2\pi)^3/V$. There are, therefore, V/V_L allowed values of k in the Brillouin zone.

The *density of states* $g(\omega)$ is the number of modes per unit frequency range. The number of vibrational states between ω and $\omega + d\omega$ is therefore:

$$g(\omega)d\omega = w(k)dk \tag{3.23}$$

where $w(k)dk$ is the number of states in k-space in a spherical shell of thickness dk, between k and $k + dk$. If (Table 3.1) we take the volume of the crystal equal to the molar volume V, and if the crystal has n atoms per formula unit and Z unit cells per mole, there are nN_A atoms in the mole (N_A is Avogadro's number) and $3nN_A$ modes in the volume of the Brillouin zone (see Kieffer, 1979a). We have:

$$w(k)dk = \frac{3nN_A V_L}{(2\pi)^3}\cdot 4\pi k^2 dk = \frac{3nZV}{(2\pi)^3}\cdot 4\pi k^2 dk$$

We will now calculate the density of states in the case of the very useful Debye approximation.

3.3 Debye's approximation

3.3.1 Debye's frequency

Debye's approximation consists in assuming that the long wave or continuum approximation, with a linear dispersion curve $\omega = \bar{v}k$ (where $\bar{v}$ is an average velocity of sound waves), holds for the whole vibrational spectrum. In other words, all the modes are considered to be acoustic, with the same average value of the velocity. The allowed ks are assumed to be uniformly distributed in the Brillouin zone. If we take for the volume V of the crystal the molar volume, the crystal contains nN_A atoms, where n is the number of atoms in the formula unit and N_A is Avogadro's number.

The density of states (3.23) is therefore given by:

$$g(\omega) = \frac{3nZV}{(2\pi)^3} \cdot 4\pi \frac{\omega^2}{\bar{v}^3}$$

or

$$g(\omega) = A\omega^2 \tag{3.24}$$

with

$$A = \frac{3nZV}{2\pi^2 \bar{v}^3} \tag{3.25}$$

The curve of the density of states vs frequency is the vibrational spectrum. We see that in Debye's approximation it is parabolic (Fig. 3.5).

Debye's calculation of the average sound velocity gives:

$$\bar{v} = \sqrt[3]{3} \left(\frac{1}{v_P^3} + \frac{2}{v_S^3} \right)^{-1/3} \tag{3.26}$$

O. L. Anderson (1963) showed that the Debye average sound velocity is accurately estimated by using the Voigt–Reuss–Hill averaging method (see Section 2.2) for calculating the longitudinal and transverse sound velocities v_P and v_S from single-crystal elastic constants.

The Brillouin zone is assumed to have the simple shape of a sphere with radius k_D given by:

$$\frac{4}{3}\pi k_D^3 = \frac{(2\pi)^3}{V_L}$$

The maximum radius k_D corresponds to a maximum cut-off frequency ω_D, called *Debye frequency*: $\omega_D = k_D \bar{v}$.

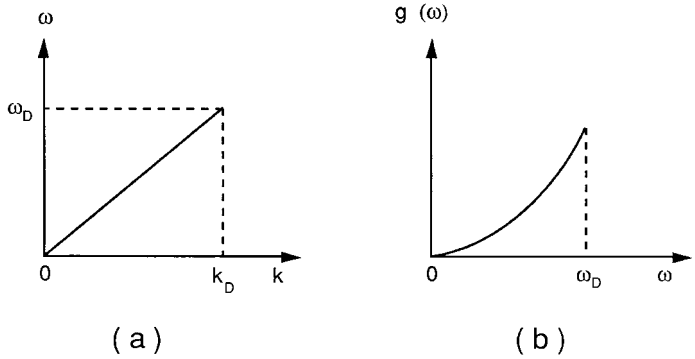

Figure 3.5 Dispersion curve (a) and vibrational spectrum (b) in the case of the Debye approximation. The vibrational spectrum is the curve of the density of states $g(\omega)$ vs frequency. ω_D and k_D are the Debye frequency and wave number respectively.

$$\omega_D = \bar{v}\left(\frac{6\pi^2}{V_L}\right)^{1/3} = \bar{v}\left(\frac{6\pi^2 N_A}{Z}\right)^{1/3} V^{-1/3} \tag{3.27}$$

However, if we assume that all the different atoms play equivalent mechanical roles in the vibrations, it is then possible to consider the individual atom (of any chemical nature) as the vibrational unit. In that case, we can take for V_L the average volume of one atom:

$$V_L^{-1} = \frac{nN_A}{V} = \frac{nN_A\rho}{M}$$

where M is the mass of the formula unit.

Hence:

$$\omega_D = \bar{v}(6\pi^2 n N_A)^{1/3} V^{-1/3} \tag{3.28}$$

Introducing the mean atomic mass $\bar{M} = \dfrac{M}{n}$, we find the expression of Debye's frequency in general use (O. L. Anderson, 1988; Robie and Edwards, 1966):

$$\omega_D = (6\pi^2 N_A)^{1/3}\left(\frac{\rho}{\bar{M}}\right)^{1/3} \bar{v} \tag{3.29}$$

Since this approach assumes that there is only one atom per unit cell, it follows that all the modes are assumed to be acoustic, which is consistent with Debye's approximation.

3.3.2 Vibrational energy and Debye temperature

In the limit of the linear continuum approximation, the normal vibration modes are independent, hence the energy of one lattice mode (state) depends only on its frequency ω and on the number of quanta of vibration occupying that state (phonon occupancy). In thermal equilibrium, the phonon occupancy is given by the Bose–Einstein distribution, (phonons are bosons):

$$\langle n \rangle = \left[\exp\left(\frac{\hbar\omega}{k_B T} \right) - 1 \right]^{-1} \tag{3.30}$$

where $\hbar = \dfrac{h}{2\pi} = 1.0546 \times 10^{-34}\,\mathrm{J\,s}$ ($h = 6.626\,08 \times 10^{-34}\,\mathrm{J\,s}$ is Planck's constant) and $k_B = 1.380\,66 \times 10^{-23}\,\mathrm{J/K}$ is Boltzmann's constant.

The crystal, with all its modes of oscillation, can be considered as a collection of oscillators. *Einstein's approximation* assumes that all the oscillators have the same frequency; neglecting the zero-point energy, the energy of a crystal with N oscillators is therefore:

$$E = 3N\langle n \rangle \hbar\omega = 3N\hbar\omega \left[\exp\left(\frac{\hbar\omega}{k_B T} \right) - 1 \right]^{-1}$$

and the specific heat:

$$C_V = \left(\frac{dE}{dT} \right)_V = 3Nk_B \left(\frac{\hbar\omega}{k_B T} \right)^2 \exp\left(\frac{\hbar\omega}{k_B T} \right) \left[\exp\left(\frac{\hbar\omega}{k_B T} \right) - 1 \right]^{-2}$$

In *Debye's approximation*, we have various permissible frequencies: $\omega(k) \leq \omega_D$. The energy per oscillator (per mode) is equal to $\hbar\omega$; as we have $g(\omega)d\omega$ modes in the frequency range ω to $\omega + d\omega$, the energy (neglecting the zero-point energy) is:

$$E = \int_0^{\omega_D} \langle n(\omega, T) \rangle \hbar\omega g(\omega) d\omega \tag{3.31}$$

With (3.24), (3.25) and (3.30) we have:

$$E = \frac{3\hbar n Z V}{2\pi^2 \bar{v}^3} \int_0^{\omega_D} \frac{\omega^3 d\omega}{\exp\left(\dfrac{\hbar\omega}{k_B T} \right) - 1} \tag{3.32}$$

It is convenient to change variables and express (3.32) in terms of the non-dimensional variables $x = \hbar\omega/k_B T$ and $x_D = \Theta_D/T$, where Θ_D is the *elastic Debye temperature*, defined by:

$$\Theta_D = \frac{\hbar\omega_D}{k_B} \tag{3.33}$$

With (3.27):

$$\Theta_D = \frac{\hbar}{k_B}\left(\frac{6\pi^2 N_A}{Z}\right)^{1/3} V^{-1/3}\bar{v} = \frac{h}{k_B}\left(\frac{3N_A}{4\pi Z}\right)^{1/3} V^{-1/3}\bar{v} \tag{3.34}$$

which, if $Z = 1$, gives:

$$\Theta_D = 251.2 V^{-1/3}\bar{v} \tag{3.35}$$

with V in cm^3/mol and $\bar{v}$ in km/s given by (3.26).

With (3.28) and (3.29), i.e. if all the atoms play an equivalent mechanical role:

$$\Theta_D = \frac{h}{k_B}\left(\frac{3nN_A}{4\pi}\right)^{1/3} V^{-1/3}\bar{v} = \frac{h}{k_B}\left(\frac{3nN_A}{4\pi}\right)^{1/3}\left(\frac{\rho}{\bar{M}}\right)^{1/3}\bar{v} \tag{3.36}$$

or:

$$\Theta_D = 251.2\left(\frac{\rho}{\bar{M}}\right)^{1/3}\bar{v} \tag{3.37}$$

There are various more or less sophisticated ways of calculating Debye's temperature from elastic constants (Alers, 1965) or from specific heats (Blackman, 1955) (see below) and the resulting numerical values are often quite different. When comparing and using Debye's temperatures of various materials found in the literature, it is always advisable to check whether they have been calculated in the same way (e.g. using (3.35) or (3.37) see Table 3.2).

Using (3.34) we have:

$$E = \frac{3nZVk_B^4 T^4}{2\pi^2\hbar^3\bar{v}^3}\int_0^{x_D}\frac{x^3}{\exp x - 1}dx \tag{3.38}$$

or:

$$E = 9nN_A k_B T x_D^{-3}\int_0^{x_D}\frac{x^3}{\exp x - 1}dx \tag{3.39}$$

3.3.3 *Specific heat*

The specific heat or heat capacity at constant volume C_V is obtained by differentiating (3.39) with respect to temperature:

Table 3.2. *Physical constants of some typical and important crystals*

Material	Formula	ρ	$\bar{M}$	K_S	μ	v_P	v_S	$\bar{v}$	Θ_D	T_m
Iron[1]	Fe	7.87	55.85	172.7	83.1	6.00	3.25	3.63	474	1808
Nickel[1]	Ni	8.91	58.69	185.6	88.2	5.83	3.15	3.51	471	1726
Lead[1]	Pb	11.34	207.20	39.9	9.0	2.14	0.89	1.00	96	600
Copper[1]	Cu	8.92	63.55	144.9	49.4	4.86	2.35	2.64	345	1356
Diamond[1]	C	3.51	12.01	584.8	346.3	17.27	9.93	11.03	1839	3823
Silicon[1]	Si	2.33	28.09	97.9	66.7	8.95	5.35	5.92	649	1683
Halite[2]	NaCl	2.16	29.22	24.7	14.4	4.51	2.58	2.87	302	1075
Periclase[2]	MgO	3.58	20.15	162.8	129.4	9.68	6.01	6.63	936	3125
Stishovite[2]	SiO_2	4.29	20.03	277.4	232.2	11.70	7.36	8.10	1217	
Corundum[2]	Al_2O_3	3.99	20.39	251.9	162.0	10.83	6.37	7.06	1030	2345
Forsterite[2]	Mg_2SiO_4	3.21	20.10	128.2	80.5	8.57	5.00	5.55	757	2183
β-phase[3]	Mg_2SiO_4	3.47	20.10	174.0	114.0	9.69	5.73	6.35	888	
Spinel[4]	Mg_2SiO_4	3.56	20.10	184.0	119.0	9.81	5.78	6.41	904	
Pyrope[2]	$Mg_3Al_2Si_3O_{12}$	3.56	20.16	176.6	89.6	9.12	5.02	5.59	788	
Enstatite[2]	$MgSiO_3$	3.20	20.08	107.5	75.4	8.06	4.85	5.37	731	
Ilmenite[5]	$MgSiO_3$	3.80	20.08	212.0	132.0	10.10	5.89	6.54	943	
Perovskite[6]	$MgSiO_3$	4.11	20.08	246.4	184.2	10.94	6.69	7.39	1094	
Perovskite[2]	$CaTiO_3$	4.04	27.19	177.0	104.0	8.84	5.07	5.64	750	2248

Notes: Specific mass ρ in g/cm^3, mean atomic mass $\bar{M}$ in g/at. Melting temperature T_m and Debye temperature Θ_D calculated from (3.37), in Kelvin. Voigt–Reuss–Hill, at room temperature and ambient pressure, bulk modulus K_S and shear modulus μ in GPa. Velocities $\bar{v}$, v_P and v_S in km/s.

Sources: [1]Simmons and Wang (1971); [2]Sumino and Anderson (1984); [3]Sawamoto *et al.* (1984); [4]Weidner *et al.* (1984); [5]Weidner and Ito (1985); [6]Yeganeh-Haeri *et al.* (1989).

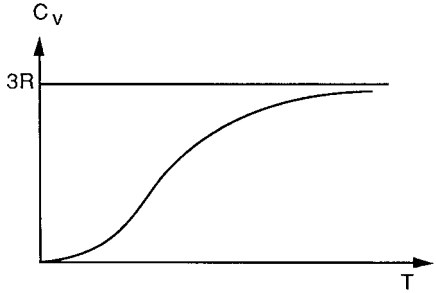

Figure 3.6 Typical curve of the specific heat at constant volume C_V vs temperature T. At low temperatures, C_V varies as T^3 and at high temperatures C_V approaches the classical Dulong and Petit value $3R$.

$$C_V = \left(\frac{\partial E}{\partial T}\right)_V = 9nN_A k_B x^{-3} \int_0^{x_D} \frac{x^4 \exp x}{(\exp x - 1)^2} dx \tag{3.40}$$

or:

$$C_V = 9nN_A k_B \mathscr{D}\left(\frac{\Theta_D}{T}\right) \tag{3.41}$$

The *Debye function* $\mathscr{D}\left(\frac{\Theta_D}{T}\right)$ is calculated and tabulated (e.g. in Landolt–Börnstein tables).

At $T \gg \Theta_D$ the heat capacity approaches the classical value given by the Dulong and Petit law:

$$C_V = 3nNk_B = 3nR \tag{3.42}$$

with the gas constant $R \cong 2\,\text{cal/mol K}$.

At low temperatures, the heat capacity is approximately equal to:

$$C_V \cong 234nNk_B\left(\frac{T}{\Theta_D}\right)^3 \tag{3.43}$$

(Debye's T^3 law).

The values of $C_V(T)$, (Fig. 3.6), can be experimentally determined by calorimetry and fitted to (3.41) by choosing the best value of the Debye temperature. The Debye temperature determined in this fashion is called the *calorimetric Debye temperature* (at temperature T).

3.3.4 Validity of Debye's approximation

Debye's approximation is only as good as its basic assumptions. It is

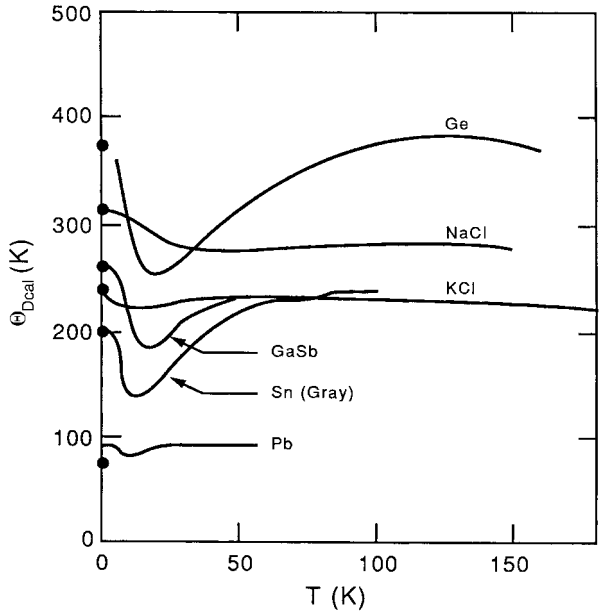

Figure 3.7 Variation with temperature of the calorimetric Debye temperature for a few simple substances. Elastic Debye temperatures at 0 K are shown by closed circles (after Kieffer, 1979).

therefore valid if the actual vibrational spectrum can reasonably be approximated by a parabolic curve $g(\omega)$ and if most of the spectrum corresponds to frequencies lower than the cut-off Debye frequency ω_D. If Debye's model is valid, then the calorimetric Debye temperature Θ_{Dcal} must be independent of temperature and equal to the elastic Debye temperature Θ_{Del} (usually calculated with (3.37) and reasonably assuming that the elastic constants, varying little with temperature, can be taken equal to their values at room temperature). This is practically the case for elements and simple close-packed substances, for which it can be reasonably assumed that all atoms are mechanically equivalent (Kieffer, 1979a) (Fig. 3.7). Plots of the ratio $\Theta_{Dcal}/\Theta_{Del}$ as a function of temperature, for minerals with open structures (Fig. 3.8) exhibit a dip at low temperatures corresponding to the actual presence of more low-frequency modes (optical modes) than are taken into account in Debye's model, and rise steadily at high temperatures, indicating an excess of modes near Debye's frequency and a deficit at higher frequencies in the model (Kieffer, 1979a). O. L. Anderson (1988) finds that Debye's model is satisfactory for close-packed minerals with a volume per atom $V_a = \bar{M}/\rho$ smaller than about $5.8\,cm^3/mol$, like

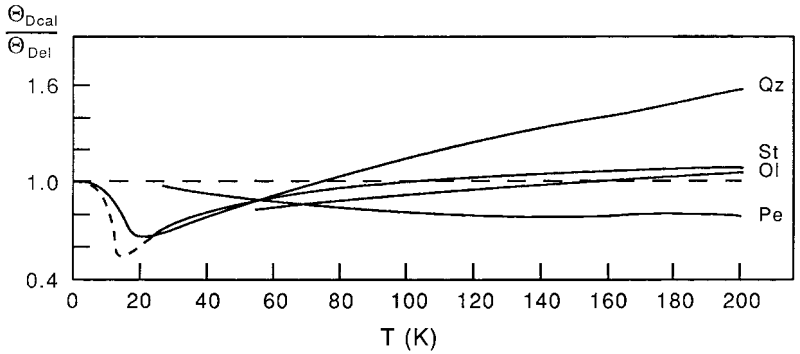

Figure 3.8 Variation with temperature of the ratio of the calorimetric to the elastic Debye temperatures for quartz (Qz), olivine (Ol), stishovite (St), and periclase (Pe) (after Kieffer, 1979).

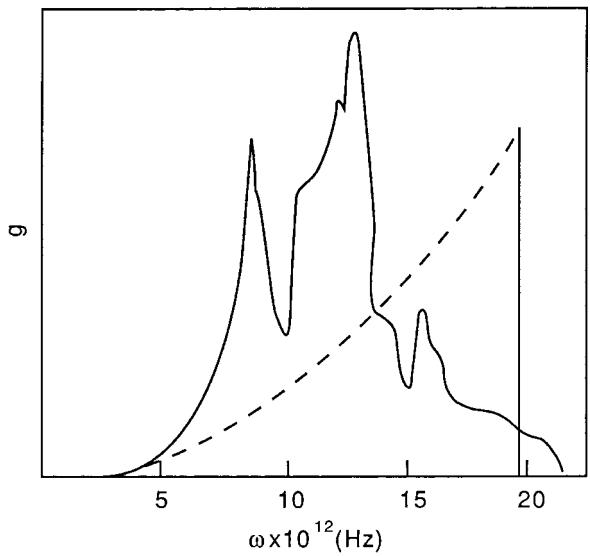

Figure 3.9 Vibrational spectrum (density of states) for periclase compared with the Debye spectrum (dashed curve). The frequencies of the modes, including the optical modes, are nearly all below the Debye frequency and both spectra converge at low frequencies (after O. L. Anderson, 1988).

stishovite, corundum and periclase (Fig. 3.9), since only a small fraction of the phonon spectrum has frequencies higher than the Debye cut-off frequency. This is also the case for the dense lower-mantle perovskite form of $MgSiO_3$ ($V_a = 4.8$), whose thermoelastic properties are satisfactorily accounted for by Debye's theory (O. L. Anderson, 1998) (Fig. 3.10).

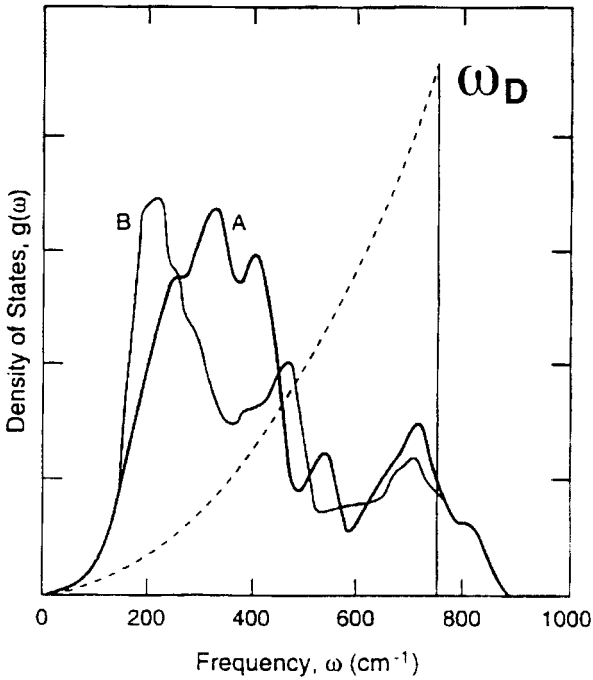

Figure 3.10 Calculated phonon density of states (two sets of calculations, A and B) for $MgSiO_3$ perovskite. The greater portion of the spectra is at frequencies lower than the Debye cut-off frequency ω_D. The dashed curve is the Debye spectrum (after O. L. Anderson, 1998).

Kieffer (1979a–c) developed a generalized model based on lattice dynamics and observational vibrational data (infrared and Raman spectroscopy, inelastic neutron scattering) that allows a better calculation of thermodynamic data of minerals (specific heat and entropy) than Debye's model.

3.4 Mie–Grüneisen equation of state

We have calculated, in Debye's approximation, the vibrational (i.e. thermal) energy of a solid. We are now in a position to calculate the total energy of the solid and its equation of state, i.e. the expression of pressure P as a function of specific volume V and temperature T.

Since $P = -(\partial F/\partial V)_T$, let us start with Helmholtz' free energy F and consider it as the sum of two terms:

$$F = E_c + F_D \tag{3.44}$$

where E_c is the cohesive energy at 0 K, calculated in Section 3.2 equation (3.16), and F_D is the free energy of the phonon "gas" in Debye's approximation:

$$F_D = E_D - TS_D = E_D + T\left(\frac{\partial F_D}{\partial T}\right)_V \tag{3.45}$$

E_D is given by (3.39) and we will write it:

$$E_D = Tf\left(\frac{\Theta_D}{T}\right)$$

Now, from (3.45) we have:

$$E_D = F_D - T\left(\frac{\partial F_D}{\partial T}\right)_V = \frac{d(F_D/T)}{d(1/T)} \tag{3.46}$$

It will be convenient to express F_D also as a function of T and Θ_D/T:

$$F_D = Tg\left(\frac{\Theta_D}{T}\right) \tag{3.47}$$

which, with (3.46), gives:

$$E_D = \Theta_D \frac{dg(\Theta_D/T)}{d(\Theta_D/T)} \tag{3.48}$$

Let us now write the expression of pressure:

$$P = -\left(\frac{\partial F}{\partial V}\right)_T = -\frac{dE_c}{dV} - \frac{dF_D}{d\Theta_D}\frac{d\Theta_D}{dV} \tag{3.49}$$

Now:

$$\frac{dF_D}{d\Theta_D} = \frac{dF_D}{d(\Theta_D/T)}\frac{d(\Theta_D/T)}{d\Theta_D} = \frac{1}{T}\frac{d(Tg(\Theta_D/T))}{d(\Theta_D/T)}$$

and, with (3.48):

$$\frac{dF_D}{d\Theta_D} = \frac{E_D}{\Theta_D} \tag{3.50}$$

We can therefore write:

$$P = -\frac{dE_c}{dV} - \frac{E_D}{\Theta_D}\frac{d\Theta_D}{dV} \tag{3.51}$$

We have thus expressed P in terms of known quantities and of the

variation of Debye's temperature with volume. It is convenient to introduce the *Debye–Grüneisen parameter*:

$$\gamma_D = -\frac{d\ln\Theta_D}{d\ln V} = -\frac{d\ln\omega_D}{d\ln V} \tag{3.52}$$

We have then:

$$P = -\frac{dE_c}{dV} + \gamma_D \frac{E_D}{V} \tag{3.53}$$

This is the complete Mie–Grüneisen equation of state, that we first encountered in Section 2.3.3. The thermal pressure was then related to the increase in thermal energy by the thermodynamic Grüneisen parameter γ_{th}. Now we see that the thermal energy is the energy of the phonon gas and we have introduced a more physical definition of the Grüneisen parameter, expressing the volume dependence of the Debye frequency.

We will now show that the two definitions are equivalent and that $\gamma_{th} = \gamma_D$.

Assuming that the mode frequencies are independent of temperature (quasi-harmonic approximation, see below), we can differentiate (3.53) with respect to T and obtain:

$$\left(\frac{dP}{dT}\right)_V = \frac{\gamma_D}{V}\left(\frac{dE_D}{dT}\right)_V = \frac{\gamma_D}{V} C_V$$

now, by definition of the coefficient of thermal expansion α and (1.27), we have:

$$\alpha = \frac{1}{V}\left(\frac{\partial V}{\partial T}\right)_P = -\frac{1}{V}\left(\frac{\partial V}{\partial P}\right)_T \left(\frac{\partial P}{\partial T}\right)_V = \frac{1}{K_T}\left(\frac{\partial P}{\partial T}\right)_V \tag{3.54}$$

hence:

$$\gamma_D = \frac{\alpha V K_T}{C_V} = \gamma_{th} \tag{3.55}$$

3.5 The Grüneisen parameters

So far we have introduced two definitions of the Grüneisen parameter, a thermodynamic, i.e. macroscopic one: γ_{th} and a microscopic one: γ_D. Now, there are many more ways of defining a Grüneisen parameter or "gamma" and we will review here those that are the more important and currently encountered in the literature (see Stacey, 1977b).

We should indeed start with Grüneisen's own definition: he considered what we call the "*mode gamma*" γ_i expressing the volume dependence of the frequency of the i^{th} vibration mode of the lattice:

$$\gamma_i = -\frac{\partial \ln \omega_i}{\partial \ln V} = \frac{\partial \ln \omega_i}{\partial \ln \rho} \tag{3.56}$$

If all the ω_is have the same volume dependence and there is only one Debye cut-off frequency, all the mode gammas are equal to the *Debye gamma* γ_{D} defined above. If, in addition, we make the assumption that the mode frequencies are independent of temperature, it can be shown to be equivalent to the thermodynamic gamma (see Section 3.4).

Slater (1939) asserted that Debye's theory implied that all mode frequencies varied in the same ratio as the cut-off frequency, hence that all the mode gammas were equal. He also made the assumption that Poisson's ratio ν was independent of the volume and derived another expression for Grüneisen's parameter in terms of the variation of the bulk modulus K with volume as follows.

From (3.28) we have:

$$\omega_{\text{D}} \propto \bar{v} V^{-1/3} \propto \bar{v} \rho^{1/3} \tag{3.57}$$

we can show, from (2.12), (2.14) and (2.15) that the velocities of the longitudinal (P) and transverse (S) waves can be expressed as the square root of K/ρ times a function of Poisson's ratio:

$$\begin{aligned} v_{\text{P}} &= \left(\frac{K}{\rho}\right)^{1/2} \left[\frac{3(1-\nu)}{1+\nu}\right]^{1/2} \\ v_{\text{S}} &= \left(\frac{K}{\rho}\right)^{1/2} \left[\frac{3(1-2\nu)}{2(1+\nu)}\right]^{1/2} \end{aligned} \tag{3.58}$$

N.B.: We clearly see here that the assumption that Poisson's ratio is independent of volume is, in fact, already included in Debye's model *stricto sensu*, since a dependence of ν on volume would mean that the longitudinal and transverse velocities, hence the frequencies of the corresponding modes, would have different volume dependences. The modes would not all have the same gammas, in contradiction with Debye's assumptions.

The average Debye velocity can therefore be written:

$$\bar{v} = K^{1/2} V^{1/2} f(\nu) \tag{3.59}$$

It follows that:

$$\ln \omega_{\text{D}} = \frac{1}{2} \ln K + \frac{1}{6} \ln V + \ln f(\nu) \tag{3.60}$$

and, since v is assumed to be independent of volume:

$$\gamma_{\mathrm{SI}} = -\frac{\partial \ln \omega_{\mathrm{D}}}{\partial \ln V} = -\frac{1}{6} - \frac{1}{2}\frac{d \ln K}{d \ln V} \tag{3.61}$$

or:

$$\gamma_{\mathrm{SI}} = -\frac{1}{6} + \frac{1}{2}\frac{d \ln K}{d \ln \rho} \tag{3.62}$$

or:

$$\gamma_{\mathrm{SI}} = -\frac{1}{6} + \frac{1}{2}\frac{dK}{dP} \tag{3.63}$$

This defines the *Slater gamma*, which explicitly depends on the assumption that Poisson's ratio is independent of volume (or pressure). Using the definition of the bulk modulus:

$$K_T = -V\left(\frac{\partial P}{\partial V}\right)_T$$

we can write:

$$\gamma_{\mathrm{SI}} = -\frac{1}{6} - \frac{1}{2}\left[1 + \frac{\partial \ln\left(-\dfrac{\partial P}{\partial V}\right)_T}{\partial \ln V}\right]$$

which gives another expression of Slater's gamma:

$$\gamma_{\mathrm{SI}} = -\frac{2}{3} - \frac{V}{2}\frac{\left(\dfrac{\partial^2 P}{\partial V^2}\right)_T}{\left(\dfrac{\partial P}{\partial V}\right)_T} \tag{3.64}$$

A full lattice dynamical computer simulation on a monatomic cubic lattice has confirmed the linear dependence of the Grüneisen parameter on dK/dP (Vočadlo and Price, 1994).

Conversely, knowing Slater's gamma, we can obtain the variation with density or pressure of the bulk modulus:

$$\frac{d \ln K}{d \ln \rho} = \frac{dK}{dP} = 2\gamma_{\mathrm{SI}} + \frac{1}{3} \tag{3.65}$$

Since the ratio K/μ depends only on Poisson's ratio, which is assumed

not to depend on volume, we also have:

$$\frac{d\ln\mu}{d\ln\rho} = 2\gamma_{\mathrm{Sl}} + \frac{1}{3} \tag{3.66}$$

and:

$$\frac{d\mu}{dP} = \frac{\mu}{K}\left(2\gamma_{\mathrm{Sl}} + \frac{1}{3}\right) \tag{3.67}$$

The assumption that Poisson's ratio does not vary as specific volume decreases is of course not strictly correct, as Slater perfectly knew; Poisson's ratio does, in fact, slightly increase with pressure. Slater's gamma is nevertheless a rather good approximation for close-packed solids (O. L. Anderson, 1988) and formulas (3.64) to (3.67) are useful expressions of the pressure dependence of the elastic moduli.

The restriction that Poisson's ratio be independent of volume can be lifted by dealing separately with the longitudinal and transverse acoustic branches of the phonon spectrum and defining a transverse gamma γ_{t} and a longitudinal gamma γ_{l}; this, of course, is in contradiction with the original Debye's assumptions (see N.B. above) and implies a modification of Debye's model (Stacey, 1977b). The weighted average of γ_{t} and γ_{l} defines a new gamma called *acoustic gamma* or *high-temperature gamma* (Vashchenko and Zubarev, 1963; Stacey, 1977b):

$$\gamma_{\mathrm{a}} = \gamma_{\mathrm{HT}} = \frac{1}{3}(\gamma_{\mathrm{l}} + 2\gamma_{\mathrm{t}}) \tag{3.68}$$

Defining γ_{l} and γ_{t} in the same way as γ_{D}, but replacing $\bar{v}$ by v_{P} and v_{S} respectively, and using (3.58), we obtain:

$$\gamma_{\mathrm{a}} = -\frac{1}{6} + \frac{1}{2}\frac{d\ln K}{d\ln\rho} + \frac{1}{3}\frac{5v^2 - 4v}{(1-v^2)(1-2v)}\frac{d\ln v}{d\ln\rho} \tag{3.69}$$

We see that the acoustic gamma is equal to the Slater gamma plus a term which is a function only of Poisson's ratio and its dependence on specific mass. Knopoff and Shapiro (1969) show that in the acoustic gamma the pressure derivative of the shear modulus plays a role significantly more important than the pressure derivative of the bulk modulus.

The acoustic gamma is also called high-temperature gamma because it can be derived from the expression for thermal pressure, assuming that at high temperature the thermal energy $E_{\mathrm{th}} = 3RT$ is equally distributed between the P-mode and the two S-modes. We have then:

$$P_{th} = \frac{RT}{V}(\gamma_l + 2\gamma_t) = \frac{3RT}{V}\gamma_{HT}$$

and the definition (3.68) immediately follows.

Quareni and Mulargia (1988) propose to use what they call the *Debye–Brillouin gamma*:

$$\gamma_{Br} = \frac{1}{3} - V\left(\frac{dv_P}{dV} + 2\frac{dv_S}{dV}\right)(2v_S + v_P)^{-1} \tag{3.70}$$

To compare it with the other formulations, it is convenient to write:

$$\gamma_{Br} = \frac{1}{3} + \frac{d\ln\left(\dfrac{2v_S + v_P}{3}\right)}{d\ln\rho} \tag{3.71}$$

Note that we could write the acoustic gamma as:

$$\gamma_a = \frac{1}{3} + \frac{1}{3}\left(\frac{d\ln v_P}{d\ln\rho} + 2\frac{d\ln v_S}{d\ln\rho}\right) = \frac{1}{3} + \frac{d\ln\left(\dfrac{v_P v_S^2}{3}\right)}{d\ln\rho} \tag{3.72}$$

and, of course, Debye's gamma is:

$$\gamma_D = \frac{1}{3} + \frac{d\ln\left[\left(\dfrac{1}{v_P^3} + \dfrac{2}{v_S^3}\right)/3\right]^{-1/3}}{d\ln\rho} \tag{3.73}$$

We see that in practice these formulations differ only in the way the velocities are averaged; they can all be written:

$$\gamma_D = \frac{1}{3} + \frac{d\ln\bar{v}}{d\ln\rho} \tag{3.74}$$

with:

$$\begin{aligned}
\bar{v}_D &= \sqrt[3]{3}\left(\frac{1}{v_P^3} + \frac{2}{v_S^3}\right)^{-1/3} && \text{for the Debye gamma} \\
\bar{v}_a &= (v_P v_S^2)^{1/3} && \text{for the acoustic gamma} \\
\bar{v}_{Br} &= \frac{1}{3}(v_P + 2v_S) && \text{for the Debye–Brillouin gamma.}
\end{aligned} \tag{3.75}$$

The pressure dependence of Poisson's ratio is obviously included in the last two expressions and the cut-off frequencies for the longitudinal and

transverse branches may or may not be assumed equal without affecting their validity.

All these approaches use the same fundamental assumptions of the Debye approximation: the optical modes are not specifically taken into account and all the modes are assumed to be independent and non-dispersive (i.e. the group velocity is equal to the phase velocity and does not depend on the frequency), an approximation valid only at low frequency and for acoustic modes only. Now, at high temperatures, the high-frequency modes carry an important proportion of the thermal energy and they are dispersive. Furthermore, they interact and cannot be considered as independent.

Irvine and Stacey (1975) proposed another way of calculating an expression of the Grüneisen parameter in the high-temperature classical limit, still as a function of the pressure derivative of the bulk modulus, but avoiding consideration of lattice modes (see also Stacey, 1977b). The expression they found is identical with the one derived earlier by Vashchenko and Zubarev (1963) from the free-volume theory. In view of the fact that the *Vashchenko–Zubarev gamma* or *free-volume gamma* is widely quoted and used, I will reconstitute the derivation of formula (3.80) (see below), of which Vashchenko and Zubarev, in their original paper, only say that it was "obtained by starting from the free-volume theory". I will then give Irvine and Stacey's derivation.

The free-volume theory was proposed by Lennard-Jones and Devonshire (1937) to account for the properties of dense gases and liquids. The main idea is that the atoms can be regarded as confined in cells and that their average environment is approximately the same as in a crystal. The atoms are in potential wells resulting from the attractive and repulsive parts of the pair-interaction potentials with their neighbors. This is in a way similar to the Einstein approximation where the atoms are considered as independent oscillators in harmonic, parabolic, potential wells, except that here the wells do not have to be parabolic. (Interestingly enough, Vashchenko and Zubarev used for solids a theory that was devised for dense fluids, assuming they could be locally regarded as solid-like!) Due to the fact that the energy is high near the cell boundaries, the atoms are in effect confined to a "free volume" V_F smaller than the cell size:

$$V_F = \int_{\text{cell}} \exp\left[-\frac{\chi(r) - \chi(0)}{kT} \right] dV \tag{3.76}$$

where $\chi(r)$ is the potential energy of the atom in its cell at the distance r from

its equilibrium position.

The thermodynamic properties can be determined from the translation partition function of the atoms of mass m, in their free volume, which is known from statistical mechanics (see e.g. Gurney, 1966):

$$Z = \left(\frac{2\pi m k_B T}{h^2}\right)^{3/2} V_F \tag{3.77}$$

Vashchenko and Zubarev start from the Mie–Grüneisen definition of the thermodynamic gamma (2.63):

$$\gamma_{th} = \frac{V P_{th}}{E_{th}}$$

where P_{th} and E_{th} are the thermal pressure and thermal energy respectively, which can be expressed in terms of the partition function Z:

$$P_{th} = k_B T \left(\frac{d \ln Z}{dV}\right)_T$$

$$E_{th} = k_B T^2 \left(\frac{d \ln Z}{dT}\right)_V$$

Note, incidentally, another interesting formulation of the thermodynamic gamma:

$$\gamma_{th} = \frac{(d \ln Z/dV)_T}{(d \ln Z/dT)_V} \cdot \frac{V}{T} \tag{3.78}$$

Inserting (3.77) into (3.78), we obtain:

$$\gamma_{th} = \left(\frac{\partial \ln V_F}{\partial \ln V}\right)_T \left[\frac{3}{2} + \left(\frac{\partial \ln V_F}{\partial \ln T}\right)_V\right]^{-1} \tag{3.79}$$

From (3.76), expanding $\chi(r)$ in powers of r for small displacements of the atoms, integrating and approximating the energy by the pair-interaction potential, Vashchenko and Zubarev find:

$$\gamma_{VZ} = -\frac{V}{2}\left[\frac{d^2(PV^{4/3})}{dV^2}\right]\left[\frac{d(PV^{4/3})}{dV}\right]^{-1} \tag{3.80}$$

to be compared with Slater's gamma formulation (3.64).

Irvine and Stacey (1975) start from an analysis of the three-dimensional oscillations of atoms on a simple cubic lattice and calculate the thermal energy and thermal pressure in the classical limit to obtain the Mie–

Grüneisen thermal gamma. The outline of their demonstration is given here:

Let us consider a pair of neighboring atoms vibrating independently in the three directions x, y, z. At equilibrium ($T = 0$ K), the atomic separation is r_e in the x direction and the force constant of the bond is $F(r_e)$. At finite temperature, the atoms vibrate and their interatomic separation is $r = [(r_e + \Delta x)^2 + \Delta y^2 + \Delta z^2]^{1/2}$, where $\Delta x, \Delta y, \Delta z$ are the components of the elongation of the bond; as they are small compared to r_e, r^{-1} can be expanded to second order in $\Delta x, \Delta y, \Delta z$. The force constant can be expanded to second order in $(r - r_e)$, and its x-component $F_x = F(r)(r_e + \Delta x)r^{-1}$ is expressed to second order using the expansions of $F(r)$ and r^{-1}. Its time average $<F_x>$ must be balanced by the force created by the external pressure P over the area r_e^2 so that the specific volume remains constant; P is then equal to the thermal pressure. In taking the time average of F_x, the time average $<\Delta x>$ is taken equal to zero since the external pressure prevents thermal expansion and in the classical limit the potential energy of each bond is equal to $(1/2)k_B T$. The quadratic terms in the expansion of $<F_x>$ can therefore be written as functions of r_e and of $F(r_e)$ and its derivatives with respect to r, taken at r_e: $F'(r_e), F''(r_e)$. The thermal pressure appears in a Mie–Grüneisen type equation, using the high-temperature classical Dulong and Petit value for the specific heat at constant volume: $C_V = 3k_B$ per atom. The Grüneisen parameter is calculated as:

$$\gamma = -\frac{1}{3}\left[\frac{1}{2}F''(r_e) + \frac{F'(r_e)}{r_e} - \frac{F(r_e)}{r_e^2}\right]\left[\frac{F'(r_e)}{r_e} + \frac{2F(r_e)}{r_e^2}\right]^{-1}$$

Since $P_0 = F(r_e)/r_e^2$, we can express r_e, $F(r_e)$, $F'(r_e)$ and $F''(r_e)$ in terms of P and of the bulk modulus K and its derivative dK/dP.

The Grüneisen parameter can thus be written:

$$\gamma_{VZ} = \left(\frac{1}{2}\frac{dK}{dP} - \frac{5}{6} + \frac{2}{9}\frac{P}{K}\right)\left(1 - \frac{4}{3}\frac{P}{K}\right)^{-1} \tag{3.81}$$

which is equivalent to (3.80) and can be easily derived from it by using the definition of the bulk modulus: $K = -V\partial P/\partial V$. The calculation can be generalized to other lattices than the simple cubic one; the expression (3.81) still holds, as long as the interatomic forces are purely central.

A "modified free-volume" gamma, adapted to the high pressures of the lower mantle and core, is given in Stacey (1995).

Dugdale and MacDonald (1953) proposed another expression for the Grüneisen parameter correcting the alleged error made by Slater in neglecting to take into account the effect of finite strain under applied pressure:

$$\gamma_{DM} = \left(\frac{1}{2}\frac{dK}{dP} - 1 + \frac{2}{9}\frac{P}{K}\right)\left(1 - \frac{2}{3}\frac{P}{K}\right)^{-1} \tag{3.82}$$

or:

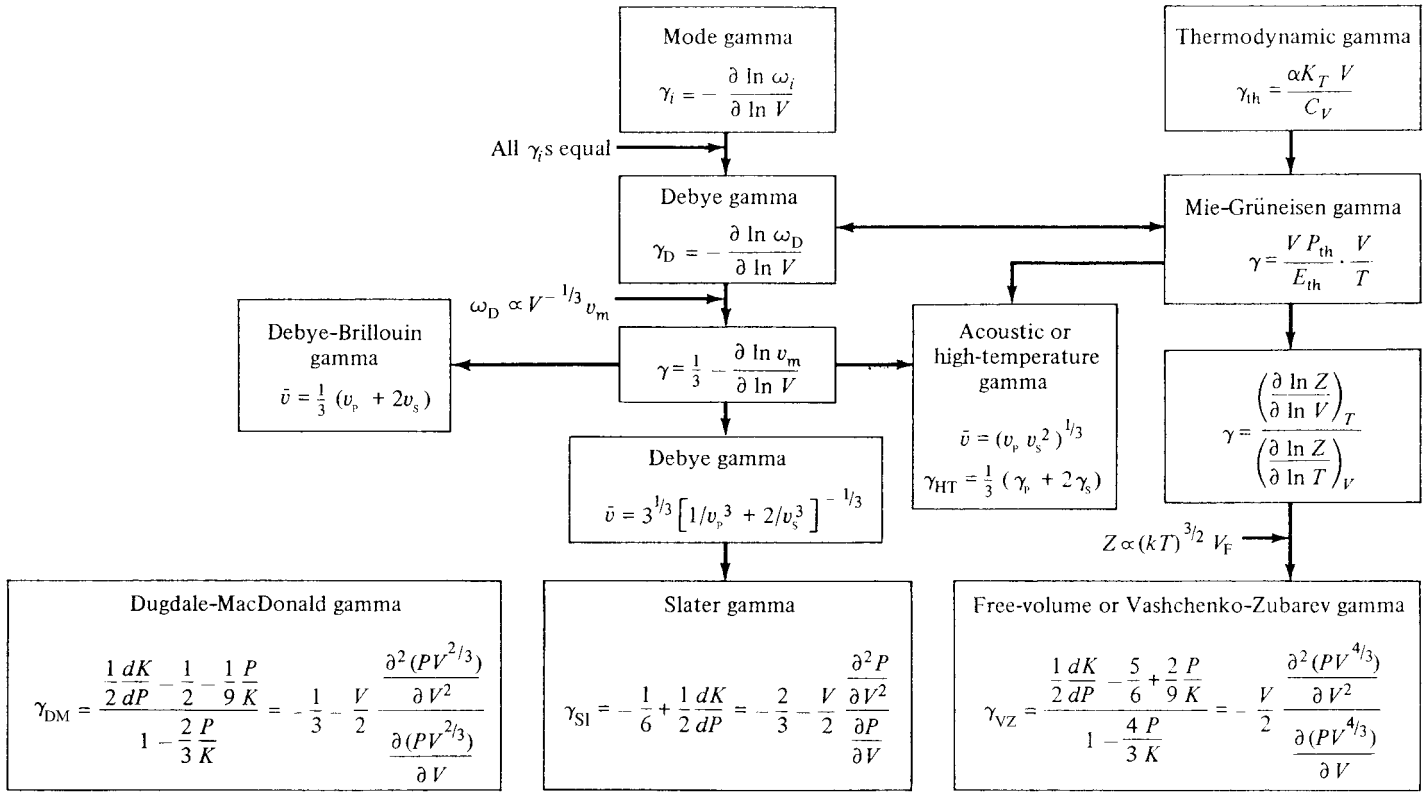

Figure 3.11 Relations among the various definitions of the Grüneisen parameter.

$$\gamma_{DM} = -\frac{1}{3} - \frac{V}{2}\left[\frac{\partial^2(PV^{2/3})}{\partial V^2}\right]\left[\frac{\partial(PV^{2/3})}{\partial V}\right]^{-1} \tag{3.83}$$

However, Gilvarry (1956d) showed that use of the formal theory of finite strain also leads to Slater's gamma and that no physical basis exists for the modification proposed by Dugdale and MacDonald. Irvine and Stacey (1975) found that their derivation of the free-volume gamma leads to the Dugdale and MacDonald gamma if they assume one-dimensional atomic motions, thus displaying the weakness of the model.

N.B. Incidentally, note that at P = 0, we have: $\gamma_{DM} = (1/2)(\gamma_{SI} + \gamma_{VZ})$

The relations between the various gammas are summarized in Fig. 3.11.

That Grüneisen's parameter varies with pressure clearly appears from the calculations, but the variation depends on how the sound velocities or the elastic moduli vary with pressure and the data do not always exist or, if they exist, they are not always easy to extrapolate to high pressures. Depending on which equations of state (i.e. $K = f(P)$) are used, the results may widely differ (Irvine & Stacey, 1975).

A useful empirical law relates the Grüneisen parameter to the density ρ (O. L. Anderson, 1979):

$$\gamma\rho^q = \text{const} \tag{3.84}$$

with values of q between 0.8 and 2.2 acceptable for the lower mantle.

Boehler & Ramakrishnan (1980) determined the pressure dependence of the thermodynamic gamma by measuring the temperature change associated with adiabatic compression up to 5 kbar, using the expression:

$$\gamma_{th} = \frac{\alpha K_S}{\rho C_P} = \frac{K_S}{T}\left(\frac{\partial T}{\partial P}\right)_S$$

they found values of q between 0.6 (for Fe) and 1.7, with an average value of 1.3 for metals and alkali halides.

It is simpler, not necessarily more inaccurate in view of all the other sources of uncertainty, and often experimentally correct to assume that $q = 1$. Indeed, O. L. Anderson (1998) finds that, for $MgSiO_3$ perovskite, q varies from 1.12 to 0.82 between 800 and 1800 K, and Fei *et al.* (1992) find that $q = 1.1$ for magnesiowüstite $(Mg_{0.6}, Fe_{0.4})O$. From $q \approx 1$, it follows that:

$$\gamma\rho = \gamma_0\rho_0 = \text{const} \tag{3.84}$$

The formula can be given some justification by considering the thermo-

Table 3.3. *Grüneisen parameters of some typical crystals*

Crystal	γ_{th}	γ_a	γ_{SI}	γ_{DM}	γ_{VZ}	γ_D	γ_{Br}	Source
MgO	1.52	1.41						A
	1.54		1.12	0.78	0.45	0.92	0.95	QM (a)
	1.54		1.89	1.55	1.22	1.40	1.48	QM (b)
Al_2O_3	1.13	1.15						A
	1.28		1.92	1.59	1.25	1.25	1.39	QM (b)
$MgAl_2O_4$	1.40	0.67						A
	1.40		2.18	1.84	1.51	0.44	0.85	QM (b)
Mg_2SiO_4	1.16	1.49						A
	1.18		2.39	2.05	1.72	1.26	1.51	QM (b)
$SrTiO_3$	1.63	1.96						A
Fe	1.65		3.14	2.80	2.47	2.26	2.48	QM (a)
	1.65		2.65	2.31	1.98	1.76	1.99	QM (b)

Notes: γ_{th} = thermodynamic gamma; γ_a = acoustic gamma; γ_{SI} = Slater gamma; γ_{DM} = Dugdale–MacDonald gamma; γ_{VZ} = Vashchenko–Zubarev gamma; γ_D = Debye gamma; γ_{Br} = Debye–Brillouin gamma.
Sources: A: O. L. Anderson (1988). QM (a): Quareni and Mulargia (1988) (Hashin–Shtrickman). QM (b): Quareni and Mulargia (1988) (Voigt–Reuss–Hill).

dynamic gamma: $\gamma_{th} = \alpha K_T/\rho C_V$; at high temperature in the classical limit $C_V = 3nR$, and:

$$\gamma\rho = \frac{\alpha K_T}{3nR} \tag{3.86}$$

Now, there is reasonable experimental evidence that αK_T remains constant at high temperatures for a number of crystals (Birch, 1968; Brennan & Stacey, 1979; Steinberg, 1981).

The Grüneisen parameter can reasonably be considered as independent of temperature to a first approximation (Irvine & Stacey, 1975).

Table 3.3 gives values of the various gammas for a few important crystals and mantle minerals, from Quareni and Mulargia (1988) and O. L. Anderson (1988). Two observations can be made:

(i) For all materials, the values of gamma at ambient pressure roughly lie between 0.5 and 3 and are generally close to 2.
(ii) For a given material the values of gamma vary widely, depending of course on which gamma is calculated, but also on the origin of the experimental data used and even on the way the elastic data are averaged (Voigt–Reuss–Hill or Hashin–Shtrickman).

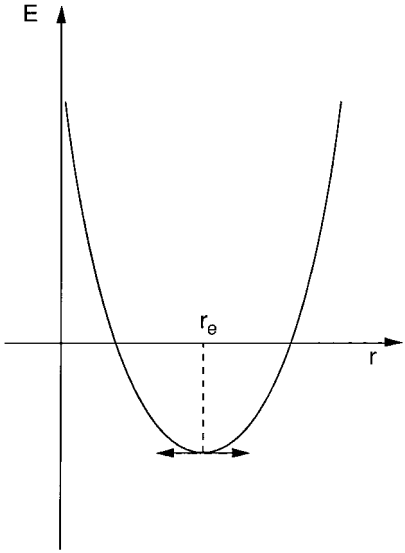

Figure 3.12 Harmonic curve of interatomic potential. The equilibrium interatomic distance r_e corresponds to the minimum of the parabolic curve.

3.6 Harmonicity, anharmonicity and quasi-harmonicity

3.6.1 Generalities

Let us come back to the schematic case of a lattice of atoms vibrating as harmonic oscillators about their equilibrium position. The restoring force $F = k(r - r_e)$ is proportional to the elongation $r - r_e$, and the symmetrical interatomic pair potential is parabolic (Section 3.2.1) (Fig. 3.12). This case corresponds to the linear infinitesimal elasticity, with elastic moduli independent of strain (or stress).

In reality, the equilibrium distance between atoms r_e is determined by the balance between a long-range attractive force and a short-range repulsive force. The interatomic potential $E(r)$ can be expressed as the sum of an attractive and a repulsive potential e.g. by Mie's formula:

$$E(r) = -\frac{a}{r^m} + \frac{b}{r^n} \tag{3.87}$$

with $n > m$, since the repulsive potential has a shorter range. A simple case is that of ionic crystals, for which $m = 1$ (Coulombic attraction) and $n \approx 9$ (Born potential). The curve of bond energy (Fig. 3.13) is therefore asymmetrical, steeper towards small interatomic distances. This results in non-

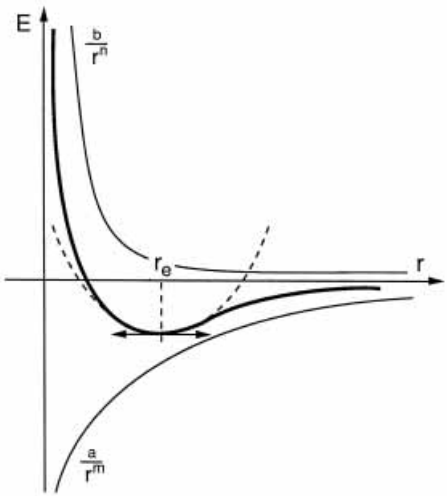

Figure 3.13 Anharmonic curve of interatomic potential (bold curve). The potential is the sum of the attractive Coulombic potential and a short-range repulsive potential (thin curves). The osculatory parabola at $r = r_e$ (dashed curve) corresponds to the harmonic approximation.

linear anharmonic oscillations. As the interatomic spacing decreases with increasing applied pressure, the restoring force (i.e. the opposite of the slope of the curve) increases more rapidly than in the harmonic case: compression becomes more and more difficult, in other words the bulk modulus increases with pressure.

Of course, near its minimum, the curve of bond energy can be assimilated to its osculatory parabola (with the same curvature) and the linear approximation is valid.

3.6.2 Thermal expansion

Another important consequence of the asymmetry of the potential curve appears when temperature is taken into consideration. At low temperatures, the quantized energy levels are near the bottom of the potential well and the vibrational amplitudes are small; the harmonic approximation holds. However, as temperature increases, the energy levels climb higher up in the well and the amplitudes increase. The asymmetry of the well cannot be neglected any longer and causes the oscillations to become non-sinusoidal or, in other words, anharmonic.

The interatomic distance oscillates between r_1 and r_2, with $r_2 - r_e > r_e - r_1$, i.e. the extension of the bond is greater than its compression (Fig.

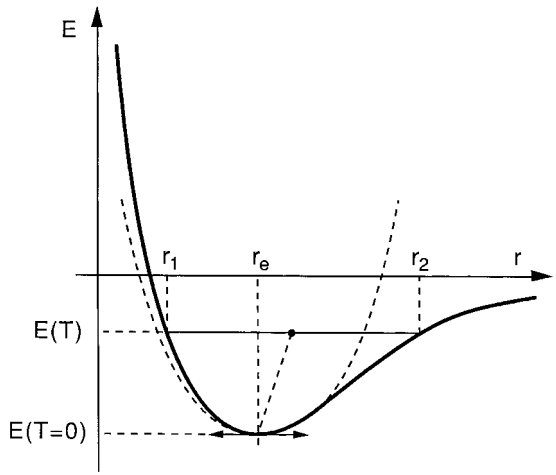

Figure 3.14 Thermal expansion. At $T = 0$ K, the interatomic potential is minimum for the equilibrium distance r_e. At a finite temperature, the potential $E(T)$ is higher and due to the asymmetric shape of the anharmonic curve, the equilibrium distance is the average between r_1 and r_2, which is greater than r_e.

3.14). In addition, the restoring force is smaller on the extension side, so that, on average, the bond spends a longer time in extension than in compression. The mean value of the bond length becomes longer than the equilibrium value at low temperature: $r_1 + r_2 > 2r_e$.

The asymmetry of the potential curve of anharmonic solids can be seen as the cause of thermal expansion. However, it does not follow that the coefficient of thermal expansion of harmonic solids is zero (nor that their bulk modulus is independent of pressure). Stacey (1993a) has shown that, for a 3-D harmonic lattice, $K'_0 = 1$ and that the Grüneisen parameter is necessarily negative, which implies that the coefficient of thermal expansion is negative.

We have already seen (Section 2.3.3) that we can relate thermal expansion to thermal pressure by considering that heating a solid at constant volume increases the internal (negative) pressure, which, in turn, would cause the solid to expand if the constraint of constant volume were lifted:

$$\left(\frac{\partial P}{\partial T}\right)_V = \alpha K_T = \gamma_{\text{th}} \rho C_V$$

The Grüneisen ratio is therefore a good parameter of anharmonicity and we have seen in Section 3.5 that it can be related to dK/dP, which is also

linked to the bond asymmetry. It can also be expressed as a function of the exponents m and n of the bond potential in Mie's formula (3.87) (Zwikker, 1954). By expanding the potential $E(r)$ in a series of powers of the vibrational elongations, the thermal energy can be expressed as a function of m and n and Grüneisen's parameter is found to be (see also Section 4.4):

$$\gamma_{\text{th}} = \frac{1}{2} + \frac{m+n}{6} \tag{3.88}$$

It is possible to introduce an intrinsic anharmonic parameter a_i for every vibration mode, that can be experimentally determined by measuring separately the variation with temperature and pressure of the mode frequencies by infrared or Raman spectroscopy (Gillet *et al.*, 1989). There are therefore two mode Grüneisen parameters:

$$\gamma_{i,T} = -\left(\frac{\partial \ln \omega_i}{\partial \ln V}\right)_T \text{ and } \gamma_{i,P} = -\left(\frac{\partial \ln \omega_i}{\partial \ln V}\right)_P$$

We can write:

$$d \ln \omega_i = a_i dT - \gamma_{i,T} d \ln V = a_i \frac{\partial T}{\partial P} dP + \left(a_i \frac{\partial T}{\partial \ln V} - \gamma_{i,T}\right) d \ln V \tag{3.89}$$

Hence:

$$\left(\frac{\partial \ln \omega_i}{\partial \ln V}\right)_P = -\gamma_{i,P} = a_i \frac{\partial T}{\partial \ln V} - \gamma_{i,T}$$

or:

$$a_i = \left(\frac{\partial \ln \omega_i}{\partial T}\right)_V = \alpha(\gamma_{i,T} - \gamma_{i,P}) \tag{3.90}$$

We can also deal with the effect of temperature on the vibration modes and elastic moduli by considering that an increase in temperature causes an increase in volume by thermal expansion and calculating the effect of the increase in volume on the elastic properties through quantities such as $-d \ln K / d \ln V = dK/dP$. This is the so-called *quasi-harmonic approximation*, which takes into account the effect of temperature through the volume change due to thermal expansion only. In the quasi-harmonic approximation, the vibrations are considered to be harmonic about the new equilibrium positions of the atoms corresponding to the expanded state.

Table 3.4. *Typical values of thermal expansion coefficient*

Mineral	P(GPa)	T(K)	$\alpha(10^{-5}/\mathrm{K})$	Reference
MgO	0	298	3.1	(Suzuki, 1975)
α-Mg_2SiO_4 (forsterite)	0	1700	2.5	(Isaak *et al*., 1989)
γ-Mg_2SiO_4	0	23	2.7	(Suzuki *et al*., 1979)
$MgSiO_3$ (perovskite)	0	298–381	2.2	(Ross & Hazen, 1989)
$MgSiO_3$ (perovskite)	10.7	677–1024	1.9	(Wang *et al*., 1994)
$MgSiO_3$ (perovskite)	0–20	298–773	1.8–2.5	(Utsumi *et al*., 1995)
$MgSiO_3$ (perovskite)	25	298–1473	2.0	(Kato *et al*., 1995)
$MgSiO_3$ (perovskite)	30	2000	2.1	(Funamori *et al*., 1996)
$MgSiO_3$ (perovskite)	0	300–1600	2.6	(Jackson & Rigden, 1996)
Fe	243	4500	1.3	(Stacey, 1993)

However, we must not overlook the fact that there are anharmonic effects due to temperature that are not accounted for by the quasi-harmonic approximation (e.g. changes in the electronic configuration of the bonds). D. L. Anderson (1987, 1988) distinguishes between the *intrinsic* derivatives of the elastic moduli expressing the effect of temperature or pressure at constant volume and the *extrinsic*, or volume-dependent derivatives. They are conveniently expressed as dimensionless logarithmic derivatives with respect to specific mass ρ (Dimensionless Logarithmic Anharmonic or DLA parameters).

An often-used DLA parameter (D. L. Anderson, 1987a) is the *Anderson–Grüneisen parameter* (proposed by O. L. Anderson) δ_T or δ_S:

$$\delta_T = \left(\frac{\partial \ln \alpha}{\partial \ln V}\right)_T = -\frac{1}{\alpha}\left(\frac{\partial \ln K_T}{\partial T}\right)_P = \left(\frac{\partial \ln K_T}{\partial \ln \rho}\right)_P \tag{3.91}$$

$$\delta_S = \left(\frac{\partial \ln \alpha}{\partial \ln V}\right)_S = -\frac{1}{\alpha}\left(\frac{\partial \ln K_S}{\partial T}\right)_P = \left(\frac{\partial \ln K_S}{\partial \ln \rho}\right)_P \tag{3.92}$$

The Anderson–Grüneisen parameter embodies the pressure dependence of the thermal expansion coefficient. Chopelas and Boehler (1989) determined the pressure dependence of the thermal expansion coefficient of MgO and forsterite by putting experimentally determined values of thermodynamic parameters in the equation:

$$\alpha = \frac{K_S C_V}{K_T V T}\left(\frac{\partial T}{\partial P}\right)_S$$

They found values of $\delta_T = -(\partial \ln \alpha / \partial \ln \rho)_T$ equal to 6.5 and 6.1 respect-

ively. A systematics of $(\partial \ln \alpha / \partial \ln \rho)_T$ for many minerals yields an average value $\delta_T = 5.5 \pm 0.5$. A more recent systematics has shown that δ_T is proportional to the compression V/V_0 (Chopelas and Boehler, 1992). The value of δ_T therefore decreases at high pressure.

Typical values of the thermal expansion coefficient for minerals are given in Table 3.4.

4

Equations of state

4.1 Generalities

The thermodynamic state of a system is usually defined by pressure P, temperature T and specific volume V (or specific mass ρ), linked by the *equation of state* (EOS) (see e.g. Eliezer *et al.*, 1986). The best known EOS is the one for ideal gases:

$$PV = RT$$

We are concerned here with the various possible EOSs for solids at high pressures and high temperatures (see Zharkov & Kalinin, 1971; O. L. Anderson, 1995a) because, in order to build compositional (mineralogical) Earth models, it is indispensable to have an EOS for the regions of the interior of the Earth, as well as for the candidate minerals. Inversion of seismic travel-times yields seismic velocities at all depths (pressures), and to compare the velocities, or the inferred values of densities or elastic moduli, with those of mineral assemblages, one needs either to "compress" the assemblages to high pressures or "decompress" the Earth material to ambient pressure. Hence the need for EOS.

Since in the case of solids the effect of temperature is much less than for gases, it is often introduced only as a thermal expansion correction to the *isothermal EOS* : $V(P)$ or $\rho(P)$, which is the one usually experimentally determined for minerals at high pressures (Stacey *et al.*, 1981). We will therefore start by considering isothermal equations of state (see reviews by Boschi and Caputo, 1969; Stacey *et al.*, 1981; and Poirier, 1999).

The simplest isothermal EOS one can think of, for solids, is given by the definition of the bulk modulus K:

$$K = -\frac{dP}{d\ln V} = \frac{dP}{d\ln \rho} \tag{4.1}$$

If we consider infinitesimal strains resulting from the application of hydrostatic pressure to an initially unstressed solid, we are in the case of linear elasticity, with constant bulk modulus, and the EOS is obtained by integrating (4.1) with $K = K_0$:

$$V = V_0 \exp\left(-\frac{P}{K_0} \right) \tag{4.2}$$

This simple EOS is obviously not correct for high pressures since it does not take into account the fact that it is more and more difficult to compress the solid, i.e. that the bulk modulus increases with pressure. Seismic waves in the Earth, as well as ultrasonic waves in laboratory experiments, propagate in media that have undergone a finite strain under high pressure, and even though the strain corresponding to the propagation of the waves can be considered infinitesimal and treated in the linear approximation, we must not neglect the fact that the large finite strain has modified the elastic moduli of the medium.

4.2 Murnaghan's integrated linear equation of state

Let us consider infinitesimal strains resulting from the application of hydrostatic pressure P to a solid initially compressed to a finite strain by pressure P_0.

Murnaghan (1967) demonstrated that the effective local bulk modulus is (see note, p. 71):

$$K = \frac{1}{3}(3\lambda + 2\mu + P_0) \tag{4.3}$$

In the case of isotropic solids, this is equivalent to having three elastic constants: λ, μ and P_0. The constants λ and μ depend on the initial pressure P_0 and are equal to λ_0 and μ_0 (Lamé constants of the solid in the natural state) for $P = P_0$. If we make the assumption that λ and μ are linear functions of P_0, the local bulk modulus is also a linear function of P_0:

$$K = \frac{1}{3}(3\lambda_0 + 2\mu_0) + kP_0 \tag{4.4}$$

where k is a constant.

Using (4.1), we have:

$$d \ln \rho = \frac{dP}{K_0 + kP_0}$$

P_0, being arbitrary, can be replaced by P and we obtain by integration:

$$P = \frac{K_0}{k}\left[\left(\frac{\rho}{\rho_0}\right)^k - 1\right] \tag{4.5}$$

If we made the drastic assumption that λ and μ do not depend on P_0, we would have $k = 1/3$. If, now, we assume that the dependence of K on the pre-applied pressure is the same as that of K_0 on pressure about $P = 0$, i.e. if we assimilate k to $K_0' = (dK/dP)_{P=0}$, we can write (4.5) as:

$$P = \frac{K_0}{K_0'}\left[\left(\frac{\rho}{\rho_0}\right)^{K_0'} - 1\right] \tag{4.6}$$

which can also be written as:

$$\rho = \rho_0\left(1 + \frac{K_0'}{K_0}P\right)^{1/K_0'} \tag{4.7}$$

This is *Murnaghan's integrated linear EOS*, (Murnaghan, 1967), usually simply called *Murnaghan's EOS*.

An equation formally identical to (4.6) could be derived by expanding K to first order in P about $P = 0$:

$$K \approx K_0 + K_0'P \tag{4.8}$$

inserting (4.1) into (4.8) and integrating, but this apparently simpler procedure is not physically rigorous and hides the important role of the finite strain.

The assumption that the bulk modulus is a linear function of pressure is also at the basis of the *polytropic* equation of state used by astrophysicists (Eddington, 1930), which links the pressure inside a star, considered as a self-gravitating sphere of perfect gas, to the density of the gas:

$$P = C\rho^\gamma$$

where C and γ are constants. We see that:

$$K = \rho\frac{dP}{d\rho} = \gamma C\rho^\gamma = \gamma P$$

γ is equivalent to K_0', but $K_0 = 0$, since density is zero for zero pressure in a gas.

Laplace (1825) also used the assumption that the bulk modulus is a linear function of pressure to calculate the density at the center of the Earth (see Section 7.2.1).

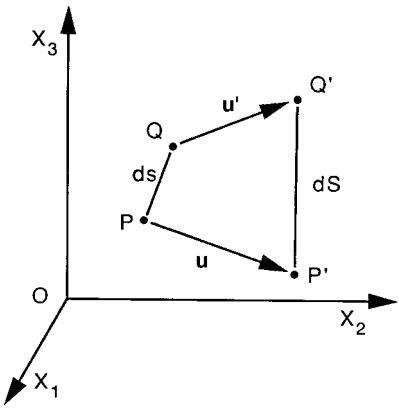

Figure 4.1 The distance *ds* between two neighboring points P, P′ becomes *dS* after straining, due to the nonuniformity of the displacement field **u**.

4.3 Birch–Murnaghan equation of state

4.3.1 Finite strain

The EOS most currently used, especially in the treatment of experimental compression data of minerals, is the Eulerian finite strain Birch–Murnaghan EOS. In view of its importance, we will devote some space to presenting it here, first introducing the necessary background, starting with the expression for finite strain.

Let us consider a solid in the coordinate axes $Ox_1x_2x_3$ (Fig. 4.1), and let *ds* be the distance between two neighboring points P of coordinates x_i ($i = 1, 2, 3$) and Q of coordinates $x_i + dx_i$. We have:

$$ds^2 = \sum_i (dx_i)^2 \tag{4.9}$$

Let points P and Q be displaced to P' and Q' by a *displacement* vector $\mathbf{u}(x_i)$, which is a function of the coordinates of the points:

$$\mathrm{P}(x_i) \rightarrow \mathrm{P}'(x_i + u_i)$$
$$\mathrm{Q}(x_i + dx_i) \rightarrow \mathrm{Q}'(x_i + dx_i + u_i + du_i)$$

Since **u** is not constant for all points, which would correspond to a rigid-body translation, the distance *dS* between P' and Q' is different from *ds*: the solid undergoes a *strain*.

To define the notion of strain and perform all the necessary calculations, we can use either of two schemes.

- The *Lagrangian* scheme, in which one expresses the coordinates X_i of a point in the strained state as a function of its coordinates x_i in the initial, unstrained state:

$$X_i = x_i + u_i \tag{4.10}$$

- The *Eulerian* scheme, in which one expresses the coordinates x_i of a point in the initial unstrained state as a function of its coordinates X_i in the strained state:

$$x_i = X_i - u_i \tag{4.11}$$

The two schemes yield definitions of strain that are equivalent for infinitesimal strain but not for finite strain. The Lagrangian scheme yields a finite strain for an infinite pressure (see below), and anyway, the Eulerian scheme is more physically meaningful for finite strain conditions, since every quantity is expressed in terms of the coordinates of the points in the strained solid, which are the experimentally accessible ones. As a consequence, the Eulerian scheme is commonly used to determine experimental equations of state and we will adopt it in what follows.

We have:

$$dS^2 - ds^2 = \sum_i (dX_i)^2 - \sum_i (dx_i)^2 = 2\sum_i dX_i du_i - \sum_i (du_i)^2 \tag{4.12}$$

If the displacements **u** are continuous and differentiable functions of x_i, we have:

$$du_i = \sum_k \frac{du_i}{dX_k} dX_k \tag{4.13}$$

The Eulerian finite strain tensor ε_{ij} is defined by:

$$dS^2 - ds^2 = 2\sum_{ij} \varepsilon_{ij} dX_i dX_j \tag{4.14}$$

with:

$$\varepsilon_{ij} = \frac{1}{2}\left(\frac{\partial u_i}{\partial X_j} + \frac{\partial u_j}{\partial X_i}\right) - \frac{1}{2}\sum_k \frac{\partial u_k}{\partial X_i}\frac{\partial u_k}{\partial X_j} \tag{4.15}$$

For infinitesimal strains, we can neglect the quadratic term and we obtain the definition of strain given by (2.1).

The Eulerian strain is sometimes written:

$$\varepsilon_{ij} = \frac{1}{2}\left(\delta_{ij} - \sum_k \frac{\partial x_k}{\partial X_i}\frac{\partial x_k}{\partial X_j}\right) \tag{4.16}$$

where $\delta_{ij} = 1$ if $i = j$ and $\delta_{ij} = 0$ if $i \neq j$.

N.B. It is easy to show that (4.16) is equivalent to (4.15) by carrying $x_k = X_k - u_k$ into (4.16). We have then:

$$2\varepsilon_{ij} = \delta_{ij} - \sum_k \left(\frac{\partial X_k}{\partial X_i}\frac{\partial X_k}{\partial X_j} + \frac{\partial X_k}{\partial X_i}\frac{\partial u_k}{\partial X_j} + \frac{\partial X_k}{\partial X_j}\frac{\partial u_k}{\partial X_i} - \frac{\partial u_k}{\partial X_i}\frac{\partial u_k}{\partial X_j}\right)$$

$$2\varepsilon_{ij} = \delta_{ij} - \delta_{ij} + \delta_{ki}\frac{\partial u_k}{\partial X_j} + \delta_{kj}\frac{\partial u_k}{\partial X_i} - \sum_k \frac{\partial u_k}{\partial X_i}\frac{\partial u_k}{\partial X_j}$$

which can be immediately reduced to (4.15).

N.B. The Lagrangian finite strain is:

$$\varepsilon_{ij} = \frac{1}{2}\left(\sum_k \frac{\partial X_k}{\partial x_i}\frac{\partial X_k}{\partial x_j} - \delta_{ij}\right) \tag{4.17}$$

Let us now focus our attention on the isotropic compressional strain caused by the application of hydrostatic pressure, and let us write:

$$\frac{\partial u_1}{\partial X_1} = \frac{\partial u_2}{\partial X_2} = \frac{\partial u_3}{\partial X_3} = \frac{\theta}{3} \tag{4.18}$$

$\theta = \sum_i \frac{\partial u_i}{\partial x_i} = \frac{\Delta V}{V_0}$ is the trace of the infinitesimal strain tensor.

From (4.15) and (4.18), we have:

$$\varepsilon_{ij} = \varepsilon\delta_{ij}$$

with:

$$\varepsilon = \frac{\theta}{3} - \frac{1}{2}\frac{\theta^2}{9} \tag{4.19}$$

An elementary cube of volume $V = (dX_1)^3$ in the strained state had a volume equal to $V_0 = \left[dX_1\left(1 - \frac{\partial u_1}{\partial X_1}\right)\right]^3$ in the unstrained state, hence:

$$\frac{V_0}{V} = \frac{\rho}{\rho_0} = \left(1 - \frac{\partial u_1}{\partial X_1}\right)^3 = \left(1 - \frac{\theta}{3}\right)^3$$

Using the simple trick of writing:

$$\left(1 - \frac{\theta}{3}\right)^3 = \left[\left(1 - \frac{\theta}{3}\right)^2\right]^{3/2}$$

we see that:

$$\frac{\rho}{\rho_0} = \left(1 - \frac{2\theta}{3} + \frac{\theta^2}{9}\right)^{3/2} = \left[1 - 2\left(\frac{\theta}{3} - \frac{\theta^2}{18}\right)\right]^{3/2} = (1 - 2\varepsilon)^{3/2} \quad (4.20)$$

As ε (dilatation) is negative for positive pressures, we introduce the "compression" $f = -\varepsilon$:

$$\frac{\rho}{\rho_0} = \frac{V_0}{V} = (1 + 2f)^{3/2} \quad (4.21)$$

We see that for infinitesimal strains, we obtain the well-known result:

$$\frac{\rho}{\rho_0} = \frac{V_0}{V} \approx 1 - \theta \quad (4.22)$$

The isothermal bulk modulus at $P = 0$ is:

$$K_{0T} = -\lim_{P\to 0}\left(\frac{PV}{\Delta V}\right)_T = -\lim_{P\to 0}\left(\frac{P}{\theta}\right)_T \quad (4.23)$$

and, since $P = -\left(\frac{\partial F}{\partial V}\right)_T$:

$$K_{0T} = -\lim_{P\to 0}\left(\frac{1}{\theta}\frac{\partial F}{\partial V}\right)_T \quad (4.24)$$

where F is the Helmholtz free energy.

Now, to first order, we have:

$$\frac{V}{V_0} = (1 + 2f)^{-3/2} \approx 1 - 3f \quad (4.25)$$

and:

$$dV \approx -3V_0\, df$$

Since f tends toward zero with P, we can write:

$$9K_{0T}V_0 = \lim_{P\to 0}\left(\frac{1}{f}\frac{\partial F}{\partial f}\right)_T \quad (4.26)$$

Let us now expand the free energy F in powers of f. If we take the energy of the unstrained state equal to zero and remembering that the elastic strain energy is quadratic for infinitesimal strains, we have:

$$F = a(T)f^2 + b(T)f^3 + c(T)f^4 + \cdots \quad (4.27)$$

4.3.2 Second-order Birch–Murnaghan equation of state

We will follow Bullen (1975) for the demonstration of the Birch–Murnaghan EOS. Let us consider only the expansion of F to second order:

$$F \approx af^2 \tag{4.28}$$

From (4.26) and (4.27), we obtain:

$$a = \frac{9}{2} K_{0T} V_0 \tag{4.29}$$

The pressure is:

$$P = -\left(\frac{\partial F}{\partial V}\right)_T = -\left(\frac{\partial F}{\partial f}\right)_T \frac{df}{dV} \tag{4.30}$$

Differentiating (4.21), we get:

$$\frac{dF}{dV} = -\frac{1}{3V_0}(1 + 2f)^{5/2} \tag{4.31}$$

hence:

$$P = 3K_{0T} f(1 + 2f)^{5/2} \tag{4.32}$$

Using (4.21), we can express f in terms of ρ/ρ_0:

$$f = \frac{1}{2}\left[\left(\frac{\rho}{\rho_0}\right)^{2/3} - 1\right] \tag{4.33}$$

and carrying it into (4.32), we obtain the *second-order Birch–Murnaghan equation of state* (Birch, 1938, 1947):

$$P = \frac{3K_{0T}}{2}\left[\left(\frac{\rho}{\rho_0}\right)^{7/3} - \left(\frac{\rho}{\rho_0}\right)^{5/3}\right] \tag{4.34}$$

The bulk modulus can be calculated directly from (4.34):

$$K = \frac{\rho}{\rho_0} \frac{dP}{d\left(\frac{\rho}{\rho_0}\right)} \tag{4.35}$$

$$K = \frac{K_{0T}}{2}\left[7\left(\frac{\rho}{\rho_0}\right)^{7/3} - 5\left(\frac{\rho}{\rho_0}\right)^{5/3}\right] \tag{4.36}$$

and, using (4.21) again:

$$K = K_{0T}(1 + 7f)(1 + 2f)^{5/2} \tag{4.37}$$

The seismic parameter Φ is, then, a simple polynomial in f:

$$\Phi \equiv \frac{K}{\rho} = \frac{K_0}{\rho_0}(1 + 2f)(1 + 7f)$$

or:

$$\Phi = \Phi_0(1 + 9f + 14f^2) \tag{4.38}$$

The pressure derivative of the bulk modulus is calculated from (4.37) and (4.31):

$$\left(\frac{dK}{dP}\right)_{P=0} = K_0' = \frac{dK}{df}\frac{df}{dP}$$

$$K_0' = \frac{12 + 49f}{3 + 21f} \tag{4.39}$$

It is interesting to note that purely from finite strain theory, we obtain the numerical value $K_0' = 4$, for the infinitesimal case $f \to 0$. It turns out that the experimental values of K_0' for many close-packed minerals are usually close to 4 (see Table 4.1, below).

Note also that $K_0' = 4$ corresponds to reasonable values of the Grüneisen parameters:

$$\gamma_{\mathrm{SI}} = 1.8 \qquad \gamma_{\mathrm{VZ}} = 1.2$$

Introducing the value $K_0' = 4$ in Murnaghan's equation of state (4.6), we can compare the pressure P' it predicts with the pressure P predicted by the Birch–Murnaghan EOS (4.34) for the same values of ρ/ρ_0. We see (Fig. 4.2) that P' is slightly greater than P, but for values of $\rho/\rho_0 < 1.25$ given by the seismological PREM model for the lower mantle, the relative difference is about 3%.

N.B. Let us consider the results we obtain if, expanding the strain energy to second order in the finite strain f as we have done in (4.29), we calculate P, K and K_0' in the limit $f \to 0$. We see from (4.32) that: $P = 3fK_{0T}$, when $f \to 0$; we have from (4.22): $\rho/\rho_0 = 1 + 3f$, hence:

$$P = K_{0T}\left(\frac{\rho}{\rho_0} - 1\right)$$

$$K = \rho\frac{\partial P}{\partial \rho} = K_{0T}\frac{\rho}{\rho_0} = K_{0T} + P$$

This physically corresponds to a situation, where, having applied pressure P and compressed the solid to a finite compression f, we then increase the strain f by

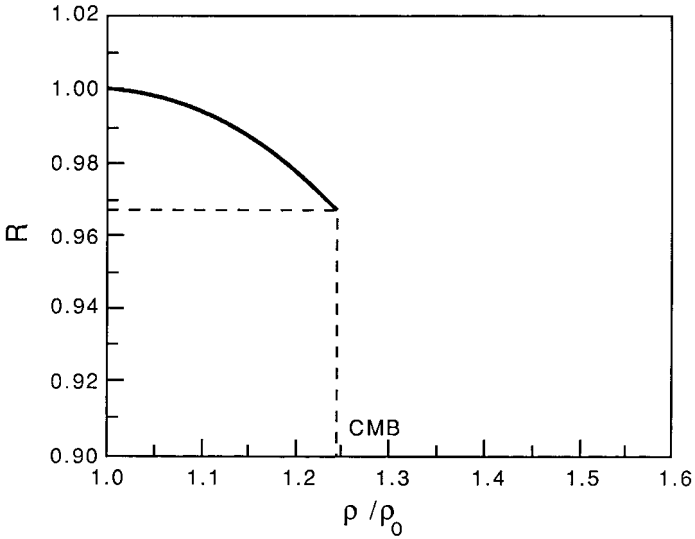

Figure 4.2 Ratio R of the pressure given by the second-order Birch–Murnaghan equation of state to the pressure given by Murnaghan's equation (with $K'_0 = 4$) as a function of ρ/ρ_0 (ratio of the density to the density at zero pressure) for the material of the lower mantle. At the core–mantle boundary (CMB) $R = 0.968$.

infinitesimal increments. The effective bulk modulus is then increased by P (see (4.3)).

4.3.3 Third-order Birch–Murnaghan equation of state

If we expand F to third order in f:

$$F = a(T)f^2 + b(T)f^3 \tag{4.40}$$

we have:

$$P = 3K_{0T}f(1 + 2f)^{5/2}\left(1 + \frac{3bf}{2a}\right) \tag{4.41}$$

For $P = 0\,(f = 0)$, $K = K_0$ and $K' = K'_0$. Expressing these conditions as a function of the coefficients a and b yields the third-order Birch–Murnaghan EOS, after a simple, but tedious, calculation:

$$P = \frac{3K_{0T}}{2}\left[\left(\frac{\rho}{\rho_0}\right)^{7/3} - \left(\frac{\rho}{\rho_0}\right)^{5/3}\right]\left\{1 + \frac{3}{4}(K'_0 - 4)\left[\left(\frac{\rho}{\rho_0}\right)^{2/3} - 1\right]\right\} \tag{4.42}$$

usually written:

$$P = \frac{3K_{0T}}{2}\left[\left(\frac{\rho}{\rho_0}\right)^{7/3} - \left(\frac{\rho}{\rho_0}\right)^{5/3}\right]\left\{1 - \xi\left[\left(\frac{\rho}{\rho_0}\right)^{2/3} - 1\right]\right\} \tag{4.43}$$

Table 4.1. *Elastic moduli at room temperature of mantle materials, and their pressure derivatives*

Mineral	K_0 (GPa)	K'_0	μ_0 (GPa)	μ'_0	Reference
α-$(Mg_{0.9}Fe_{0.1})_2SiO_4$	131.1	3.8			Zha *et al.* (1998a)
α-$(Mg_{0.9}Fe_{0.1})_2SiO_4$	126.3	4.28	78	1.71	Abramson *et al.* (1997)
α-Mg_2SiO_4	129	4.2	79	1.4	Zha *et al.* (1998b)
α-Mg_2SiO_4	128	4.44	80	1.32	Li *et al.* (1998)
α-Mg_2SiO_4	125	4.45	77	1.79	Fujisawa (1998)
β-Mg_2SiO_4	170	4.24	108	1.49	Li *et al.* (1998)
β-Mg_2SiO_4	170	4.3	115	1.4	Zha *et al.* (1998b)
β-Mg_2SiO_4	166	6.04	111	2.15	Fujisawa (1998)
γ-$(Mg_{0.6}Fe_{0.4})_2SiO_4$	183	5.38			Zerr *et al.* (1993)
$MgSiO_3$ (Pv)	261	4			Funamori *et al.* (1996)
$MgSiO_3$ (En) [>4.2 GPa]	123	5.6			Angel & Ross (1996)
MgO	153	4			Utsumi *et al.* (1998)

Pv = perovskite; En = enstatite.

Note that if $K'_0 = 4$, we obtain the second-order equation (4.34).

Static equations of state of minerals are currently obtained up to pressures of several hundred kilobar (tens of GPa) (e.g. Will *et al.*, 1986) and even sometimes above a megabar (100 GPa) (Knittle and Jeanloz, 1987). The method consists in measuring the lattice parameters by X-ray diffraction *in situ* in a diamond-anvil cell at various pressures; the curve $V/V_0 = f(P)$ is usually fitted by a third-order Birch–Murnaghan EOS. However, there is a trade-off between the values of K_0 and K'_0 and, in many cases, the accuracy of the measurement is too low to obtain a good value of K'_0, so $K'_0 = 4$ is assumed (which, in fact, amounts to fitting the data by a second-order Birch–Murnaghan EOS).

Knittle (1995) gives a review of the experimental techniques and the values of K_0 and K'_0 for a great number of minerals. Recent values for mantle minerals are given in Table 4.1.

The errors involved in parameter-fitting of the compression curves have been analyzed by Bell *et al.* (1987). Angel and Ross (1996) point out that fitting the compression curve with a unique equation of state may lead to erroneous results when the mineral undergoes a structural change, as is the case for orthopyroxene at 4.2 GPa.

More generally, Stacey *et al.* (1981) and O. L. Anderson (1995a) note that the Birch–Murnaghan equation is subject to a truncation problem due to

the fact that the coefficient of the term of degree 4 of the polynomial expansion of the free energy is larger than that of the term of degree 3, leading to bad convergence for large strains . However, it turns out that the coefficient of the term of degree 3 vanishes for $K'_0 = 4$, which accounts for the fact that, despite its shortcomings, the second-order Birch–Murnaghan equation works rather well in this case. Indeed, Stacey *et al.* (1981) write that: "In spite of its apparently rigorous, classical origin, the Love–Murnaghan–Birch formalism has no more fundamental theoretical basis than [. . .] other, mostly completely empirical, approaches . . .", and O. L. Anderson (1995a) remarks: "The long use and wide application of this [Birch–Murnaghan] EoS has engendered for it a certain authority in the literature. Nevertheless, this EoS, like all other isothermal EoSs, is based on an unproven assumption. In this case, the EoS rests on the assumption of Eulerian strain."

We will now examine an equation of state, based on another definition of finite strain, that is free from many of the shortcomings of the Birch–Murnaghan EOS.

4.4 A logarithmic equation of state

4.4.1 The Hencky finite strain

When the finite strain is defined by the change in distance between two neighboring points during deformation (Section 4.3.1), the problem arises of choosing between the Eulerian and the Lagrangian schemes. Now, the Lagrangian and Eulerian strains behave very differently for large extensions and compressions and are equivalent only for small strains.

As a function of V/V_0 or ρ/ρ_0, the Eulerian and Lagrangian strains are:

$$\varepsilon_{\mathrm{E}} = \frac{1}{2}\left[1 - \left(\frac{V_0}{V}\right)^{2/3}\right] = \frac{1}{2}\left[1 - \left(\frac{\rho}{\rho_0}\right)^{2/3}\right] \tag{4.44}$$

and:

$$\varepsilon_{\mathrm{L}} = \frac{1}{2}\left[\left(\frac{V}{V_0}\right)^{2/3} - 1\right] = \frac{1}{2}\left[\left(\frac{\rho_0}{\rho}\right)^{2/3} - 1\right] \tag{4.45}$$

It is easily seen that for infinite extension ($V \to \infty$) the Eulerian strain takes the finite value $\frac{1}{2}$, while for infinite compression ($V \to 0$) the Lagrangian strain takes the finite value $-\frac{1}{2}$. This obviously makes the Lagrangian strain unsuitable for large compressions. However, the choice remains fraught with an uncomfortable arbitrariness.

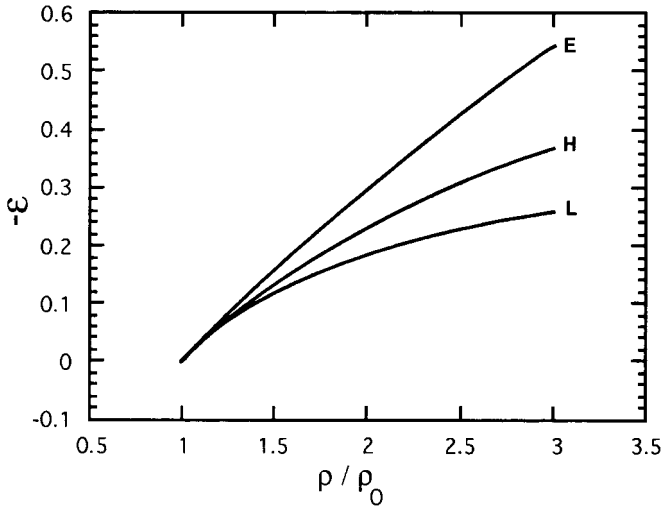

Figure 4.3 Eulerian, Lagrangian, and Hencky strains (see text).

Engineers and structural geologists, dealing with large finite strains, have taken a different approach (see e.g. Means, 1976; Poirier, 1985). In uniaxial deformation (compression or extension), they do not take as a reference state either the deformed or undeformed state. Instead, they define an increment of strain $d\varepsilon$ corresponding to the increase (or decrease) by dl of the current length l of a sample during deformation:

$$d\varepsilon = \frac{dl}{l} \tag{4.46}$$

When the body undergoes a finite extension (or compression) from l_0 to l, the total finite strain is:

$$\varepsilon_{\mathrm{H}} = \int_{l_0}^{l} d\varepsilon_{\mathrm{H}} = \ln \frac{l}{l_0} \tag{4.47}$$

The finite strain thus defined is called the *Hencky strain* (Fig. 4.3). For compression under hydrostatic pressure, the Hencky strain has a simple expression (Reiner, 1969, p. 43):

$$\varepsilon_{\mathrm{H}} = \frac{1}{3} \ln \left(\frac{V}{V_0} \right) = \frac{1}{3} \ln \left(\frac{\rho_0}{\rho} \right) \tag{4.48}$$

It is clear that the Hencky strain satisfactorily tends to $-\infty$ for infinite compression, and to $+\infty$ for infinite extension.

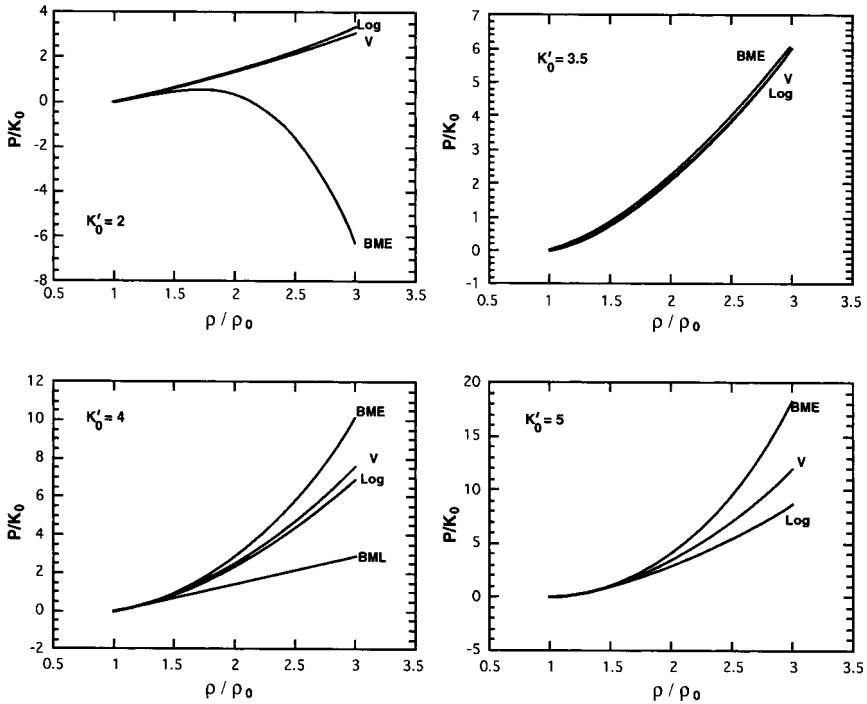

Figure 4.4 P/K_0 as a function of ρ/ρ_0 for the logarithmic (Log) and Birch–Murnaghan EOS, for different values of K_0' ($K_0' = 2$, 3.5, 4, 5). BME: Birch–Murnaghan Eulerian. BML: Birch–Murnaghan Lagrangian, V: Vinet.

4.4.2 The logarithmic EOS

An equation of state can be derived by expanding the free energy in powers of the Hencky strain (exactly as the Birch–Murnaghan EOS was derived by expanding the free energy in powers of the Eulerian strain). In this case the convergence of the expansion is better.

For the expansion to second order, we obtain the simple expression (Poirier and Tarantola, 1998):

$$P = K_0 \frac{\rho}{\rho_0} \ln \frac{\rho}{\rho_0} \tag{4.49}$$

and to third order:

$$P = K_0 \frac{\rho}{\rho_0} \ln \frac{\rho}{\rho_0} \left[1 + \left(\frac{K_0' - 2}{2} \right) \ln \frac{\rho}{\rho_0} \right] \tag{4.50}$$

Fig. 4.4 shows the compression curves $P/K_0 = f(\rho/\rho_0)$, for the logarith-

mic and the Birch–Murnaghan EOS, and different values of K_0'. We see that, if the curves are very similar for $K_0' \approx 3.5$, they diverge for $K_0' > 3.5$ and $K_0' < 3.5$. In the latter case, the Birch–Murnaghan EOS would lead to the unphysical result of negative pressures for very large compressions.

4.5 Equations of state derived from interatomic potentials

4.5.1 EOS derived from the Mie potential

Equations of state expressed as functions of (ρ/ρ_0) can be justified by the choice of appropriate interatomic attractive and repulsive potentials (see Section 3.6) (Gilvarry, 1957a; Stacey *et al.*, 1981).

Let us, for example, consider *Mie's potential* (3.87):

$$F(r) = -\frac{a}{r^m} + \frac{b}{r^n} = -aV^{-m/3} + bV^{-n/3} \tag{4.51}$$

Adjusting a and b to obtain $r = r_0$ and $K = K_0$ for $P = 0$, we obtain:

$$F(V) = \frac{9K_0V_0}{n-m}\left[-\frac{1}{m}\left(\frac{V}{V_0}\right)^{-m/3} + \frac{1}{n}\left(\frac{V}{V_0}\right)^{-n/3}\right] \tag{4.52}$$

and:

$$\begin{aligned} P &= \frac{3K_0}{n-m}\left[\left(\frac{V_0}{V}\right)^{[1+(n/3)]} - \left(\frac{V_0}{V}\right)^{[1+(m/3)]}\right] \\ &= \frac{3K_0}{n-m}\left[\left(\frac{\rho}{\rho_0}\right)^{[1+(n/3)]} - \left(\frac{\rho}{\rho_0}\right)^{[1+(m/3)]}\right] \end{aligned} \tag{4.53}$$

K_0' has the simple expression (see D. L. Anderson, 1989b):

$$K_0' = \frac{1}{3}(m + n + 6) \tag{4.54}$$

We see that the second-order Birch–Murnaghan equation is obtained for $m = 2$ and $n = 4$ and that, as expected, we have $K_0' = 4$.

N.B.: Using Slater's relation (3.65):

$$\gamma_{SI} = -\frac{1}{6} + \frac{1}{2}\frac{dK}{dP}$$

we find an expression for Slater's Grüneisen parameter for $P = 0$:

$$\gamma_{SI} = \frac{1}{6}(m + n + 5) \tag{4.55}$$

For $m = 2$ and $n = 4$, Slater's gamma is equal to 1.83.

In the case of ionic or ionocovalent crystals, it is physically more realistic to take $m = 1$, corresponding to a Coulombic attractive potential, we then obtain a *Born–Mie potential*:

$$F(V) = \frac{9K_0V_0}{n-1}\left[-\left(\frac{V}{V_0}\right)^{-1/3} + \frac{1}{n}\left(\frac{V}{V_0}\right)^{-n/3}\right] \tag{4.56a}$$

which can be expressed in terms of the Hencky strain, given by (4.48)

$$F(\varepsilon_H) = \frac{9K_0V_0}{n-1}\left[-\exp(-\varepsilon_H) + \frac{1}{n}\exp(-n\varepsilon_H)\right] \tag{4.56b}$$

Expanding F in powers of the Hencky strain to third order, and following the same procedure as above, we find the logarithmic EOS (4.50).

Other equations of state, derived from various more or less empirical interatomic potentials are given in Stacey *et al.* (1981).

4.5.2 The Vinet equation of state

At very high pressures, i.e. for large compressions, it is understandable that EOSs derived from expansions of a potential truncated to low orders become invalid. The Vinet EOS (Vinet *et al.*, 1987, 1989), derived from an empirical potential, has a special interest, since it gives good results for very compressible solids, such as hydrogen (Hemley *et al.*, 1990). It also gives good results for $MgSiO_3$ perovskite (Hama and Suito, 1996, 1998).

Partly due to an unfortunate choice of notations, the derivation of the EOS in the original paper (Vinet *et al.*, 1987) is unnecessarily complicated. It is, however, very simple to derive it, starting from the empirical potential used by the authors, and following the same steps as above.

The empirical potential is:

$$F(a) - F_0(1 + a)\exp(-a) \tag{4.57}$$

where:

$$a = \frac{r - r_0}{l} \tag{4.58}$$

and where r and r_0 have the same meaning as above and l is a scaling length.

Taking $V = (4/3)\pi r^3$, we find:

$$P = -\frac{\partial F(V)}{\partial V} = -\frac{F_0}{4\pi l r^2} a \exp(-a) \tag{4.59}$$

and setting:

$$K_0 = \frac{F_0}{12\pi l^2 r_0}$$

and:

$$K_0' = 1 + \frac{2r_0}{3l}$$

yields the Vinet EOS:

$$P = 3K_0 \left(\frac{V}{V_0}\right)^{-2/3} \left[1 - \left(\frac{V}{V_0}\right)^{1/3}\right] \exp\left\{\frac{3}{2}(K_0' - 1)\left[1 - \left(\frac{V}{V_0}\right)^{1/3}\right]\right\} \tag{4.60}$$

The compression curves corresponding to the Birch–Murnaghan, logarithmic and Vinet equations of state, for several values of K_0', are compared in Fig. 4.4. We see that the curve for the Vinet EOS is situated between the curves for the Birch–Murnaghan and logarithmic EOS, but closer to the curve for the logarithmic EOS. It is remarkable that, for $K_0' \approx 3.5$, all three curves are practically indistinguishable.

4.6 Birch's law and velocity–density systematics

4.6.1 Generalities

Having measured the compressional wave velocities v_P of some 250 specimens of rocks by ultrasonic methods, up to 10 kbar (1 GPa), Birch (1961a) found that at pressures above a few kilobars (when most cracks are closed), the principal factors determining velocity were the specific mass ρ and the mean atomic mass $\bar{M}$ (usually, although improperly, called "density" and mean atomic "weight" respectively). The mean atomic mass is equal to the sum of the atomic masses of all atoms in a formula unit, divided by the number of atoms. The mean atomic mass of Mg_2SiO_4 for instance is equal to: $\bar{M} = (2 \times 24.3 + 28.3 + 4 \times 16)/7 = 20.13$. It turns out that most close-packed mantle oxides and silicates have a value of $\bar{M}$ close to 20 (e.g. 20.12 for $MgSiO_3$; 20.15 for MgO). In most cases, an increase in $\bar{M}$ above these values corresponds to the replacement of magnesium by the heavier iron. One can consider that, for the mantle $\bar{M} = 21.1$ and for the core $\bar{M} = 49.3$.

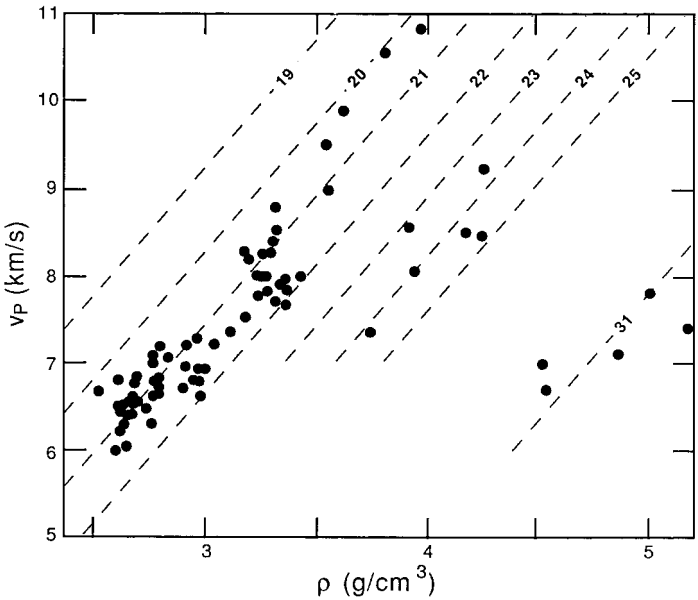

Figure 4.5 Velocity of P-waves at 1 GPa vs specific mass for silicates and oxides. The dashed lines show the trend for a constant mean atomic mass (after Birch, 1961a).

Birch (1961a) was able to fit the data corresponding to the same $\bar{M}$ by a linear law (Fig. 4.5) and, for values corresponding to the mantle ($20 \leq \bar{M} \leq 22$), he found:

$$v_P = -1.87 + 3.05\rho \tag{4.61}$$

with v_P in km/s and ρ in g/cm^3.

More generally, Birch (1961b) noted that: "The experimental data suggest that, regardless of crystal structure, the representative points on the velocity–density diagram will move along a line of constant mean atomic weight," and that, in general:

$$v_P = a(\bar{M}) + b\rho \tag{4.62}$$

Also, isostructural compounds plot on lines roughly perpendicular to the iso-$\bar{M}$ lines.

Birch further wrote: "*As a provisional hypothesis, it will be postulated that the velocity–density relations, as expressed above, hold for all changes of density in the Earth's mantle, however produced.*" In other words, the changes in density produced by compression or by replacing a mineral by an "analog" compound of same $\bar{M}$ but of different chemical composition,

cause the same change in elastic wave velocity. Forty years later, the "provisional hypothesis" still holds and relation (4.62), known as *Birch's law*, has given rise to the vast field of velocity–density systematics on analog compounds.

Analog compounds of minerals relevant to geophysics (mostly silicates) are usually isostructural crystals (see below for the importance of structure) with different cations: in the perovskite structure, for instance, silicon can be replaced by germanium, titanium or even aluminum, while magnesium and iron can be replaced by other alkaline earths or transition elements (Liebermann *et al*., 1977). The replacement of divalent oxygen by the univalent fluoride anion gives rise to another class of analogs: fluorides, with weaker ionic bonds, which are indeed rather good models of oxides (e.g. BeF_2 for SiO_2) and have been used to infer their elastic or thermal properties (Jones and Liebermann, 1974; Jackson, 1977).

The velocity–density systematics are currently used for three main purposes (Liebermann, 1973):

- Determining the density profiles from measured seismic velocities in regions of the mantle assumed to be chemically homogeneous.
- Assessing the chemical homogeneity of regions of the mantle and relating the inhomogeneity to changes in chemical composition.
- Relating the velocity jump at seismic discontinuities to the density increase known to occur for certain phase transitions.

The contribution of this approach to geophysics has been immense, but specific conclusions are usually not unique and must sometimes be taken with a grain of salt. Indeed, Schreiber and Anderson (1970) found that Birch's curves for various rocks such as diabase, gabbro and eclogite, fitted the data on various cheeses extremely well and that it was not possible to reject the hypothesis that the Moon is made of green cheese, on acoustic grounds.

As the elastic wave velocities depend on the elastic constants and density, Birch's law is indeed an equation of state, if the changes in density are assumed to be produced by hydrostatic pressure. Furthermore, if one justifiably assumes that the velocities are insensitive to frequency at first order, i.e. that the velocity–density relationship established in the laboratory at ultrasonic frequencies (≈ 1 MHz) is valid for seismic frequencies (≤ 10 Hz), we have then a *seismic equation of state* (D. L. Anderson, 1967).

In what follows, we will try to extract the most important results from a considerable amount of published literature and, for details, we will refer the reader to the original papers and review articles (e.g. Wang, 1978;

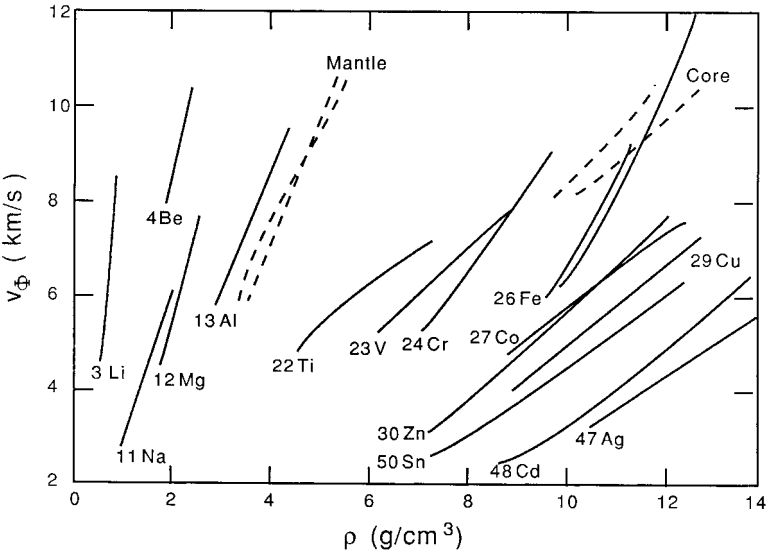

Figure 4.6 Bulk sound velocity vs specific mass for metals, from shock-wave data (solid curves). The corresponding atomic masses are indicated. The curves (dashed) for mantle and core materials, from seismic data, are also shown (after Birch, 1963).

Liebermann, 1973, 1982; O. L. Anderson, 1988). We will deal only with bulk-velocity–density systematics, since, despite some attempts (Davies, 1976), the systematics on shear velocity are extremely unreliable, due to the great influence of the structure-sensitive non-central bonding forces in shear.

4.6.2 Bulk-velocity–density systematics

Using published values of the bulk (or hydrodynamical) velocity $v_\Phi = \sqrt{\Phi} = \sqrt{K/\rho}$, obtained by shock-wave experiments or isothermal compression on metals, Birch (1961b, 1963) found that the bulk-velocity–density plots occurred in a sequence corresponding to the sequence of the atomic numbers of the metals (Fig. 4.6). Superimposing on the plots of the metals the plots corresponding to the mantle and to the core obtained from seismic data, Birch was led to the conclusion that the mantle was composed of light elements and that the core was essentially made of iron. McQueen *et al.* (1964), using shock-wave data, obtained a bulk-velocity–density Birch's diagram for oxides and silicates (Fig. 4.7).

Wang (1968a) used an experimental shock-wave equation of state to show that the bulk-velocity–density plot for MgO was indeed linear up to 1.26 Mbar (126 GPa), in agreement with Birch's postulate. He established a

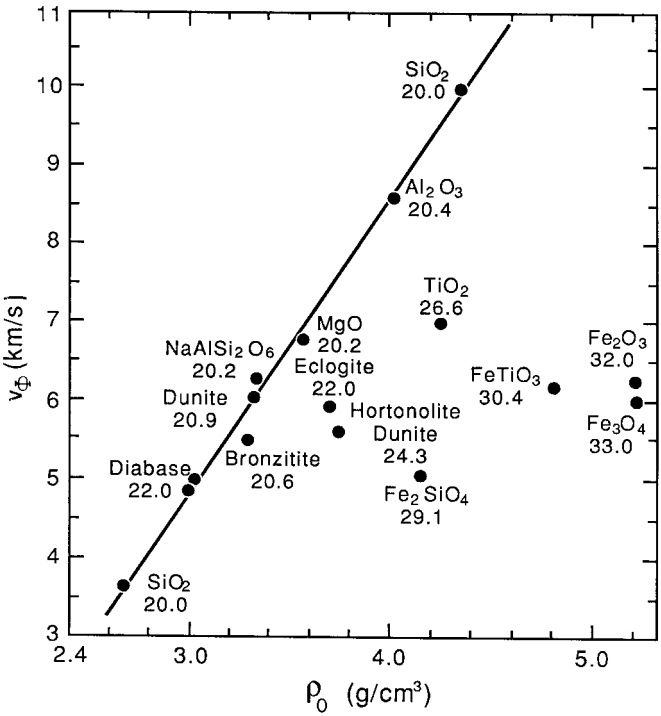

Figure 4.7 Bulk sound velocity vs specific mass for minerals and rocks of the mantle and crust. The mean atomic mass is indicated. The solid line is the locus of the points corresponding to material of mean atomic mass 20.1 (after McQueen *et al.*, 1964).

systematics similar to that of McQueen *et al.* (1964) with an equation:

$$v_\Phi = a(\bar{M}) + b\rho \tag{4.63}$$

For the values $20 \leq \bar{M} \leq 22$ corresponding to mantle minerals, Wang proposed:

$$v_\Phi = -1.75 + 2.36\rho \tag{4.64}$$

Wang (1970) compared the plots of Φ/Φ_0 vs ρ/ρ_0 corresponding to the empirical relationship (4.64) with the plot derived from the Birch–Murnaghan expression of the seismic parameter:

$$\frac{\Phi}{\Phi_0} = 7\left(\frac{\rho}{\rho_0}\right)^{4/3} - 5\left(\frac{\rho}{\rho_0}\right)^{2/3} \tag{4.65}$$

He found that the values of ρ/ρ_0 at given Φ/Φ_0, predicted by the linear relation, with coefficients consistent with experimental data were only 1% higher than those predicted by the Birch–Murnaghan EOS.

Shankland (1972, 1977) and Chung (1972) showed that Birch's law was consistent with Debye's theory: The sound velocity is $\bar{v}_D = \omega/k$ and we have, from (3.28) and (3.56):

$$\frac{d \ln \bar{v}_D}{d \ln \rho} = \gamma_D - \frac{1}{3} \tag{4.66}$$

As the values of Grüneisen's ratio for most materials are in the range of 1 to 2, the slopes of the constant mean atomic mass lines in Birch's diagram are roughly identical as a consequence of the near constancy of γ_D for the "isochemical" compounds. Integration of (4.66) would lead to a power law (see 4.68 below) and Chung (1972) showed that Birch's law is a linearization of the power law over a certain range of densities corresponding to those of most rocks and minerals.

Chung (1972) and Shankland (1972), using a reasoning based on interatomic potentials for ionic crystals, also proposed that the isostructural variation of the bulk velocity with $\bar{M}$ is given by:

$$\left(\frac{d \ln v_\Phi}{d \ln \bar{M}}\right)_{\text{struct.}} \cong -\frac{1}{2}$$

or

$$v_\Phi \sqrt{\bar{M}} = \text{const} \tag{4.67}$$

This relation can be justified by considering the acoustic velocity:

$$\bar{v}_a = \frac{\omega}{k} \propto \omega R_0$$

where R_0 is the interatomic distance at equilibrium and remembering that for harmonic atomic oscillations, the frequency ω is given by:

$$\omega \propto \sqrt{\frac{E_c''}{m}}$$

where E_c'' is the second derivative of the cohesive energy with respect to interatomic distance and m is the mass (see Section 3.2.1). For interatomic potentials appropriate for ionic crystals, such as (3.15), the cohesive energy is given by (3.18) and we have:

$$E_c'' = \frac{N\alpha q^2 (n-1)}{R_0^3}$$

hence:

$$\bar{v}_a \propto \left[\frac{N\alpha q^2 (n-1)}{m R_0}\right]^{1/2} \tag{4.68}$$

The quantity $\alpha q^2(n-1)/R_0$ is practically constant for a given structure and $\bar{M}$ is proportional to m. It follows that the logarithmic derivative of the velocity with respect to the mean atomic mass is equal to $-\frac{1}{2}$, hence equation (4.67).

The relation (4.67) has been verified for various oxides (Chung, 1972) (Fig. 4.8) and also for the geophysically interesting compounds with ilmenite (Liebermann, 1982) and perovskite (Liebermann *et al.*, 1977) structures (Fig. 4.9).

Birch's postulate that, whatever the cause of the density change, the relation between v_Φ and ρ can be represented by a straight line of constant slope, must be somewhat qualified, although it remains valid as a general principle. It appears, for instance, that crystal structure has some effect on the coefficient b of the linear relation (4.63): the slope of the iso-$\bar{M}$ lines tends to be smaller ($b \leq 3$) for close-packed structures such as corundum, rocksalt and perovskite than for open structures such as olivine, pyroxene or quartz ($b \geq 4$) (Liebermann, 1982). Furthermore, when the density change is caused by a phase transformation, b tends to be smaller when there is an increase in coordination than when the coordination remains unchanged (Liebermann and Ringwood, 1973; Liebermann, 1982).

A power-law form of the bulk-velocity–density relation can indeed be derived from (4.66), which we can write:

$$v_\Phi = a(\bar{M})\rho^{(\gamma - 1/3)} \tag{4.69}$$

D. L. Anderson (1967, 1989b) proposed a power-law seismic equation of state, derived from the expression of pressure in terms of interatomic potentials (see Section 4.5). Following Gilvarry (1957), Anderson writes equation (4.53) as:

$$P = (N-M)^{-1}K_0\left[\left(\frac{\rho}{\rho_0}\right)^N - \left(\frac{\rho}{\rho_0}\right)^M\right] \tag{4.70}$$

with: $N = 1 + (n/3)$ and $M = 1 + (m/3)$. Taking the derivative of pressure with respect to density and remembering that $\Phi = dP/d\rho$, we have:

$$\Phi = \Phi_0(N-M)^{-1}\left[N\left(\frac{\rho}{\rho_0}\right)^{N-1} - M\left(\frac{\rho}{\rho_0}\right)^{M-1}\right] \tag{4.71}$$

and:

$$\frac{d\ln\Phi}{d\ln\rho} = \frac{\rho}{\rho_0}\left[N(N-1)\left(\frac{\rho}{\rho_0}\right)^{N-2} - M(M-1)\left(\frac{\rho}{\rho_0}\right)^{M-2}\right] \cdot \left[N\left(\frac{\rho}{\rho_0}\right)^{N-1} - M\left(\frac{\rho}{\rho_0}\right)^{M-1}\right]^{-1}$$

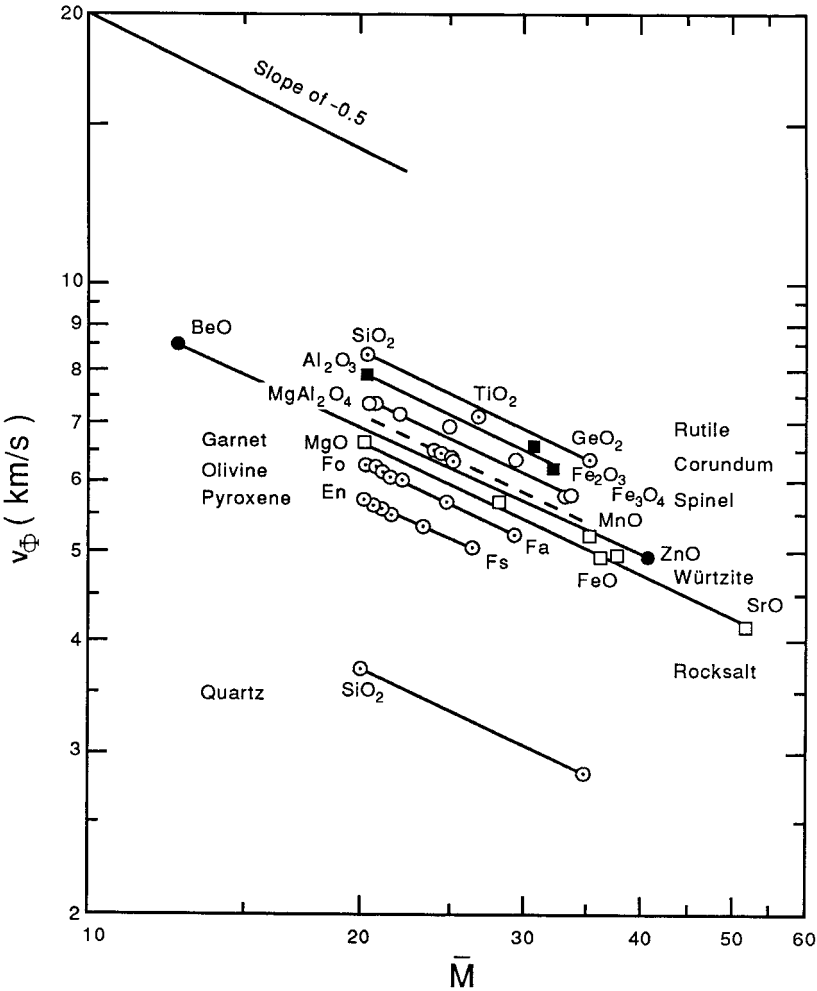

Figure 4.8 Bulk sound velocity vs mean atomic mass for various minerals. For minerals of the same structure and different chemical composition (e.g. Fe content), the empirical relation $v_\Phi \propto \bar{M}^{-1/2}$ is verified (after Chung, 1972).

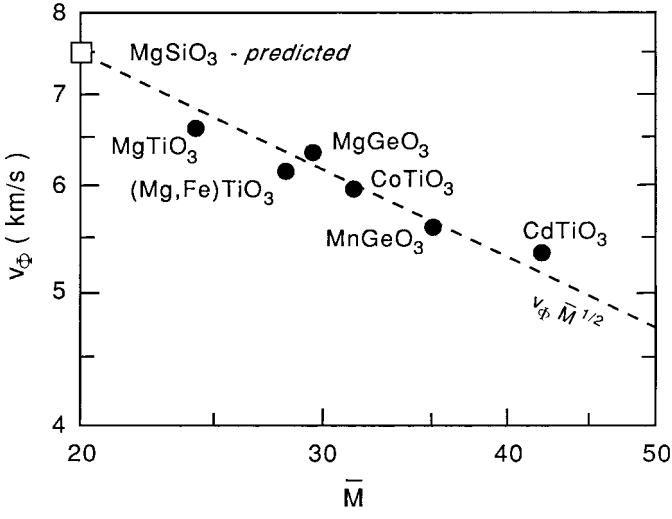

(a)

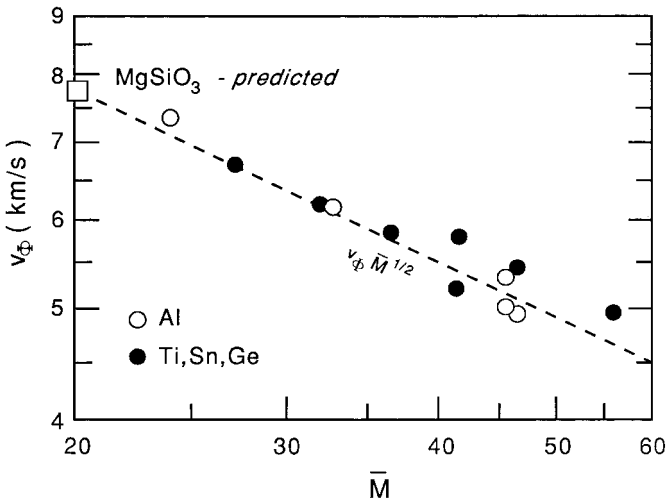

(b)

Figure 4.9 Bulk sound velocity vs mean atomic mass for crystals with ilmenite structure (a) and perovskite structure (b) (after Liebermann, 1982).

If $\rho/\rho_0 \approx 1$, i.e. for small compressions, we have:

$$\frac{d\ln\Phi}{d\ln\rho} \approx N + M - 1 = \frac{1}{3}(n + m + 3) \tag{4.72}$$

or:

$$\frac{\rho}{\rho_0} = \left(\frac{\Phi}{\Phi_0}\right)^{3/(n+m+3)} \tag{4.73}$$

Taking into account the expression for Slater's gamma (4.55), we can write:

$$\frac{\rho}{\rho_0} = \left(\frac{\Phi}{\Phi_0}\right)^{1/2[\gamma_{SI} - (1/3)]} \tag{4.74}$$

identical to (4.69). Note that (4.74) can be written:

$$\frac{d\ln\Phi}{d\ln\rho} = 2\left(\gamma_{SI} - \frac{1}{3}\right) \tag{4.75}$$

For $N = 4 = K_0'$ and $M = 0$, equation (4.69) becomes Murnaghan's linear integrated EOS and (4.73) becomes:

$$\frac{\rho}{\rho_0} = \left(\frac{\Phi}{\Phi_0}\right)^{1/3} \tag{4.76}$$

which, of course, can be directly obtained by taking the derivative of (4.6), with $K_0' = 4$:

$$\Phi = \frac{dP}{d\rho} = \Phi_0\left(\frac{\rho}{\rho_0}\right)^{K_0' - 1} \tag{4.77}$$

For $N = 7/3$ and $M = 5/3$ ($n = 4$, $m = 2$), equation (4.70) becomes the Birch–Murnaghan EOS and we also have:

$$\frac{\rho}{\rho_0} = \left(\frac{\Phi}{\Phi_0}\right)^{1/3} \tag{4.78}$$

which corresponds to a value of Slater's gamma of 1.83.

From an experimental correlation on 31 minerals and rocks, Anderson (1967) gives:

$$\frac{\rho}{\bar{M}} = 0.048\Phi^{0.323} \tag{4.79}$$

in good agreement with the theoretical considerations (Fig. 4.10).

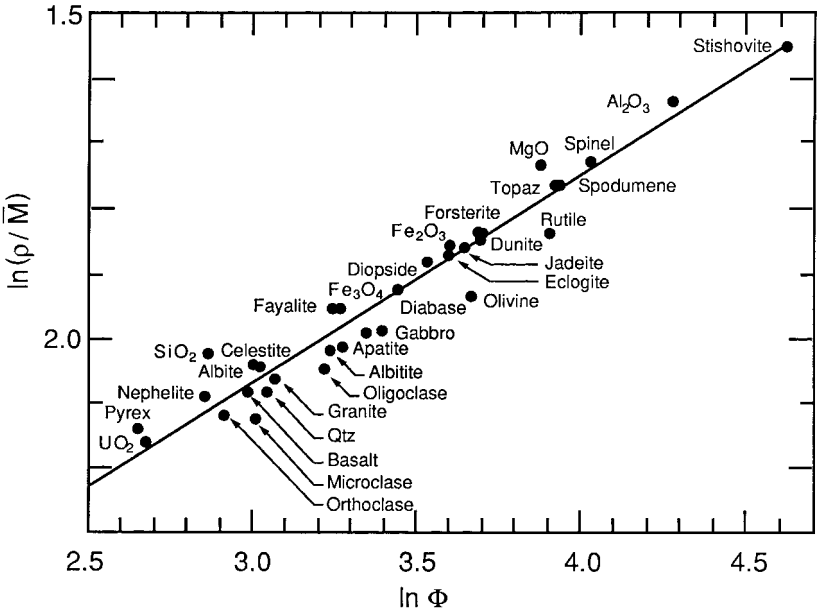

Figure 4.10 Seismic equation of state for selected rocks and minerals (after Anderson, 1967).

Equation (4.78) can be written:

$$\ln \rho = \frac{1}{3}\ln \Phi + \text{const} = \frac{1}{3}(\ln K - \ln \rho) + \text{const}$$

or:

$$\ln K = 4 \ln \rho + \text{const} \tag{4.80}$$

Relation (4.80) can be directly derived by setting $dK/dP = 4$ in

$$\Phi = \frac{d \ln K}{d \ln \rho} = -\frac{d \ln K}{d \ln V} = \frac{dK}{dP}$$

Anderson and Nafe (1965) verified that in the case of oxides the slope of the Φ–V logarithmic plot takes values between -4 and -3, whether the change in volume is due to compression or compositional variation. However, alkali halides, fluorides, sulfides and covalent compounds behaved differently and obeyed a relation:

$$K_0 V_0 = \text{const} \tag{4.81}$$

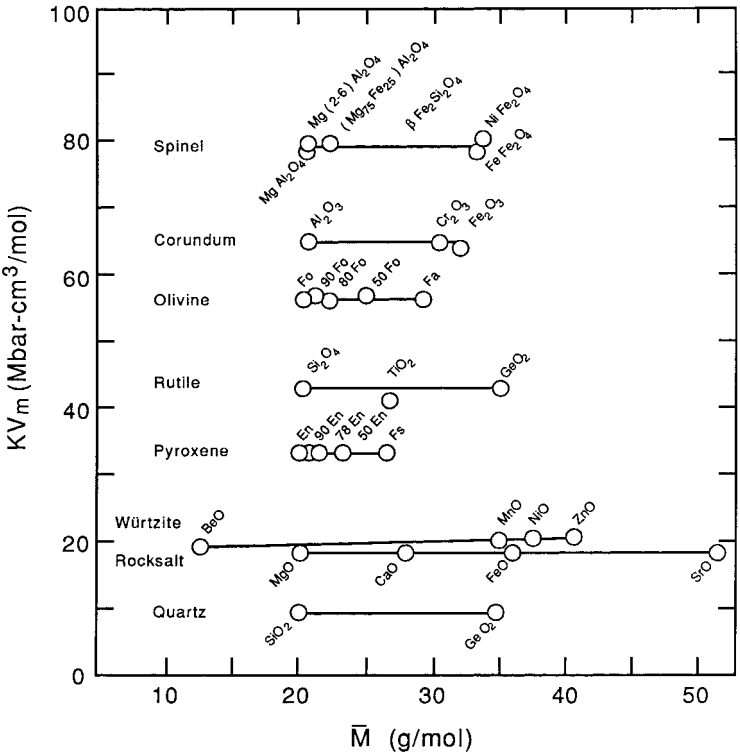

Figure 4.11 The product KV_m of the bulk modulus by the molar volume is almost constant for materials of the same crystal structure and independent of the mean atomic mass (after Chung, 1972).

where the bulk modulus and the specific molar volume are taken at ambient pressure.

Anderson and Anderson (1970) and Chung (1972) showed that the relation (4.81) is indeed applicable to oxides, provided they have the same structure (Fig. 4.11). This results from the near constancy of the quantity $\alpha q^2(n-1)/R_0$, in (4.68), which is equal to K_0V_0 (or $K_0R_0^3$), (see (3.20)).

4.7 Thermal equations of state

So far, we have only dealt with isothermal equations of state, whose material parameters are experimentally determined at room temperature. We will now consider equations of state valid at high temperatures (above Debye temperature) or with explicit temperature dependence. For a recent review see O. L. Anderson (1995a).

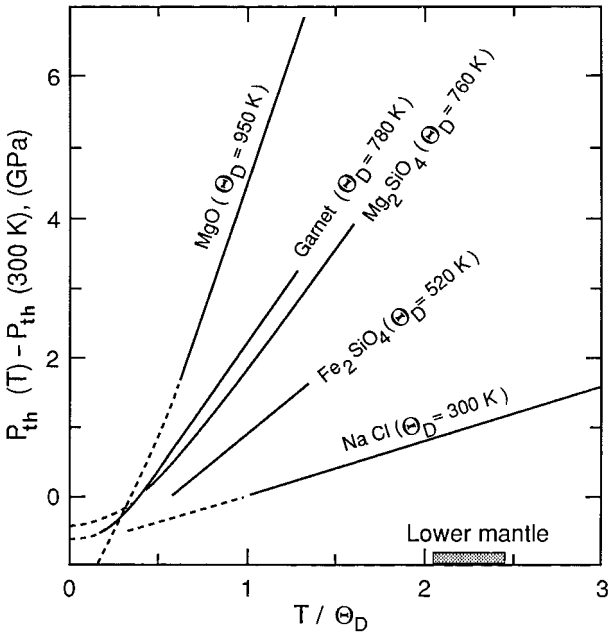

Figure 4.12 Experimentally determined thermal pressure (relative to the thermal pressure at room temperature) vs T/Θ_D (Θ_D = Debye temperature). In most cases the thermal pressure is proportional to temperature (after O.L. Anderson, 1984).

(i) At temperatures above the Debye temperature, we already know, of course, one appropriate EOS: the Mie–Grüneisen equation of state (3.53). However, it has the important drawback of containing a thermal pressure term: $P_{th} = \gamma_{th}E_{th}/V$, which is not directly accessible to experiment. O. L. Anderson (1984) circumvented the difficulty by proposing for P_{th} an empirical expression, independent of volume and linear in temperature: $P_{th} = a + bT$. The coefficients a and b are given a physical meaning by writing the thermal pressure along an isochore:

$$P_{th} = \int_0^T \left(\frac{\partial P}{\partial T}\right)_V dT = \int_0^T \alpha K_T dT \tag{4.82}$$

Assuming that αK_T is a constant independent of temperature for $T > \Theta_D$, an assumption valid in most cases (Birch, 1968; Brennan and Stacey, 1979; O. L. Anderson, 1980), Anderson finds:

$$P_{th} = -\int_0^{\Theta_D} \alpha K_T dT + \alpha K_T (T - \Theta_D) \tag{4.83}$$

The Mie–Grüneisen EOS, thus modified, is claimed to be universal, as the linear correlation (4.83) holds for most materials (Fig. 4.12). The bulk modulus can be measured at high temperatures by resonance methods (Sumino *et al.*, 1983) and the thermal expansion coefficient α can be measured by dilatometry.

(ii) Brennan and Stacey (1979) derived a high-temperature, thermodynamically based EOS by equating the expression of the thermodynamic gamma (3.55) with that of the Vaschenko–Zubarev gamma (3.81), both valid in the classical high-temperature range ($T > \Theta_D$). If $C_V = \text{const}$ and $(dK_T/dT)_V = 0$, αK_T is independent of T and P (or ρ) and we can write:

$$\gamma = \gamma_0 x^{-1}$$

with $x = \rho/\rho_0$. Denoting the derivatives with respect to x by primes, we have:

$$K = xP' \tag{4.84}$$

$$\frac{dK}{dP} = 1 + \frac{xP''}{P'} \tag{4.85}$$

Inserting (4.84) and (4.85) into the expression of the Vaschenko–Zubarev gamma (3.81), Breenan and Stacey obtain a differential equation:

$$9x^3P'' - (6x^2 + 18\gamma_0 x)P' + (4x + 24\gamma_0)P = 0 \tag{4.86}$$

whose solution is the EOS:

$$P = \frac{K_0}{2\gamma_0}\left(\frac{\rho}{\rho_0}\right)^{4/3}\left\{\exp\left[2\gamma_0\left(1 - \frac{\rho}{\rho_0}\right)\right] - 1\right\} \tag{4.87}$$

$$K = \frac{K_0}{3\gamma_0}\left(\frac{\rho}{\rho_0}\right)^{1/3}\left\{\left[2\frac{\rho}{\rho_0} + 3\gamma_0\right]\exp\left[2\gamma_0\left(1 - \frac{\rho}{\rho_0}\right)\right]^{-2}\frac{\rho}{\rho_0}\right\} \tag{4.88}$$

For $P = 0$, $K_0' = 2\gamma_0 + 5/3$ and for infinite pressure, K' asymptotically tends to 4/3.

(iii) Gilvarry (1957a) started from the isothermal general form of equations of state (4.53), which he wrote:

$$P = (N - M)^{-1}K_0\left[\left(\frac{V_0}{V}\right)^N - \left(\frac{V_0}{V}\right)^M\right] \tag{4.89}$$

$$K = (N - M)^{-1}K_0\left[N\left(\frac{V_0}{V}\right)^N - M\left(\frac{V_0}{V}\right)^M\right] \tag{4.90}$$

and he generalized it to arbitrary temperatures by replacing V_0 and K_0 by quantities $\mathscr{V}$ and $\mathscr{K}$, functions only of temperature. The temperature dependence of $\mathscr{V}$ and $\mathscr{K}$ is determined by considerations of thermodynamic consistency, writing that the expressions of $(\partial P/\partial T)_V$ and $(\partial K/\partial T)_V$ obtained by differentiating (4.89) and (4.90) are equal to:

$$\left(\frac{\partial P}{\partial T}\right)_V = \alpha K_T$$

and:

$$\left(\frac{\partial K}{\partial T}\right)_V = -\alpha V\left(\frac{\partial K}{\partial V}\right)_T + K^2\left(\frac{\partial \alpha}{\partial P}\right)_T$$

After various reasonable approximations, Gilvarry finds:

$$\mathscr{V}(T) = V_0 \exp\left[\int_0^T \alpha_0 dT\right] \tag{4.91}$$

$$\mathscr{K}(T) = K_0 \exp\left[\int_0^T \eta_0 \alpha_0 dT\right] \tag{4.92}$$

with $\eta = -K\alpha^{-1}\left(\frac{\partial \alpha}{\partial P}\right)_T$.

$\mathscr{V}(T)$ and $\mathscr{K}(T)$ are thus the volume of the solid at temperature T and zero pressure and the bulk modulus at temperature T and zero pressure respectively. The equation of state obtained by replacing V_0 and K_0 by $\mathscr{V}(T)$ and $\mathscr{K}(T)$ in (4.89 and 4.90) can be approximated at high pressure by retaining only the first terms in the expansion of the exponentials:

$$P = P(T_0) + (N-M)^{-1}K_0\left[N\left(\frac{V_0}{V}\right)^N - M\left(\frac{V_0}{V}\right)^M\right]\int_0^T \alpha_0 dT \tag{4.93}$$

Gilvarry found a very good agreement between the pressure as a function of compression measured for potassium at 77 K and the prediction of his EOS based on experimental results at 4.2 K.

(iv) Recent progress in experimental techniques at high pressures and temperatures, and the use of synchrotron radiation has made it possible to obtain thermal equations of state of mantle minerals in relevant pressures and temperature ranges (see e.g. Jeanloz and Hemley, 1994). In more and more cases, the derivatives of the bulk modulus and the thermal expansion coefficient with respect to pressure and temperature are measured.

The P–V–T equation of state of magnesiowüstite $(Mg_{0.6}, Fe_{0.4})O$ has been determined up to 30 GPa and 800 K (Fei *et al.*, 1992). The thermoelastic properties of $(Mg, Fe)SiO_3$ perovskite have been investigated by Wang *et al.* (1994) up to 11 GPa and 1300 K, and those of $MgSiO_3$ by Funamori *et al.* (1996) up to 30 GPa and 2000 K and by Fiquet *et al.* (1998) up to 57 GPa and 2500 K. Dubrovinsky *et al.* (1998), using X-ray diffraction at high temperature and pressure, determined the equation of state of corundum (Al_2O_3) and ε-iron up to 68 GPa.

Experimental results have also been used in thermodynamic modeling of the high-temperature, high-pressure thermoelastic properties of the silicate perovskite (O. L. Anderson, 1998; Hama and Suito, 1998).

A thorough critical analysis of the experimental data and of the constraints on the P–V–T equations of state of mantle minerals has been provided by Jackson and Rigden (1996) and Jackson (1998), and in the case of silicate perovskite by Bina (1995), who points out the importance of measuring the thermoelastic properties in the stability field of the mineral.

4.8 Shock-wave equations of state

4.8.1 Generalities

Although pressures up to above 5 Mbar (500 GPa) have been obtained in diamond-anvil cells (Xu *et al.*, 1986), in practice, equations of state of minerals obtained by static compression using the diamond-anvil cell cover a pressure range seldom extending above 1 Mbar (100 GPa). For the measure of density as a function of pressure from 1 bar (100 kPa) to 3.7 Mbar (370 GPa) (pressure at the center of the Earth), the shock-wave technique still has no competitors. Shock waves are generated in target samples by a variety of methods, essentially using explosives or high-velocity projectiles launched by a light-gas (hydrogen) gun. The quantities measured are the shock-wave velocity and the "particle velocity" (i.e. the velocity imparted to the particles of the sample by the shock wave) as well as the temperature. Details on the experimental apparatus and methods of measurement are given in review articles (Ahrens, 1980, 1987).

The results of the shock-wave experiments are embodied in *Hugoniot curves* or "Hugoniots", loci of the peak shock states achieved from the initial state by experiments with different impact velocities. The Hugoniots are usually given as Pressure vs Density curves or sometimes as Pressure vs Volume curves. Typically, they exhibit several stages (Fig. 4.13).

(i) Up to the pressure of the *Hugoniot Elastic Limit* (HEL), which can

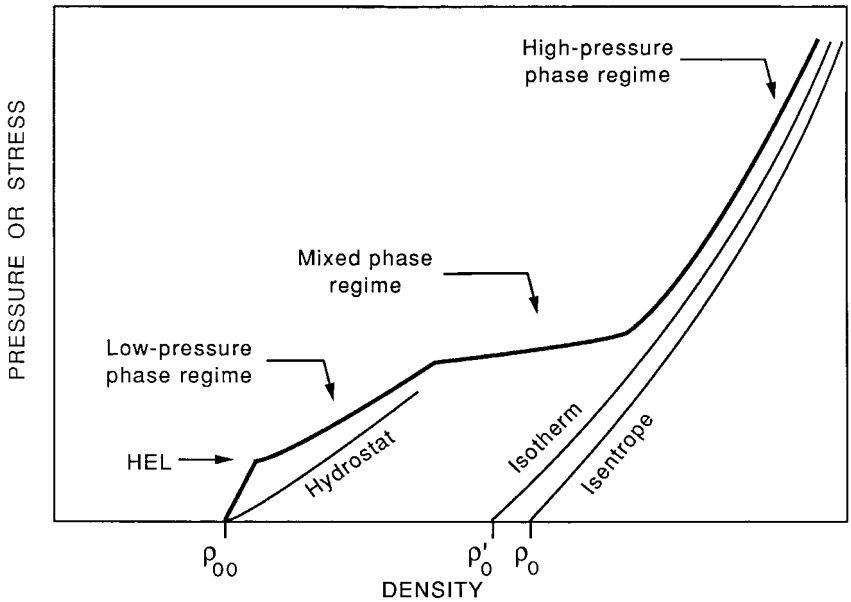

Figure 4.13 Typical Hugoniot curve showing the Hugoniot elastic limit (HEL). The hydrostatic compression curve (hydrostat) of the low-pressure phase is given for comparison (after Ahrens, 1980).

vary from about 0.2 GPa (for halite) to about 20 GPa (for diamond), the regime is one of finite elastic strain, corresponding to the propagation of the longitudinal shock wave.

(ii) Above the Hugoniot elastic limit, the material yields plastically at the microscopic level and loses most or all of its shear strength, behaving in effect hydrostatically like a fluid. The Hugoniot then differs little, if at all, from the theoretical hydrostatic Hugoniot or "hydrostat".

(iii) Most Earth materials at high pressure exhibit one or several phase transitions toward higher-density phases, giving rise to new stages on the Hugoniot corresponding to the behavior of the high-pressure phases. Between the low-pressure phase and the high-pressure phase regimes (and between successive high-pressure phase regimes), a transitional "mixed-phase regime" occurs.

It is important to note that the Hugoniot is just the locus of the final shock state achieved, but that it is not the thermodynamic path followed by the material. In other words, "successive shock states along the Hugoniot cannot be achieved one from another by the shock process" (Ahrens, 1987). The actual thermodynamic path followed is a straight line from the initial

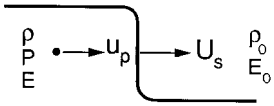

Figure 4.14 Profile of a shock wave propagating with velocity U_s in a material of density ρ_0 and energy E_0 at rest. Behind the front, the density, pressure, and energy are ρ, P, and E, respectively, and the particle velocity is u_p.

to the final state, called the *Rayleigh line* (see below). Similarly, the pressure–density relation represented by the Hugoniot in the low- or high-pressure phase regimes does not correspond to an isothermal equation of state, any more than it is adiabatic. Isotherms or isentropes (adiabats) can however be derived from the Hugoniot (reduction of the Hugoniot to isothermal EOS) (see below).

We will now derive the Rankine–Hugoniot equations governing the thermodynamics of shock-wave experiments.

4.8.2 The Rankine–Hugoniot equations

Let us consider a steady planar shock front, with a rise time short compared to the characteristic decay time, propagating in a solid at rest (Fig. 4.14). The shock front propagates with a velocity U_s with respect to the frame of reference of the laboratory and imparts a velocity u_p to the particles of the solid. The specific mass and the internal energy per unit mass change from the values ρ_0 and E_0 at rest to ρ and E behind the shock front.

We will now perform the calculations in the frame of reference of the shock front, considered as at rest.

Let us assume that the sample is a cylinder of unit area cross-section at rest in the frame of reference of the laboratory and that the shock wave goes through it from left to right with a velocity U_s (Fig. 4.15).

In the frame of reference of the shock front, the particles of matter arrive from the right with a velocity U_s (from right to left) and they acquire a velocity u_p (from left to right), the velocity with respect to the shock front therefore becomes $U_s - u_p > 0$ (the positive sense is taken from right to left).

Let us now write the conservation of mass, momentum and energy in a slice containing the shock front.

(i) Per unit time, the mass entering the slice is equal to the mass leaving it:

$$\rho_0 U_s = \rho(U_s - u_p) = m \tag{4.94}$$

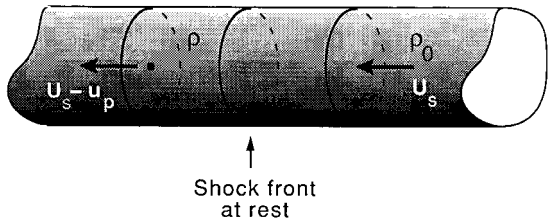

Figure 4.15 Velocities of the particles in the frame of reference of the shock front.

(ii) The sum of the forces exerted on the slice is equal to the rate of change of momentum. The forces on the unit area cross-section ends of the slice are equal to the normal stresses σ_0 and σ, i.e. to the pressures P_0 and P in the hydrostatic case, above the HEL:

$$m[(U_s - u_p) - U_s] = \sigma_0 - \sigma$$

or:

$$P - P_0 = mu_p \tag{4.95}$$

and, with (4.94):

$$P - P_0 = \rho_0 U_s u_p \tag{4.96}$$

(iii) The work done by the forces is equal to the sum of the increments of kinetic energy and internal energy per unit time:

$$P_0 U_s - P(U_s - u_p) = m\left[E - E_0 + \frac{1}{2}(U_s - u_p)^2 - \frac{1}{2}U_s^2\right]$$

or, with (4.95):

$$-mu_p U_s + P_0 u_p + mu_p^2 = m\left[E - E_0 - u_p U_s + \frac{1}{2}u_p^2\right]$$

and, with (4.94):

$$\rho_0 U_s\left(E - E_0 - \frac{1}{2}u_p^2\right) = P_0 u_p \tag{4.97}$$

We can set $P_0 = 0$ in (4.94), (4.96) and (4.97) and we obtain the usual form of the Rankine–Hugoniot equations:

$$\rho = \frac{\rho_0 U_s}{U_s - u_p} \tag{4.98}$$

$$P = \rho_0 u_p U_s \tag{4.99}$$

$$\Delta E = E - E_0 = \frac{1}{2}u_p^2 \tag{4.100}$$

We see that the increase in internal energy is equal to the kinetic energy (per unit mass).

If, now, we retain P_0 for symmetry and eliminate u_p between (4.94) and (4.96), we obtain:

$$U_s^2 = (P - P_0)\left[\frac{\rho}{\rho_0}(\rho - \rho_0)\right]$$

or, in terms of the specific volumes:

$$U_s = V_0\left(\frac{P - P_0}{V_0 - V}\right)^{1/2} \tag{4.101}$$

Eliminating U_s between (4.96) and (4.101), we obtain:

$$u_p = [(P - P_0)(V_0 - V)]^{1/2} \tag{4.102}$$

With (4.101) and (4.102), (4.97) gives:

$$E = E_0 + \frac{1}{2}(P + P_0)(V_0 - V) \tag{4.103}$$

For a final shock state characterized by u_p and U_s, the energy is known, since it is a function of the shock-wave and particle velocities only, and the pressure and specific volume are, from (4.101) and (4.102):

$$P = P_0 + \frac{u_p U_s}{V_0} \tag{4.104}$$

$$V = V_0 - V_0\frac{u_p}{U_s} \tag{4.105}$$

The initial specific volume is that of the sample, equal to that of the material for non-porous samples only. If an artificially porous sample is used (V_0 large), shock states of higher energy at higher pressures can be reached for the same shock-wave velocity. For a given specific volume (or mass), one can achieve different energy states (at different pressures) by driving shock waves into samples of different initial porosities. The Grüneisen parameter can then be obtained by carrying the finite differences ΔP and ΔE obtained from (4.104) and (4.103) into the definition (2.60): $\gamma_{th} = V(\Delta P/\Delta E)_V$.

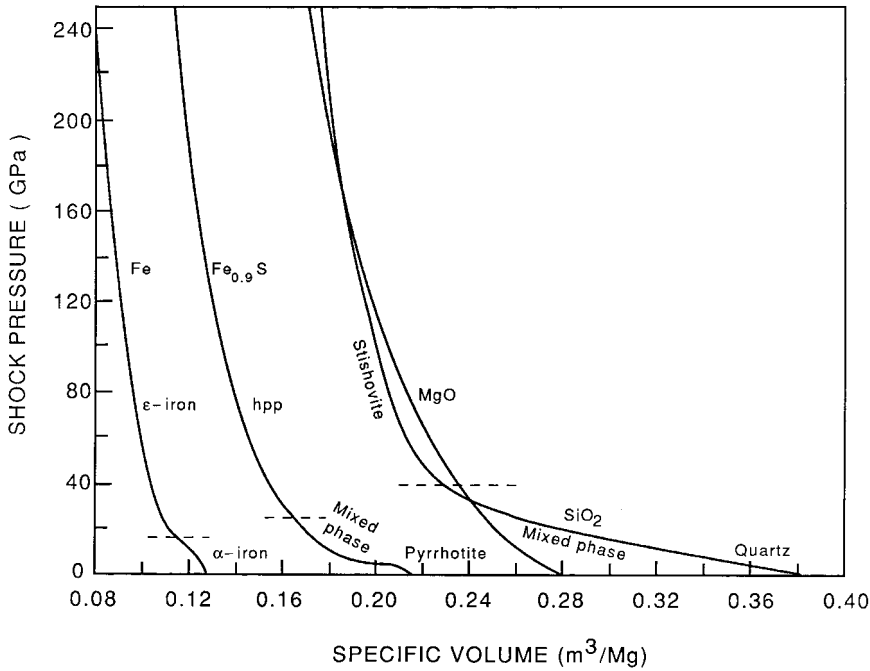

Figure 4.16 Pressure–volume Hugoniots for periclase, iron, pyrrhotite, and quartz. Except periclase, these minerals exhibit phase changes (after Ahrens, 1987). hpp: high-pressure phase.

The Hugoniot $P(V)$ (Fig. 4.16) or $P(\rho)$ is, as seen above, the locus of the final shock states of given internal energy, which cannot be reached by following the Hugoniot but a straight line, the Rayleigh line.

For a constant shock-wave velocity U_s and starting from $P_0 = 0$, we have, from (4.104):

$$P = \frac{u_p U_s}{V_0}$$

and, from (4.105):

$$u_p = \frac{U_s}{V_0}(V_0 - V)$$

hence:

$$P = \frac{U_s^2}{V_0^2}(V_0 - V) \tag{4.106}$$

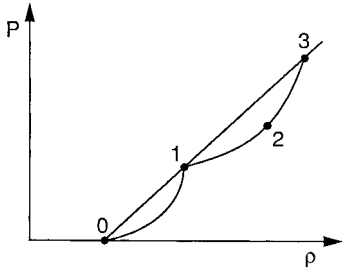

Figure 4.17 Multiple shock waves occur if the Rayleigh line from initial to final state intersects the Hugoniot. Point 1 corresponds to a phase transition or to the Hugoniot elastic limit. To obtain a final state between 1 and 3 (e.g. 2) two shock waves will form, one leading to the intermediate shock state 1, followed by a slower one leading from 1 to 2.

The slope of the Rayleigh line is equal to $-U_s^2/V_0^2$, it depends on the shock-wave velocity and the initial specific volume only.

The Hugoniots generally exhibit a change in slope at the pressure corresponding to the Hugoniot elastic limit (Fig. 4.17). The states between the HEL and the intersection of the HEL Rayleigh line with the Hugoniot can be reached only by a bifurcation of the shock wave: two successive shock waves form, the first one is an elastic wave that brings the material to the HEL state, the second one is slower and brings the material to the final state (Ahrens, 1971, 1987).

After the passage of the shock wave, the shocked material is released from the high-pressure shock state to ambient pressure in a very short time (10^{-6} to 10^{-5} s), following a *release isentrope* (Ahrens, 1987).

4.8.3 Reduction of the Hugoniot data to isothermal equation of state

For most materials, in a range of pressure where there is no phase transition, there exists an empirical linear relation between U_s and u_p, usually written (Takeuchi and Kanamori, 1966):

$$U_s = C_0 + \lambda u_p \tag{4.107}$$

Although there is no satisfactory theoretical explanation for this relation, Berger and Joigneau (1959) and, later, Ruoff (1967), have shown that by combining the Rankine–Hugoniot equations, the Mie–Grüneisen equation of state and an expansion of the pressure in a series of powers of the compression, it is possible to construct an expansion of U_s in a series of powers of u_p, whose first-order terms represent (4.107). The particle velocity

tends toward zero with pressure and the shock-wave velocity is then equal to the bulk sound velocity, hence:

$$C_0 = \left(\frac{K}{\rho}\right)^{1/2} = \Phi^{1/2} \tag{4.108}$$

The slope of the line is found to be:

$$\lambda \approx \frac{(dK/dP)_0 + 1}{4} = \frac{\gamma_{\mathrm{DM}} + 1}{2} \tag{4.109}$$

With (4.107), (4.101) and (4.102), we obtain the Hugoniot centered at the zero-pressure state (metastable state, if relation (4.107) corresponds to a high-pressure phase) (McQueen *et al.*, 1963):

$$P = P_0 + C_0^2 \frac{V - V_0}{[V_0 - \lambda(V_0 - V)]^2} \tag{4.110}$$

where P is the pressure at high temperature under the shock conditions.

Raw Hugoniot data can also be fitted with a two-parameter Birch–Murnaghan type equation constrained by choosing a zero-pressure density related to the slope of the $P(\rho)$ Hugoniot at zero pressure ($dP/d\rho = \Phi_0$) by the Anderson (1967) seismic equation of state (Anderson and Kanamori, 1968; Ahrens *et al.*, 1969).

It is then necessary to remove the thermal pressure to obtain an isothermal equation of state at $T = 0\,\mathrm{K}$.

Takeuchi and Kanamori (1966) use the Mie–Grüneisen equation of state:

$$P - P_{\mathrm{K}} = \gamma_{\mathrm{th}} \frac{E - E_{\mathrm{K}}}{V} \tag{4.111}$$

where P_{K} is the pressure needed to compress the material at 0 K to the same specific volume as that obtained under shock and E_{K} is the internal energy corresponding to the isothermal compression at 0 K. The isothermal equation of state relates P_{K} to V and V_{K0} (specific volume at 0 K and zero pressure). It is found by integrating a system of differential equations essentially obtained by carrying (4.103) into the expression of γ_{th} from (4.111) and identifying it with Slater's or Dugdale–McDonald expressions in terms of the derivatives of pressure and in using the definition: $P_{\mathrm{K}} = (\partial E_{\mathrm{K}}/\partial V)_T$. The specific volume at 0 K is estimated using the definition of the thermodynamic gamma in terms of the coefficient of thermal expansion.

Shapiro and Knopoff (1969) proposed a method based on the same principles, but which they claim to be mathematically simpler.

4.9 First principles equations of state

4.9.1 Thomas–Fermi equation of state

The Thomas–Fermi equation of state (TF EOS) is an EOS in which the atomic structure of the solid is not taken into consideration; the pressure is assumed to be entirely that of a degenerate electron gas and is calculated using the semi-classical Thomas–Fermi approximation. These assumptions are justified for elements at extremely high pressures, inside stars for instance. Even the pressure at the center of the Earth is much below the domain of validity of the TF EOS, which does not extend below 1000 GPa. This, apparently, should suffice to confine the interest in the TF EOS to astrophysics and exclude it from geophysics. It turns out however that considerable attention was given in the geophysical literature to the TF EOS (see e.g. Boschi and Caputo, 1969), extrapolating it below its validity range down to the range of shock-wave and static pressure experimental data. Although these attempts generally met with indifferent success, interpolation between the TF EOS and experimental P–V curves is possible (Elsasser, 1951) and it provided a useful constraint on the composition of the core (Birch, 1952) (Fig. 4.18). It is therefore justified to devote some space here to outlining the basic physics of the TF EOS.

(i) The Thomas–Fermi approximation

The Thomas–Fermi approximation is a method for finding the density of electrons in an atom of atomic number Z. It essentially rests on the following assumptions (see Eliezer *et al*., 1986):

- The system as a whole is in its lowest quantum state.
- In a volume so small that within it the change in the potential energy is small compared with the mean total energy of an electron, the number of electrons is large.

It is therefore possible to consider that the free electrons form a gas that can be treated classically rather than by quantum mechanical methods. The only contribution of quantum mechanics is that the electrons are subject to the exclusion principle, hence obey Fermi–Dirac stastistics (Fermi–Dirac gas). The approximation works better for heavy metals.

Let the electrostatic potential due to the nucleus and electrons inside the

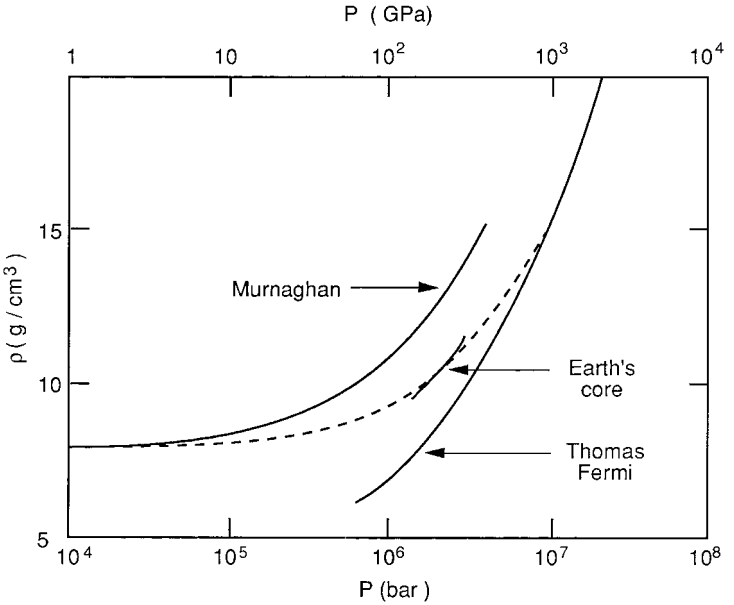

Figure 4.18 Estimated density of iron as a function of pressure. The dashed curve is interpolated to pass through the data for the core (after Birch, 1952).

atom be $V(\mathbf{r})$, $\mathbf{r}$ being the distance from the nucleus, and let the maximum energy of an electron be $E_{\max} = -eV_0$, (e is the charge of the electron). At any point, we have:

$$\frac{p^2}{2m} - eV \leq E_{\max}$$

where p is the momentum of an electron, whose maximum value is:

$$p_{\max} = (2me)^{1/2}[V(r) - V_0]^{1/2} \tag{4.112}$$

According to Fermi–Dirac stastistics, each volume of phase space $d\mathbf{p}d\mathbf{r}$ contains $(2/h^3)d\mathbf{p}d\mathbf{r}$ electrons and the volume of the momentum space corresponding to points which are occupied is $(4\pi/3)p_{\max}^3$, hence the number of electrons per unit volume in real space is:

$$n(\mathbf{r}) = \frac{8\pi}{3h^3}(2me)^{3/2}[V(r) - V_0]^{3/2} \tag{4.113}$$

The electrostatic potential $V(r)$ and the density of charge $n(r)$ are related by Poisson's equation:

$$\nabla^2 V = 4\pi n e \tag{4.114}$$

With spherical symmetry, the Laplacian is written:

$$\nabla^2 V = \frac{1}{r^2}\frac{d}{dr}\left(r^2 \frac{dV}{dr}\right) \tag{4.115}$$

As $r \to 0$, the potential is due mostly to the nucleus and behaves as Ze/r, it is therefore convenient to introduce the dimensionless quantity:

$$\Phi(\mathbf{r}) = [V(r) - V_0]\left(\frac{Ze}{r}\right)^{-1} \tag{4.116}$$

with the boundary condition $\Phi(0) = 1$. We have therefore:

$$\nabla^2 V = \frac{Ze}{r}\frac{d^2\Phi}{dr^2} \tag{4.117}$$

With (4.117) and (4.113), we can write (4.114) as:

$$\frac{d^2\Phi}{dr^2} = \frac{32\pi^2}{3h^3}(2me^2)^{3/2} Z^{1/2}\Phi(r)^{3/2} r^{-1/2} \tag{4.118}$$

Introducing the dimensionless variable $x = r/\mu$, with $\mu \propto Z^{-1/2}$ (see Eliezer *et al.*, 1986), we obtain the dimensionless Thomas–Fermi differential equation, valid for any value of Z:

$$\frac{d^2\Phi}{dx^2} = \Phi^{3/2} x^{-1/2} \tag{4.119}$$

The equation can be solved numerically (Feynman *et al.*, 1949), with $\Phi(x)$ expanded in a series of powers of x:

$$\Phi = 1 + a_2 x + a_3 x^{3/2} + a_4 x^4 + \cdots \tag{4.120}$$

The coefficients are expressed as functions of a_2. The values of Φ are tabulated as a function of $x_0 = r_0/\mu(Z)$, where r_0 is the atomic radius of the element of atomic number Z.

(ii) Pressure–volume relation at $T = 0$ K

From (4.113) and (4.116), the electronic density of an isolated atom is:

$$n = \frac{8\pi}{3h^3}(2me)^{3/2}\left[\frac{Ze}{r}\Phi\right]^{3/2} \tag{4.121}$$

The solid is considered as a gas of atoms, each atom being surrounded by a sphere of atomic size; the pressure is due to the bombardment of the free electrons on the boundary of the atomic sphere and is given by the kinetic theory:

$$P = \frac{2}{3}\frac{E}{V_0} = \frac{2}{3}\frac{E_0 n}{N} \tag{4.122}$$

$n = N/V$ is the number of free electrons per unit volume and E_0/N is the internal energy (equal to the kinetic energy) per electron:

$$\frac{E_0}{N} = \frac{3h^2}{10m}\left(\frac{3}{8\pi}\right)^{2/3} n^{2/3} \tag{4.123}$$

Hence:

$$P = \frac{h^2}{5m}\left(\frac{3}{8\pi}\right)^{2/3} n^{5/3} \tag{4.124}$$

With (4.124) and (4.121) and remembering that $r = \mu x$, we have:

$$PV = \frac{2}{15}\frac{Ze^2}{\mu} x_0^{1/2}[\Phi(x_0)]^{5/2} \tag{4.125}$$

where V is the atomic volume:

$$V = (4\pi/3)(\mu x_0)^3 \tag{4.126}$$

The values of $\Phi(x_0)$, for a given atomic number are found in tables (Feynman *et al.*, 1949).

At high enough pressures, for an element of atomic number Z, the pressure can be directly found from (4.124), by taking for n the number of electrons in the atomic volume, $n = Z/V$:

$$P = \frac{h^2}{5m}\left(\frac{3}{8\pi}\right)^{2/3} Z^{5/3} V^{-5/3} \tag{4.127}$$

or:

$$PV = \frac{h^2}{5m}\left(\frac{3}{8\pi}\right)^{2/3} Z^{5/3} V^{-2/3} \tag{4.128}$$

Brillouin (1954, p. 245) estimated the electronic pressure for metals by taking one free electron per atom; he found values of the order of 10 GPa.

Scaled pressure–volume curves, valid for all values of Z, are often given as $PZ^{-10/3}$ vs ZV. This can be justified by writing (4.125) as:

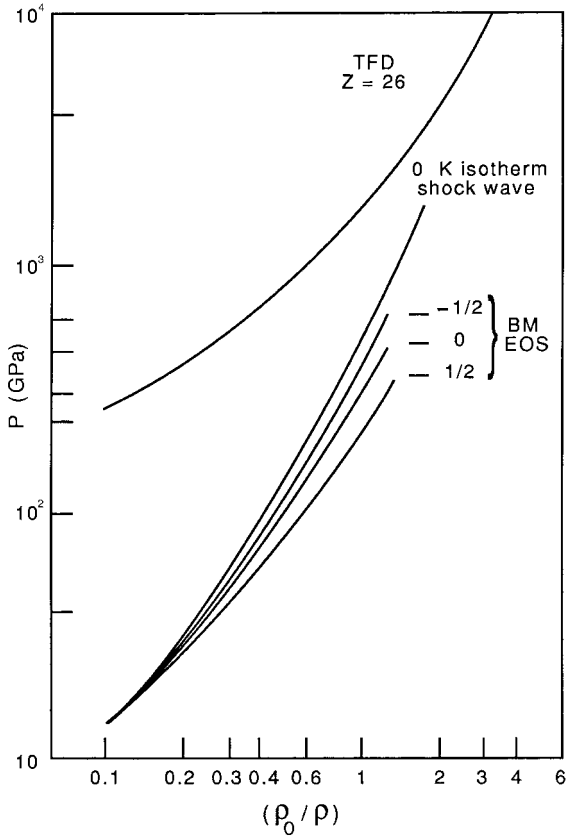

Figure 4.19 Pressure–density isotherms for iron at 0 K. TFD: Thomas–Fermi–Dirac approximation; BM: Birch–Murnaghan equation of state for $\xi = -\frac{1}{2}, 0, \frac{1}{2}$ (after Boschi and Caputo, 1969).

$$P \propto Z^2 \mu^{-4} \left[\frac{\Phi(x_0)}{x_0} \right]^{5/2} \tag{4.129}$$

Remembering that $\mu \propto Z^{-1/3}$, we see from (4.126) that x_0 is a function only of ZV and we can write:

$$PZ^{-10/3} \propto \left[\frac{\Phi(x_0)}{x_0} \right]^{5/2} = f(ZV) \tag{4.130}$$

Dirac modified the Thomas–Fermi theory to include the quantum exchange effects (TFD model). The resulting equation cannot be put in a scaled form and has to be solved for every value of Z (see Eliezer *et al.*, 1986;

Boschi and Caputo, 1969). The results for iron, compared with the isotherm derived from shock-wave experiments and the Birch–Murnaghan EOS (Takeuchi and Kanamori, 1966) are given Fig. 4.19.

Feynman *et al.* (1949) treated the more complicated case of the TF EOS at high temperature.

4.9.2 Ab-initio *quantum mechanical equations of state*

In recent years, progress in computer performance and in calculation methods have led to considerable advances in the field of construction of parameter-free, ab-initio equations of state for specific minerals, using molecular dynamics and quantum mechanics. It is beyond the scope of this book to enter into the quantum mechanical details of the methods. We will only and very briefly give the physical basis of the more popular models. More information can be found in Vočadlo *et al.* (1995), Price and Vočadlo (1996) and Gillan (1997).

Isothermal equations of state at 0 K (neglecting thermal vibrations) are usually calculated by two different approaches.

(i) The static binding energy of the crystal $U(\rho)$, where ρ is the total charge-density, is considered as the sum of two contributions: a long-range attractive Culombic pair potential between ions, usually calculated by the Ewald summation method, and a term embodying the electronic interactions. The pair potential can be given a priori or fitted to experimental values of some material parameter (e.g. elastic moduli). The electronic energy may also be fitted to experimental data or to *ab-initio* data, obtained by using quantum mechanical simulation methods.

    It is also possible to neglect the long-range electronic interactions and, using molecular orbital theory, to calculate the energy of a finite cluster of atoms in a vacuum over a range of bond lengths (see e.g. McCammon *et al.*, 1991).

    The energy of the infinite lattice (finite in the computer, with periodic boundary conditions), or of the cluster of atoms, is computed as a function of interatomic distance, and minimized to obtain the equilibrium volume at 0 K. The pressure, hence the equation of state, is obtained by taking the derivative of the energy as a function of volume.

(ii) In the second, truly *ab-initio*, approach, the electronic energy is calculated from first principles, by solving the Schrödinger equation for a many-electron system. A popular formalism consists in describing the

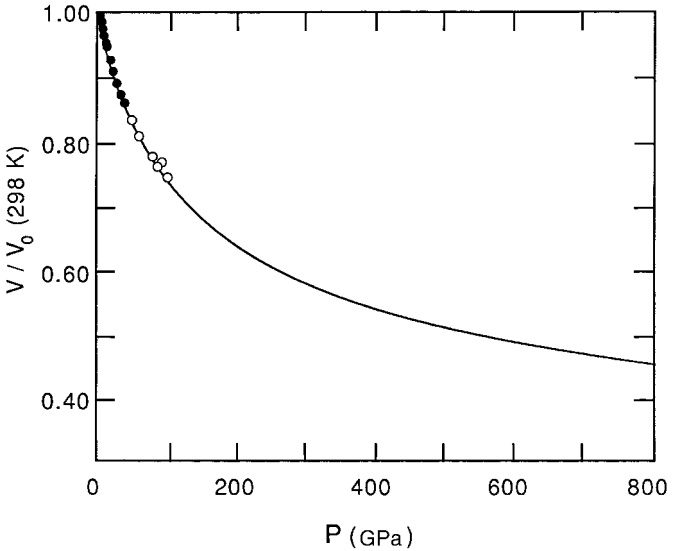

Figure 4.20 Calculated isothermal compression curve for MgO at 298 K. The circles represent experimental results (after Hemley *et al.*, 1985).

ground state of the system in terms of a unique functional of charge-density alone (density functional theory). As the exact form of this functional is unknown, approximations such as local density approximation (LDA) (e.g. for $MgSiO_3$ perovskite, Stixrude and Cohen, 1993; Karki *et al.*, 1997) or generalized gradient approximation (GGA) are used.

Thermal equations of state are obtained by introducing atomic lattice vibrations. This can be done in different ways.

(i) The phonon spectrum of the system can be described by lattice dynamics in the quasi-harmonic approximation (below the Debye temperature). This has been done by Hemley *et al.* (1985) for MgO at room temperature, yielding an *ab-initio* EOS in good agreement with the experimental data of Mao and Bell (1979) (Fig. 4.20). Hemley *et al.* (1987b) and Wolf and Bukowinski (1985, 1987), using the same method, calculated the thermal EOS of $MgSiO_3$ and $CaSiO_3$ perovskites. Cohen (1987) calculated the EOS of $MgSiO_3$ perovskite, using the "potential induced breathing" model, in which the constraint on the rigidity of ions is lifted. He found a very good agreement with the experimental results of Yagi *et al.* (1982) and Knittle and Jeanloz (1987) (Fig. 4.21).

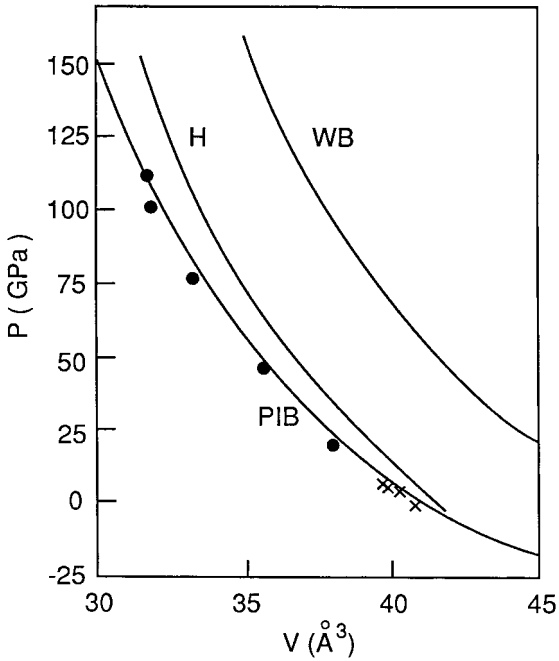

Figure 4.21 Calculated and experimental equation of state for $MgSiO_3$ perovskite at room temperature. WB: Wolf and Bukowinski (1987); H: Hemley *et al.* (1987b); PIB: potential induced breathing (Cohen, 1987). The experimental results of Yagi *et al.* (1982) and Knittle and Jeanloz (1987) are indicated by crosses and circles, respectively (after Cohen, 1987).

(ii) Different configurations of the system can be drawn at random (Monte-Carlo simulation).

(iii) Each atom may wander in the potential field of the static lattice, but is confined in its Wigner–Seitz cell. (see e.g. Wasserman *et al.*, 1996).

(iv) In the molecular dynamics (MD) technique, each vibrating ion is assigned position and velocity in a potential field. The forces acting on the ion are calculated from the derivative of the potential. Position and velocity are calculated at each time step by solving Newton's equation of motion (e.g. for $MgSiO_3$ perovskite, Patel *et al.*, 1996).

(v) Finally, *ab-initio* quantum molecular dynamics (QMD), is independent of the choice of an arbitrary (or fitted) potential. The forces are directly calculated by fully self-consistent electronic structure methods at every step of the dynamics (e.g. for perovskites, Wentzcovitch *et al.*, 1995).

5
Melting

5.1 Generalities

Melting (or fusion) is an extremely important phenomenon for solids since it causes them to cease being solids and to transform to the liquid state of matter, thereby losing crystalline long-range order and resistance to shear. Melting is a first-order phase transition, i.e. it exhibits discontinuities in the first derivatives of the free energy: volume and entropy.

Pure metals (and more generally elements) have a fixed melting point T_m at a given pressure. The equilibrium between solid and liquid is univariant and the variation of the melting point with pressure is represented by the *melting curve*: T_m (P).

The situation is more complicated for multicomponent systems such as alloys and mineral crystals. Several cases may arise and are best understood by referring to phase diagrams (see also Section 7.4.1). A *phase diagram* at constant pressure is a map of the stability domains of the various possible phases in the composition–temperature space. For the sake of simplicity, let us consider only binary systems, whose composition can be defined by the proportions (in atom or mole percents) of two simple end-members. The end-members that will concern us here can be elements (e.g. Fe, S) or simple binary oxides (e.g. MgO, SiO_2) that exhibit *congruent melting* like elements (i.e. the solid melts at fixed temperature, giving a liquid with the same chemical composition). For various definite proportions of the end-members, compounds may exist, e.g. FeS, FeS_2 or MgO,SiO_2 ($MgSiO_3$) or $2MgO$, SiO_2 (Mg_2SiO_4). The compounds may sometimes in turn be used as end-members in other, more restricted phase diagrams, e.g. $MgSiO_3$–Mg_2SiO_4.

The most typical melting situations are schematically represented in Fig. 5.1:

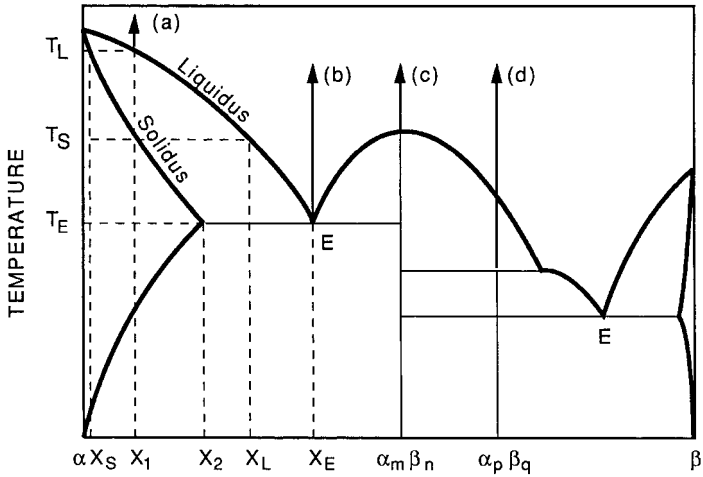

Figure 5.1 Typical phase diagram for compositions intermediate between α and β. (α, β in the cases that interest us are often simple oxides.) (a) For compositions such as x_1, when temperature T_S is reached during heating (cooling) the first (last) drop of liquid of composition x_1 appears (disappears); when temperature T_1 is reached during heating (cooling) the last (first) crystal of composition x_S disappears (appears). (b) For the eutectic composition x_E, the solid (liquid) melts (freezes) at the fixed temperature T_E of the eutectic point E. (c) For the definite composition $\alpha_m\beta_n$, the solid melts congruently, yielding a liquid of the same composition. (d) For the definite composition $\alpha_p\beta_q$, the solid melts incongruently, decomposing into a liquid in equilibrium with crystals of composition $\alpha_m\beta_n$.

(i) Close to one end-member, (e.g. α), there usually is a region where the stable phase is a solid solution of β in α. For a composition x_1 (Fig. 5.1(a)) melting occurs over a temperature interval, with a variable composition of the liquid: When the temperature reaches the value T_S, the first drop of liquid of composition x_L appears, in equilibrium with a solid solution of composition x_1; if the temperature is increased, the proportion of liquid increases and its composition varies until the temperature T_L is reached, at which the last crystal of composition x_S disappears.

The locus of the points in the diagram corresponding to the appearance of the first drop of liquid is called *solidus* and the locus of points corresponding to the disappearance of the last crystals (or appearance of first crystals during cooling) is called *liquidus*.

The situation in Fig. 5.1(a) corresponds to a rather usual case, where the melting point of a crystal is lowered by impurity elements in solution. A geophysically important example is that of the lowering of

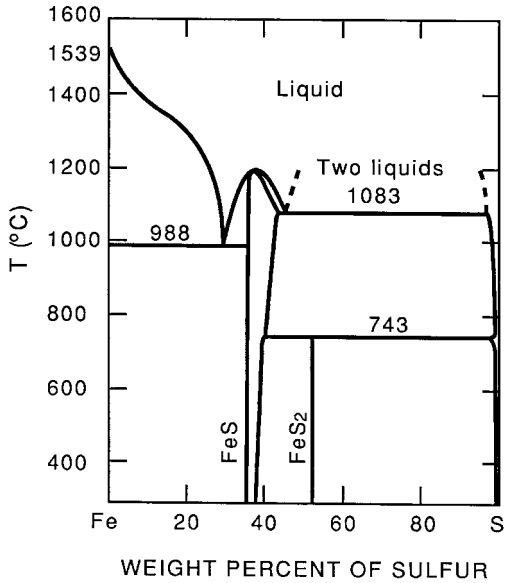

Figure 5.2 Phase diagram for the iron–sulfur system at ambient pressure (after Verhoogen, 1980).

the melting point of iron by sulfur (Fig. 5.2). When end-members differ only by the chemical nature of atoms of comparable size on the same crystalline sites (e.g. forsterite Mg_2SiO_4 and fayalite Fe_2SiO_4), a continuous solid solution can exist and the spindle formed by the solidus and liquidus extends over the whole composition range (Fig. 5.3).

(ii) A common feature of phase diagrams is the existence of one or several compositions for which melting occurs at a fixed temperature. For these compositions, the liquidus exhibits an angular point corresponding to a deep minimum of the melting temperature (*eutectic point*), as shown in Fig. 5.1(b).

(iii) Intermediate compounds may melt congruently (Fig. 5.1(c)) and can be considered as end-members, thus dividing the phase diagram into independent binary diagrams; such is for instance the case of forsterite Mg_2SiO_4 in the MgO–SiO_2 diagram (Fig. 5.4). Others melt, also at a fixed temperature, but incongruently (Fig. 5.1(d)), decomposing into a liquid and another compound; such is the case of enstatite $MgSiO_3$ at atmospheric pressure, which gives forsterite and a silica-rich liquid (Fig. 5.4). At pressures higher than 0.5 GPa, melting becomes congruent and a eutectic appears between forsterite and enstatite. The tem-

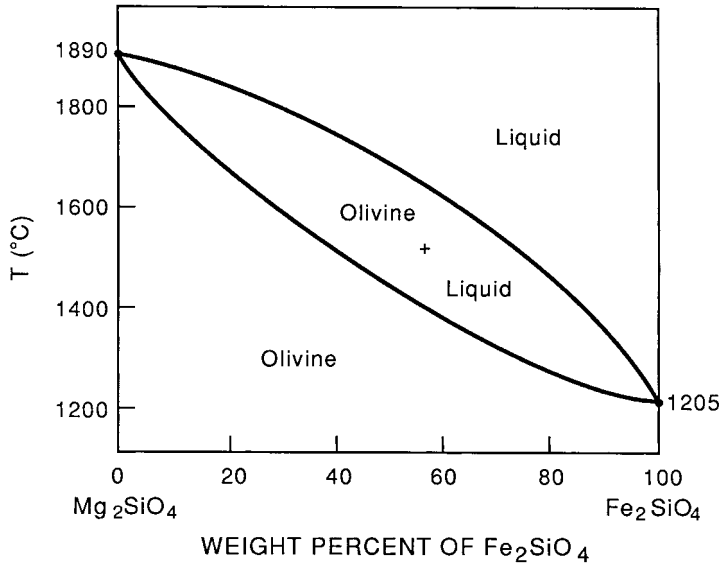

Figure 5.3 Phase diagram of the forsterite–fayalite system at ambient pressure.

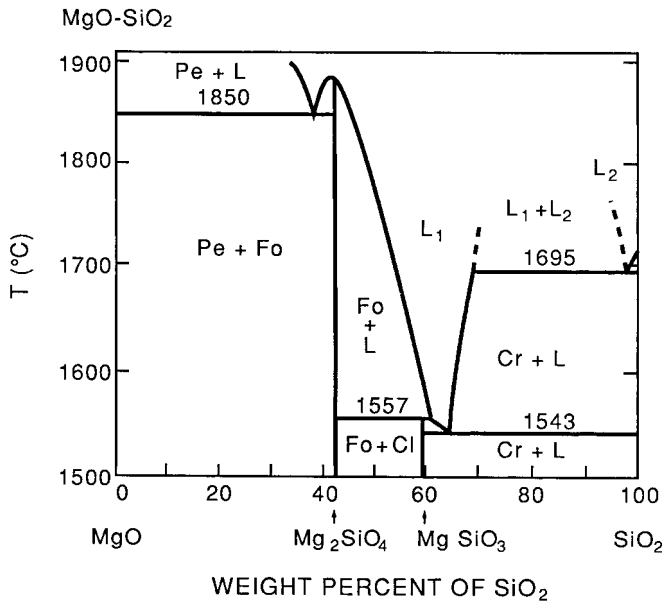

Figure 5.4 Phase diagram of the MgO–SiO_2 system at ambient pressure (after Levin *et al.*, 1964). Fo: Forsterite, Cl: Clinopyroxene, Cr: Cristobalite, Pe: Periclase.

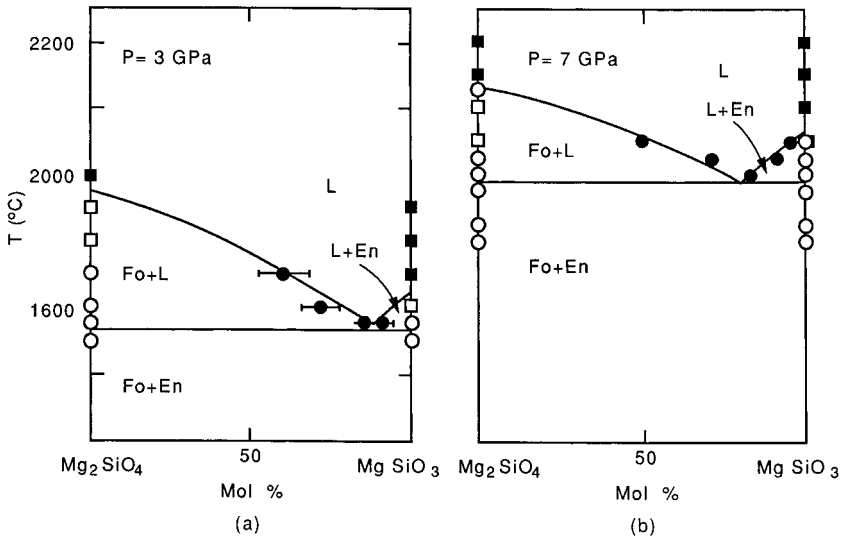

Figure 5.5 Phase diagram of the forsterite–enstatite system at pressures of 3 GPa (a) and 7 GPa (b) (after Kato and Kumazawa, 1985b).

perature of the eutectic point increases with pressure, in parallel with the melting point of enstatite, and its composition shifts towards the Mg-rich side (Kato and Kumazawa, 1985b) (Fig. 5.5).

Many minerals exhibit anomalous rapid variations of physical properties (specific heat at constant pressure, thermal expansion, compressibility, etc.) a few hundred degrees below the nominal melting point. These *premelting effects*, notably observed in diopside ($Ca_2MgSi_2O_7$), anorthite ($CaAl_2Si_2O_8$) and (Ca,Mg)Ge_2O_4 olivine, have been attributed to cation disordering in the crystalline phases (Richet *et al.*, 1994). In natural diopside, containing some iron, very small droplets of a liquid consisting of almost pure silica start forming at 1150 °C (200 °C below the solidus). This incongruent *early partial melting* has been observed by transmission electron microscopy (Doukhan, 1995).

Melting of rocks is even more complicated: Minerals with the lowest melting point melt first when temperature increases and the liquid reacts with other minerals. To a given temperature above the melting point of the most fusible mineral, corresponds a given degree of *partial melting*. One still can define a liquidus, on which the first fractions of melt are in equilibrium with the "liquidus phases"; see e.g. Takahashi (1986) and Ito

and Takahashi (1987b), on the melting of peridotites at pressures of the upper and lower mantle.

Melting in the Earth obviously concerns rocks, and melting of rocks is an important research topic in experimental petrology; it is however a complicated phenomenon, little amenable to physical extrapolations to high pressures. As a consequence, geophysicists generally use the melting curves of the mantle minerals and of iron to obtain constraints on the temperature profile in the Earth. In what follows we will consider the physics of melting of simple solids as a basis for studying the effect of pressure on melting, and we will review the various melting laws giving T_m as a function of pressure.

5.2 Thermodynamics of melting

5.2.1 Clausius–Clapeyron relation

Let us express the equilibrium between solid and liquid at the melting point by writing that the total differential change in Gibbs free energy G is equal to zero, when a small volume element of the solid changes to liquid:

$$dG = (V_L - V_S)dP - (S_L - S_S)dT = 0 \tag{5.1}$$

V_L, S_L and V_S, S_S are the specific volume and entropy per unit mass of the liquid and solid respectively. The slope of the melting curve is given by the Clausius–Clapeyron relation:

$$\frac{dT_m}{dP} = \frac{\Delta V_m}{\Delta S_m} \tag{5.2}$$

where $\Delta V_m = V_L - V_S$ is the *melting volume* at pressure P, and $\Delta S_m = S_L - S_S$ is the *melting entropy* at pressure P.

The latent heat of melting is:

$$L = T_m \Delta S_m \tag{5.3}$$

5.2.2 Volume and entropy of melting

(i) The melting volume is usually positive, since in most cases the specific volume of the liquid is greater than that of the solid. For metals, the ratio of the melting volume to the specific volume of the solid is of the order of a few percent, whereas it is an order of magnitude greater for alkali halides; the silicates have intermediate values (see Table 5.1). When the short-range structure of the liquid is very different from that of the solid, due to a

Table 5.1. *Melting volume* ΔV_m *in* cm^3/mol, *melting entropy* ΔS_m *in* $J/mol\,K$, *and slope of the melting curve at* 1 *bar* (100 *kPa*) *for various crystals*

Crystal	ΔV_m	$\frac{\Delta V_m}{V}$	ΔS_m	$\left(\frac{dT_m}{dP}\right)_0$
Na	0.60	0.025	7.10	8.5
Mg	0.46	0.041	9.43	7.2
Al	0.64	0.060	11.3	5.9
K	1.20	0.026	7.10	16.9
Fe	0.28	0.036	8.32	3.5
Cu	0.32	0.042	9.58	3.64
Ag	0.42	0.038	9.27	6.04
Pb	0.46	0.041	8.28	7.23
LiF	3.47	0.327	24.12	11.2
NaCl	7.01	0.238	26.04	23.8
KCl	7.02	0.173	25.4	26.7
KBr	7.72	0.165	25.3	38.0
RbI	8.05	0.126	24.0	15.0
Quartz	2.5	0.105	5.53	35.5
Forsterite	3.8	0.081	70	4.8
Fayalite	3.7	0.076	60.9	7.5
Pyrope	18.3	0.158	162	5.5
Enstatite	5.4	0.160	41.1	12.8
Diopside			82.7	13.2

Sources: The values of ΔV_m and ΔS_m are from Ubbelohde (1978) for metals and from Jackson (1977) for alkali halides. The values of ΔV_m for silicates and of ΔS_m for forsterite are from Bottinga (1985). The values (averaged) of ΔS_m for the other silicates are from Richet and Bottinga (1986). The values of the slopes of the melting curves are from Jackson (1977).

change in the type of bonding on melting, the liquid can be denser than the solid ($\Delta V_m < 0$). This is, for instance, the case for water, denser than ice I_h, and silicon that becomes metallic on melting. Since the melting entropy is always positive (the liquid is always more disordered than the solid), the melting curve of these substances has therefore a negative slope; the melting point decreases as pressure increases. In some cases (e.g. Rb, Ba, Eu), the melting curve may exhibit a maximum at high pressures (Kawai and Inokuti, 1968).

(ii) The entropy of melting is generally the sum of two terms:

$$\Delta S_m = \left(\frac{\partial S}{\partial V}\right)_T \Delta V_m + \Delta S_d \tag{5.4}$$

The first term corresponds to the entropy change due to the modification

of the vibrational frequencies following the isothermal expansion at melting, and the second term is the entropy of disorder due to the structural differences between the solid and the less well-ordered liquid. The disorder is generally positional and can also be rotational if the structural units of the liquid have no spherical symmetry.

Oriani (1951) calculated the expansion contribution to the entropy for metals, starting from Maxwell's relations:

$$\left(\frac{\partial S}{\partial V}\right)_T = \left(\frac{\partial P}{\partial T}\right)_V = -\left(\frac{\partial P}{\partial V}\right)_T \cdot \left(\frac{\partial V}{\partial T}\right)_P = \alpha K_T \tag{5.5}$$

The first term in (5.4) can therefore be written:

$$\Delta S_V = \alpha K_T \Delta V_m \tag{5.6}$$

or:

$$\Delta S_V = \gamma_{th} C_V \frac{\Delta V_m}{V} \tag{5.7}$$

where γ_{th} is the thermodynamic gamma and V, the specific volume of the solid.

The existence of a linear relation between the entropy and the volume of melting for various metals is implicit in Oriani's analysis and directly obtains if the entropy of disorder is independent of the metal and if it can be assumed that αK_T is a constant for a given solid (see Section 3.5). Indeed, Stishov *et al.* (1973) noticed that the function $\Delta S_m/(\Delta V_m/V)$ is the same for argon and for sodium and tends to $R\ln 2 = 0.69R$ when $\Delta V_m/V$ vanishes. Lasocka (1975) further reported that, for a number of metals, the representative points on a diagram of ΔS_m vs $\Delta V_m/V$ were scattered about a straight line passing through the point with ordinate $R\ln 2$ for $\Delta V_m = 0$. Tallon (1980), probably unaware of Oriani's work, again justified the relationship:

$$\Delta S_m = R\ln 2 + \alpha K_T \Delta V_m \tag{5.8}$$

He also showed that the relationship is verified for sodium along its melting curve, but he did not provide an explanation for the fact that the entropy of disorder is close to $R\ln 2$.

Rivier and Duffy (1982) showed that, for dense atomic liquids, the configurational entropy of disorder is, indeed, equal to $R\ln 2$, by identifying the configurations of the liquid to its topological degrees of freedom, linked to the existence of line defects in the liquid that are absent in the solid.

From statistical mechanical theories of the entropy of the liquid and

crystal, Wallace (1991) estimated the entropy of fusion for 25 elements. For 19 "normal" elements, he found constant-density entropies of fusion $\Delta S_m = (0.79 \pm 0.11)R$. The elements that did not fall into this group and had larger entropies of fusion were those that had a change in electronic structure between solid and liquid states (e.g. Si and Ge which go from semi-conducting solid to metallic liquid).

The linear relationship between entropy and volume of melting is apparently valid only for dense atomic liquids (metals, rare gases, etc.); it is not verified for alkali halides and silicates, probably due to unaccounted for contributions. In the case of silicates, for instance, the entropy of melting must comprise a compositional (mixing) term that is larger for minerals with isolated SiO_4 tetrahedra like olivine and garnet than for chain silicates like enstatite and is, of course, zero for quartz (Stebbins *et al.*, 1984).

Jackson (1977), searching for melting systematics, compared the melting curves of fluorides and fluoroberyllates analogs of silicates (e.g. BeF_2, Li_2BeF_4). He found that the entropy of melting is primarily a function of the crystal structure, while the volume of melting is controlled by the molar volume of the crystal within each isostructural series. The magnitude of dT_m/dP is a function of the way in which the SiO_4 and BeF_4 tetrahedra are linked. It is small for structures with isolated tetrahedra and large for structures where the tetrahedra form a 3-D framework, the melting entropy being low in this case due to the similarity between the solid and liquid phases.

Experimental values of ΔS_m, ΔV_m and dT_m/dP are given in Table 5.1.

5.2.3 Metastable melting

For solids, such as ice, which melt with a decrease of volume ($\Delta V_m < 0$), the melting curve has a negative slope and usually ends at a triple point at high pressure, where another phase becomes stable. However, the melting curve of the low-pressure phase can be extrapolated in the stability domain of the high-pressure phase. From this observation, Mishima *et al.* (1984) deduced that, if a low-pressure phase were pressurized at temperatures low enough to remain in a metastable state, it would melt when the trajectory of the representative point in the P,T plane crosses the extrapolated melting curve. Of course, for temperatures lower than the glass transition temperature, "melting" would produce not a liquid, but an amorphous glass. Mishima *et al.* (1984) performed the experiment on ice I_h at 77 K and succeeded in "melting" it at 1 GPa, producing a new high-density (1.31) amorphous phase of ice. In later experiments, (Mishima, 1996), the cross-

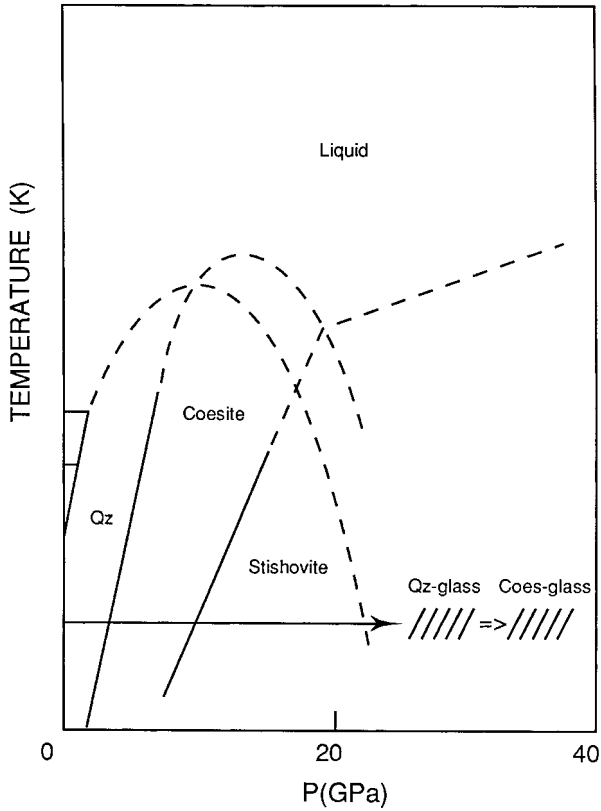

Figure 5.6 Phase diagram of SiO_2. The horizontal arrow indicates the path of pressure-induced amorphization (after Hemley *et al.*, 1988).

over from equilibrium melting of ice to sluggish amorphization could be followed during pressurization at about 140–165 K.

Hemley *et al.* (1988), compressing SiO_2 quartz and coesite at 300 K, transformed them into glass at 25–35 GPa, bypassing the stable higher-pressure phases, thus confirming that metastable melting can also occur in minerals (Fig. 5.6). Molecular dynamics simulation on the SiO_2 system also suggests that the amorphization curve and the metastable extension of the melting curve of quartz are identical (Badro *et al.*, 1998).

Richet (1988) observed that there is no reason why such "melting" (or rather vitrification) should be restricted to solids with $\Delta V_m < 0$ only; high-pressure phases with $\Delta V_m > 0$ should be decompressed rather than compressed to achieve vitrification. He gave a thermodynamic analysis of direct vitrification from the solid state and argued that the fact that

high-pressure $CaSiO_3$ perovskite cannot be quenched and immediately vitrifies on release of pressure represents metastable melting.

Reviews of the pressure-induced amorphization of materials and minerals, have been given by Sharma and Sikka (1996) and by Richet and Gillet (1997).

5.3 Semi-empirical melting laws

5.3.1 Simon equation

The equation proposed by Simon and Glatzel (1929) satisfactorily describes the melting curve of many substances: solidified gases, metals, organic crystals, silicates. It was originally proposed in the form:

$$\log(a + P) = c \log T_m + b$$

and tested for alkali metals and organic molecular compounds. Nowadays, it is usually written:

$$\frac{P - P_0}{a} = \left(\frac{T_m}{T_0}\right)^c - 1 \tag{5.9}$$

where P_0 and T_0 are the pressure and temperature of the triple point and a and c, parameters that depend on the substance (they do not have the same meaning as in the original equation). For most substances, P_0 is close to zero and can be neglected. The slope at the triple point, close to the melting point at ambient pressure, is: $dT_m/dP = T_0/ac$.

Several authors have shown that a melting equation of the same form as Simon's equation could be derived from physically based melting models: Domb (1951) started from the Lennard-Jones and Devonshire model (see below) and found that it led to a formula of the right type, at high enough pressure and for solids with central forces, but that the melting temperatures predicted were too high. Salter (1954) derived Simon's equation by eliminating the atomic volume between the Mie–Grüneisen equation of state and the Lindemann equation of melting, he found a relation between the constant c and the Grüneisen parameter γ: $c = (6\gamma + 1)/(6\gamma - 2)$. Gilvarry (1956c) (see also Babb, 1963b) used Lindemann's law and the Murnaghan integrated linear equation of state to obtain an equation of the fusion curve similar to Simon's equation.

The Simon equation has been fitted to the melting curve of many substances (mostly organic crystals) by Babb (1963a) and of silicates by Bottinga (1985) (Table 5.2). It is convenient to analytically fit melting

Table 5.2. *Parameters of Simon equation for a few substances*

Substance	T_0 (K)	a (GPa)	c
Fe	1805	107	1.76
Hg	234.3	38.22	1.177
Forsterite	2163	10.83	3.7
Fayalite	1490	15.78	1.59
Pyrope	2073	1.98	9.25
Enstatite	1830	2.87	5.01
Quartz	2003	1.60	3.34
Albite	1373	6.10	2.38

Note: $P_0 = 0$ for all substances, except for pyrope ($P_0 = 4$ GPa).
Sources: The parameters for Fe and Hg are from Babb (1963a); those for silicates are from Bottinga (1985).

curves but, even though it has been given some theoretical justification, it cannot be used to extrapolate the melting curve outside of the interval in which it has been experimentally determined.

5.3.2 Kraut–Kennedy equation

Kraut and Kennedy (1966a,b) found that, for many substances and in a wide pressure range, the melting temperature varies linearly as a function of the compression of the solid $\Delta V/V_0 (> 0)$ or, in other terms, that the melting curve is a straight line, if plotted against compression instead of pressure:

$$T_m = T_m^0 \left(1 + C\frac{\Delta V}{V_0}\right) \tag{5.10}$$

They claimed that the linear relation can be safely extrapolated up to a maximum compression of 0.5. For iron (Fig. 5.7) Kraut and Kennedy find:

$$T_m(^\circ\mathrm{C}) = 1513\left(1 + 3.3209\frac{\Delta V}{V_0}\right) \tag{5.11}$$

The relation also holds for solids whose melting curve has a negative slope (e.g. germanium).

Gilvarry (1966) and Vaidya and Gopal (1966) independently showed that the Kraut–Kennedy relation can be derived from Lindemann's law (see Section 5.4.2) and that the constant C can be expressed as a function of

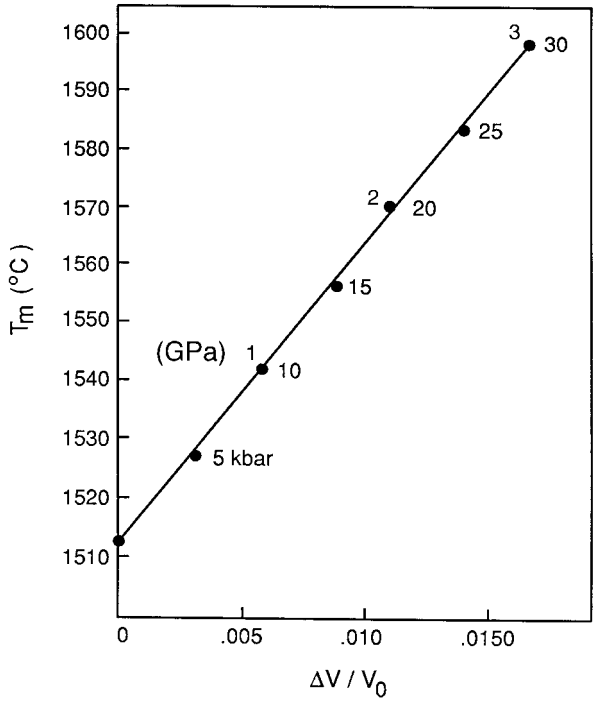

Figure 5.7 Melting temperature vs isothermal compression of iron at room temperature (after Kraut and Kennedy, 1966a, b).

the Grüneisen parameter at P_0, T_0: $C = 2(\gamma_0 - 1/3)$. The Kraut–Kennedy law can also be derived from the Clausius–Clapeyron relation, as shown by Libby (1966) and Mukherjee (1966). If the pressure dependence of the bulk modulus is neglected and if $\Delta V_m/\Delta S_m$ is assumed to remain constant along the melting curve, integration of the Clausius–Clapeyron relation (5.2) then yields:

$$T_m - T_m^0 = \frac{\Delta V_m}{\Delta S_m}(P - P_0) = \frac{\Delta V_m}{T_m \Delta S_m} T_m^0 K_0 \frac{\Delta V}{V_0} \tag{5.12}$$

the value of the Kraut–Kennedy constant is therefore: $C = K_0(\Delta V_m/L)$.

As pointed out by Gilvarry (1966), the Kraut–Kennedy relation is a linear approximation that, like Simon's equation, should properly be used as an interpolation formula only. While Kraut and Kennedy (1966b) dispute this conclusion, Kennedy and Vaidya (1970) indeed reported that the linear Kraut–Kennedy relation gives a good fit for the experimental

results on metals, but that the melting curves of van der Waals solids, concave toward the T axis, are best fitted by Simon's law. The melting curves of ionic crystals and silicates are concave toward the $(\Delta V/V_0)$ axis. Use of the Kraut–Kennedy relation and a fortiori Simon relation for extrapolation would therefore overestimate the melting temperature of minerals.

5.4 Theoretical melting models

5.4.1 Shear instability models

Brillouin (1938, 1940) analyzed the thermal vibrations in strained solid bodies and gave a physical justification to the already old idea that, since liquids have no shear strength, the shear modulus of a solid should decrease with increasing temperature and vanish at the melting point (Sutherland, 1891; Brillouin, 1898). He remarked, however, that it would be difficult to imagine that the shear modulus should decrease smoothly up to the melting point, since this would mean melting without heat of fusion, i.e. it would not account for the first-order character of melting.

Durand (1936) in the course of an experimental study of the elastic moduli of alkali halides and MgO had earlier observed that c_{12} (see Section 2.2) was almost independent of temperature while c_{11} decreased linearly. He extrapolated the data to the temperature at which $c_{11} = c_{12}$, assumed to be the melting temperature (thus implicitly defining the melting point as the temperature for which the modulus $\mu = (c_{11} - c_{12})/2$ vanishes) and calculated values of the melting points quite close to the experimental values (e.g. 1170 K instead of 1077 K for NaCl).

Born (1939) unambiguously chose the loss of shear resistance as a criterion for melting and stated that "a theory of melting should consist of an investigation of the stability of a lattice under shearing stress". He calculated a second-order expansion of the free-energy density of a cubic crystal as a function of finite strain and wrote the conditions for stability which guarantee that the energy is positive definite:

$$3K = c_{11} + 2c_{12} > 0; \quad c_{11} - c_{12} > 0; \quad c_{44} > 0 \tag{5.13}$$

Born considered (without offering much justification for it) that melting occurs when the modulus c_{44}, corresponding to shear along the $\{100\}$ planes, vanishes first and that a gel would be produced if $c_{11} - c_{12}$, corresponding to shear along the $\{110\}$ planes, vanished first. He then proceeded to calculate explicit expressions for the coefficients in the expan-

sion of the free energy, using lattice dynamics within Debye's quasi-harmonic approximation and determined the variation of the elastic moduli with T/Θ_D for different pressures and, finally, the melting curve T_m/Θ_D vs P. Born was quite aware that the latent heat of fusion could not be calculated from his theory by using the Clausius–Clapeyron relation, since the change of volume on melting depended on the properties of the liquid state. It is also worth remarking that Born showed that his theory led to an expression of vibrational frequencies as a function of T_m similar to Lindemann's (see Section 5.4.2) with a slightly different numerical coefficient:

$$\omega_B = CR^{1/2}N^{1/3}T_m^{1/2}M^{-1/2}V^{-1/3} \tag{5.14}$$

May (1970), instead of plotting the shear moduli $c' = (c_{11} - c_{12})/2$ and c_{44} against temperature, plotted them for metals and argon, against $u = (V - V_0)/V_0$, where V and V_0 are the specific volume at temperature T and at 0 °C respectively. He found that the plots were straight lines and that c' vanished for a value of u slightly higher than but quite close to that of the melt (e.g. for Al, $c' = 0$ for $u = 0.125$, while melting occurs with $u = 0.123$).

Jackson and Liebermann (1974) calculated the critical temperatures for shear instability and their initial pressure dependences for alkali halides and oxides. They used the instability criterion $c' = 0$ for halides with NaCl structure (B1) and $c_{44} = 0$ for those with CsCl structure (B2). They found that, although the critical temperatures were higher than the melting temperatures by 30 to 200 K, the initial pressure dependence was the same as for melting; also, the critical temperatures and the initial pressure dependences ordered in the same sense as the melting points and the initial slopes of the melting curves. There was an excellent correspondence between these parameters for oxides and for their "weakened" fluoride analogues (Table 5.3).

Tallon and co-workers (1977) modified the Born shear instability model to account for the first-order character of melting. Plotting the logarithm of the isothermal bulk modulus against the true dilatation $\ln(V/V_0)$, for solid alkali halides and for their melts, they found that the plot is linear over a large temperature range including the melting point and that one can write:

$$\frac{\partial \ln K_T}{\partial \ln V} = -g_K$$

where g_K is analogous to a Grüneisen parameter. The main point is that the variation of the bulk modulus with dilatation is continuous through the melting point. From similar plots for c_{44} and c' (Fig. 5.8), extrapolations

Table 5.3. *Comparison of the critical temperatures for shear instability* T_c *and melting point* T_m *and their initial pressure variation for oxides* (*OX*) *and their fluoride* (*FL*) *analogs*

Analogs	$\frac{T_c^{OX}}{T_c^{FL}}$	$\frac{T_m^{OX}}{T_m^{FL}}$	$\frac{dT_m^{FL}}{dP}$	$\frac{dT_c^{FL}}{dP}$	$\frac{dT_c^{OX}}{dP}$
LiF–MgO	2.8	2.8	12	10	11
NaF–CaO	2.4	2.3	15.1–18	14	13
KF–SrO	2.6	2.4	22.6	21	19

Source: From Jackson and Liebermann (1974).

show that, for B1 halides, c_{44} is finite at the melting point and that c' vanishes at the melting point on the melt side. Using these considerations, Tallon and co-workers proposed that the free energy of the system is a minimum when the elastic energy increase due to expansion is balanced by the entropic term $2RT$, where $2R$ is the "communal" entropy, corresponding to the fact that, when the shear modulus vanishes, the onset of fluidity allows the ions to have access to every part of the volume.

5.4.2 Vibrational instability: Lindemann law

(i) Sutherland relation

At the end of the last century, the idea of thermal vibrations of atoms in solids was well accepted. Sutherland (1890) thought that "at some characteristic temperature each solid ought to have a period of vibration characteristic of its molecule. The question is, at what temperature? At the melting point in each case the vibratory motion just breaks down, so that we ought to expect some simple relation amongst the periods of vibration of the elements at their melting points." He then proceeded to calculate the vibrational period at the melting point for an element of molecular mass M and specific heat C by writing that the kinetic energy of the molecule, $(M\bar{v}^2)/2$ is proportional to the heat received from 0 K to the melting point, MCT_m. The period was taken equal to the maximum amplitude possible at the melting point, $\alpha T_m V^{1/3}$ (where α is the linear expansion coefficient and V, the molecular volume) divided by the mean velocity $\bar{v}$.

Assuming that $MC = \text{const}$ for elements and using an empirical relation $\alpha T_m V^{1/6} = \text{const}$, which he claimed to have verified for metals, Sutherland obtained an expression for the vibrational period p:

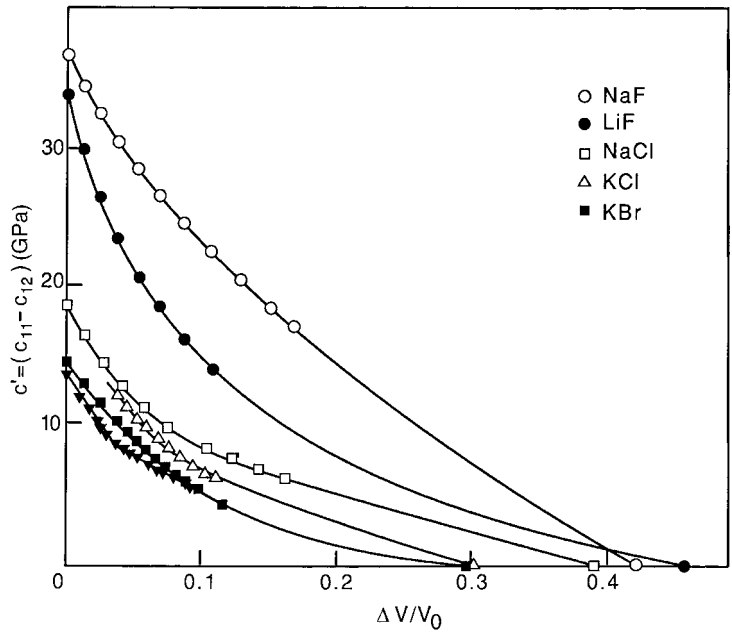

Figure 5.8 Evolution of shear modulus with dilatation for alkali halides. From top to bottom: NaF, LiF, NaCl, KCl, KBr (after Tallon *et al.*, 1977).

$$p \propto V^{1/3} M^{1/3} T_{\mathrm{m}}^{-1/2} \tag{5.15}$$

Using the data available in the literature, he concluded that "the periods of vibration of the molecules of solids at their melting points show very simple harmonic relations."

We have devoted some attention to Sutherland's paper to make it clear that, despite some recent contentions (e.g. Mulargia and Quareni, 1988), Sutherland did not give a theory of melting and that the semi-empirical (and incorrect) relation (5.15) is not an earlier form of Lindemann's law, which we will now examine.

(ii) Lindemann law

In point of fact, Lindemann (1910) did not propose a theory of melting either; his purpose was to calculate the Einstein vibrational frequency of a solid. He assumed a harmonic solid, whose atoms vibrate sinusoidally with a frequency:

$$\omega_{\mathrm{L}} = \left(\frac{\kappa}{m}\right)^{1/2} \tag{5.16}$$

where κ is the force constant and m, the mass of the atom.

As a step in his calculations, Lindemann assumed that, at the melting point, the amplitude of the vibration is so large that the atomic spheres collide, i.e. the parameter δ, expressing the ratio of the distance between the surfaces of the spheres to the distance of their centers, vanishes. It is then possible to write that the integral of the work done on one atom by the restoring force κx (where x is the elongation), from the equilibrium position to the value $x = \delta r/2$, corresponding to the contact of two neighboring spheres of radius r, is equal to the thermal energy calculated with Einstein's model (Section 3.3.2):

$$\frac{\kappa\delta^2 r^2}{8} = \hbar\omega_{\mathrm{L}}\left[\exp\left(\frac{\hbar\omega_{\mathrm{L}}}{k_{\mathrm{B}}T_{\mathrm{m}}}\right) - 1\right]^{-1} \cong T_{\mathrm{m}} - \frac{\hbar\omega_{\mathrm{L}}}{2k_{\mathrm{B}}} \tag{5.17}$$

Replacing κ by its expression as a function of ω_{L} from (5.16), solving for ω_{L} and neglecting small terms, Lindemann finds:

$$\omega_{\mathrm{L}} = 2^{3/2}R^{1/2}\delta^{-1}\left(\frac{T_{\mathrm{m}}}{Mr^2}\right)^{1/2} \tag{5.18}$$

The ratio δ is calculated from Clausius–Mossotti equation, relating the dielectric constant to the number of atoms per unit volume and it is assumed to be constant; hence, in c.g.s units:

$$\omega_{\mathrm{L}} = 4.12{\cdot}10^{12}\pi T_{\mathrm{m}}^{1/2}M^{-1/2}V^{-1/3} \tag{5.19}$$

where V is the atomic (molar) volume and $M = Nm$, the atomic (molar) mass.

Lindemann used the melting points to calculate the frequencies and at no point in the original paper did he suggest using relation (5.19) to predict melting points.

Gilvarry (1956a, 1957b) gave a firmer basis to the Lindemann equation. Instead of assuming that melting occurs when neighboring spheres collide, he wrote that the root mean square amplitude of atomic vibrations at fusion is a critical fraction f of the distance r_{m} of separation of nearest-neighbor atoms:

$$\langle u^2\rangle = f^2 r_{\mathrm{m}}^2 \tag{5.20}$$

(Strangely enough, the introduction of the critical ratio f, without which Lindemann's law would not have been so successful, is usually attributed to Lindemann, although it is nowhere to be found in the original 1910 paper and clearly belongs to Gilvarry.)

In Debye's approximation, at high temperatures, for a monatomic solid of atomic mass M, we have (see Ziman, 1965):

$$\langle u^2 \rangle \cong \frac{9k_B T}{m\omega_D^2} = \frac{9\hbar^2 T}{mk_B \Theta_D^2} \tag{5.21}$$

hence, with (5.20):

$$T_m = f^2 \frac{k_B}{9\hbar^2} M\Theta_D^2 r_m^2 \tag{5.22}$$

which can be written in terms of the atomic volume V, assuming that $r_m = (V/N)^{1/3}$:

$$T_m = 0.00321 f^2 M V^{2/3} \Theta_D^2 \tag{5.23}$$

Noting that Debye's frequency can be expressed as a function of the elastic constants (see Section 3.3.1), Gilvarry (1956a) obtains an interesting expression for Lindemann's law:

$$RT_m = \Omega(\nu) K V \tag{5.24}$$

where $\Omega(\nu)$ is a function of Poisson's ratio at the melting point, proportional to f^2 and K and V are the bulk modulus and the atomic volume at the melting point. The critical ratio f is calculated for a few metals from experimental data and found identical and equal to about 0.08, which supports the theory.

Ross (1969) reformulated Lindemann's law in terms of the statistical mechanical partition function of a Lennard-Jones–Devonshire cell model of a solid and found again that the Simon and Kraut–Kennedy relations could be derived from it.

Wolf and Jeanloz (1984) noted that in its usual form, Lindemann's law is derived using a quasi-harmonic Debye approximation valid only for monatomic solids. They found that the anharmonic contribution to the root mean square atomic displacement can be quite large at the melting point and they gave a lattice dynamics formulation of Lindemann's criterion for polyatomic, anharmonic crystals; in many cases, however, due to the lack of experimental data on the frequency spectra, the complete formulation cannot be used.

Stacey and Irvine (1977a) starting from the definition of the thermodynamic gamma in the Mie–Grüneisen equation of state, equated the thermal pressure with the pressure increase that would obtain if melting occurred at constant volume:

$$2\gamma\rho T_m \Delta S_m = K\rho\Delta V_m$$

and, with the Clausius–Clapeyron equation, they obtained the relation:

$$\frac{d\ln T_m}{dP} = \frac{2\gamma}{K}$$

that resembles equation (5.27) (see below) and, in these authors view, gives a sound thermodynamic basis to Lindemann's law.

Despite such attempts, the single-phase approach to melting, derived from the Lindemann relation, has generally been criticized – and rightly so – on thermodynamic grounds: melting is defined as a vibrational instability of the solid and no acccount is taken of the liquid phase (the same criticism can be leveled at the shear instability models). The only valid thermodynamic criterion of melting should be the equality of the free energies of the solid and liquid phases. However, in the absence of any good theory of melting, Lindemann's law represents a valuable tool. In fact, in the rather common case where the structure and coordination of the liquid is close to that of the solid and the free energies of both phases differ very little, one may find good justification for using Lindemann's law.

Martin and O'Connor (1977) experimentally determined the value of $\langle u^2 \rangle$ near the melting point for Al, Cu and alkali halides (LiF, NaCl, KCl, KBr) by measuring the reduction in intensity of the elastically scattered component of a Bragg diffraction peak caused by thermal vibrations. They found that the Gilvarry critical ratio f is equal to about 0.08 for metals (in agreement with the value determined by Gilvarry, 1956a) and to about 0.11 for alkali halides. They concluded that the vibrational melting relationship can be applied to simple crystals of similar type but that the factor f varies with the crystal structure and the nature of the interaction force law.

Stern and Zhang (1988) determined $\langle u^2 \rangle$ in Pb using X-ray absorption spectroscopy (EXAFS) with synchrotron radiation. They found a value of the critical ratio at melting $f = 0.068$. They also showed that in solid solutions of Hg in Pb, the Hg impurity atoms have a larger vibrational amplitude than the Pb atoms and suggested that local premelting of the Hg—Pb bonds occurs below the bulk melting temperature (this may provide a physical reason for the lowering of melting point by impurities).

The case of polyatomic complex minerals is more difficult since the Lindemann–Gilvarry approach is properly restricted to Debye monatomic solids. It is, however, possible to use Lindemann's law (5.23) as a semi-empirical relation between melting temperature, acoustic Debye temperature, molar volume and mean atomic mass $\bar{M}$. Poirier (1989) found that for

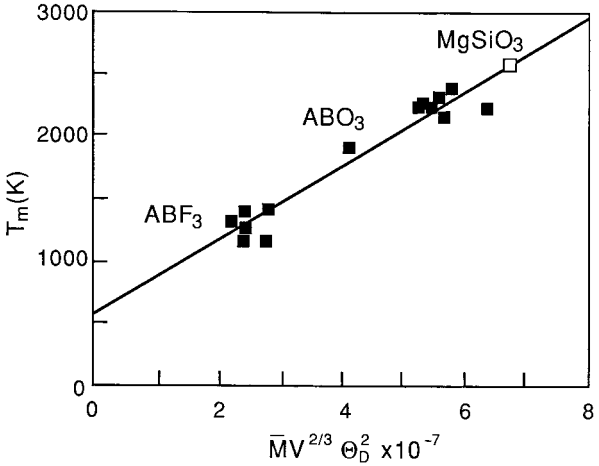

Figure 5.9 Correlation between actual melting temperature and the temperature predicted by the Lindemann law (proportional to the quantity plotted as abscissa) for oxide and fluoride perovskites: $ScAlO_3$, $GdAlO_3$, $SmAlO_3$, $EuAlO_3$, $YAlO_3$, $CaTiO_3$, $BaTiO_3$ (point in the middle), $SrTiO_3$, $KMgF_3$, $KMnF_3$, $KZnF_3$, $KNiF_3$, $KCoF_3$, $RbMnF_3$, and $RbCoF_3$ (after Poirier, 1989).

15 crystals with perovskite structure (fluorides and oxides) whose melting points and elastic moduli are known, there exists a good systematic correlation (Fig. 5.9) between T_m and $\bar{M}V^{2/3}\Theta_D^2$ where Θ_D is calculated using (3.37). For these crystals, the Gilvarry ratio is found to be $f = 0.11$ for perovskite oxides and about $f = 0.13$ for perovskite fluorides (Table 5.4).

Lindemann's law is, in most cases, used together with an equation of state (Gilvarry, 1956c) to extrapolate melting points to high pressures, i.e. obtain an estimate of the melting curve $T_m(P)$ or $T_m(V)$ when none is experimentally available. Wolf and Jeanloz (1984) extrapolated the experimental melting data for a few minerals to the V, T plane, using available thermodynamic data; they used the Mie–Grüneisen equation of state, taking into account anharmonicity and they found that the agreement between the predicted and experimental melting curves was poor or bad for most minerals (fayalite, diopside, pyrope, etc.), with the exception of forsterite for which the agreement was excellent. Mulargia and Quareni (1988) avoided using an equation of state by directly calculating T_m as a function of pressure from the values of the sound velocities at high pressures derived from experimental data. They compared the predicted slopes of the melting curves with the experimental ones for five metals, three alkali halides, and two minerals: bronzite and "peridotite" (?!); they found that the agreement was satisfactory and concluded that Lindemann's law could profitably be

Table 5.4. *Critical Gilvarry–Lindemann factor f for various fluorides and oxides with perovskite structure*

ABX_3	$\bar{M}$	ρ	$\bar{v}_D$	T_m	Θ_D	f
$KMgF_3$	24.08	3.15	4.29	1413	320	0.13
$KMnF_3$	30.21	3.42	3.43	1308	244	0.14
$KZnF_3$	32.26	4.02	3.43	1143	252	0.12
$KNiF_3$	30.99	3.99	3.53	1403	262	0.13
$KCoF_3$	31.00	3.82	3.38	1305	247	0.14
$RbMnF_3$	39.48	4.32	3.13	1259	221	0.13
$RbCoF_3$	40.31	4.76	3.31	1148	239	0.11
$ScAlO_3$	24.00	4.28	6.19	2143	513	0.11
$GdAlO_3$	46.45	7.44	4.43	2303	354	0.11
$SmAlO_3$	45.07	7.18	4.57	2373	364	0.11
$EuAlO_3$	45.39	7.25	4.41	2213	353	0.11
$YAlO_3$	32.78	5.35	5.09	2223	410	0.11
$CaTiO_3$	27.20	4.04	5.63	2248	438	0.11
$BaTiO_3$	46.25	6.04	3.77	1898	280	0.12
$SrTiO_3$	27.70	5.12	5.29	2213	403	0.11

Note: $\bar{M}$ is the mean atomic mass in g/at., ρ is the specific mass in g/cm^3, $\bar{v}_D$ is the average Debye acoustic velocity in km/s, T_m is the melting point in K, and Θ_D is the Debye temperature in K, calculated from (3.37).

used as a semi-empirical scaling law.

Another interesting way of using Lindemann's law to extrapolate melting curves consists in starting from its differential form giving the slope of the melting curve in terms of the Grüneisen parameter.

Gilvarry (1956a) showed that at high temperature and in the limits of Slater's approximation (Poisson's ratio constant along the melting curve), differentiation of (5.24) gives:

$$\frac{d\ln T_m}{d\ln V} = 1 + \left(\frac{d\ln K}{d\ln V}\right)_{T=T_m}$$

and, with Slater's definition of gamma (at the melting temperature):

$$\gamma_{SI} = -\frac{1}{6} - \frac{1}{2}\frac{d\ln K}{d\ln V}$$

we have:

$$\frac{d\ln T_m}{d\ln V} = -2\gamma_{SI} + \frac{2}{3} \tag{5.25}$$

or:

$$\frac{d\ln T_m}{d\ln \rho} = 2\left(\gamma_{SI} - \frac{1}{3}\right) \tag{5.26}$$

or:

$$\frac{dT_m}{dP} = 2\frac{T_m}{K}\left(\gamma_{SI} - \frac{1}{3}\right) \tag{5.27}$$

The same relations can of course be obtained by taking the logarithmic derivative of (5.23) and using the definition: $\gamma = -d\ln\Theta_D/d\ln V$.

Note that:

$$\frac{d\ln T_m}{d\ln \rho} = \frac{d\ln \Phi}{d\ln \rho}$$

where $\Phi = K/\rho$ is the seismic parameter.

Equation (5.26) is a useful differential form of Lindemann's law, very convenient for extrapolating melting curves. Its integrated form, taking into account the variation of γ with density ($\gamma\rho = \gamma_0\rho_0$) is:

$$T_m = T_m^0 \exp\left[2\gamma_0\left(1 - \frac{\rho_0}{\rho}\right) + \frac{2}{3}\ln\left(\frac{\rho_0}{\rho}\right)\right] \tag{5.28}$$

It can be used with a theoretical or an experimental EOS.

Note that writing (5.25) as a finite difference equation (taking into account the fact that $\Delta V < 0$):

$$\frac{\Delta T_m}{T_m^0} = \frac{T_m - T_m^0}{T_m^0} = 2\left(\gamma - \frac{1}{3}\right)\frac{\Delta V}{V_0}$$

one obtains the Kraut–Kennedy relation (5.10):

$$T_m = T_m^0\left[1 + 2\left(\gamma - \frac{1}{3}\right)\frac{\Delta V}{V_0}\right]$$

where the constant C is explicitly stated in terms of gamma (Vaidya and Gopal, 1966; Gilvarry, 1966).

We clearly see here that the Kraut–Kennedy relation replaces the melting curve in the T, V plane by its tangent at the origin and generally cannot be used for extrapolations to very high pressures.

5.4.3 Lennard-Jones and Devonshire model

The two essential characteristics of the liquid state are that it has a

vanishing shear modulus and no long-range order, and indeed it can be shown that the loss of rigidity is a direct consequence of the loss of long-range order (P. W. Anderson, 1984). We have seen that the problem with the shear instability melting theories is that one defines melting by the vanishing of the shear modulus of the solid, without reference to the melt and that, consequently, these theories have no sound thermodynamic grounding. No such inconvenience arises if one, instead, defines melting by the transition from an ordered to a disordered state, which can be thermodynamically defined. This is what Lennard-Jones and Devonshire (1939a,b) did in constructing what is probably the most rigorous theory of melting of simple solids.

An atom of the solid or the liquid is regarded as vibrating in the available space of a small cell (the free volume, defined in Section 3.5). Lennard-Jones and Devonshire consider a crystal made up of identical atoms on regular lattice sites α; the interstitial sites β are positions of higher energy. The proportion of atoms on interstitial sites (Fig. 5.10) is taken as a measure of disorder: The order parameter Q is defined as the ratio of the number of atoms on α-sites, N_α to the total number of atoms N:

$$Q = \frac{N_\alpha}{N} \tag{5.29}$$

$$1 - Q = \frac{N_\beta}{N}$$

Q varies between $\frac{1}{2}$ for total disorder and 1 for perfect order.

In a first paper, Lennard-Jones and Devonshire (1939a) calculated the effect of disorder on the partition function of atoms by determining the probability of various configurations about atoms on α- and β-sites. They found a critical temperature at which long-range order disappears and they determined the additional free energy and pressure due to disorder, in terms of the extra energy W of a pair of atoms on neighboring α- and β-sites. To calculate the melting temperature, they expressed W in terms of interatomic potentials. This method gave good results for rare gases, but the calculations were rather elaborate and Lennard-Jones and Devonshire (1939b) proposed a simpler method derived from the Bragg–Williams theory for order–disorder transformations in binary metallic alloys. Simultaneously and independently, Frank (1939) published a paper developing exactly the same method, showing that a cooperative disorder of the Bragg–Williams type leads to the right kind of two-phase, first-order melting transition. However, he did not go into detailed calculations and

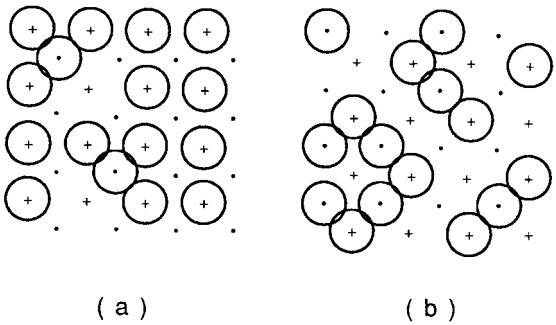

Figure 5.10 Melting by atomic disordering (after Lennard-Jones and Devonshire, 1939). (a) Local displacement of atoms, but long-range order preserved. (b) Long-range order broken: equal number of atoms on regular lattice sites (crosses) and interstitial sites (dots).

we will now return to the Lennard-Jones and Devonshire (1939b) quantitative model.

Instead of calculating the configurations about a given atom, they assume that its environment is governed by the average state of order throughout the system. To change the position of a single atom from an α-site to a β-site when all the atoms are on α-sites requires much more energy, owing to the repulsive field of the neighbors, than when the change is made simultaneously for several atoms. The phenomenon of interchange is therefore regarded as a cooperative one.

The partition function of N atoms in perfect order is equal to f_N, where f is the partition function of each atom of mass m vibrating in its cell, given by:

$$f = \left(\frac{2\pi m k_B T}{h^2}\right)^{3/2} V_F \exp\left(-\frac{\phi_0}{N k_B T}\right) \tag{5.30}$$

where V_F, the free volume, is given by (3.76) and ϕ_0 is the potential energy of the system when all the atoms are in their equilibrium positions. The partition function of the disordered system is:

$$Z = f^N \mathscr{D}(Q) \tag{5.31}$$

where $\mathscr{D}(Q)$ is a factor introduced to take account of the disorder, Q being the order parameter defined in (5.29).

Assuming that the disorder is homogeneous, an atom on a β-site is surrounded on average by zQ atoms on α-sites and an atom on an α-site is surrounded by $z(1-Q)$ atoms on β-sites, z being the number of β-sites

adjacent to a α-site, equal to the number of α-sites adjacent to a β-site in the system considered by Lennard-Jones and Devonshire. Now, if the interaction energy of a pair of neighbors on α- and β-sites is W, the average extra energy of an atom due to its neighbors is: $W_\alpha = Wz(1 - Q)$ for an atom on an α-site and $W_\beta = WzQ$ for an atom on a β-site. Hence, the energy required to transfer an atom from an α-site to a β-site is:

$$\Delta W = W_\beta - W_\alpha = Wz(2Q - 1) \tag{5.32}$$

The total energy of interaction due to the disorder is:

$$N_\alpha W_\alpha = N_\beta W_\beta = zNWQ(1 - Q) \tag{5.33}$$

Note that W is a function of the distance between two sites and therefore of the volume of the solid as a whole; this is how the cooperative feature of the model is introduced.

The number of configurations such that there are N_α atoms on α-sites and N_β atoms on β-sites is:

$$\gamma(Q) = \frac{N!}{(N - N_\alpha)!(N_\alpha)!} \times \frac{N!}{(N - N_\beta)!(N_\beta)!} = \frac{N!}{(NQ)! - [N(1 - Q)]!}$$

The disorder factor $\mathscr{D}(Q)$ is therefore:

$$\mathscr{D}(Q) = \gamma(Q) \exp\left[- \frac{zNWQ(1 - Q)}{k_B T} \right] \tag{5.34}$$

and the partition function of the system of atoms vibrating in disordered cells is, from (5.31):

$$Z = f^N \gamma(Q) \exp\left[- \frac{zNWQ(1 - Q)}{k_B T} \right] \tag{5.35}$$

The maxima of the partition function for given volume, temperature and W are found for $dZ/dQ = 0$, which, if one uses Stirling's approximation: $\ln(N!) \cong N \ln N - N$, can be written:

$$\frac{zW(2Q - 1)}{2k_B T} = \ln Q - \ln(1 - Q) \tag{5.36}$$

and, if one remembers that:

$$\arg\tanh x = \frac{1}{2} \ln\left(\frac{1 + x}{1 - x} \right)$$

one can write (5.36) as:

$$2Q - 1 = \tanh\left[\frac{zW(2Q-1)}{4k_BT}\right] \tag{5.37}$$

Equation (5.37) always has one root for $Q = \frac{1}{2}$ and, if $zW/4k_BT > 1$, it has another root $Q_{max} > \frac{1}{2}$, corresponding to a maximum of the partition function Z and given in terms of W/k_BT by (5.36). The Helmholtz free energy, $F = -k_BT\ln Z_{max}$, is then:

$$\begin{aligned} F = &- Nk_BT\ln f + zNWQ_{max}(1-Q_{max}) \\ &+ 2Nk_BT[Q_{max}\ln Q_{max} + (1-Q_{max})\ln(1-Q_{max})] \end{aligned}$$

The free energy consists of two terms. The first one: $F' = -NkT\ln f$, corresponds to the perfectly ordered crystal and the second term:

$$\begin{aligned} F'' = &zNWQ_{max}(1-Q_{max}) \\ &+ 2Nk_BT[Q_{max}\ln Q_{max} + (1-Q_{max})\ln(1-Q_{max})] \end{aligned} \tag{5.38}$$

corresponds to the extra contribution of the disorder of the centers about which the atoms vibrate.

The internal energy, entropy and pressure can be similarly separated into terms corresponding to the ordered crystal and extra terms due to the state of positional disorder.

Since $F'' = U'' - TS''$, the disorder contributions to the internal energy and entropy are:

$$U'' = zNWQ_{max}(1-Q_{max}) \tag{5.39}$$

$$S'' = -2[Q_{max}\ln Q_{max} + (1-Q_{max})\ln(1-Q_{max})] \tag{5.40}$$

The extra pressure due to disorder $P'' = -(\partial F''/\partial V)_T$ is:

$$P'' = -zNQ_{max}(1-Q_{max})\left(\frac{dW}{dV}\right)_T - \left(\frac{dF''}{dQ}\right)_{V,T}\left(\frac{dQ}{dV}\right)_T \tag{5.41}$$

Since F'' is maximum for Q_{max}, the last term vanishes and, as W is a function of volume alone, we have:

$$P'' = -zNQ_{max}(1-Q_{max})\frac{dW}{dV} \tag{5.42}$$

Denoting by $n'' = zNQ_{max}(1-Q_{max})$, the number of atoms in adjacent α- and β-sites, we have:

$$P'' = -n''\frac{dW}{dV}$$

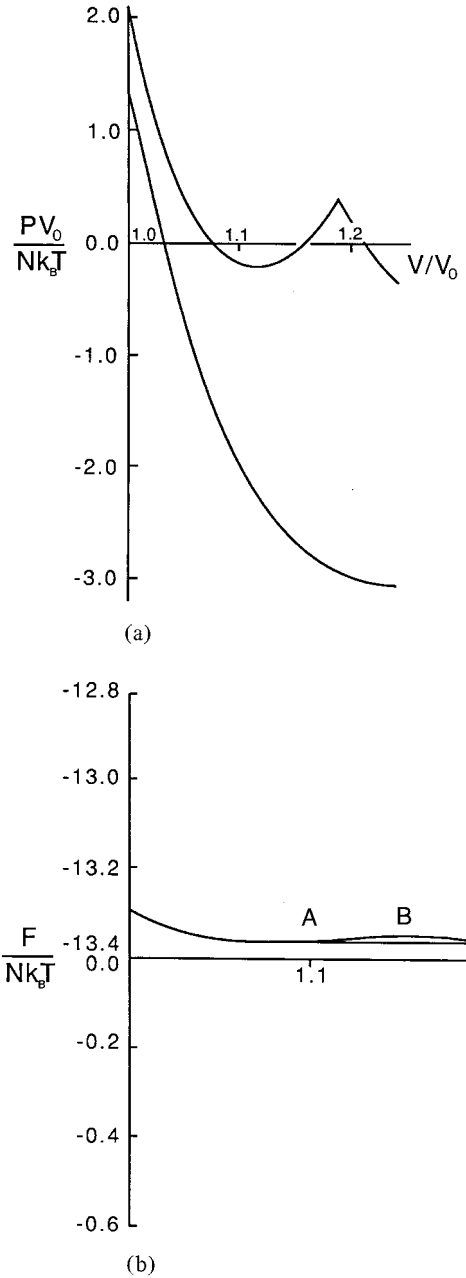

Figure 5.11 Lennard-Jones and Devonshire theory of melting (after Lennard-Jones and Devonshire, 1939). (a) Pressure as a function of volume at a given temperature. The lower curve gives P', the pressure for a state of order, and the upper one gives the total pressure, the sum of P' and P'', the disorder pressure. (b) Free energy as a function of volume.

Since Q_{max} is a function of W/k_BT only , as seen in equation (5.36), and W is a function of volume only, it follows that, for a given temperature, n'' is a function of volume only and that P'' rises from zero for small volumes to a maximum and decreases to zero again for large volumes.

Owing to the existence of the term P'' in the equation of state, the shape of the isotherm is drastically modified from that of the ordered solid (Fig. 5.11(a)). The curve of free energy F as a function of volume is shown in Fig. 5.11(b) for solid argon. It displays a maximum B between two minima A and C. The minimum A, for small volume, corresponds to a relatively ordered state (solid) and the other minimum C corresponds to nearly total disorder (liquid). Between A and C the system will have less free energy by following the straight line AC corresponding to a two-phase mixture of solid and liquid in equilibrium. The volume of melting can be directly read as the difference of the abscissae of the two minima. Now, the total pressure depends on volume and temperature ; if the interaction energy W varies with volume as $W = W_0(V_0/V)^m$ and if $\phi_0 \propto W_0$, it can be shown that: $P = f(V/V_0, k_BT/\phi_0)$. Therefore, there exists a functional relationship between V/V_0 and k_BT/ϕ_0 at $P = 0$.

As we have seen (Fig. 5.11), P goes to zero for three values of V/V_0, the smallest one corresponding to the volume of the solid at melting and it is found that for many solid gases the corresponding value of k_BT/ϕ_0 is about 0.7. The melting temperature is therefore: $T_m \cong 0.7\,\phi_0/k_B$.

There is a good agreement between observed and calculated values of the temperature and volume of melting for solid gases.

Lennard-Jones and Devonshire (1939b) calculated the vibrational frequency of a solid with an interatomic potential (Lennard-Jones potential) given by:

$$\phi = \phi_0 \left[\left(\frac{r}{r_0} \right)^{-12} - 2 \left(\frac{r}{r_0} \right)^{-6} \right] \tag{5.43}$$

They were able to find a correlation between the vibrational frequency of the solid and the melting temperature calculated by their model, thus verifying Lindemann's law: they found that for a number of solid gases, they had:

$$T_m = \left(\frac{1}{163} \right)^2 \Theta_D^2 M V^{2/3} \tag{5.44}$$

in good agreement with formula (5.23), if the Gilvarry factor f is taken equal to about 0.1.

5.4.4 Dislocation-mediated melting

The loss of long-range order is the fundamental feature of the melting phenomenon and, as we have seen in the case of the Frank and Lennard-Jones and Devonshire models, the cooperative appearance of disorder (the order parameter being a function of the total volume) accounts for the first-order character of the melting transition.

However, for energetic reasons, long-range order cannot be destroyed simultaneously over the whole crystal and disorder must be caused by the proliferation of lattice defects that locally break the order. This is the origin of defect-mediated theories of melting.

The simplest defect is the vacancy, a vacant lattice site. The equilibrium atomic fraction of vacancies in a crystal increases with temperature as $\exp(-\Delta G/k_B T)$, where ΔG is the free energy of formation of vacancies (see e.g. Poirier, 1985, p. 40). It is therefore tempting to envision melting as due to the increase in the number of vacancies up to a point where the vacancy-filled solid becomes so disordered that it can be considered as a liquid. However, the cooperative effects necessary to produce a first-order transition would appear only for unrealistically high vacancy concentrations.

Dislocations (see e.g. Friedel, 1964; Nabarro, 1967) are linear lattice defects that break the order along their cores. They also have a long-range stress field and cause elastic energy to be stored in the volume of the crystal. Motion of dislocations in the lattice causes slip and plastic deformation. It is easy to see how a crystal filled with dislocations can be so disordered and fluid as to be liquid-like. It probably was Shockley (1952) who first regarded the liquid as being a solid densely packed with dislocations and calculated its viscosity by consideration of the motion of dislocations.

Dislocation-melting theories indeed rest on the assumption that a liquid is a solid saturated with dislocation cores (Fig. 5.12) (Mizushima, 1960; Kuhlmann-Wilsdorf, 1965; Ninomiya, 1978; Cotterill, 1980; Suzuki, 1983; Poirier, 1986; Joos, 1996). The dislocation-melting models invoke a cooperative effect: The free energy of the solid increases with dislocation density but the introduction of new dislocations becomes easier and easier and, for a finite density, the free energy of the solid saturated with dislocations (i.e. a liquid) is equal to that of the dislocation-free solid . A first-order transition is then thermodynamically possible between solid and liquid at equilibrium.

The various dislocation-melting theories are reviewed by Poirier (1986) and a model based on Ninomiya's (1978) model is developed, giving the

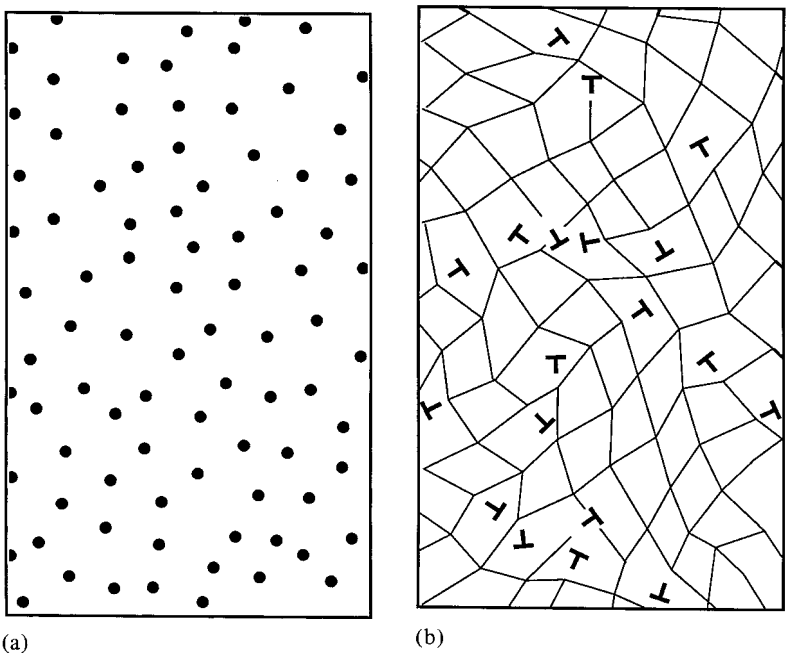

Figure 5.12 Dislocation melting (two-dimensional example): a disordered liquid (a) can be represented by a solid saturated with dislocations (b); the dislocation cores are traditionally represented by "nails."

melting volume, entropy and temperature as a function of the elastic moduli and the Grüneisen parameter. We will only give here the main outline of the model.

The total elastic internal energy ΔE of one mole of crystal containing a dislocation concentration C_d consists of:

- The core energy:

$$\Delta E_c \propto C_d b^3 \tag{5.45}$$

  C_d is defined by: $C_d = LV/N_A b$, where L is the dislocation length per unit volume, V is the molar volume, N_A is Avogadro's number and b is the Burgers vector of the dislocations (a vector of the Bravais lattice, expressing the strength of the dislocation).
- The elastic energy stored in the bulk of the crystal, which can be written, taking into account the interaction of dislocations (Poirier, 1986):

$$\Delta E_e \propto -C_d \mu b^3 \ln\left(\frac{\pi r_0^2 N_A C_d b}{V}\right)^{1/2} \tag{5.46}$$

where μ is the shear modulus and r_0 is the core radius.

Now, the strain field of a dislocation has a dilatation component and the concentration C_d of dislocations introduces a dilatation $\varepsilon(C_d)$, which, in turn, causes the shear modulus to decrease. Using Slater's formula (3.66), we can write:

$$\mu = \mu_0 \left[1 + \left(2\gamma_{SI} + \frac{1}{3} \right) \varepsilon \right] \tag{5.47}$$

where γ_{SI} is Slater's gamma, and carry the value of μ into (5.46).

- A third energy term corresponds to the dilatation ε:

$$\Delta E_\varepsilon \propto K\varepsilon^2 \tag{5.48}$$

where K is the bulk modulus.

The total energy is therefore:

$$\Delta E = \Delta E_c + \Delta E_e + \Delta E_\varepsilon \tag{5.49}$$

The equilibrium value of ε corresponding to C_d is obtained by minimizing ΔE with respect to ε. For $C_d = C_d^{sat} \cong \frac{1}{3}$ at saturation, we have:

$$\varepsilon^{sat} \cong \frac{A}{2\pi} \frac{\mu_0}{K} \left(\gamma_{SI} - \frac{1}{3} \right) C_d^{sat} \tag{5.50}$$

where A is a geometric factor depending on the crystal structure.

The melting volume is then:

$$\Delta V_m = V\varepsilon^{sat} \tag{5.51}$$

The melting entropy can be written:

$$\Delta S = R[3\varepsilon^{sat}\gamma_{SI} + 2C_d^{sat}] \tag{5.52}$$

The first term corresponds to the entropy increase due to the lowering of lattice frequencies caused by anharmonic dilatation and the second term corresponds to the vibrational entropy of dislocation lines.

The total extra free energy of the crystal with a dislocation concentration C_d, at temperature T is:

$$\Delta F = \Delta E - T\Delta S \tag{5.53}$$

and the melting temperature is obtained by taking $C_d = C_d^{sat}$ in (5.53) and setting $\Delta F = 0$ (Fig. 5.13), since ΔF corresponds to the difference in free energy between the liquid (dislocation saturated crystal) and the dislocation-free solid. We have:

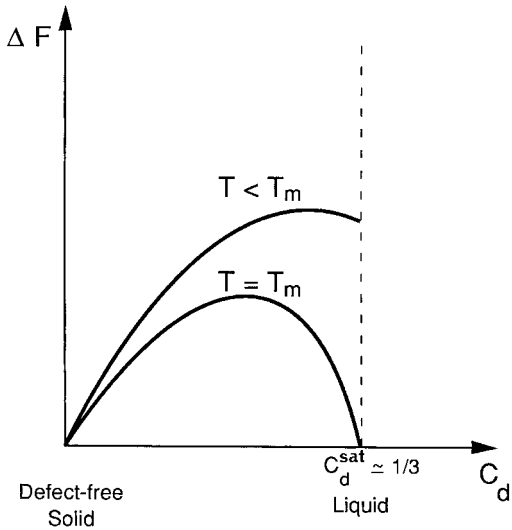

Figure 5.13 Extra free energy of a crystal containing a dislocation concentration C_d. At the melting temperature, $\Delta F = 0$ for $C_d = C_d^{sat}$.

$$T_m = \frac{KV}{2R}\varepsilon^{sat}\frac{1-\varepsilon^{sat}\left(\gamma_{SI}-\frac{1}{3}\right)}{\left(\gamma_{SI}-\frac{1}{3}\right)(3\varepsilon^{sat}\gamma_{SI}+2C_d^{sat})} \tag{5.54}$$

Using (5.51), (5.52) and the Clausius–Clapeyron rule, we obtain the slope of the melting curve:

$$\frac{dT_m}{dP} = \frac{\Delta V_m}{\Delta S_m} = \frac{V}{R}\frac{\varepsilon^{sat}}{(3\varepsilon^{sat}\gamma_{SI}+2C_d^{sat})} \tag{5.55}$$

and:

$$\frac{d\ln T_m}{d\ln \rho} = \frac{2\left(\gamma_{SI}-\frac{1}{3}\right)}{1+\varepsilon^{sat}\left(\gamma_{SI}-\frac{1}{3}\right)} \tag{5.56}$$

We see that (5.56) differs from the differential Lindemann law (5.26) only by the coefficient $[1 + \varepsilon^{sat}(\gamma_{SI} - 1/3)]$, slightly larger than 1 if $\gamma_{SI} > \frac{1}{3}$, which is always the case.

The melting parameters of iron were calculated using this model

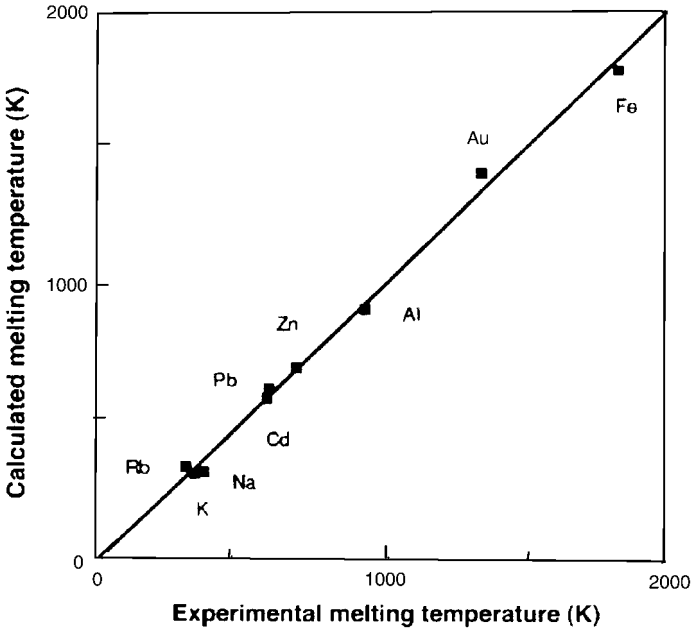

Figure 5.14 Calculated vs experimental melting temperature of the metals potassium, sodium, rubidium, lead, cadmium, zinc, aluminum, gold and iron (after Poirier and Price, 1992).

(Poirier, 1986) and found to be in good agreement with the experimental values, as we will see in the next section. Poirier and Price (1992) found an agreement better than 90% between the calculated and experimental melting point of nine metals (Rb, K, Na, Cd, Pb, Zn, Al, Au, Fe) (Fig. 5.14).

Stacey and Irvine (1977b) derived the differential Lindemann law from what they claimed to be a dislocation theory of melting and the Clausius–Clapeyron rule. However, their model has no cooperative feature and the liquid state is not characterized by a saturation concentration of dislocations; instead, they assume that the latent heat of melting and the melting volume are, respectively, equal to the extra energy and the anharmonic dilatation corresponding to the removal of an atom from one of a pair of linear mass-and-spring type chains – a system only very remotely connected to a crystal dislocation.

5.4.5 Summary

All melting theories are imperfect because to construct a good theory for the first-order melting transition, one must write that the free energies of

the solid and the liquid are equal at equilibrium. This would necessitate a better description of the liquid state than the ones currently available – indeed, the structure of the liquid state is a standing problem in physics. *Ab-initio* calculations of the free energies of liquid and solid phases, using density functional theory, are very promising and have recently given good results in the case of metals (Vočadlo *et al*., 1997; de Wijs *et al*., 1998), but they do not constitute theories of melting.

Such as they are, the disorder theories of melting of the Frank–Lennard-Jones–Devonshire type or the dislocation theories of melting are closer to being acceptable theories. The main objection to these theories is that they lead to homogeneous melting kinetics in the bulk, while there is more and more experimental evidence that melting is initiated from the surface, or grain boundaries (see e.g. Joos, 1996).

The shear instability theories, even though they provide some interesting correlations, are not good theories of melting, nor are the vibrational theories in which, to quote Frank (1939), one assumes that "at the melting point, the crystal shakes itself to pieces". We must, however, remark that Lindemann (1910) never claimed to have done anything else than find a correlation between the melting point and the vibrational frequency, and it is no surprise that the Lindemann law can be found as a by-product of any theory of melting worth its salt, even though that does not constitute a justification of a "Lindemann theory of melting". As a correlation, and especially in its differential form, in terms of the Grüneisen parameter, Lindemann's law is very valuable and its status is not impaired by the fact that it does not embody a theory of melting.

It remains that even the best theories of melting, developed for simple solids like solid gases or metals, dismally fail in the case of minerals due to the complexity of the structure of their liquids. The Lindemann correlation, however, if applied to crystals of the same structure, may be the base of fruitful systematics and reasonable extrapolations of the melting curve.

5.5 Melting of lower-mantle minerals

The melting curve of the lower-mantle minerals provides an upper bound to the temperature profile in the deep Earth, except possibly near the core–mantle boundary (CMB), where it has been suggested that partial melting may occur in an ultra-low velocity zone (Williams and Garnero, 1996; Holland and Ahrens, 1997). Also, as many transport phenomena (diffusion, viscosity, etc.) have been empirically shown to scale with melting temperature, it is important to obtain information on melting of minerals at very high pressures.

5.5.1 Melting of $MgSiO_3$ perovskite

Heinz and Jeanloz (1987) first determined the melting curve of $(Mg_{0.9}Fe_{0.1})SiO_3$ perovskite up to 65 GPa in a YAG laser-heated diamond-anvil cell. They found that the melting point was independent of pressure ($dT_m/dP \approx 0$) and equal to 3000 ± 300 K. Knittle and Jeanloz (1989) pursued the experiments up to 96 GPa, and found that above 60 GPa the melting curve had a small slope $dT_m/dP \approx 20$ K/GPa; they attributed the change of slope to a structural transition in the melt.

Melting experiments on $MgSiO_3$ between 22 and 25 GPa in a multi-anvil apparatus by Ito and Katsura (1992) gave a melting temperature of about 2800 K at 23 GPa, in agreement with Heinz and Jeanloz (1987), but a finite slope of the melting curve $dT_m/dP \approx 30 \pm 5$ K/GPa, close to that estimated by Poirier (1989).

Sweeney and Heinz (1993), using a diamond-anvil cell up to 94 GPa, found melting temperatures of $(Mg_{0.86}Fe_{0.14})SiO_3$ slightly lower than those reported by Heinz and Jeanloz (1987), and a small negative slope $dT_m/dP \approx -2.5 \pm 0.6$ K/GPa, without any change in slope at 60 GPa.

Zerr and Boehler (1993), using argon as the pressure medium in a CO_2 laser-heated diamond-anvil cell up to 63 GPa, found a much higher slope for the melting curve of $(Mg_{0.88}Fe_{0.12})SiO_3$, $dT_m/dP \approx 60$ K/GPa at 22 GPa, smoothly decreasing to 40 K/GPa at 60 GPa. This leads to an extrapolated melting temperature at the CMB higher than 7000 K. The wide discrepancy with the results of Heinz and Jeanloz (1987) and Sweeney and Heinz (1993) was attributed to differences in experimental set-ups and melting criteria; a heated controversy followed (Heinz *et al.*, 1994; Boehler and Zerr, 1994). The experiments of Shen and Lazor (1995) on $MgSiO_3$ (Fig. 5.15) are in agreement with Zerr and Boehler (1993), while Sweeney and Heinz (1998) find that the slope of the melting curve of $(Mg_{0.88}Fe_{0.12})SiO_3$ up to 85 GPa is $dT_m/dP \approx 5 \pm 0.8$ K/GPa, leading to a melting temperature at the CMB, extrapolated by Simon's equation, of about 4500 K.

5.5.2 Melting of MgO and magnesiowüstite

Due to the fact that the melting temperature of MgO at atmospheric pressure is already very high (3060 K), there have been fewer attempts at determining its pressure dependence by experiment than by calculation. Zerr and Boehler (1994) measured the melting point up to 31.5 GPa. Fit of the experimental data to a Lindemann relation yields a slope $dT_m/dP \approx$ 36 K/GPa near 1 atm (smaller than the slope found by the same authors for

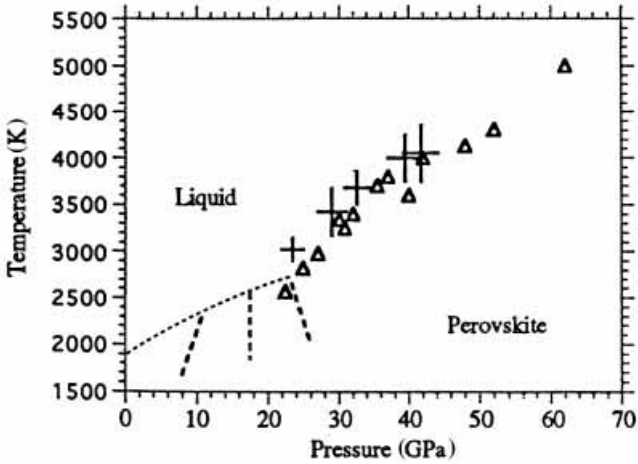

Figure 5.15 Experimental melting curves of silicate perovskite $MgSiO_3$, from Shen *et al.*, (1993) (crosses), and Zerr and Boehler (1993) (triangles) (after Shen and Lazor, 1995).

perovskite), and an extrapolated melting point slightly above 5000 K at the pressure of the CMB. The melting point of $(Mg_{0.85}Fe_{0.15})O$ magnesiowüstite was found to be 3400 K at 18 GPa.

Vočadlo and Price (1996) calculated the melting curve of MgO up to 150 GPa, by classical molecular dynamics. They found a much larger slope than did Zerr and Boehler (1994): $dT_m/dP \approx 98$ K/GPa at 1 atm, with a melting point tending to 8000 K near the CMB. Also using molecular dynamics, but an *ab-initio*, non-empirical potential, Cohen and Weitz (1998) found results in agreement with Vočadlo and Price (1996): $dT_m/dP \approx 114$ K/GPa at 1 atm.

5.6 Phase diagram and melting of iron

There is strong evidence for the Earth's core being essentially composed of iron (Birch, 1952; O. L. Anderson, 1985) and, as we will see below, a knowledge of the melting curve of iron at core pressures allows us to place a constraint upon the temperature at the inner core boundary and anchor the Earth's temperature profile. The melting curve, however, is part of the phase diagram (see Section 7.4.1) and represents the equilibrium boundary between the liquid and the solid phase stable at a given pressure. It is therefore the whole phase diagram and not just the melting curve at ambient pressure that must be extrapolated at high pressure.

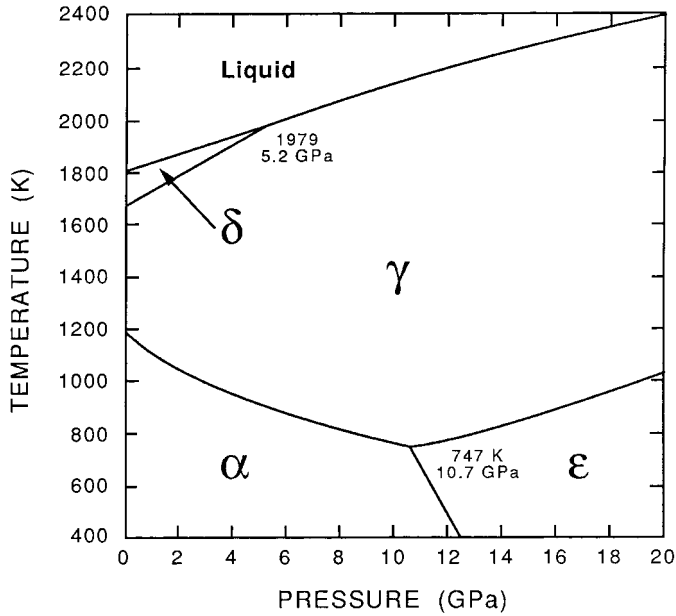

Figure 5.16 Phase diagram of iron up to 20 GPa (after Guillermet and Gustafson, 1984).

At pressures lower than about 20 GPa, the phase diagram of iron is reasonably well known (Guillermet and Gustafson, 1984; Boehler, 1986) (Fig. 5.16): The phase stable at room temperature and ambient pressure is α-Fe with a body-centered-cubic (bcc) structure, at high temperature it changes into face-centered-cubic (fcc) γ-Fe, which reverts to a bcc δ-Fe phase below the melting point (Strong *et al.*, 1973). At high pressure, α-Fe transforms into hexagonal-close-packed (hcp) ε-Fe. The $\alpha \rightarrow \varepsilon$ transformation has been studied *in situ* by X-ray diffraction, using synchrotron radiation and appears to take place by a diffusionless mechanism (Bassett and Huang, 1987). The experimental values of the triple point between the α, γ and ε phases are given in Table 5.5.

At low and moderate pressures, the phase that melts is γ-Fe and the melting curve has been determined up to 20 GPa (Liu & Bassett, 1975) and 43 GPa (Boehler, 1986) by resistive heating of an iron wire in a diamond-anvil cell.

For more than ten years, the phase diagram of iron at high pressure has been the subject of a controversy in the "iron workers" community, which is not entirely over at the date of this writing. Whether the melting curve extrapolated to a melting point at the pressure of the inner core boundary

Table 5.5. *Triple points in the Fe phase diagram. Pressure in GPa, temperature in K.*

	α–γ–ε		ε–γ–L		γ–β–L		ε–β–L	
Reference	*P*	*T*	*P*	*T*	*P*	*T*	*P*	*T*
Bundy (1965)	11	763						
Liu (1975b)			94	3243				
Guillermet & Gustafson (1984)	10.7	747						
Anderson (1986)			280	5760				
Boehler (1986)	11.6	810	75	2773				
Akimoto *et al.* (1987)	8.3	713						
Williams et al. (1991)			300	7500				
Saxena *et al.* (1993)					70	2700		
Boehler (1993)			100	2750				
Saxena *et al.* (1994)					76.5	2946	205	40
Yoo *et al.* (1995)			50	2500				
Mao *et al.* (1998)			60	2800				

L: liquid.

(330 GPa) higher than 7000 K or lower than 5000 K was the main bone of contention. As more and more experiments were performed, the problem arose of the presence (or absence) of new high-pressure phases and of their crystallographic structures, with obvious consequences as to the nature of the iron phase of the inner core.

In shock-wave experiments, Brown and McQueen (1980, 1982, 1986) found a first discontinuity in sound wave velocity near 200 GPa, and a second discontinuity at 243 GPa, at a higher temperature, between 5000 and 5700 K; they attributed the first discontinuity to a solid–solid phase transition, which they suggested might be $\varepsilon \rightarrow \gamma$, and the second discontinuity was considered as due to melting. Most later extrapolations of experimental data were forced to go through the (wide) error bar of the Brown and McQueen melting point at 243 GPa.

Williams *et al.* (1987b) combined shock-wave experiments and melting experiments in a laser-heated diamond-anvil cell up to 100 GPa, and found a very steep melting curve, extrapolating to a melting point of 7600 ± 500 K at 330 GPa. The melting curve calculated *ab initio* by Hausleitner and Hafner (1989) goes approximately through the Williams *et al.* experimental points at lower pressures, but extrapolates to 5200 K at 330 GPa.

Boehler *et al.* (1990), in Mainz, also from experiments in a laser-heated

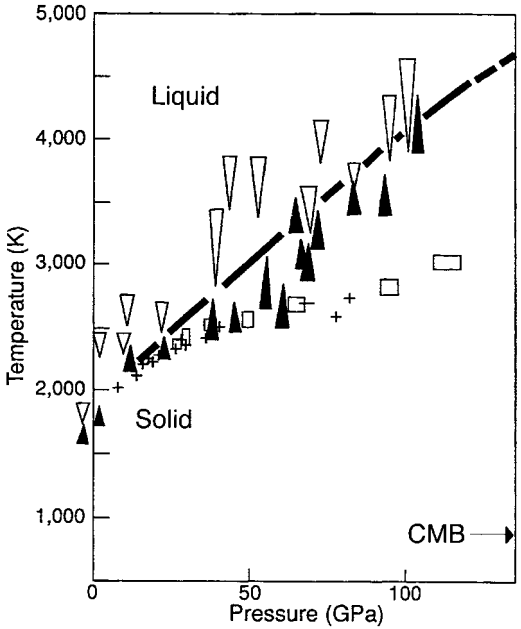

Figure 5.17 Experimental melting curves of iron from Williams *et al.*, (1987b) (triangles) and Boehler *et al.*, (1990) (crosses and rectangles) (after Duba, 1992).

diamond-anvil cell, found that the melting point of γ-Fe at 120 GPa was 3000 K, more than 1000 K lower than the value found by Williams *et al.* (1987b). Williams *et al.* (1991) then confirmed a melting point $T_m = 4300 \pm 200$ K at 105 GPa and the extrapolation of the melting curve to the ε–γ–liquid triple point at 300 GPa and 7500 K. Duba (1992) summarized the arguments from both sides (Fig. 5.17), pointing out that the determination of melting in a diamond-anvil cell is very difficult and that the discrepancy between experimentalists might come from the different melting criteria used. Boehler (1993) confirmed his previous results by extending his measurements up to a pressure of 200 GPa, and found the ε–γ–liquid triple point at 100 GPa and 2750 K. The melting curve extrapolated to 4850 K at 330 GPa. At this point, a third team entered the fray: Shen *et al.* (1993) in Uppsala, also using a laser-heated diamond-anvil cell, measured the melting point of iron up to 60 GPa. Below 20 GPa, their results agreed with both those of Williams *et al.* (1987b) and Boehler *et al.* (1990), but above this pressure they were much closer to those of Boehler *et al.* New shock-wave measurements at Livermore National Laboratory, however, yielded melting temperatures of 6350 K and 6720 K at 235 GPa

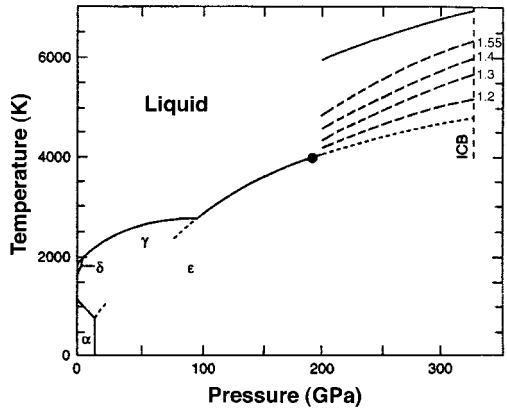

Figure 5.18 Phase diagram of iron. Dashed curves are extrapolations, for P between 200 and 330 GPa, using values of the Grüneisen parameter $\gamma = 1.55$, 1.4, 1.3, 1.2. The dotted curve is the extrapolation from Boehler (1993). The full curve between 200 and 330 GPa is from experiments by Yoo *et al.* (1993) (after Anderson and Duba, 1997).

and 300 GPa respectively, extrapolating to 6830 $\pm$ 500 K at 330 GPa (Yoo *et al.*, 1993).

Chen and Ahrens (1995) calculated the phase diagram of iron from equations of state and found that their calculations favored Boehler's melting curve over that of Williams *et al.* (1987b).

Ten years after the controversial paper of Williams *et al.* (1987b), it was time again for an assessment of the situation. On the basis of X-ray diffraction identifications of the liquid phase in later work, and a more or less general consensus, Anderson and Duba (1997) removed the steep melting curve of Williams *et al.* (1987b) from further consideration. They constructed a phase diagram from the published diamond-anvil cell data, in reasonable agreement up to 200 GPa, and extrapolated the melting curve to the pressure of the inner core boundary (ICB), using the Lindemann law (5.28), for various values of the Grüneisen parameter (Fig. 5.18). With their preferred value $\gamma = 1.4$, they find an extrapolated melting temperature at 330 GPa between 5600 and 6500 K, in rather good agreement with the calculated values of Poirier and Shankland (1994) ($T_m = 6060$–6160 K) and Chen and Ahrens (1995) ($T_m = 5800$ K). More recent measurements by Mao *et al.* (1998) up to 84 GPa agreed with those of Saxena *et al.* (1993) and Boehler (1993) below 60 GPa and yielded slightly higher melting points above 60 GPa. They inferred a position of the ε–γ–liquid triple point at 60 $\pm$ 5 GPa and 2800 $\pm$ 200 K.

From Boehler's (1993) data, the triple point at about 2700 K and

100 GPa thought to be the ε–γ–liquid triple point would be at too low a pressure to make it possible for the solid–solid transition observed by Brown and McQueen to be an $\varepsilon \rightarrow \gamma$ transition. If a fifth phase of iron existed, the transition could be explained. Boehler (1997) interpreted the transition reported by Brown and McQueen as due to incomplete shock melting, which eliminated the need for a fifth phase and extended the field of ε-Fe to the temperature and pressure of the inner core.

However, Saxena *et al.* (1993) at Uppsala claimed to have identified a phase β between the ε and γ phases, with the ε–β–γ triple point near 30 GPa and 1200 K. A triple point near 70 GPa and 2700 K could then be the γ–β–liquid triple point. A further study up to 150 GPa led Saxena *et al.* (1994) to propose a phase diagram with the γ–β–liquid triple point at 2946 ± 100 K and 76.5 ± 4 GPa and the ε–β–liquid triple point at 4015 K and 205 GPa. The melting curve extrapolates to between 5980 and 6680 K at 330 GPa.

Another controversy was soon to appear. Yoo *et al.* (1995) used a combined laser-heated diamond-anvil cell and X-ray diffraction technique to determine the structure of the high-pressure high-temperature phases up to 130 GPa and 3500 K. They observed that ε-Fe was stable from 50 to at least 110 GPa, and found no evidence for the β phase. The triple point at 2500 ± 200 K and 50 ± 10 GPa was identified as the ε–γ–liquid triple point. However, they found evidence for a double hcp phase (ε′) inside the stability field of the γ phase. Saxena *et al.* (1995) and Saxena *et al.* (1996), using synchrotron X-ray diffraction, confirmed the transition from ε to β at 38 GPa and temperatures between 1200 and 1500 K. They indexed the structure of the β phase as double hcp. In a technical comment in *Science*, Saxena and Dubrovinsky (1997) and Yoo *et al.* (1997) expounded their respective viewpoints. More recent determinations of structures by X-ray diffraction, while the sample is at high temperature and pressure (strangely called "*in-situ*" experiments) did not clarify the situation. Shen *et al.* (1998) still do not observe the β phase, while Saxena and Dubrovinsky (1998) and Dubrovinsky *et al.* (1998) define its stability field and confirm a double hcp structure, although Saxena and Dubrovinsky (1998) propose a positive slope of the P, T boundary between ε and β phases, while Dubrovinsky *et al.* (1998) find a negative slope (Fig. 5.19). Andrault *et al.* (1997) confirm the existence of the β phase, and agree with the Uppsala team on its stability field (with a positive slope of the ε–β boundary) (Fig. 5.20), but assign to it an orthorhombic structure, that can be derived by small distortions from ε and γ phases. O. L. Anderson (1997) sums up the situation.

Considering the controversy about the β phase, involving pressures of

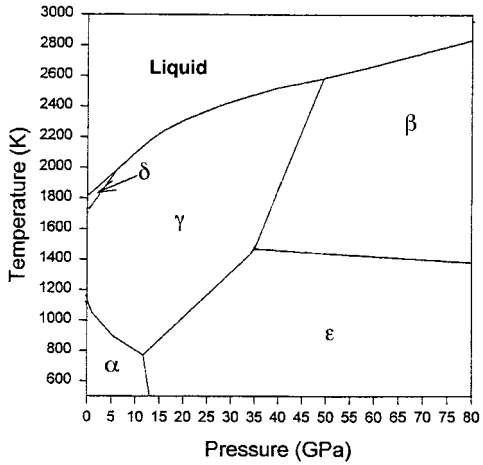

Figure 5.19 Phase diagram of iron. Stability field of the β phase (after Dubrovinsky *et al.*, 1998b).

the order of 50 GPa, it is not surprising that the existence or non-existence of a high-pressure phase above 200 GPa (α' or θ) is entirely hypothetical. It was suggested by Brown and McQueen (1986) from their shock-wave experiments, and thought to be body-centered cubic, since this structure had been predicted to be stable at very high pressures (Ross *et al.*, 1990; Bassett and Weathers, 1990). However, Stixrude and Cohen (1995) performed *ab-initio* calculations of the energies of the various iron phases at high pressure and found the bcc structure to be unstable with respect to a body-centered-tetragonal structure above 150 GPa.

At the time of writing, it is still impossible to guess whether the inner core phase is hexagonal close packed (ε), double hcp or orthorhombic (β), or something else (α'). It seems however probable that it is not face-centered cubic (γ), as there is good evidence that the stability field of this phase does not extend to very high pressures.

The seismologically determined density of the outer core is lower than that of pure iron, at core pressure and temperature, deduced from equations of state. Light elements (S, O, Si, etc.) must therefore be present in solution in the liquid metal. Besides decreasing the density of the core, they also decrease the melting (freezing) point of the alloy, with respect to that of pure iron. As the inner core boundary corresponds to freezing of the liquid iron alloy, a knowledge of the freezing-point depression, together with that of pure iron, would allow an estimation of the temperature at the inner core boundary, thus providing an anchoring point for the geotherm. There is

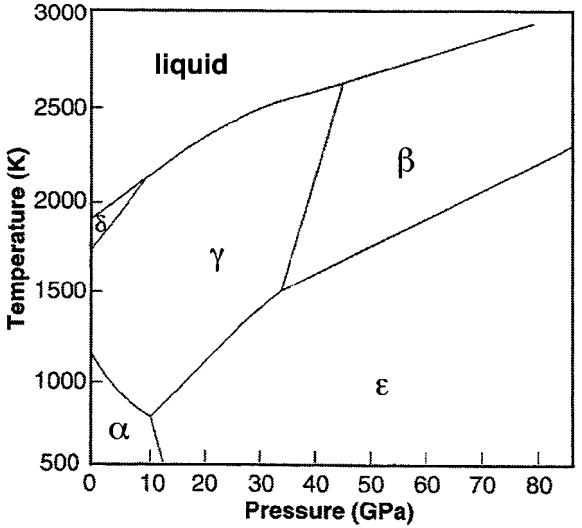

Figure 5.20 Phase diagram of iron. Stability field of the β phase (after Andrault *et al.*, 1997).

still much uncertainty about the nature and concentration of the light elements in the core (Poirier, 1994a), although some progress has recently been made in estimates of the chemical composition of the core and mantle (Allègre *et al.*, 1995). In addition, very little is known about the phase diagrams of iron alloys at core pressures.

Sulfur is known to depress the melting point of iron at atmospheric pressure and forms a eutectic, but it is not obvious that this effect persists up to core pressures. Williams and Jeanloz (1990) investigated the melting of iron–sulfur alloys up to 120 GPa. They determined the melting curve of FeS and of a 10 wt% S alloy (Fig. 5.21), and they calculated the composition and temperature of the eutectic as a function of pressure.

Boehler (1992) measured the melting curve of FeS and FeS_2 between 7 and 44 GPa, as well as the melting point of a mixture of Fe with about 10–20 wt% FeS at several pressures. At 17.6 GPa, the mixture begins to melt at 1650 ± 50 K, 600 K below the melting point of iron and 300 K below that of FeS. Fei *et al.* (1997) report that the formation of the definite compound Fe_3S_2 above 14 GPa changes the melting relation in the Fe–FeS system.

Oxygen is another candidate as a light alloying element in the core. Knittle and Jeanloz (1991) measured the melting curve of $Fe_{0.94}O$ up to 100 GPa and found that it lies above that of pure Fe. The melting tempera-

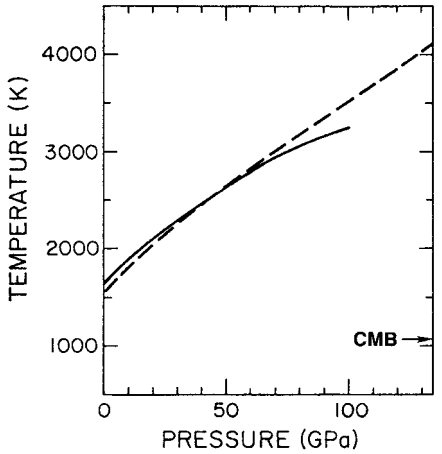

Figure 5.21 Experimental (full) and calculated (dashed) melting curve of an Fe–10 wt% S alloy (after Williams and Jeanloz, 1990).

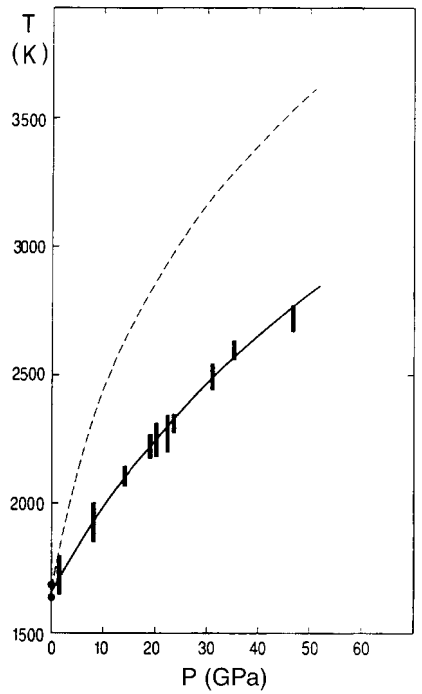

Figure 5.22 Experimental melting curve of $Fe_{0.96}O$. The melting curve of Knittle and Jeanloz (1991b) is given for comparison (dashed) (after Boehler, 1992).

ture of an alloy with 10 wt% oxygen ($Fe_{0.69}O_{0.31}$) lies between that of Fe and FeO at 83 GPa. Boehler (1992) measured a melting curve of $Fe_{0.96}O$, lying much below that measured by Knittle and Jeanloz (1991) (Fig. 5.22). Boehler (1993) found that alloys with 10 wt% and 30 wt% oxygen had melting temperatures lower than those of Fe and FeO, but that above 60 GPa the melting-point depression disappeared.

6

Transport properties

6.1 Generalities

All dynamic processes inside the Earth are governed by the transport of certain physical quantities, or at least depend on materials constants (conductivities or diffusivities) that express how easily those quantities are transported in a given region of the Earth.

- Solid-state reactions between minerals and kinetics of phase transformations are controlled by transport of matter (atoms) by diffusion.
- Viscous flow of matter in the convecting mantle is controlled by diffusion of momentum (viscosity).
- Cooling of the Earth is controlled by heat transfer in the thermal boundary layers.
- The propagation of electromagnetic signals in the mantle depends on its electrical conductivity.

Transport of a physical quantity (e.g. momentum or heat) or of particles (e.g. atoms or electrically charged particles) always results from the application of a *driving force* **F**. In all cases it produces a *flux* **J** (measured per unit area and unit time).

In the case of particles, the velocity **v** of the particle depends on the driving force and in the linear approximation, we have:

$$\mathbf{v} = M\mathbf{F} \tag{6.1}$$

where M is the *mobility* of the particle, which depends on the nature of the particle, on the properties of the medium in which it moves and on temperature and pressure. The flux **J** is then equal to the number of particles per unit volume times the velocity.

In general, if the driving force derives from a potential U, $\mathbf{F} = -\operatorname{grad} U$, the linear approximation gives:

$$\mathbf{J} = -C \operatorname{grad} U \tag{6.2}$$

where C is the kinetic coefficient expressing the ease of transport.

The driving force may be external and imposed on the system (e.g. flow due to a pressure gradient, electric current due to a difference of potential). It can also reflect the existence of heterogeneities in the system, which the resulting flow will tend to eliminate (e.g. diffusion of matter, diffusion of momentum or viscosity, diffusion of heat). In that case, as we will see below, equations of the type (6.2), together with conservation equations, yield diffusion equations.

Diffusion is an out-of-equilibrium, dissipative, irreversible process. Steady state flow in such processes corresponds to a minimum of the rate of entropy production dS/dt. It can be shown (Prigogine, 1962) that the rate of entropy production can be written as the product of a generalized driving force $\mathbf{F}$ by the corresponding flux $\mathbf{J}$.

Let us now consider a few important cases of transport phenomena mentioned above.

(i) Fluid flow through a porous medium

The external driving force is a pressure gradient. The flow of an incompressible fluid per unit area and second is given by *Darcy's equation*:

$$\mathbf{J} = -\frac{k}{\eta} \operatorname{grad} P \tag{6.3}$$

where k is the permeability of the medium, expressed in darcys (1 darcy $= 1\,\mu m^2$) and η is the dynamical viscosity (see below).

(ii) Electrical conduction

The external force is an electric field $\mathscr{E}$ deriving from a potential: $\mathscr{E} = -\operatorname{grad} V$. The transport equation is *Ohm's law*:

$$\mathbf{J} = \sigma_{el} \mathscr{E} = -\sigma_{el} \operatorname{grad} V \tag{6.4}$$

where σ_{el} is the electrical conductivity, expressed in siemens/m ($1\,S/m = 1\,\Omega^{-1}\,m^{-1}$).

The electric current density $\mathbf{J}$ is equal to the number of charge-carrying particles per unit volume times the electric charge they carry times their velocity.

(iii) Diffusion of matter

Diffusion is an irreversible process and, as such, can be best treated in the framework of the thermodynamics of irreversible processes (TIP). For a short and clear presentation of the formalism in the simpler case of metallic alloys, see Bocquet *et al.* (1983).

The driving force for the diffusion of species A (atom or point defect) is the gradient of its chemical potential μ_A. The flux of matter is given by:

$$\mathbf{J}_A = -L_A \operatorname{grad} \mu_A \tag{6.5}$$

where $\mathbf{J}_A$ is the flux of atoms A per second, and L_A is called the phenomenological coefficient. It is, however, more convenient to use *Fick's equation*, expressed in terms of the concentration c_A of atoms (number of atoms per unit volume):

$$\mathbf{J}_A = -D_A \operatorname{grad} c_A \tag{6.6}$$

where D_A is the *diffusivity* or diffusion coefficient of species A, expressed in m^2/s or cm^2/s.

Concentration c_A is defined as the number of atoms of species A per unit volume. If n is the total number of atoms per unit volume in the medium and N_A the atomic fraction of atoms A, we have:

$$nN_A = c_A \tag{6.7}$$

By definition, the chemical potential is:

$$\mu_A = \mu_A^0 + RT \ln \gamma_A N_A \tag{6.8}$$

where μ_A^0 is the chemical potential in the standard state and γ_A the activity coefficient of species A. In the simple case of ideal solutions, $\gamma_A = 1$ and we have:

$$\operatorname{grad} \mu_A = \frac{\partial \mu_A}{\partial \mathbf{x}} = \frac{\partial \mu_A}{\partial N_A} \frac{\partial N_A}{\partial \mathbf{x}} = \frac{RT}{nN_A} \frac{\partial c_A}{\partial \mathbf{x}} \tag{6.9}$$

hence:

$$\mathbf{J}_A = -L_A \operatorname{grad} \mu_A = -\frac{L_A RT}{c_A} \operatorname{grad} c_A \tag{6.10}$$

and, by comparison with (6.6):

$$D_A = \frac{L_A RT}{c_A} \tag{6.11}$$

Now, from (6.1), we have the velocity $\mathbf{v}_A = -M_A \operatorname{grad} \mu_A$ and, since $\mathbf{J} = c_A \mathbf{v}_A$, we have $L_A = c_A M_A$. Carrying into (6.11), we obtain *Einstein's relation*, linking the diffusivity with the mobility:

$$D_A = RTM_A \tag{6.12}$$

The conservation equation for species A is written:

$$\operatorname{div} \mathbf{J}_A + \frac{\partial c_A}{\partial t} = 0 \tag{6.13}$$

hence, with (6.6):

$$\frac{\partial c_A}{\partial t} = \operatorname{div}(D_A \operatorname{grad} c_A) \tag{6.14}$$

if diffusivity is independent of concentration (an approximation generally valid only for dilute systems), we obtain the diffusion equation (Fick's second equation):

$$\frac{\partial c_A}{\partial t} = D_A \nabla^2 c_A \tag{6.15}$$

where $\nabla^2 = \operatorname{div} \operatorname{grad}$ is the Laplacian operator in cartesian coordinates.

The irreversibility of diffusion is clearly seen in the equation, since it is not invariant under transformation of t into $-t$.

(iv) Diffusion of momentum

The viscosity of a flowing fluid is due to the diffusional transfer of momentum per unit volume ρv (ρ is the specific mass and v, the velocity) down the momentum gradient, i.e. from regions of higher velocity to regions of lower velocity in an incompressible fluid.

The linear relation (6.2) can be written here:

$$\sigma = -v \operatorname{grad} (\rho v) \tag{6.16}$$

σ is the shear stress (force per unit area) equal to the flux of momentum (momentum transferred per unit area and second) and v is the *kinematic viscosity* expressed in m^2/s or cm^2/s.

Equation (6.16) can be written:

$$\sigma = \eta \dot{\varepsilon} \tag{6.17}$$

where $\eta = \rho v$ is the *dynamic viscosity* expressed in Pa s or poise (1 Pa s = 10 poise) and $\dot{\varepsilon} = d\varepsilon/dt = -\operatorname{grad} v$ is the shear rate (Fig. 6.1). This

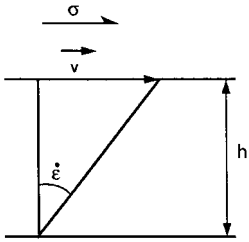

Figure 6.1 In laminar shear flow, the shear rate is given by $\dot{\varepsilon} = v/h$.

is *Newton's relation*, which often serves as a definition of the viscosity.

The corresponding diffusion equation of momentum is a simple form of the Navier–Stokes equation for an incompressible fluid:

$$\frac{\partial(\rho v)}{\partial t} = v\nabla^2(\rho v) \tag{6.18}$$

(v) Diffusion of heat

The driving force here is (see Callen, 1985):

$$\mathbf{F} = -\operatorname{grad}\left(\frac{\partial S}{\partial Q}\right) = -\operatorname{grad}\left(\frac{1}{T}\right) \tag{6.19}$$

where S is the entropy, T the temperature and Q the internal energy (heat). The linear equation given by experiment:

$$\mathbf{J} = -k \operatorname{grad} T \tag{6.20}$$

where k is the thermal conductivity, can be rewritten, as (6.2):

$$\mathbf{J} = kT^2 \operatorname{grad}\left(\frac{1}{T}\right)$$

where kT^2 is the kinetic coefficient.

The diffusion equation (conservation of heat) is *Fourier's equation*:

$$\frac{\partial T}{\partial t} = \frac{k}{\rho C_P}\nabla^2 T \tag{6.21}$$

where C_P is the specific heat at constant pressure. It can also be written:

$$\frac{\partial T}{\partial t} = \kappa\nabla^2 T \tag{6.22}$$

where $\kappa = k/\rho C_P$ is the *thermal diffusivity* , expressed in m^2/s or cm^2/s.

The solutions of the differential equation for the diffusion of heat have

been determined for a great variety of initial and boundary conditions by Carslaw and Jaeger (1959) and can, of course, be applied to the diffusion of matter.

For the sake of example, let us give here the solution of Fourier's equation in the case of a semi-infinite medium bounded by the plane $x = 0$ (extending to infinity in the direction of $x > 0$), whose initial temperature at time $t = 0$ is a constant T_0, the surface ($x = 0$) being kept at $T = 0$. The temperature T of the medium at time t and depth x is given by:

$$T = T_0 \operatorname{erf}\left[\frac{x}{2(\kappa t)^{1/2}}\right] \tag{6.23}$$

where erf is the (tabulated) error function defined by:

$$\operatorname{erf}(y) = \frac{2}{\sqrt{\pi}} \int_0^y \exp(-u^2) du \tag{6.24}$$

We see that since the temperature at a given time and depth depends only on the dimensionless parameter $x/(\kappa t)^{1/2}$, the time required for a point to reach a given temperature is proportional to the square of its distance to the surface, e.g. the time to reach $T = \frac{1}{2}T_0$ is:

$$t = \frac{1.099}{\kappa} x^2 \tag{6.25}$$

Incidentally, these are the simplified boundary conditions Kelvin used to estimate the age of the Earth (see Carslaw and Jaeger, 1959 and Burchfield, 1990). The temperature gradient, from (6.23) and (6.24), is

$$\frac{\partial T}{\partial x} = T_0 (\pi \kappa t)^{-1/2} \exp\left(-\frac{x^2}{4\kappa t}\right) \tag{6.26}$$

hence the geothermal gradient at the surface is:

$$G = \left(\frac{\partial T}{\partial x}\right)_{x=0} = T_0 (\pi \kappa t)^{-1/2} \tag{6.27}$$

Taking $T_0 = 1200\,^\circ\mathrm{C}$ (for molten rock) and a typical value of $\kappa = 0.118\,\mathrm{cm}^2/\mathrm{s}$, Kelvin found that it took about nine million years for the geothermal gradient at the surface to reach its present value taken to be equal to be $37\,^\circ\mathrm{C/km}$. Note that Kelvin did not calculate the time it would take the whole Earth to cool down to its present temperature and that, using the same numerical values and (6.25), we find that it would take more than 10^9 years to reduce by half the temperature at a depth of 200 km. It is generally thought that Kelvin found an erroneous age of the Earth because he did not take into account the production of heat by radioactivity. However, Richter (1986) showed that it would not have been enough to obtain the correct value. Indeed, as noted by Perry (1895), if Kelvin had accepted that the

coefficient of thermal conduction could increase with depth (which is in effect equivalent to assuming the existence of convection), he could have found an age of the Earth greater than four billion (4×10^9) years.

(vi) Dimensionless numbers

The diffusion coefficient D, the kinematic viscosity ν and the thermal diffusivity κ have the same dimensions and represent material properties . Dimensionless numbers characterizing a fluid can be constructed with these parameters (see e.g. Tritton, 1977). Particularly interesting are the *Prandtl number*: $\mathscr{P} = \nu/\kappa$, the *Schmidt number*: $\mathscr{S} = \nu/D$ and the *Lewis number* $\mathscr{L} = \kappa/D$.

6.2 Mechanisms of diffusion in solids

There are various definitions of diffusion coefficients, corresponding to different experimental conditions (see Bocquet *et al.*, 1983). Let us incidentally mention here that the *chemical* diffusion coefficient (a term loosely used in earth sciences) only corresponds to the interdiffusion of two different solids A and B (A into B and B into A), as seen in the laboratory reference frame (as opposed to the lattice frame). It generally depends on concentration. For simplicity, we will only consider solute diffusion coefficients at infinite dilution.

It is a fact of experience that diffusivity in solids varies with temperature according to an Arrhenius law (Fig. 6.2(a)):

$$D = D_0 \exp\left(-\frac{\Delta H}{RT}\right) \tag{6.28}$$

where ΔH is the activation enthalpy for diffusion, given by the slope of the Arrhenius plot:

$$\Delta H = -R\frac{\partial \ln D}{\partial(1/T)} \tag{6.29}$$

The activation enthalpy is a function of pressure and the pressure dependence of the diffusion coefficient is expressed by an apparent activation volume (Fig. 6.2(b); see p. 170 below):

$$\Delta H = \Delta H_0 + P\Delta V \tag{6.30}$$

$$\Delta V = -RT\frac{\partial \ln D}{\partial P} \tag{6.31}$$

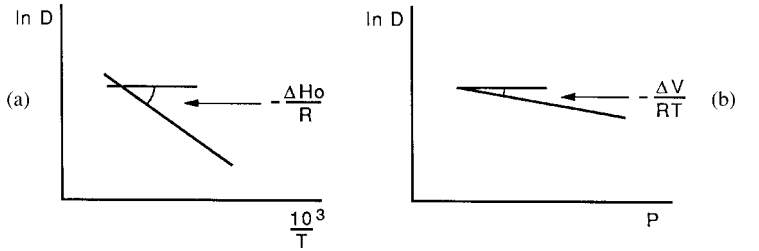

Figure 6.2 (a) Typical Arrhenius plot for diffusion. The activation enthalpy ΔH is given by the slope of the straight line. (b) Typical variation of diffusion coefficient with pressure. The activation volume is given by the slope of the straight line.

The linear expression (6.30) is of course valid only at relatively low pressures; at pressures of the lower mantle, the pressure dependence of the activation volume would have to be taken into account.

In most cases relevant to geophysics, transport of atoms is effected by exchange with vacant lattice sites or *vacancies*, that migrate through the crystal.

Let us consider the important case of *self-diffusion*, i.e. diffusion of an atom A in a crystal constituted totally or partially of atoms A (e.g. diffusion of Fe in Fe or diffusion of O in MgO).

The probability for an atom to exchange with a vacancy, i.e. to diffuse by one jump, is equal to the probability of finding a vacancy in a neighboring site multiplied by the probability of successfully jumping into it. Hence the self-diffusion coefficient is given by:

$$D_{sd} = N_v D_v \tag{6.32}$$

where N_v is the equilibrium atomic fraction of vacancies at temperature T and D_v is the diffusion coefficient of vacancies.

It can be shown (see e.g. Poirier, 1985) that the equilibrium concentration of (thermal) vacancies is:

$$N_v = \exp\left(-\frac{\Delta G_f}{RT}\right) \tag{6.33}$$

with:

$$\Delta G_f = \Delta H_f - T\Delta S_f \tag{6.34}$$

where ΔG_f, ΔH_f, ΔS_f, are the Gibbs free energy of formation, the enthalpy of formation and the entropy of formation of vacancies, respectively.

Vacancies diffuse by a random walk process described by another of

Einstein's relations (there are many Einstein's relations!):

$$\langle R^2 \rangle = \Gamma t(\delta l)^2 \tag{6.35}$$

where $\langle R^2 \rangle$ is the mean square distance covered by a vacancy during time t, Γ is the jump frequency and δl, the jump distance. The diffusion coefficient of vacancies is defined by:

$$D_v = \frac{\langle R^2 \rangle}{6t} = \frac{1}{6}\Gamma(\delta l)^2 \tag{6.36}$$

Note that the root mean square distance covered in time t by vacancies (or any particle diffusing by random walk) is proportional to the square root of time, as expected from (6.23):

$$x \propto \sqrt{Dt} \tag{6.37}$$

The jump frequency Γ is thermally activated, with an activation enthalpy equal to the activation enthalpy for migration of vacancies ΔH_m. Hence:

$$\Delta H_{sd} = \Delta H_f + \Delta H_m \tag{6.38}$$

In ionic compounds, each ionic species diffuses on its own sublattice and one can define the coefficients of self-diffusion of cations D_c and of anions D_a. In the case of binary compounds, we have:

$$D_c = D_{cv} N_{cv} \tag{6.39}$$

$$D_a = D_{av} N_{av} \tag{6.40}$$

where D_{cv} and D_{av} are the diffusion coefficients of cationic and anionic vacancies, respectively.

Cationic vacancies are negatively charged and anionic vacancies are positively charged; they are formed in electrically neutral pairs (Schottky pairs). In pure ionic crystals, at equilibrium, the product of the atomic fractions of cationic and anionic vacancies depends only on temperature:

$$N_a N_c = N_0^2 = \exp\left(\frac{\Delta S_f}{R}\right)\exp\left(-\frac{\Delta H_f}{RT}\right) \tag{6.41}$$

with, for electrical neutrality:

$$N_a = N_c$$

The activation enthalpies for diffusion of cations and anions are then:

$$\Delta H_c = \tfrac{1}{2}\Delta H_f + \Delta H_{mc} \tag{6.42}$$

$$\Delta H_a = \tfrac{1}{2}\Delta H_f + \Delta H_{ma} \tag{6.43}$$

Now, there can be, and often are, aliovalent cationic impurities in solution (e.g. Ca^{2+} replacing Na^+ ions in NaCl). If a Na^+ is replaced by a Ca^{2+}, there is an excess of positive charge that must be compensated by the creation of one negatively charged cationic vacancy. If the atomic fraction of impurities is C, electrical neutrality demands that:

$$N_a + C = N_c \tag{6.44}$$

Hence, with (6.41):

$$N_0^2 = N_a(C + N_a) \tag{6.45}$$

and:

$$N_a = \frac{C}{2}\left[\left(1 + \frac{4N_0^2}{C}\right)^{1/2} - 1\right] \tag{6.46}$$

$$N_c = \frac{C}{2}\left[\left(1 + \frac{4N_0^2}{C}\right)^{1/2} + 1\right] \tag{6.47}$$

If $C \ll N_0$, diffusion is controlled by the thermally activated formation and migration of vacancies and the activation enthalpies are given by (6.42) and (6.43). (It is the *intrinsic regime*.)

If $C \gg N_0$, the concentration of thermal vacancies is negligible compared to that of the charge-compensating vacancies fixed by the concentration of impurities:

$$N_c \cong C \tag{6.48}$$

The cationic vacancies are freely available for diffusion and no formation activation enthalpy has to be spent:

$$\Delta H_c = \Delta H_{mc} \tag{6.49}$$

Conversely, the concentration of anionic vacancies is reduced, $N_a = N_0^2/C$, thus reducing the diffusion coefficient of the anions. (It is the *extrinsic regime*.) At lower temperatures, the charge-compensating vacancies may remain associated with the aliovalent cations; the activation enthalpy for diffusion then includes the dissociation energy (equal to the binding energy) of the complex (*association regime*).

On an Arrhenius plot (Fig. 6.3), the intrinsic and extrinsic regimes are represented by straight line segments with different slopes and the transition temperature increases with impurity content:

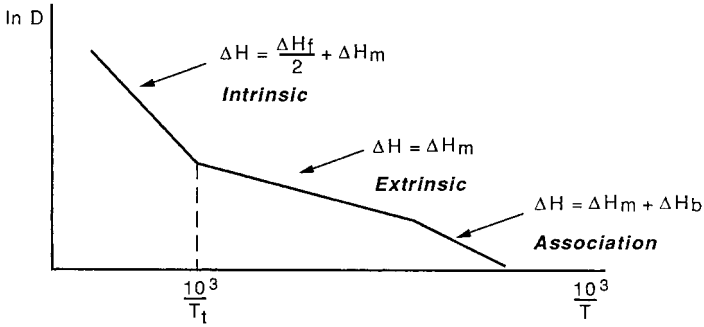

Figure 6.3 Diffusion regimes for ionic crystals: At high temperature, the concentration of vacancies is the thermal equilibrium concentration; below a temperature T_t that depends on the concentration of aliovalent impurities, the concentration of vacancies is imposed by charge balance requirements; at still lower temperatures, the charge-compensating vacancies remain associated to the impurities and have to be dissociated to participate in diffusion. ΔH_f is the formation enthalpy, ΔH_m is the migration enthalpy, and ΔH_b is the binding enthalpy of the vacancies.

$$T_t = \frac{\Delta H_f}{\Delta H_f - 2k_B \ln C} \tag{6.50}$$

In the case of compounds where a cation can take several degrees of oxidation (as often happens with transition-metal oxides and silicates), the concentration of vacancies is sensitive to the oxygen partial pressure. For instance, in a binary oxide such as magnesiowüstite (Mg, Fe)O, Fe^{2+} ions can be oxidized to Fe^{3+} and we have (Chen and Peterson, 1980):

$$\tfrac{1}{2}(O_2)_g + 2Fe^{2+} \rightarrow O^{2-} + V_M^{2'} + 2Fe^{3+} \tag{6.51}$$

$V_M^{2'}$ represents an Fe^{2+} vacancy, with effective charge $2-$; an electron hole h is associated with an Fe^{3+} ion. The law of mass action gives:

$$\frac{[V_M^{2'}][h]^{1/2}}{(p_{O_2})^{1/2}} = K \tag{6.52}$$

where K is called the reaction constant. Electrical neutrality imposes $2[V_M^{2'}] = [h]$, hence, for a diffusion controlled mechanism:

$$D_M \propto [V_M^{2'}] \propto (p_{O_2})^{1/6} \tag{6.53}$$

Nonstoichiometry, that in turn is often a function of oxygen partial pressure p_{O_2}, obviously considerably complicates the problem (see Kofstad, 1983; Dieckmann, 1984).

The transport of matter by diffusion in a compound involves transport

of all cations and anions corresponding to the formula group. The case of binary ionic crystals $A_\alpha B_\beta$ has been treated by Ruoff (1965) (see Poirier, 1985, for a summary), who defined an effective diffusion coefficient:

$$D_{\text{eff}} = \frac{D_A D_B}{n_A D_B + n_B D_A} \tag{6.54}$$

where D_A, n_A and D_B, n_B are the diffusion coefficients and atomic fractions of species A and B respectively $\left(n_A = \frac{\alpha}{\alpha+\beta}, n_B = \frac{\beta}{\alpha+\beta}\right)$. The case of multicomponent diffusion in silicates has been treated by Lasaga (1979) and by Jaoul (1990) in the case of olivine.

Some values of the pre-exponential coefficient D_0 and of the activation enthalpies for self-diffusion of silicon and oxygen in olivine and quartz are given in Table 6.1. See also Freer (1980) for a review on oxides and Freer (1981) for a review on silicates. A compilation of diffusion data for silicate minerals, glasses and liquids can be found in Brady (1995). Experimental methods of determination of the diffusion coefficients are reviewed in Ryerson (1987). For more details on the mechanisms of diffusion, the reader is referred to the book by Borg and Dienes (1988).

(i) Empirical relations

(*i*) A systematic empirical proportionality relation, the *van Liempt relation*, has been found between the activation enthalpy of self-diffusion and the melting point of metals (van Liempt, 1935; Bocquet *et al.*, 1983):

$$\Delta H_{\text{sd}} = 34\, T_{\text{m}} \tag{6.55}$$

with ΔH_{sd} in calories per mole and T_{m} in kelvin (Fig. 6.4). In other words, the activation enthalpy of self-diffusion of metals scales with their melting points, and the self-diffusion coefficient can be written:

$$D = D_0 \exp\left(-\frac{g_{\text{sd}} T_{\text{m}}}{RT}\right) \tag{6.56}$$

with $g_{\text{sd}} = 17$, hence:

$$\Delta H_{\text{sd}} = g_{\text{sd}} R T_{\text{m}} \tag{6.57}$$

The van Liempt relation does not hold for oxides and silicates: Plots of published values of activation enthalpies for the self-diffusion of oxygen or cations (Freer, 1980, 1981) against the melting temperatures of oxides or silicate minerals yield only a scattered cloud of points (Fig. 6.5 shows, for

Table 6.1. *Pre-exponential factor and activation enthalpy for the diffusion of O and Si in olivine and quartz*

System	ΔT(°C)	D_0 (cm^2/s)	ΔH (kJ/mol)	Reference
^{18}O in forsterite	1275–1625	3.5×10^{-3}	372 ± 13	Reddy *et al.* (1980)
^{18}O in forsterite	1300–1600	2.3×10^{-6}	293 ± 42	Jaoul *et al.* (1983)
^{18}O in forsterite	1472–1734	2.9×10^{-2}	416	Oishi & Ando (1984)
^{18}O in olivine	1636–2046	6.7×10^{-2}	318 ± 17	Gérard & Jaoul (1989)
^{30}Si in forsterite	1300–1700	1.5×10^{-6}	376 ± 42	Jaoul *et al.* (1981)
Si in olivine	1130–1530	1.3×10^{-8}	291 ± 15	Houlier *et al.* (1990)
Si in quartz	1400–1600	1.3×10^{6}	734 ± 96	Jaoul *et al.* (1995)

instance, all the measured activation enthalpies of ^{18}O in binary oxides). This is obviously due to the fact that diffusion in these compounds is often extremely sensitive to the impurity content, the oxygen partial pressure and the experimental temperature range; in most cases the published values are not comparable.

(*ii*) The *compensation law* or "isokinetic effect" was revived by Hart (1981) and applied to diffusion in minerals. It is an empirical linear correlation between the logarithm of the pre-exponential factor D_0 and the activation enthalpy for the diffusion of various elements in the same mineral or rock (Fig. 6.6). For olivine, for instance, Hart (1981) found (with ΔH in kcal/mol and D_0 in cm^2/s) (Fig. 6.7):

$$\Delta H = 78 + 7.5 \log D_0 \tag{6.58}$$

For silicon diffusion in silicates (quartz, olivine, diopside) Béjina and Jaoul (1997) found (with ΔH in kJ/mol and D_0 in cm^2/s) (Fig. 6.8):

$$\Delta H = 532.6 + 30.4 \log D_0 \tag{6.59}$$

This correlation implies that there exists an "isokinetic" temperature T^* for which all coefficients of diffusion are equal to D^*. Then:

$$\Delta H = RT \ln D_0 - RT^* \ln D^* \tag{6.60}$$

and, as D_0 is proportional to $\exp(\Delta S/R)$, this in fact is equivalent to having a linear relation between activation enthalpy and entropy. The compensation law, also applied to other thermally activated phenomena, like the thermal death of bacteria, has a long history of controversy (Exner, 1964; Banks *et al.*, 1972; Kemeny and Rosenberg, 1973; Boon, 1973; Harris, 1973). The case for the correlation being in most cases devoid of any

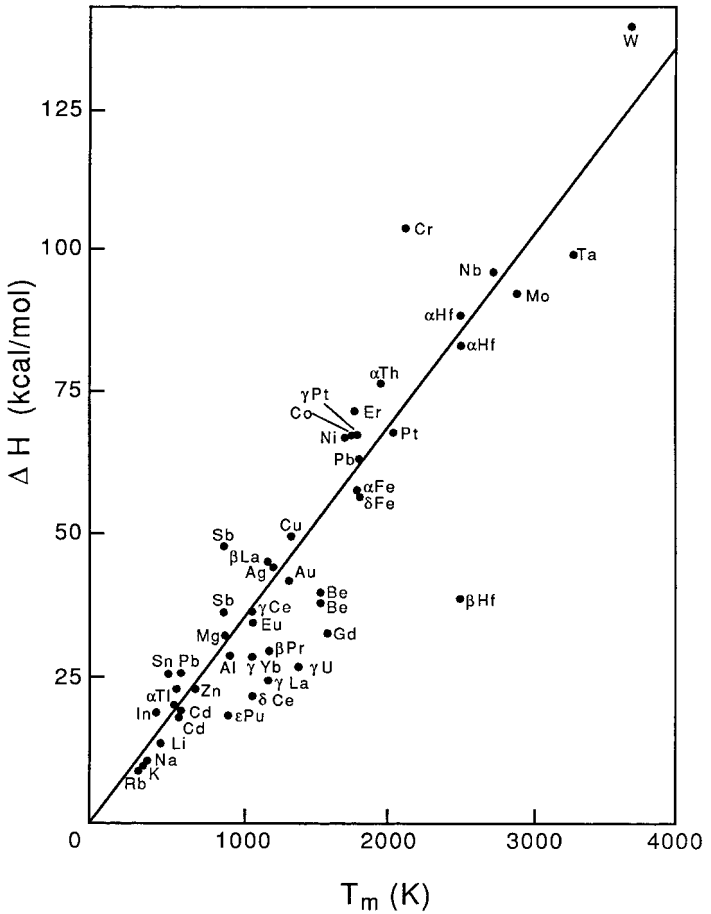

Figure 6.4 The van Liempt relation for some metals: There is a good correlation between the activation enthalpy for self-diffusion ΔH and the melting temperature T_m (after Bocquet *et al.*, 1983).

physical significance has convincingly been made (Exner, 1964; Banks *et al.*, 1972; Dosdale and Brooks, 1983; Kirchheim and Huang, 1987): It could be due to logarithmic compression in plotting $\log D$, which varies in a rather small range, since diffusion to be measurable has to be neither too rapid nor too slow. In other words, only those materials which apparently obey the compensation law are susceptible to investigation (Banks *et al.*, 1972).

Limoge and Grandjean (1996) have discussed the origin of the correlation between activation enthalpy and entropy.

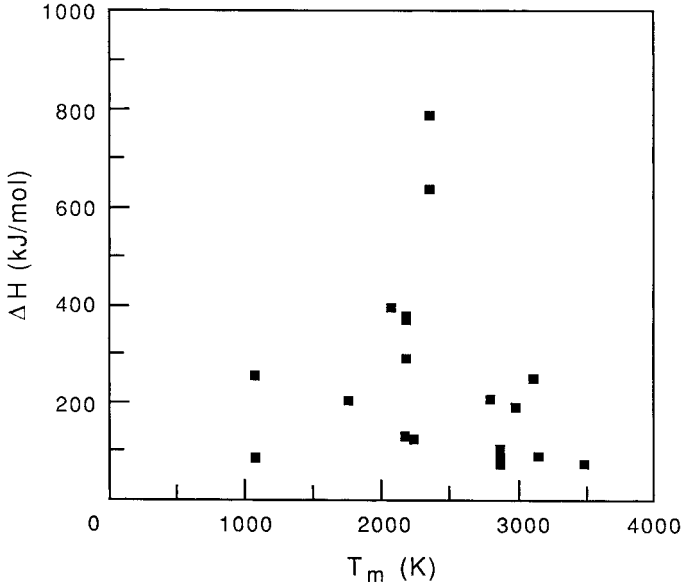

Figure 6.5 Activation enthalpy for the diffusion at high temperature of ^{18}O in binary oxides versus melting point (data from Freer, 1980). The van Liempt relation is not verified.

(ii) Effect of pressure

The pressure dependence of the diffusivity is expressed by the *activation volume*, defined as:

$$\Delta V = \frac{\partial \Delta G}{\partial P} \tag{6.61}$$

ΔG is the Gibbs free energy of the activation process; the apparent activation volume, defined by (6.31): $\Delta V' = -RT(\partial \ln D/\partial P) = (\partial \Delta H/\partial P)$, is equal to the real activation volume only if the pressure dependence of the entropic term is neglected.

As diffusion experiments under pressure are difficult to realize, it is interesting to calculate or estimate the activation volume, on theoretical grounds or from empirical relations.

Keyes (1958, 1960, 1963) proposed a semi-empirical relation:

$$\Delta V' \cong \frac{4\Delta H}{K} \tag{6.62}$$

where $\Delta V'$ is the apparent activation volume and K, the isothermal bulk

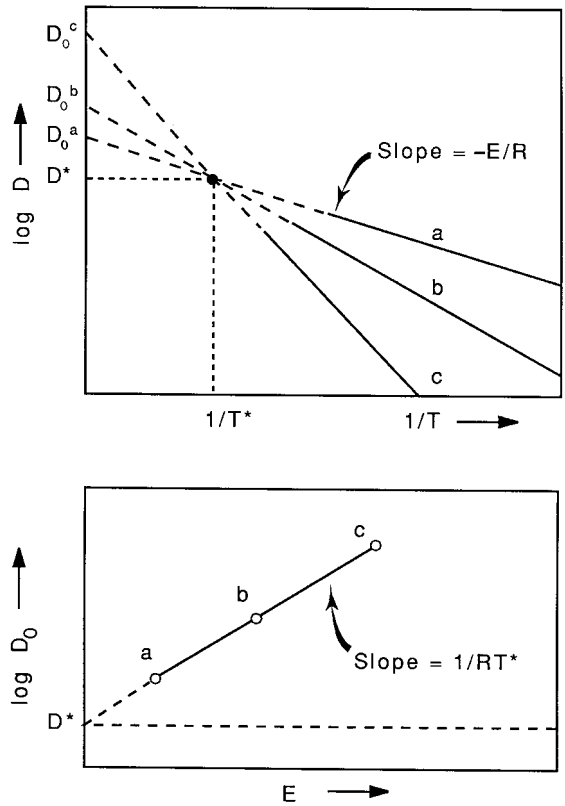

Figure 6.6 Compensation law for diffusion (after Hart, 1981).

modulus. He found it could be justified using several models of lattice defects. Assuming that the free energy of formation and migration of the defect responsible for the diffusion is essentially represented by strain energy in the crystal considered as a continuous medium, we can write:

$$\Delta G \propto \mu V \tag{6.63}$$

or:

$$\Delta G \propto K V \tag{6.64}$$

depending on whether we assume the energy is entirely due to shear or dilatation. From the definition (6.61), we can write:

$$\frac{\Delta V}{\Delta G} = \frac{\partial \ln \Delta G}{\partial P}$$

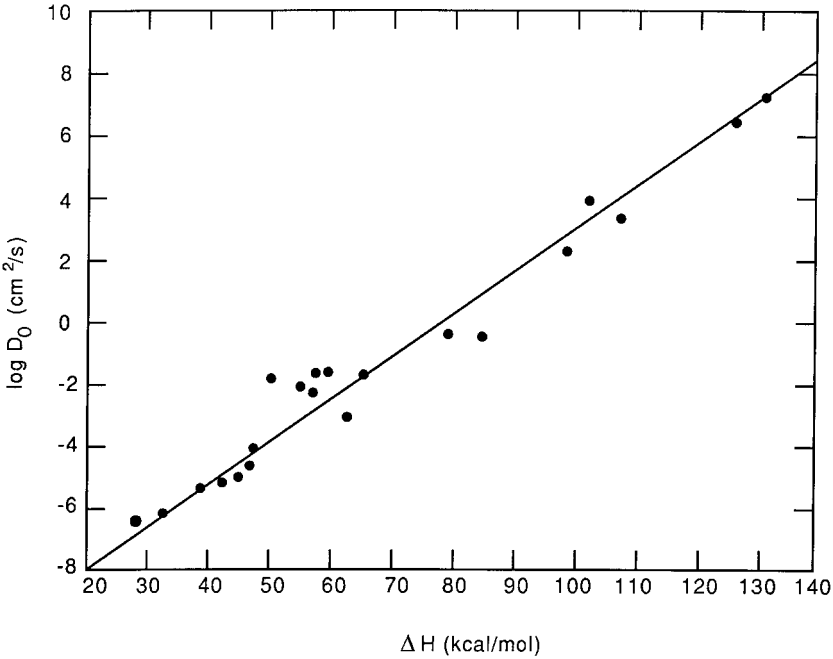

Figure 6.7 Compensation law for diffusion in a few olivines (Mg–Fe, Co, Ni, Mn) (after Hart, 1981).

If we assume that the pressure dependence of the bulk and shear moduli are equal, we can write, using Slater's relation (3.65 and 3.66):

$$\frac{\partial \ln \mu}{\partial P} = \frac{\partial \ln K}{\partial P} = \frac{2\gamma_{SI} + \frac{1}{3}}{K} \tag{6.65}$$

and, whether the energy is due to shear or dilatation:

$$\Delta V = \left[\frac{2\gamma_{SI} + \frac{1}{3}}{K} - \frac{1}{K}\right]\Delta G$$

$$\Delta V = \frac{2(\gamma_{SI} - \frac{1}{3})}{K}\Delta G \tag{6.66}$$

which is almost equivalent to (6.62) if we take $\gamma_{SI} = 1.83$, corresponding to $K' = 4$ (see Section 4.3.2) and if we assume that $\Delta G \cong \Delta H$.

Sammis *et al.* (1981) have shown that strain-energy models assuming pure shear and pure dilatation give upper and lower bounds on the activation volume.

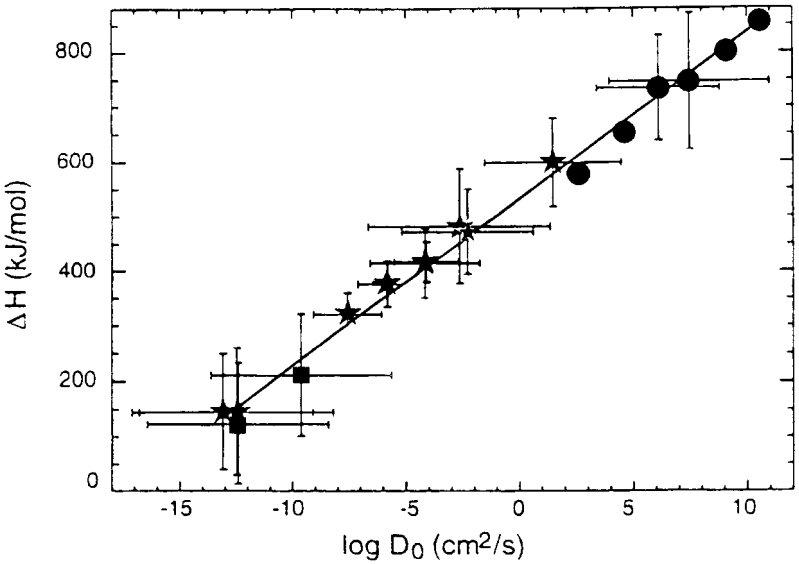

Figure 6.8 Linear relation between ΔH and $\log D_0$ for silicon diffusion in quartz (circles), forsterite (stars) and diopside (squares). The straight line is a fit to the compensation law (after Béjina and Jaoul, 1997).

Keyes (1963) also considered the case where the activation enthalpy is expressed in terms of the melting temperature (equation (6.57)): The apparent activation volume is then, using the Clausius–Clapeyron relation:

$$\Delta V' = \frac{dT_m}{T_m dP}\Delta H = \frac{\Delta V_m}{T_m \Delta S_m}\Delta H = \frac{\Delta V_m}{\Delta H_m}\Delta H \tag{6.67}$$

where T_m, ΔV_m and ΔS_m are the melting temperature, volume and entropy respectively. The relation can also be written:

$$\Delta V' = \frac{d\ln T_m}{dP}\Delta H = \frac{d\ln T_m}{d\ln \rho}\frac{1}{K}\Delta H$$

and, using the differential Lindemann law (5.26), we obtain (Poirier and Liebermann, 1984):

$$\Delta V' = \frac{2(\gamma_{SI} - \frac{1}{3})}{K}\Delta H \tag{6.68}$$

equivalent to (6.66) if $\Delta V' \cong \Delta V$.

At high pressures, the assumption that the activation volume is constant does not hold any longer. The pressure dependence of the activation

volume has been calculated, using various assumptions, by O'Connell (1977), Karato (1981b), Sammis *et al.* (1981). It can be expressed as a dimensionless parameter (Poirier and Liebermann, 1984):

Differentiating (6.66) and using (6.61), we obtain:

$$\frac{\partial \ln \Delta V}{\partial P} = \frac{\partial \ln[2(\gamma_{SI} - \frac{1}{3})K^{-1}]}{\partial P} + \frac{\Delta V}{\Delta G}$$

and:

$$\frac{\partial \ln \Delta V}{\partial P} = \frac{\partial \ln[2(\gamma_{SI} - \frac{1}{3})K^{-1}]}{\partial P} + \frac{2(\gamma_{SI} - \frac{1}{3})}{K} \tag{6.69}$$

which, with (6.65) gives:

$$\frac{\partial \ln \Delta V}{\partial P} = \frac{1}{K} + \frac{1}{\gamma_{SI} - \frac{1}{3}} \frac{\partial \gamma_{SI}}{\partial P} \tag{6.70}$$

Assuming $\gamma\rho = \text{const}$ (3.85), one obtains:

$$\frac{\partial \ln \Delta V}{\partial \ln \rho} = -1 + \gamma_{SI}(\gamma_{SI} - \tfrac{1}{3})^{-1} \tag{6.71}$$

Experimental and calculated values of activation volumes for self-diffusion can be found in Sammis *et al.* (1981).

6.3 Viscosity of solids

The viscosity of solids is defined, as for fluids, by (6.17), rewritten here:

$$\eta = \frac{\sigma}{\dot{\varepsilon}} \tag{6.72}$$

where σ is the applied shear stress and $\dot{\varepsilon}$ ($\equiv d\varepsilon/dt$) is the shear strain rate (see Fig. 6.1). The definition of viscosity as a material constant has a meaning only if it does not depend on time, i.e. if the shear strain rate is constant. This is the case for *high-temperature creep* under constant stress, in the quasi-steady state regime. The problem of the viscosity of solids is therefore that of the high-temperature creep of crystals. A summary overview of the principal physical mechanisms of creep is given in what follows and, for further information, the reader is referred to the monograph by Poirier (1985) (see also Poirier, 1995). If the viscosity depends only on the structural properties of the material and on temperature, it is said to be *Newtonian*: the creep rate $\dot{\varepsilon}$ then depends linearly on stress. In many cases,

however, the creep rate is an increasing non-linear function of stress, usually fitted by a power law: $\dot{\varepsilon} \propto \sigma^n$, with $3 \leq n \leq 5$ for most solids ("*power-law creep*").

Creep of solids is a thermally activated phenomenon, with an activation energy ΔH, and the creep rate can be put into the Arrhenian form:

$$\dot{\varepsilon} = \dot{\varepsilon}_0 \sigma^n \exp\left(-\frac{\Delta H}{RT}\right) \tag{6.73}$$

To define the viscosity in the non-Newtonian case, one must therefore specify either the stress or the strain rate (see e.g. Poirier, 1988b).

The viscosity at constant stress is given by:

$$\eta_\sigma \equiv \frac{\sigma}{\dot{\varepsilon}(\sigma)} = \dot{\varepsilon}_0^{-1/n} \sigma^{1-n} \exp\left(\frac{\Delta H}{RT}\right) \tag{6.74}$$

and the viscosity at constant strain rate by:

$$\eta_{\dot{\varepsilon}} \equiv \frac{\sigma(\dot{\varepsilon})}{\dot{\varepsilon}} = \dot{\varepsilon}_0^{-1/n} \sigma^{(1-n)/n} \exp\left(\frac{\Delta H}{RT}\right) \tag{6.75}$$

It is also interesting to consider the viscosity at constant dissipated power ($\sigma\dot{\varepsilon} = \text{const}$):

$$\eta_{\sigma\dot{\varepsilon}} \equiv (\eta_\sigma \eta_{\dot{\varepsilon}}^n)^{1/(1+n)} = \dot{\varepsilon}_0^{-2(n+1)} \sigma^{(1-n)/(1+n)} \exp\left(\frac{2\Delta H}{(n+1)RT}\right) \tag{6.76}$$

Note that the apparent activation energies (i.e. the sensitivity to temperature) of the viscosity at constant strain rate or dissipated power are smaller than that at constant stress unless, of course, $n = 1$ in which case all three viscosities are equal.

Creep deformation is due to a transport of matter by motion of lattice defects. If the defects are vacancies, creep, then, directly results from the directed diffusion of matter and vacancies in opposite directions, and it is Newtonian. If the defects are dislocations, creep is non-Newtonian and can be controlled either by diffusion-controlled climb or by glide of dislocations (see below).

(i) Diffusion creep

Diffusion creep, or *Nabarro–Herring creep*, is due to transport of matter by self-diffusion through the grains of a polycrystal.

Let us consider a crystal of size d in the shape of a cube (for the sake of

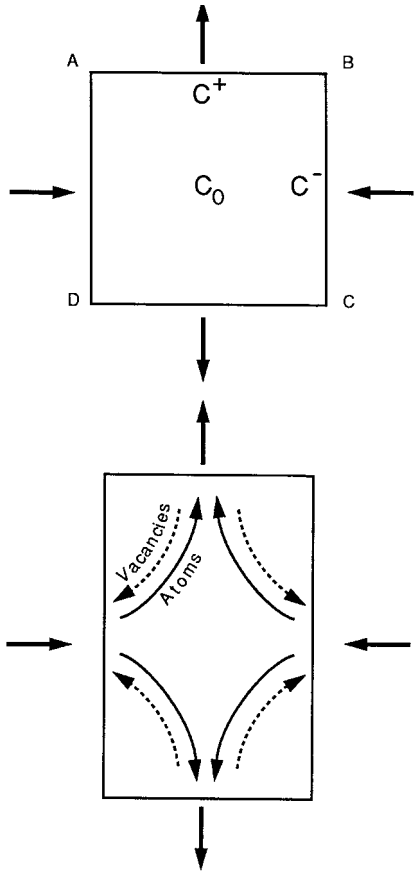

Figure 6.9 Principle of Nabarro–Herring creep. Vacancies flow from the faces in tension (concentration C^+) to the faces in compression (concentration $C^- < C^+$) and matter flow in the opposite direction.

simplicity), subjected to a normal tensile stress on a pair of faces and to normal compressive stresses on the four other faces (Fig. 6.9). The compressive normal stress hinders the formation of vacancies (to form vacancies, atoms are extracted from inside the crystal and deposited on the surface, which involves work against the stress), while the tensile stress facilitates it. The formation energy of vacancies is therefore increased by $\sigma V/k_B T$ at the faces in compression and decreased by the same amount at the faces in tension (V is the atomic volume) and the equilibrium concentrations of vacancies at the faces in compression and tension are respectively:

$$C^- = C_0 \exp\left(-\frac{\sigma V}{RT}\right) \tag{6.77}$$

$$C^+ = C_0 \exp\left(\frac{\sigma V}{RT}\right) \tag{6.78}$$

There is a flow of vacancies from the faces in tension to the faces in compression and a flow of atoms in the opposite direction. The flux of atoms is given by Fick's law:

$$\mathbf{J} = -D_v \operatorname{grad} C = -\frac{\alpha D_v (C^+ - C^-)}{d} \tag{6.79}$$

where D_v is the diffusion coefficient of vacancies and α is a geometrical constant. In unit time, a number Jd^2 of atoms leave the faces in compression and are added to the faces in tension; the crystal shortens by Δd and widens by the same quantity. We have:

$$\Delta d = \frac{Jd^2 V}{d^2} = JV$$

hence:

$$\dot{\varepsilon} = \frac{\Delta d}{d} = \frac{JV}{d} \tag{6.80}$$

With (6.77) , (6.78) and (6.79), we obtain:

$$\dot{\varepsilon} = \frac{\alpha D_v C_0 V}{d^2} \sinh\left(\frac{\sigma V}{RT}\right) \tag{6.81}$$

or, remembering that $D_v C_0 V = D_v N_v = D_{sd}$, the coefficient of self-diffusion, we obtain, for $\sigma V \ll RT$:

$$\dot{\varepsilon} = \frac{\alpha D_{sd} \sigma V}{d^2 RT} \tag{6.82}$$

The activation energy for viscosity is therefore obviously equal to the activation energy of self-diffusion.

(ii) Dislocation creep

Dislocations (Fig. 6.10) are line defects bounding an area within the crystal where slip by an interatomic distance b has taken place , i.e. the crystal on one side of the slip plane has been rigidly displaced by b with respect to the other side (see Friedel, 1964 and, for a short summary, Poirier, 1985). Dislocations move under an applied stress, extending the slipped area. When a dislocation loop sweeps a whole crystal plane and moves out of the

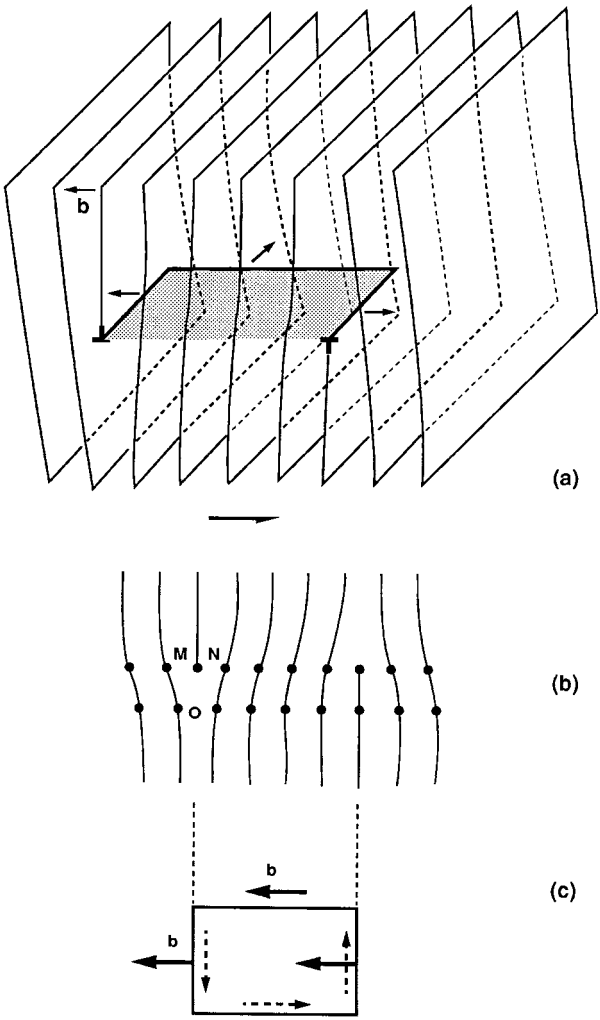

Figure 6.10 (a) Dislocation loop in a crystal represented as a stack of lattice planes (the front half is removed for clarity). The slipped area inside the dislocation is stippled. The extra half-plane above the edge portion (left) is seen to wind itself in helicoidal fashion around the screw portion (back) until it ends up as the extra half-plane below the other edge portion (right). Each turn of the screw corresponds to a displacement by the Burgers vector **b**, parallel to the screw portion and normal to the edge portions. (b) Front view of the half loop. Flipping the bond OM to ON makes the edge portion propagate toward the left. (c) Top view of the whole loop oriented continuously (dashed arrows); opposite-sign extra half-planes correspond to Burgers vectors of edge portions that would point in the opposite direction if the dislocation segments were oriented in the same direction.

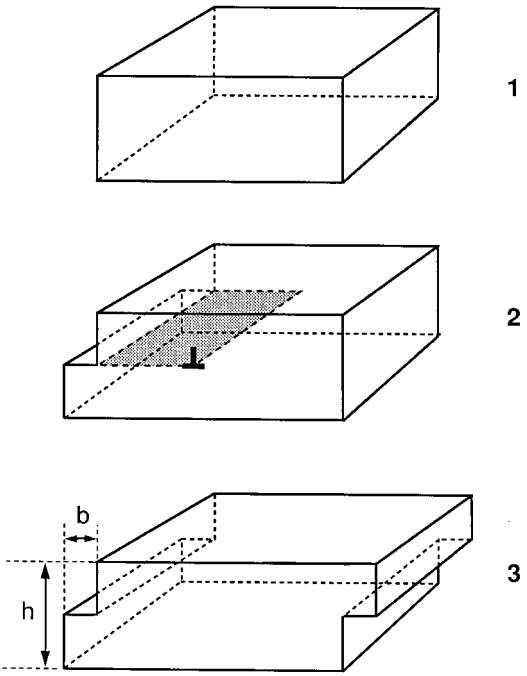

Figure 6.11 Slip by dislocation motion. (1) Undeformed crystal. (2) A dislocation line has been created at left and moved inside the crystal, causing a slip by b behind it (stippled area). (3) The dislocation has swept the whole length of the crystal and left a step of height b at the surface. The shear strain is $\varepsilon = b/h$.

crystal, it leaves at the surface a step of height b. The crystal has acquired a permanent shear deformation equal to b/h, where h is the dimension of the crystal normal to the slip plane (Fig. 6.11). The motion of dislocations by progressive breaking and re-establishment of atomic bonds is the energetically economic way of deforming crystals. Dislocations are carriers of plastic deformation in solids.

For a mobile dislocation density ρ (total length of dislocation lines per unit volume) moving an average distance ΔL, the shear strain is:

$$\varepsilon = \rho b \Delta L \tag{6.83}$$

and, for constant dislocation density, the creep rate is:

$$\dot{\varepsilon} = \rho b \bar{v} \tag{6.84}$$

where $\bar{v}$ is the average dislocation velocity. This is *Orowan's equation*, which can be seen as a transport equation, giving the creep rate as the product of the density of strain carriers (the dislocations), their strength (the *Burgers*

vector b, characteristic of the dislocation and equal to the elementary slip by an interatomic distance) and their velocity. The equation is analogous to the microscopic Ohm's law (see below). The dependence of the viscosity on stress and temperature is found by expressing the dependence of dislocation density and velocity.

For steady-state creep, the dislocation density is generally proportional to σ^2 (see Poirier, 1985) and depends little on temperature. The average dislocation velocity depends, of course, on σ and is controlled by the nature and distribution of obstacles to the motion of dislocation lines in the crystal. Two cases are especially interesting:

(a) The principal obstacle to the dislocation motion lies in the intrinsic difficulty in breaking the atomic bonds, the so-called "lattice friction". The material is said to have a high *Peierls stress* and the dislocation lines tend to be straight, lying in potential valleys. The lattice friction can be overcome with the help of thermal vibrations and of the effective stress (applied stress minus internal stress). The motion is directly thermally activated and the activation enthalpy is stress dependent, decreasing with increasing stress. The creep rate can be written:

$$\dot{\varepsilon} = \dot{\varepsilon}_0 \sigma^2 \exp\left(-\frac{\Delta H(\sigma)}{RT} \right) \tag{6.85}$$

The viscosity is said to be *glide-controlled*.

(b) If the obstacles are discrete, with an average spacing ΔL, the average velocity can be written in general:

$$\bar{v} = \frac{\Delta L}{t_g + t_0} \tag{6.86}$$

where t_g is the average time the dislocation takes in gliding over the distance ΔL between obstacles and t_0 is the average time it takes in overcoming the obstacles. If $t_g \ll t_0$, the average velocity is $\bar{v} = \Delta L / t_0$. Edge dislocations can overcome obstacles to glide by moving out of their glide plane by diffusion-controlled climb (Fig. 6.12) (*Weertman creep*). If δ is the distance a dislocation has to climb to escape the obstacle and v_c is the climb velocity, we have:

$$\dot{\varepsilon} = \rho b \Delta L v_c \delta^{-1} \tag{6.87}$$

It can be shown (Friedel, 1964) that v_c is proportional to the self-diffusion coefficient D_{sd} and, in the linear approximation, to the applied

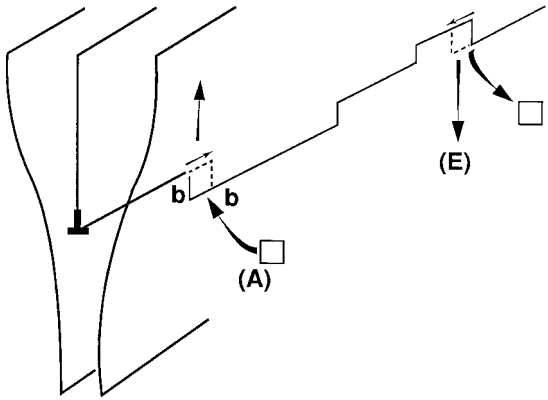

Figure 6.12 Climb of an edge dislocation. The dislocation climbs by an interatomic distance when a jog travels down its length by absorbing (A) or emitting (E) vacancies.

stress σ. Remembering that $\rho \propto \sigma^2$, we then obtain the general equation for diffusion-controlled creep:

$$\dot{\varepsilon} = \dot{\varepsilon}_0 \sigma^3 \exp\left(-\frac{\Delta H_{sd}}{RT}\right) \tag{6.88}$$

We have here a physical justification for power-law creep with $n = 3$, but the experimental values usually range between 3 and 5. Diffusion-controlled power-law creep is often observed at high temperatures in metals and minerals, although some caution is in order before issuing general pronouncements (Poirier, 1978). It is currently thought to be responsible for the viscosity of the Earth's mantle (Weertman, 1970, 1978; Poirier, 1988b). The viscosity profile of the mantle then depends on the temperature profile and on the pressure dependence of the creep rate.

In the case of diffusion-controlled creep of minerals containing iron, which can take several degrees of oxidation, the creep rate depends on oxygen partial pressure, and also on the activity of the components. Creep experiments on olivine buffered against orthopyroxene or magnesiowüstite, under various conditions of temperature, pressure and oxygen partial pressure, yield very different activation energies and oxygen partial pressure dependence (Bai *et al.*, 1991). Several creep laws are needed to account for the results, which makes extrapolation to mantle conditions difficult.

(iii) Effect of pressure

As for diffusion, the pressure dependence is expressed by an apparent activation volume:

$$\Delta V' = RT\frac{\partial \ln \eta}{\partial P} = \frac{\partial \Delta H_v}{\partial P} \tag{6.89}$$

which should, in principle, be equal to the activation volume for self-diffusion of the atomic species whose diffusion controls the creep rate. There is, however, some debate as to which species controls the creep rate, even in well-investigated minerals such as olivine (e.g. Jaoul *et al.*, 1981) and, anyway, there are very few experimental determinations of the activation volumes (Béjina *et al.*, 1997, find an activation volume close to zero for the diffusion of silicon in olivine). One must therefore resort to systematics.

Weertman (1970) applied van Liempt's relation (6.57) to the creep of metals and ice and implicitly extended it to the creep of all substances, including the minerals of the Earth's lower mantle. Weertman's relation:

$$\Delta H_v = g_v R T_m \tag{6.90}$$

where ΔH_v is the activation enthalpy for viscosity (or creep rate) and T_m is the melting temperature, is valid for metals with a value of the constant g_v close to 18. For compounds, however, things are obviously not so simple since the creep mechanisms are not always clear and, even if creep is diffusion-controlled, van Liempt's relation does not hold. Besides, the published values of activation enthalpies for creep of ceramics (Cannon and Lang-don, 1983) correspond to widely differing experimental conditions, purity of materials, grain size, oxygen partial pressure, etc. Even if the data are carefully selected, a plot of the activation energy against melting temperature for various materials exhibits a considerable scatter (Fig. 6.13 shows, for instance, the data corresponding to compression creep of single crystals of oxides and alkali halides). By grouping the compounds according to their structure, it is, however, possible to improve the systematics (Frost and Ashby, 1982) (Fig.6.14). Nevertheless, there is little hope of ever obtaining a systematics good enough to usefully predict the activation enthalpy of a compound from a knowledge of its melting temperature because the scatter on g_v remains much too large. We find, for instance, that, from the data of Fig. 6.13, we have $g_v = 27 \pm 8$ for oxides (in agreement with Frost and Ashby, 1982) but, as g_v appears in an exponential, this corresponds to an uncertainty of three orders of magnitude on the viscosity! Weertman's relation, however, remains useful for the purpose orig-

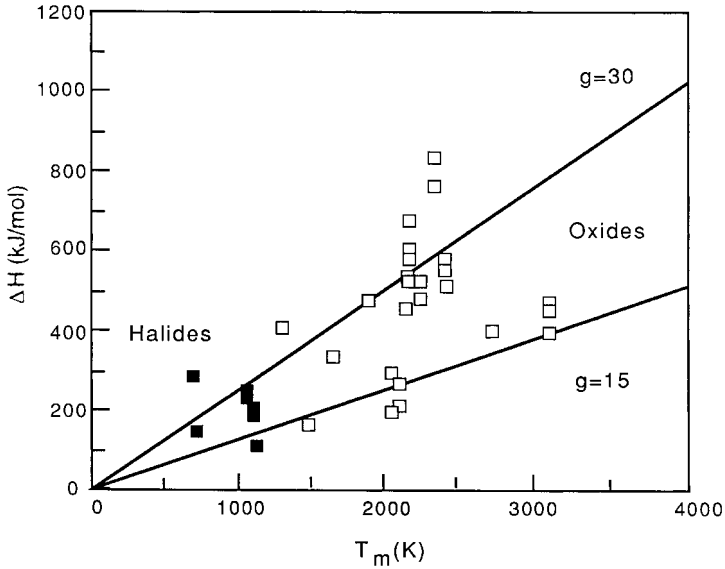

Figure 6.13 Activation enthalpy for creep versus melting point for oxides and alkali halides (data from Cannon and Langdon, 1983). Straight lines are drawn for $g_v = 15$ and $g_v = 30$.

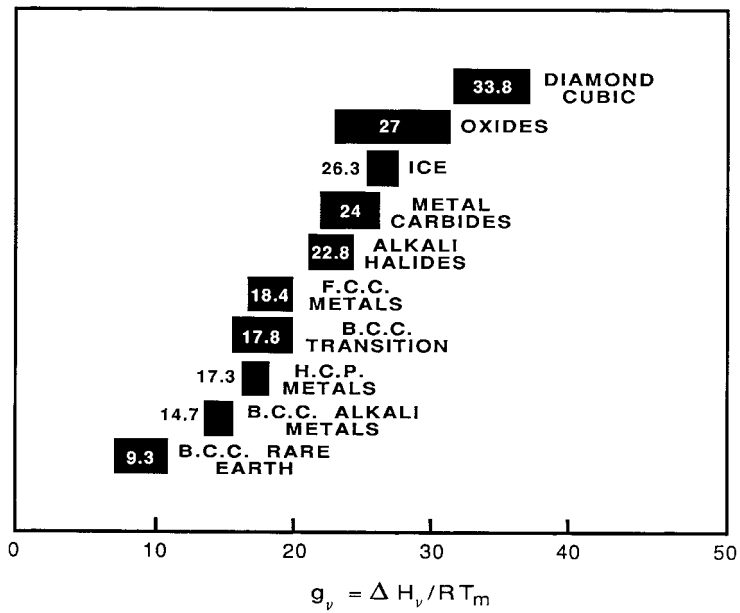

Figure 6.14 The ranges of the dimensionless quantity $g_v = \Delta H_v/RT_m$ for classes of solids (after Frost and Ashby, 1982).

inally assigned to it by Weertman (1970), i.e. to extrapolate the viscosity to high pressures, if the melting curve is known or inferred, but the value of g_v must be the one experimentally determined for the specific compound one is interested in.

The activation volume for diffusion-controlled creep of solids (and the Earth's mantle) has been estimated by several authors (e.g. Sammis *et al.*, 1981; Karato, 1981b; Ellsworth *et al.*, 1985), using either Weertman's relation (6.90), i.e. assuming that the pressure dependence of viscosity is equal to that of the melting point, or Keyes' formulation with an elastic strain model for the Gibbs free energy of activation. Poirier and Liebermann (1984) discussed these formulations and showed that they were equivalent within the limits of validity of Slater's relation and Lindemann's law. The discussion has already been presented for diffusion in Section 6.2.

6.4 Diffusion and viscosity in liquid metals

The Earth's outer core (16% of the Earth's volume) is constituted of liquid iron. Its diffusional and viscous transport properties must be placed in the wider framework of liquid metals which, being simple unassociated liquids, have been experimentally and theoretically well investigated. The reader is referred to the book by Shimoji and Itami (1986) for a complete review of the field (see also Battezzati and Greer, 1989).

There is an intimate connection in liquids between the self-diffusion coefficient and the viscosity η. It is expressed by the *Stokes–Einstein relation*:

$$D\eta = \frac{k_B T}{2\pi a} \tag{6.91}$$

where a is an atomic-size parameter. The Stokes–Einstein relation has been experimentally verified for liquid metals (Saxton and Sherby, 1962) and can be theoretically justified (e.g. Zwanzig, 1983).

Eyring (1936) considered a liquid as a collection of molecules bound to their neighbors and "dissolved holes" (similar to vacancies in solids). Transport, either by diffusion or under the action of a shear stress (viscosity), was thought to occur by thermally activated jumps of the molecules into the holes. The diffusion coefficient then can be written, as for solids (see 6.36):

$$D = \lambda^2 k' \tag{6.92}$$

where λ is the jump distance, comparable to the average interatomic

spacing, and k' is the absolute reaction rate of the diffusion process. Eyring therefore finds an expression of the diffusion coefficient that follows an Arrhenius law, like the coefficient of diffusion of crystals:

$$D = D_0 \exp\left(-\frac{Q}{RT}\right) \tag{6.93}$$

where Q is the activation energy corresponding to the potential barrier that the molecule must overcome to jump into the hole.

To calculate the viscosity, Eyring assumed that the motion takes place by individual molecules slipping by a distance λ over the potential barrier with a reaction rate k'. The viscosity is given by (6.17) with $\dot{\varepsilon} = \lambda_1/\Delta v$, where Δv is the difference in velocity of two neighboring parallel layers, which are a distance λ_1 apart. The force acting on a molecule is $\sigma\lambda_2\lambda_3$, where λ_2 and λ_3 are the distances between molecules in the parallel planes in the direction of motion and perpendicular to it respectively. The force acts to lessen the work for overcoming the barrier in the forward direction and raises it in the backward direction, so the velocity difference can be written:

$$\Delta v = \lambda k' \left[\exp\left(\frac{\sigma\lambda_2\lambda_3\lambda}{2k_B T}\right) - \exp\left(-\frac{\sigma\lambda_2\lambda_3\lambda}{2k_B T}\right)\right] \tag{6.94}$$

Now, for $\sigma\lambda_2\lambda_3\lambda \ll 2k_B T$, we have:

$$\eta = \frac{\lambda_1 k_B T}{\lambda_2\lambda_3\lambda^2 k'} \tag{6.95}$$

With (6.92) and (6.95), we see that Eyring's theory yields the Stokes–Einstein relation:

$$D\eta = \frac{\lambda_1}{\lambda_2\lambda_3} k_B T \tag{6.96}$$

The "free volume" theory of diffusion of Cohen and Turnbull (1951) assumes that atoms are enclosed in cages formed by their neighbors and can jump only when statistical fluctuations of the free volume V_f (total volume minus the volume occupied by the atoms) create a hole of volume V^* sufficient to accept an atom. The diffusion coefficient is:

$$D \propto (k_B T)^{1/2} \exp\left(-\frac{\gamma V^*}{V_f}\right) \tag{6.97}$$

where $0 < \gamma < 1$ is a numerical constant and $V_f \propto \alpha(T - T_0)$, where α is the coefficient of thermal expansion.

Swalin (1959) starts from Einstein's equation (6.36) but, instead of considering atoms jumping by a fixed distance into holes of a critical size, he assumes that local density fluctuations cause atoms to move small variable distances and finds for the diffusion coefficient of liquid metals:

$$D = (1.29 \times 10^{-8}) \frac{\beta^{-2} T^2}{\Delta H_v} \tag{6.98}$$

where β (in Å^{-1}) is related to the curvature of the potential-vs-distance curve and ΔH_v is the heat of vaporization. In this model, there is a distribution of fluctuation sizes and most atoms participate in the diffusion process at a given moment. The process has no activation energy; however, a plot of $\ln D$ vs $1/T$ yields an apparent "activation energy" equal to $2RT$, devoid of physical meaning.

Indeed, the assumption that there are identifiable holes and that there is a localized energy barrier to diffusion, inherent to Eyring's "activated state" model and its variants, is not easily tenable in liquids.

Nachtrieb (1967, 1977) found that the experimental results were best fitted by a linear relation between D and T, based on the assumption that each atom vibrates in the cage of its neighbors with a harmonic motion and that with each oscillation, the center of oscillation moves by a distance equal to the mean thermal amplitude:

$$D = \frac{k_B \Theta_D}{h\kappa} T \tag{6.99}$$

where Θ_D is the Debye temperature, h is Planck's constant and κ the force constant of the harmonic vibrations. In a sense, the entire liquid is in an activated state and the concept of activation energy has no meaning. However, and despite the fact that there is no convincing theoretical justification for it, the temperature dependence of the diffusion coefficient is still currently displayed on Arrhenius plots and "activation energies" are determined, even by those who object to it (Nachtrieb, 1967; Shimoji and Itami, 1986). Indeed, the fit of the data by an Arrhenius law is in most cases reasonably good and "activation energies" provide a convenient means of systematizing the data.

The "activation energies" for self-diffusion and heterodiffusion in liquid metals are, not surprisingly, much smaller than in the corresponding solids. As an example, average values for the heterodiffusion of H, C, N, O, S in α-,

Table 6.2. *Apparent activation energies for diffusion of various elements in α-, γ-, and liquid iron*

Diffusing element	$\bar{Q}_\alpha$ (kJ/mol)	$\bar{Q}_\gamma$ (kJ/mol)	$\bar{Q}_{\text{liq}}$ (kJ/mol)
Hydrogen	12.5	47.2	15.5
Carbon	81.3	134.4	49
Nitrogen	76.8	152.2	50.2
Oxygen	96.3	168.5	50.2 ± 8.4
Sulfur	207.2	222.4	35.6

Source: Bester and Lange (1972).

γ- and liquid iron, from Bester and Lange (1972) are given in Table 6.2.

As for diffusion, Eyring's (1936) activated state theory of viscosity is among the very few that predict an Arrhenian temperature dependence (see Brush, 1962 and Shimoji and Itami, 1986, for a review).

Andrade (1934, 1952) proposed a theory of the viscosity of unassociated liquids at their melting points, based on the idea that their structure is close to that of the solid and that their viscosity is due to the transfer of momentum by collision between parallel layers of atoms through the amplitude of thermal vibration. Andrade found an expression of the viscosity in terms of the mass m of atoms, the mean interatomic spacing a and the Lindemann vibrational frequency ω_L (equation (5.19)):

$$\eta = \frac{2m\omega_L}{3\pi a} \tag{6.100}$$

or, in c.g.s. units:

$$\eta = (5.7 \times 10^{-4})(AT_m)^{1/2} V^{-2/3} \tag{6.101}$$

where A and V are the atomic mass and volume respectively. Viscosity is thought to decrease with increasing temperature because thermal agitation interferes with the transfer of momentum at maximum amplitude. The variation of viscosity with temperature is then governed, according to Andrade (1934), by the fraction of atoms possessing the mutual potential energy at extreme amplitude, which varies according to the Boltzmann distribution formula, hence:

$$\eta \propto \exp\left(\frac{C}{T}\right) \tag{6.102}$$

where C has the dimensions of an energy. Although it is not an activation

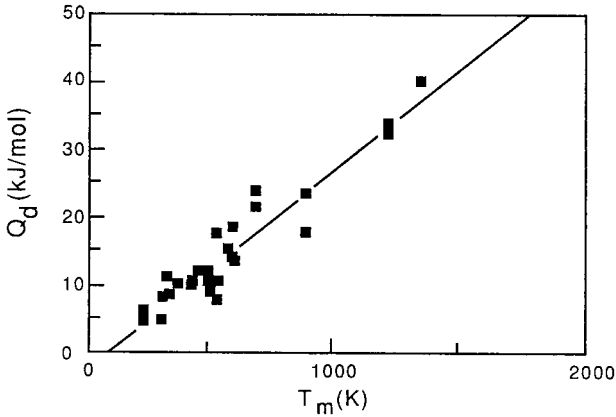

Figure 6.15 Correlation between the melting point and apparent activation energy for self-diffusion of liquid metals (after Poirier, 1988a).

energy, it can be treated like an apparent "activation energy" for systematization purposes.

(i) Empirical relations and effect of pressure

As for diffusion and viscosity in solids, there are systematic empirical relations between the apparent "activation energy" of diffusion and viscosity in liquid metals similar to (6.57) and (6.90), but the values of the constants g_d and g_v are much smaller (Saxton and Sherby, 1962; Grosse, 1963; Poirier, 1988a). This is to be expected since the activation energy for diffusion (and diffusion-controlled creep) of solids consists mostly of the formation energy of point defects, whereas in liquids the apparent "activation energy" reflects only the temperature dependence of the mobility of atoms which does not necessitate the creation of localized defects.

Poirier (1988a) found for a number of liquid metals:

$$Q_d = 3.2RT_m \tag{6.103}$$

for diffusion (Fig. 6.15) and:

$$Q_v = 2.6RT_m \tag{6.104}$$

for viscosity (Fig. 6.16). The value of $g_d \cong 3$ is in good agreement with that obtained by Saxton and Sherby (1962) and by Nachtrieb (1967), whose model for diffusion rests on the idea that the average energy of atoms vibrating in the cage of their neighbors is equal to $3RT$.

The extrapolation to high pressures of the viscosity of liquid metals (especially interesting for iron in the Earth's core) stands on a somewhat

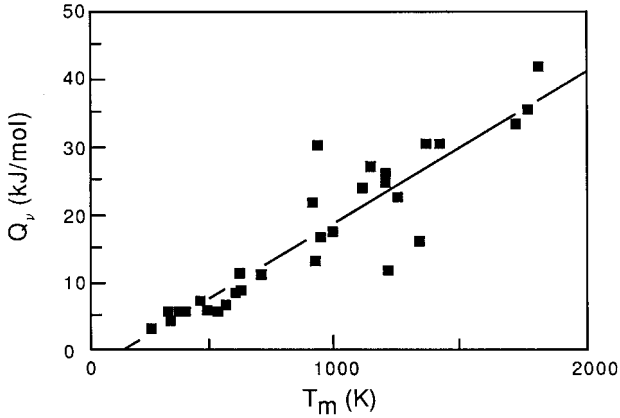

Figure 6.16 Correlation between the melting point and apparent activation energy for viscosity of liquid metals (after Poirier, 1988a).

safer ground than in the case of solids, despite the lack of theoretical justification for (6.104), because of the lesser scatter in the value of the constant (close to 3). There is an excellent agreement between the apparent "activation volume" of the viscosity of mercury, calculated from the experimental results of Bridgman, using (6.89) ($\Delta V' = 0.62\,\mathrm{cm}^3/\mathrm{mol}$) and the empirical value, calculated from (6.104) and the slope of the melting curve ($\Delta V' = 0.59\,\mathrm{cm}^3/\mathrm{mol}$).

It is interesting to consider the vicosity of a liquid metal right at its melting point ($T = T_\mathrm{m}$). Since we have:

$$\eta \propto \exp\left(\frac{g_\nu T_\mathrm{m}}{T}\right) \tag{6.105}$$

we immediately see that the viscosity stays constant along the melting curve and is equal to the viscosity at atmospheric pressure. The viscosity of liquid iron at the inner core boundary should then be equal to 6 centipoise (Poirier, 1988a). *Ab-initio* electronic structure calculations, based on density functional theory, yield a diffusion coefficient of liquid iron, at $T = 6000\,\mathrm{K}$, of $D \approx 0.4\text{–}0.5 \times 10^{-4}\,\mathrm{cm}^2/\mathrm{s}$, which, with the Stokes–Einstein relation (6.91), and $a = 1\,\text{Å}$, yields a viscosity of about 15 centipoise (de Wijs *et al.*, 1998).

6.5 Electrical conduction

6.5.1 Generalities on the electronic structure of solids

The theory of the electronic structure of solids is the corner stone of

solid-state physics and it is obviously beyond the scope of this book even to give a summary overview of it. However, since transport of electronic charges is what electrical conduction is all about, it is impossible to avoid giving some indispensable background, mostly at the hand-waving level. For an elementary or intermediate treatment, the reader is referred to Kittel (1967), Ziman (1965), Honig (1970) or Animalu (1977). An essential concept in solid-state theory is that of electronic *energy bands*, separated by *band gaps*.

Energy bands are ranges of allowed energy states for the electrons, the gaps corresponding to forbidden states for which the Schrödinger equation has no acceptable solution. They arise because of the existence of a periodic lattice potential: Electron wave functions represent running waves carrying momentum $\mathbf{p} = \hbar\mathbf{k}$ ($\mathbf{k}$ is the wave number). At the boundaries of the Brillouin zones the waves cannot propagate and two standing waves are formed with energies differing by E_g the gap energy (Fig. 6.17).

It is also convenient to envision the formation of bands as due to the spreading of atomic energy levels (orbitals) when the many atoms constituting the crystal are brought together and the atomic orbitals overlap (Fig. 6.18). The degree of overlap also characterizes the type of atomic bonding.

- For ionic bonding, the electrons are transferred from one atomic species to the other, forming ions with an inert gas electronic shell configuration. There is very little overlap of orbitals and the band formalism is not adequate. The electrons are bound to the ions and localized.
- For covalent bonding, the orbitals overlap and there is some degree of delocalization of electrons, shared between neighboring atoms.
- For metallic bonding, the overlap is large and the electrons belonging to the outer shell are completely delocalized; there is a sea of nearly free electrons, bathing the ion core lattice.

The highest occupied band is the *valence band*, the lowest unoccupied band is the *conduction band*. The gap width is given by:

$$E_g = E_c - E_v \tag{6.106}$$

where E_v is the energy of the top level of the valence band and E_c is the energy of the bottom level of the conduction band. The electronic levels are filled up to the *Fermi level* E_F.

The electrical conduction properties of crystals essentially depend on the position of the Fermi level with respect to the bands and on the gap width.

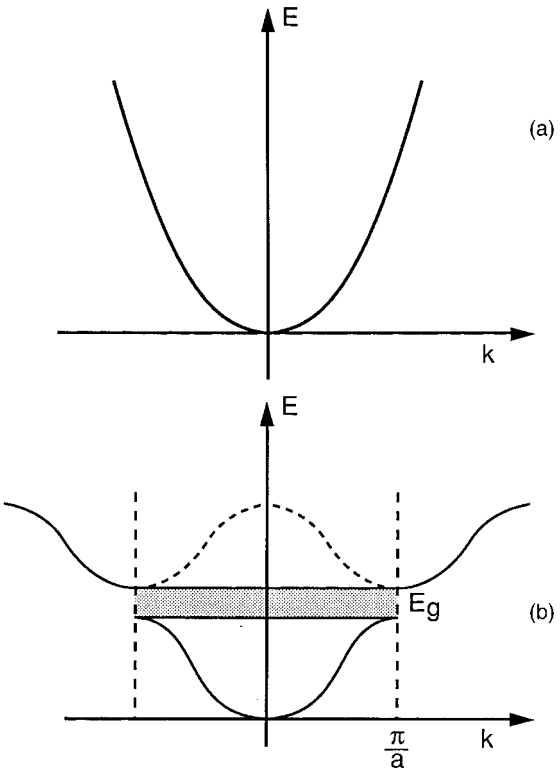

Figure 6.17 (a) Energy vs wave number curve for a free electron (parabola). (b) Energy vs wave number curve for a nearly free electron in a periodic potential (first Brillouin zone). The energies in the gap of width E_g are forbidden.

When an electrical field is applied to a crystal, the electrons are subjected to a force and are accelerated, thus acquiring energy. They must therefore be promoted to higher-energy levels. This is possible only if the Fermi level lies within a partially filled conduction band with empty levels available (metal) or if the gap is narrow enough so that thermal agitation can allow electrons to cross it, from the valence band into the empty conduction band (semi-conductor). If the valence band is completely filled and the gap is wide, the crystal is an insulator; the electric field cannot make the electrons move since there are no accessible energy levels for them. However, the bands can be distorted, giving rise to polarization (dielectric). We can now classify the crystals according to their electronic structure and electrical properties.

(i) *Insulators* (Fig. 6.19(a)). The valence band is completely filled at 0 K

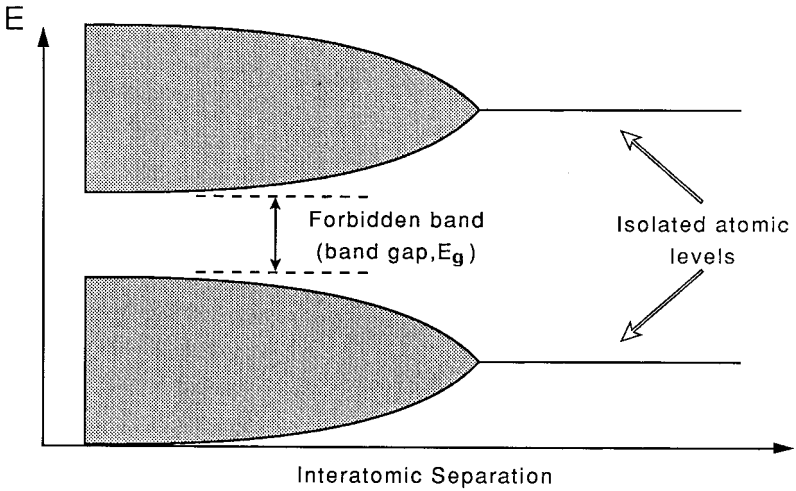

Figure 6.18 Widening of atomic levels into bands when atoms are brought close together.

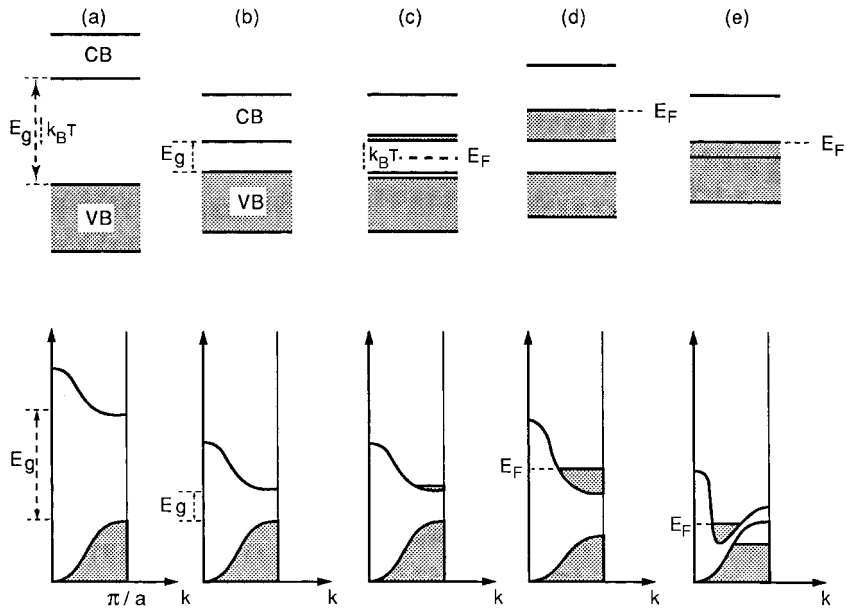

Figure 6.19 Electronic band structure of various classes of materials. (a) Insulators. (b) Intrinsic semi-conductors at $T = 0$ K. (c) Intrinsic semi-conductors at $T > 0$ K. (d) Metals at $T = 0$ K. (e) Semi-metals at $T = 0$ K. The filled levels are stippled.

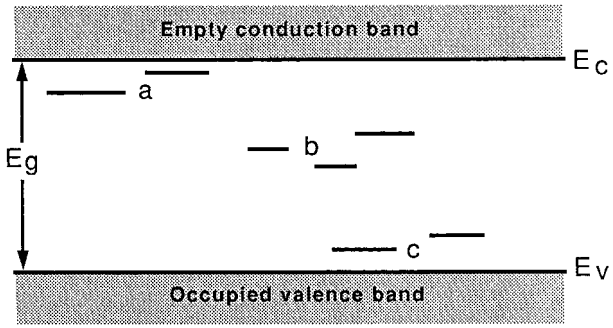

Figure 6.20 Localized levels introduced in the energy gap. (a) Shallow donor levels. (b) Deep levels. (c) Shallow acceptor levels.

and the gap is too wide for thermal agitation to allow promotion of electrons across it, even at high temperatures, i.e. ($E_g \gg k_B T$).

Typical insulators are, for instance, diamond ($E_g = 5.3\,\text{eV}$), forsterite ($E_g = 6.4\,\text{eV}$) and SiO_2 ($E_g = 8\,\text{eV}$). Incidentally, remember that $k_B T = 1/40\,\text{eV}$ at room temperature and that $k_B T = 1\,\text{eV}$ at 11 605 K. Ionic crystals generally are insulators at low temperatures. This is due to the fact that the charges can move only by thermally activated jumps from one site to another; conduction involves either diffusion of the whole ions (*ionic conduction*) or electronic charge transfer between ions of different valence (*hopping conduction*). In both cases, if the activation energy of the process is much higher than $k_B T$, the crystal behaves as a dielectric with very low conductivity. Although the band formalism is not the best suited to ionic crystals, a large value of the band gap width is associated with ionic crystals in the low-temperature insulating regime. At high temperatures, ionocovalent compounds that are insulators at low temperatures, can simultaneously exhibit electronic semi-conduction or hopping conduction and ionic conduction.

Impurity atoms in low concentrations may introduce deep energy levels in the gap, far from the gap edges (Fig. 6.20), which may allow for some electrical conductivity of the semi-conduction type if the gap is not too wide (see, e.g. Morin *et al.*, 1977, for forsterite).

(ii) *Semi-conductors* (Fig. 6.19(b,c)). Semi-conductors differ from insulators in that their gap is narrower, comparable to $k_B T$, thus allowing, in pure crystals, thermal promotion of electrons in the conduction band, leaving positively charged *holes* at the top of the valence band (*intrinsic semi-conduction*). Typical gap widths for semi-conductors are of the

order of 1 eV, e.g. $E_g = 1.14$ eV for Si, $E_g = 0.67$ eV for Ge, $E_g = 1.4$ eV for GaAs.

Impurity atoms in solution, e.g. As in Ge, can introduce shallow levels (*donor levels*) near the top of the gap, that can "donate" electrons to the conduction band and give rise to n-type conduction. If the impurity can receive electrons, e.g. Ga in Ge, it introduces levels (*acceptor levels*) near the bottom of the gap and gives rise to p-type conduction, by holes in the valence band. This is known as *extrinsic semi-conduction.*

(*iii*) *Metals* (Fig. 6.19(d)). In metals, the Fermi level falls within the conduction band, the remaining empty levels in the band are directly accessible to the electrons and there is a good electrical conductivity at 0 K. In some cases, the bottom of the conduction band is lower than the top of the valence band in certain directions of reciprocal space (k-space) and the electrons at the top of the valence band can spill over into the conduction band (Fig. 6.19(e)). There are conduction electrons and holes at 0 K. Such crystals are known as *semi-metals*, not as good conductors as metals; typical examples are the rare-earth metals.

It must be noted that the electrical properties of a given compound can change with temperature or pressure. The change can be gradual and two or more conduction mechanisms may coexist, as when an insulator at low temperatures becomes a semi-conductor and/or an ionic conductor at high temperatures or a metallic conductor at high pressure (Samara, 1967); the change may also be discontinuous, as when some oxides become metallic conductors above a critical temperature because, for a critical interatomic distance, the electronic structure with localized electrons is less stable than the metallic one (*Mott transition*). Pressure may lower the critical temperature (Mott, 1961).

6.5.2 Mechanisms of electrical conduction

(i) Generalities

Ohm's law, $I = R^{-1}V$, relates the current intensity flowing in a conductor to the difference of potential driving it and to the resistance R (or conductance R^{-1}) of the conductor.

The resistivity is: $\rho = RS/L$, where S is the section of the conductor and L its length. Ohm's law can therefore be written:

$$\mathbf{J} = \sigma \mathscr{E} \tag{6.107}$$

where $J = I/S$ (in amperes/m^2) is the current density, $\mathscr{E} = V/L$ (in volts/m) is the electric field and $\sigma = \rho^{-1}$ (in Ω^{-1}/m or siemens/m) is the electrical conductivity.

The current is equal to the rate of passage of electric charge through unit area of the conductor, it can be written:

$$J = nqv_d \tag{6.108}$$

where n is the number of mobile charge-carrying particles per unit volume, q is their electric charge and v_d their drift velocity in the direction of the electric field.

We will give here a microscopic expression of Ohm's law in the case of electronic conduction in a partially filled band (metal or semi-conductor). The electrons feel the periodic potential of the crystal (which accounts for the existence of the bands in the first place), but for the sake of simplicity and without too much loss of generality, we will consider the conduction electrons as free.

Let us consider electrons moving freely in a band. The force exerted on them by the electric field is:

$$\mathbf{F} = -e\mathscr{E} = \frac{d\mathbf{p}}{dt} = \hbar\frac{d\mathbf{k}}{dt} \tag{6.109}$$

where e is the electron charge, $\mathbf{p}$ is the momentum and $\mathbf{k}$, the wave vector.

The electrons are accelerated by the force but their velocity does not increase indefinitely, because of collisions and scattering of phonons or point defects, and it reaches a steady state drift velocity v_d. Let the relaxation time τ be the average time between scattering events, the increase in momentum between these events is:

$$\hbar\Delta\mathbf{k} = \mathbf{F}\tau \tag{6.110}$$

and the drift velocity is:

$$v_d = \hbar\frac{\Delta k}{m} = \frac{F\tau}{m} \tag{6.111}$$

where m is the mass of the electron, or with (6.109):

$$v_d = -e\mathscr{E}\frac{\tau}{m} \tag{6.112}$$

and, with (6.108):

$$J = -nev_d = \frac{ne^2\tau}{m}\mathscr{E}$$

hence:

$$\sigma = \frac{ne^2\tau}{m} \tag{6.113}$$

If Λ is the mean free path of electrons and $\bar{v}$ is the total average (rms) velocity (thermal velocity plus drift velocity), we have:

$$\sigma = \frac{ne^2\Lambda}{m\bar{v}} \tag{6.114}$$

If the band is only slightly filled, as in extrinsic n-type semi-conductors, the average kinetic energy of an electron is:

$$\tfrac{1}{2}m\bar{v}^2 = \tfrac{3}{2}k_{\mathrm{B}}T \tag{6.115}$$

hence:

$$\sigma = ne^2\Lambda(3mk_{\mathrm{B}}T)^{-1/2} \tag{6.116}$$

(ii) Metallic conduction

All the conduction electrons gain energy when the electric field is applied and most of them are shifted from the levels they occupied to those left vacant by others, with no net contribution to the electrical current. It is only the electrons near the Fermi level that are promoted to empty levels and provide a net response to the field. To a first approximation we can take for $\bar{v}$ in (6.114) the velocity at the Fermi level v_{F} given by:

$$\tfrac{1}{2}mev_{\mathrm{F}} = E_{\mathrm{F}} \tag{6.117}$$

and we obtain *Drude's formula*:

$$\sigma = \frac{ne^2\Lambda}{mv_{\mathrm{F}}} \tag{6.118}$$

The temperature dependence of the conductivity in $T^{-1/2}$ given by the free-electron approximation does not agree with experimental results. Indeed at low temperatures (a few kelvin), the conductivity is controlled by the collision of electrons with dilute impurities in the lattice; it depends on the impurity concentration and is practically independent of temperature. At high temperatures ($T > \Theta_{\mathrm{D}}$), the conductivity is controlled by phonon scattering and decreases as T^{-1}. The resistivity of metals can be written (*Matthiessen's rule*) as:

$$\sigma^{-1} = \sigma_0^{-1} + \sigma_{\mathrm{L}}^{-1} \tag{6.119}$$

where σ_0^{-1} is the impurity contribution and $\sigma_L^{-1} \propto T$ at high temperatures is the lattice-dependent part. The linear temperature dependence of the resistivity can be qualitatively explained in the following way (Mott and Jones, 1958).

The electrical resistance is due to the scattering of electrons by vibrating atoms and it is proportional to the scattering probability, which, in turn, is proportional to the mean square of the displacement of atoms $\langle u^2 \rangle$. At high temperatures ($T > \Theta_D$), the mean potential energy of vibrating atoms is:

$$\tfrac{1}{2} f \langle u^2 \rangle = \tfrac{1}{2} k_B T \tag{6.120}$$

where f is the restoring force. From the equation of motion:

$$M \frac{d^2 u}{dt^2} + fu = 0 \tag{6.121}$$

we have:

$$f = M\omega^2 \tag{6.122}$$

where M is the mass of the atoms and ω their vibrational frequency. With (6.120) and (6.122) and taking for ω the Debye frequency $\omega_D = (k_B/\hbar)\Theta_D$, we obtain:

$$\sigma^{-1} \propto \langle u^2 \rangle = \hbar^2 \frac{\Theta_D^2 T}{k_B M} \tag{6.123}$$

Since $\langle u^2 \rangle$ decreases with pressure, the conductivity of metals increases with pressure. We have, with the definition (3.52) of the Debye–Grüneisen parameter γ_D:

$$-\frac{d \ln \sigma}{d \ln V} = \frac{d \ln \sigma}{d \ln \rho} = -2 \frac{d \ln \Theta_D}{d \ln V} = 2\gamma_D \tag{6.124}$$

(iii) Semi-conduction

In the case of semi-conductors, where electron- or hole states are close to the edge of a band, the free-electron approximation cannot be used and the interaction of the electrons with the lattice and other electrons must be taken into account by introducing the *effective mass* m^*, instead of the mass m of the free electron. The expression of the effective mass can be found by considering the motion of a wave packet of states with frequencies and wave numbers near ω and k respectively. Energy $E = \hbar\omega$ is propagated with group velocity v_g:

$$v_g = \frac{d\omega}{dk} = \frac{1}{\hbar}\frac{dE}{dk} \tag{6.125}$$

hence:

$$\frac{dv_g}{dt} = \frac{1}{\hbar}\frac{d^2E}{dk^2}\frac{dk}{dt}$$

With $\hbar\dfrac{d\mathbf{k}}{dt} = \mathbf{F}$, (6.109), it becomes:

$$\mathbf{F} = \hbar\left(\frac{d^2E}{dk^2}\right)^{-1}\frac{d\mathbf{v}_g}{dt} = \frac{d\mathbf{p}}{dt} \tag{6.126}$$

We see that the role of the mass is played by the effective mass:

$$m^* = \hbar^2\left(\frac{d^2E}{dk^2}\right)^{-1} \tag{6.127}$$

For free electrons $E = \hbar k^2/2m$, hence $m^* = m$. Close to the edge of the bands, momentum transfer between the electrons and the lattice is thus taken into account by introducing the effective mass.

For a semi-conductor with band gap width E_g and Fermi level E_F, if the energy at the top of the valence band is taken as the zero of energy, the number of electrons in the conduction band (filled states) per unit volume is:

$$n = \int_{E_g}^{\infty} 2\mathscr{D}(E)f(E)dE \tag{6.128}$$

where $\mathscr{D}(E)$ is the density of states of electrons (the number of states per unit volume with energy between E and $E + dE$) and $f(E)$ is the Fermi–Dirac distribution function:

$$f(E) = \left[\exp\left(\frac{E - E_F}{k_BT}\right) + 1\right]^{-1} \cong \exp\left(\frac{E_F - E}{k_BT}\right) \tag{6.129}$$

Calculating the value of the density of states (see e.g. Kittel, 1967; Animalu, 1977), it can be shown that:

$$n = 2\left(\frac{m_e^*k_BT}{2\pi\hbar^2}\right)^{3/2}\exp\left(\frac{E_F - E_g}{k_BT}\right) \tag{6.130}$$

Similarly, the concentration of holes in the valence band is:

$$p = 2\left(\frac{m_h^*k_BT}{2\pi\hbar^2}\right)^{3/2}\exp\left(\frac{-E_F}{k_BT}\right) \tag{6.131}$$

The law of mass action for the concentrations of electrons and holes is written as:

$$np = 4\left(\frac{k_B T}{2\pi\hbar^2}\right)^3 (m_e^* m_h^*)^{3/2} \exp\left(\frac{-E_g}{k_B T}\right) \tag{6.132}$$

where m_e^* and m_h^* are the effective masses of electrons and holes respectively.

(i) *Intrinsic conduction.* For intrinsic conduction, we have $n = p$, since a hole is left in the valence band for every electron that is promoted to the conduction band. The number of intrinsic carriers is then found from (6.132):

$$n_i = p_i = 2\left(\frac{k_B T}{2\pi\hbar^2}\right)^{3/2} (m_e^* m_h^*)^{3/4} \exp\left(\frac{-E_g}{2k_B T}\right) \tag{6.133}$$

and, setting (6.130) equal to (6.131):

$$E_F = \frac{1}{2}E_g + \frac{3}{4}k_B T \ln\left(\frac{m_h^*}{m_e^*}\right) \tag{6.134}$$

One then sees that, if $m_e^* = m_h^*$, the Fermi level lies in the middle of the gap. The conductivity is given by the sum of the contributions of electrons and holes:

$$\sigma = ne\mu_e + pe\mu_h = n_i e(\mu_e + \mu_h) \tag{6.135}$$

where μ_e and μ_h are the *mobility* of electrons and holes respectively (drift velocity per unit electric field). Comparison of (6.135) with (6.113) and replacement of m by the effective masses yields:

$$\begin{aligned} \mu_e &= e\tau_e m_e^* \\ \mu_h &= e\tau_h m_h^* \end{aligned} \tag{6.136}$$

where τ_e and τ_h are the relaxation times for electrons and holes respectively.

From (6.133) and (6.135), we have therefore for intrinsic conductivity:

$$\sigma = 2\left(\frac{k_B T}{2\pi\hbar^2}\right)^{3/2} (m_e^* m_h^*)^{3/4} \exp\left(\frac{-E_g}{2k_B T}\right)(\mu_e + \mu_h) \tag{6.137}$$

Intrinsic conductivity is the conduction regime for pure crystals or crystals with a low impurity concentration at high temperature, where the concentration of intrinsic carriers, which grows exponentially with temperature, is much larger than the concentration of impurities.

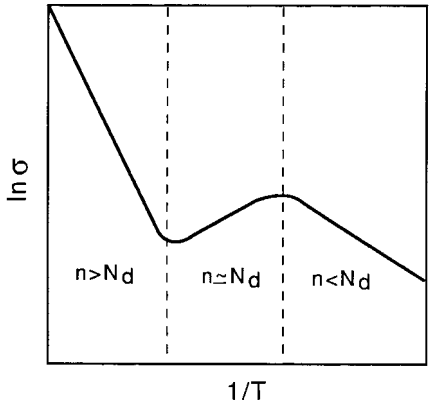

Figure 6.21 Arrhenius plot of the electrical conductivity of semi-conductor showing the intrinsic regime at high temperatures and the extrinsic regime at low temperatures; in the intermediate regime the conductivity may slightly decrease with increasing temperature due to electron–photon scattering (after Animalu, 1977).

The mobility at high temperatures is mostly controlled by phonon scattering and it can be shown that:

$$\mu_e = \mu_h \propto T^{-3/2} \tag{6.138}$$

The temperature dependence of the conductivity comes therefore essentially from the temperature dependence of the carrier concentration. The slope of the Arrhenius plot directly gives the energy gap E_g (Fig. 6.21).

(ii) *Extrinsic conduction.* The electrons in the conduction band of n-type semi-conductors (holes in the valence band of p-type semi-conductors) arise by thermal ionization of the donor (acceptor) impurities. The donor level (E_d below the conduction band) is at $E_g - E_d$, referred to the top of the valence band. The conduction electron concentration n is equal to the concentration of ionized donors N_d^+, given by the product of the total dopant concentration by the Fermi–Dirac distribution:

$$n = 2\left(\frac{m_e^* k_B T}{2\pi\hbar^2}\right)^{3/2} \exp\left(\frac{E_F - E_g}{k_B T}\right) = N_d\left[\exp\left(\frac{E_F - E_g + E_d}{k_B T}\right) + 1\right] \tag{6.139}$$

In the low-temperature limit, $E_d \gg k_B T$, we have:

$$\exp 2\left(\frac{E_F - E_d}{k_B T}\right) \approx \frac{1}{2} N_d \left(\frac{m_e^* k_B T}{2\pi\hbar^2}\right)^{-3/2} \exp\left(\frac{-E_d}{k_B T}\right)$$

and:

$$n = (2N_d)^{1/2} \left(\frac{m_e^* k_B T}{2\pi\hbar^2} \right)^{3/2} \exp\left(\frac{-E_d}{k_B T} \right) \tag{6.140}$$

The carrier concentration varies with the square root of the impurity concentration and as $T^{3/2}$; the mobility, controlled by ionized impurity scattering, varies as $T^{-3/2}$. The temperature dependence of the conductivity is therefore exponential, with the slope of the Arrhenius plot giving the ionization energy of the impurity E_d (Fig. 6.20). The same results apply to p-type semi-conductors.

Between the intrinsic and the extrinsic regimes, there is an intermediate temperature range where the concentration of intrinsic carriers is comparable with that of the dopant impurity. The conductivity in this range may slightly decrease as temperature increases because of electron–phonon scattering (Fig. 6.21).

Pressure affects the electrical conductivity of semi-conductors via the mobility and concentration of the carriers. Mobility, controlled by phonon scattering, depends on density, phonon velocity, effective mass, etc., all of which depend on pressure (Paul and Warschauer, 1963). The overall pressure dependence of mobility, however, remains of second order compared to the pressure dependence of the carrier concentration: The carrier concentration depends exponentially on the energy gap E_g which depends in a complicated way on pressure. At pressures up to 10 kbar (1 GPa), for instance, the energy gap of germanium first increases with pressure (5×10^{-6} eV/bar), then tends to decrease, whereas the energy gap of silicon decreases as pressure increases (Paul and Warschauer, 1963). At very high pressures, anyway, one should expect that bands would eventually overlap, giving rise to metallic conduction (Drickamer, 1963).

(iii) *Hopping conduction and ionic conduction.* Let us now consider the case of ionic crystals where the orbital overlap is so small that the band formalism becomes inadequate. To a first approximation, the electrons are localized and bound to the ions; they cannot freely move as an electric field is applied and the crystal behaves as an insulator at low temperatures. Such compounds, for which the effective mass of the carriers is very large are sometimes called "low-mobility semi-conductors". The only way an electrical current can be created is by bodily motion of the ions by thermally activated diffusion through the crystal (ionic conduction) or by thermally activated charge-transfer between neighboring ions of different valence (hopping conduction): for instance, a hole hops from a cation with charge $+3$ to a neighboring ion with charge $+2$ or $+1$. This occurs in the

so-called "mixed-valence compounds". The ions can be of different natures (e.g. Ni^{3+} and Li^{+} in lithium-doped NiO). They can also be of the same nature, as in the important case of transition metals, which can exist with several degrees of oxidation, e.g. Fe^{3+} and Fe^{2+} in magnetite Fe_3O_4 (Kündig and Hargrove, 1969); see also Coey *et al.* (1989).

There are also cases where the low-mobility carriers in narrow-band materials, interacting strongly with optical phonons, polarize the lattice and distort it in their neighborhood. The lattice distortion moves with the carrier (see Appel, 1968). The unit formed by the bound carrier and its induced lattice deformation, confined to a small region, is called a *small polaron*. The strain energy of the distorted lattice E_b is equal to the polaron binding energy. Conduction by polarons has been found in the case of oxides like NiO, CeO_2 and FeO (Yamashita and Kurosawa, 1958; Austin and Mott, 1969; Tuller and Nowick, 1977; Chen *et al.*, 1982). At high temperatures, small polarons move by thermally activated hopping (Emin, 1975). We will limit ourselves to the discussion of hopping and ionic conduction, both of which proceed by thermally activated diffusion jumps.

The *Nernst–Einstein relation* links the electrical conductivity to the diffusion coefficient of electrons or ions, it is obtained by equating the expression of Ohm's law (6.107) with the diffusion flux of charges:

$$\sigma\mathscr{E} = -D\,\mathrm{grad}(nq) = -qD\frac{\partial n}{\partial x} \tag{6.141}$$

where q is the charge of the carrier (ion, electron or hole) diffusing under the action of the electric field $\mathscr{E}$. In steady state, the concentration $n(x)$ of carriers at point x in the electric field follows a Boltzmann distribution law:

$$n(x) \propto \exp\left(-\frac{e\mathscr{E}x}{k_B T}\right) \tag{6.142}$$

From (6.141) and (6.142), we have:

$$\frac{\sigma}{D} = \frac{q^2 n}{k_B T} \tag{6.143}$$

For the case of hopping, the electron (hole) transfer reaction can be written for instance:

$$M_a^{3+} + M_b^{2+} \rightarrow M_a^{2+} + M_b^{3+} \tag{6.144}$$

where M_a^{q+} and M_b^{q+} are cations of charge q in neighboring sites a and b.

If θ is the fraction of lattice sites occupied by electrons or holes suscep-

tible to jump (e.g. atomic fraction of M^{3+}), the probability of finding an empty site in the neighborhood is $1 - \theta$ and the diffusion coefficient of charges (see Honig, 1970) is:

$$D = \Gamma(\delta l)^2(1 - \theta) \tag{6.145}$$

where Γ is the jump frequency and δl, the jump distance (see Section 6.2). The jump frequency is thermally activated:

$$\Gamma = \Gamma_0 \exp\left(-\frac{\Delta H}{k_B T}\right) \tag{6.146}$$

The number of carriers per unit volume n is proportional to θ, the constant of proportionality depending on the crystal structure. With (6.145) and (6.146), the Nernst–Einstein relation gives:

$$\sigma = \frac{\sigma_0 \theta(1 - \theta)}{k_B T} \exp\left(-\frac{\Delta H}{k_B T}\right) \tag{6.147}$$

where σ_0 is a constant and ΔH is the activation energy for hopping. If the atomic fraction θ of charge carriers is constant, the hopping conductivity depends on temperature according to an Arrhenius law, like diffusion, and it is maximum for $\theta = 0.5$. Deviations from the Arrhenius law obviously occur if θ changes with temperature, e.g. if the concentration of Fe^{3+} increases due to oxidation of Fe^{2+} as the oxygen partial pressure increases. The case of ionic conduction obviously reduces, via the Nernst–Einstein relation, to the case of ionic diffusion, treated in Section 6.2.

The effect of pressure, however, is quite different for hopping and ionic conductivity. In the case of ionic conductivity, we have seen in Section 6.2 that the activation energy for diffusivity increases with pressure because it is more difficult to create vacancies under pressure. The ionic conductivity therefore decreases as pressure increases. On the contrary, the activation energy for hopping conductivity decreases as pressure increases because the jump distance between sites decreases under pressure. As there is no need for vacancies, the hopping conductivity increases with pressure.

6.5.3 Electrical conductivity of mantle minerals

A review of the experimental measurements of the conductivity of various minerals and rocks at high pressure was given by Parkhomenko (1982). We will only briefly summarize here the results concerning the main mantle minerals.

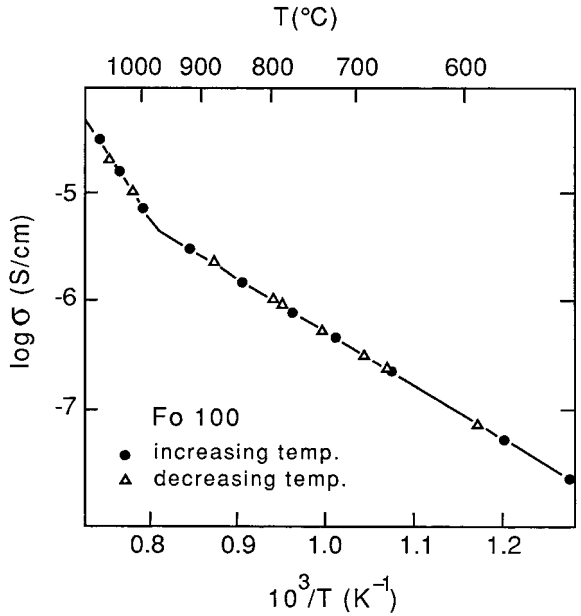

Figure 6.22 Arrhenius plot of the electrical conductivity of forsterite equilibrated with MgO (after Cemic *et al.*, 1980).

(i) Forsterite, olivines, fayalite

Pure forsterite Mg_2SiO_4 is an insulator at room temperatures ($\sigma < 10^{-7}$ S/m). Its conductivity was studied by Bradley *et al.* (1964), who found that its activation energy between 300 and 700 °C increases with pressure, from 1.1 eV at 11 kbar (1.1 GPa) to about 3 eV at 35 kbar (3.5 GPa). Measurements on single crystals in the three directions *a*, *b* and *c* (Morin *et al.*, 1977, 1979) showed a conductivity anisotropy, with the highest conductivity in the *a*-direction and the lowest conductivity in the *b*-direction .These results are not confirmed by measurements between 1000 and 1500 °C by Schock *et al.* (1989), who find that the conductivity is greatest and independent of oxygen partial pressure in the *c*-direction, intermediate in the *a*-direction and still least in the *b*-direction; they infer that conduction in forsterite is dominated by electronic conduction in the *a*- and *b*-directions and probably by magnesium vacancy diffusion along the *c*-direction. Will *et al.* (1979) and Cemic *et al.* (1980) studied the electrical conductivity of forsterite equilibrated with MgO, the thermodynamic conditions being thus well defined. They found two regimes (Fig. 6.22):

$$\sigma = 4.92 \exp(-0.98[\text{eV}]/k_B T) \quad \text{for } 520 < T < 970\,^{\circ}\text{C}$$

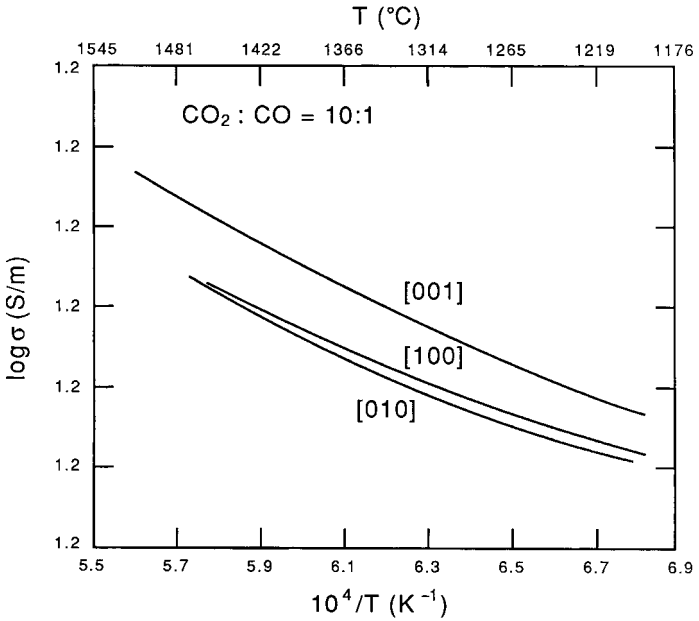

Figure 6.23 Arrhenius plot of the electrical conductivity of San Carlos olivine. The gas mixture (10 CO_2 for 1 CO) buffers the oxygen partial pressure at the value of 10^{-3} Pa at 1200 °C (after Schock *et al.*, 1989).

$$\sigma = 4.69 \cdot 10^{-6} \exp(-2.46[\text{eV}]/k_B T) \quad \text{for } 970 < T < 1075\,^{\circ}\text{C}$$

Olivines $(Mg_{1-x}Fe_x)_2SiO_4$ and fayalite Fe_2SiO_4 have been studied by many authors. Schock *et al.* (1989) find that olivine appears to show mixed conduction from 1000 to 1500 °C, as evidenced by the curvature of the Arrhenius plot (Fig. 6.23), with electron hole conduction by hopping predominant at lower temperatures and magnesium vacancy ionic conduction predominant above 1390 °C.

Wanamaker and Duba (1993) measured the conductivity along [100] of single-crystal San Carlos olivine, between 1100 and 1200 °C, as a function of oxygen partial pressure, for "self-buffered" and "pyroxene-buffered" crystals. They find that, depending on the oxygen partial pressure, conduction is dominated by polarons or electrons in self-buffered samples and by polarons and magnesium vacancies in pyroxene-buffered samples.

The experimental results for temperatures up to about 1200 °C are generally consistent with a conduction mechanism by electron transfer by hopping between Fe^{3+} and Fe^{2+} ions (Bradley *et al.*, 1964, 1973; Hirsch *et al.*, 1993).

Table 6.3. *Parameters of the Arrhenius law* $\sigma = \sigma_0 \exp(-E/k_B T)$ *for olivines* $(Mg_{1-x}Fe_x)_2SiO_4$

x (% Fe)	T range (°C)	P (GPa)	σ_0 (S/m)	E (eV)	Reference
10.4–17.5	560–1800	1.15–3.2		0.9	Hamilton (1965)
1	300–1000	1.2	11 200	1	Bradley *et al.* (1964)
1	300–1000	3.5	230	1	Bradley *et al.* (1964)
10	300–1000	1.2	200	0.92	Bradley *et al.* (1964)
10	300–1000	4.7	5	0.74	Bradley *et al.* (1964)
50	300–1000	1.2	17 380	0.74	Bradley *et al.* (1964)
100	300–1000	1.2	1900	0.72	Bradley *et al.* (1964)
100	300–1000	4.7	370	0.53	Bradley *et al.* (1964)
18	500–1200	0	29	0.86	Mizutani & Kanamori (1967)
8.4	800–1200	0	160	0.79	Kobayashi & Maruyama (1971)
19[a]	560–1120	0.2–0.8	1.3	0.98	Duba *et al.* (1974)
19[a]	1270–1440	0.2–0.8	53 700	2.33	Duba *et al.* (1974)
10[b]	870–1210	1.0	2.7	0.78	Cemic *et al.* (1980)
10[c]	820–1220	1.0	1.9	0.62	Cemic *et al.* (1980)
20[b]	800–1210	1.0	13.8	0.68	Cemic *et al.* (1980)
20[c]	875–1160	1.0	16.3	0.58	Cemic *et al.* (1980)
100[d]	340–1100	1.0		0.52	Will *et al.* (1980)
100[e]	340–1100	1.0		0.38	Will *et al.* (1980)
9[f]	1200–1250	0		1.3	Schock *et al.* (1989)
9[g]	1200–1250	0		1.6	Schock *et al.* (1989)
10	1000–1300	4.0	955	1.73	Xu *et al.* (1998b)
10	1000–1400	7.0	427	1.66	Xu *et al.* (1998b)
10	1000–1400	10.0	513	1.69	Xu *et al.* (1998b)
10[h]	1000–1400	10.0	1047	1.71	Xu *et al.* (1998b)

[a] Red Sea olivine with a low Fe^{3+}/Fe^{2+} ratio.
[b] Reducing conditions (Fe–FeO buffer).
[c] Oxidizing conditions (Quartz–Magnetite–Fayalite buffer).
[d] Reducing conditions (Quartz–Fe).
[e] Oxidizing conditions (Quartz–Magnetite).
[f] $f_{O_2} = 10^{-4}$ Pa, *a*- and *b*-directions.
[g] $f_{O_2} = 10^{-4}$ Pa, *c*-direction.
[h] Single crystal, *a*-direction.

Even though results are somewhat scattered (Table 6.3), most investigations on olivines lead to similar conclusions:

- Conductivity increases and activation energy decreases as the total iron content x increases (Bradley *et al.*, 1964; Cemic *et al.*, 1980; Hirsch *et al.*, 1993).
- Conductivity increases and activation energy decreases as the ratio of

ferric to ferrous iron content increases, for instance, when measurements are made in an oxidizing atmosphere (Duba *et al.*, 1973; Duba and Nicholls, 1973; Cemic *et al.*, 1980).

The effect of pressure is more disputed: Bradley *et al.* (1964, 1973) find that conductivity increases with pressure, with an activation energy decreasing linearly as pressure increases ($dE/dP = -0.005$ eV/kbar for olivine) from 10 to 60 kbar (1 to 6 GPa). In shock-wave experiments (Mashimo *et al.*, 1980), conductivity is found to increase by a factor of more than 10^{10} between 0 and 40 GPa. However, no systematic variation of conductivity with pressure is observed up to 0.8 GPa (Duba *et al.*, 1974) and, in experiments at pressures up to 5 GPa, Xu *et al.* (1998b) find an activation volume not significantly different from zero.

In general, a behavior similar to that of olivine is found for other orthosilicates of transition metals such as manganese, cobalt or nickel olivines (Bradley *et al.*, 1973), as well as for manganese germanate olivine (Yagi and Akimoto, 1974).

The transition from olivine to its high-pressure polymorphs wadsleyite and ringwoodite (occurring in the mantle transition zone below 400 km) is accompanied by an increase in conductivity by about two orders of magnitude (Akimoto and Fujisawa, 1965; Xu *et al.*, 1998b). This is consistent with the hopping mechanism, which is easier in the spinel structure (as, for instance, in magnetite).

(ii) Periclase and magnesiowüstite

Mitoff (1962) measured the conductivity of MgO single crystals at high temperature and various oxygen partial pressures. He found that the conduction was predominantly ionic at 1000 °C and intermediate oxygen partial pressures, whereas at 1500 °C and high (1 atm) or low ($< 10^{-6}$ atm) pressures, the conduction was mostly electronic, deviation from stoichiometry resulting in sources of electronic charge carriers. Periclase is, in most cases, at high temperatures, a mixed electronic and ionic conductor.

The behavior of the electrical conductivity of magnesiowüstites $(Mg_{1-x}Fe_x)O$ and wüstite $Fe_{1-x}O$, as a function of pressure, total Fe content and ferric/ferrous iron ratio is similar to that of olivines. It has also generally been ascribed to hopping (Tannhauser, 1962; Hansen and Cutler, 1966; Iyengar and Alcock, 1970; Mao, 1972; Bowen *et al.*, 1975; Chen *et al.*, 1982).

The conductivity of magnesiowüstites and wüstite is much higher than that of olivines and its activation energy is lower, ranging from 0.7 to 0.4 eV

for iron contents of 7.5 to 20 mol% at ambient pressure (Iyengar and Alcock, 1970). Mao (1972) found that at 15 GPa, the electrical conductivity of $(Mg_{0.78}Fe_{0.22})O$ is six orders of magnitude higher than that of olivines with the same Fe/Mg ratio, with an activation energy equal to 0.37 eV. Li and Jeanloz (1990b) studied the conductivity of magnesiowüstites with 9 and 27.5 mol% FeO at 30 GPa in a laser-heated diamond-anvil cell; they found that the magnesiowüstite with 27.5 mol% FeO was more conductive by three orders of magnitude than the more iron-poor magnesiowüstite. The activation energy decreased from 0.38 eV for 27.5% FeO to 0.29 eV for 9% FeO.

Wood and Nell (1991) investigated the electrical conductivity of $(Mg_{0.83}Fe_{0.17})O$ between 1173 and 1773 K, under controlled oxygen partial pressure. They found that the variation of conductivity with p_{O_2} roughly obeys the relation: $\sigma \propto p_{O_2}^{0.33}$ and that the highest conductivity is achieved for equal concentrations of ferric and ferrous ions, as expected for conduction by electron hopping. In experiments at 5 and 10 GPa, Dobson *et al.* (1997) find a curvature of the Arrhenius plot and suggest that conduction is controlled by small polarons below about 1000 K and by large polarons at higher temperatures.

Shock-wave and diamond-anvil cell experiments at pressures above 70 GPa and temperatures above 1000 K have shown that wüstite $Fe_{0.94}O$ undergoes an increase in conductivity by three orders of magnitude (Knittle and Jeanloz, 1986), which is interpreted as a transition to the metallic state ("metallization"). Sherman (1989) argued that the observed "metallization" is not associated with metallic bonding, but with pressure-induced 4s–3d band overlap (Mott transition). Fei and Mao (1994) performed synchrotron X-ray diffraction measurements of FeO at high pressure and temperature and found that FeO undergoes a transition to the NiAs structure above 96 GPa; they suggested that the shorter Fe–Fe distance across shared FeO_6 octahedra faces could lead to metallization by electron delocalization.

(iii) Crystals with perovskite structure

Silicate perovskite $(Mg,Fe)SiO_3$ is thought to be an essential constituent of the lower mantle but, so far, few experiments on its electrical conductivity have been reported in the literature and they are conflicting.

Li and Jeanloz (1987, 1990a) report on the results of measurements of the conductivity of $(Mg_{0.9}, Fe_{0.1})SiO_3$ perovskite in a laser-heated diamond-anvil cell, up to 85 GPa and 3500 K; they claim that the conductivity remains below 0.001 S/m at lower-mantle conditions, with a very weak

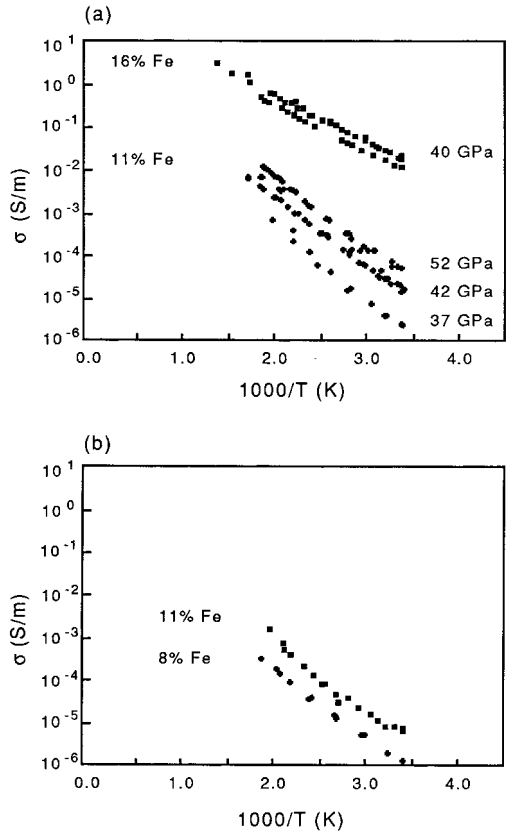

Figure 6.24 Arrhenius plot of the electrical conductivity of lower-mantle material. (a) Perovskite and magnesiowüstite assemblage obtained by decomposition of San Carlo olivine of various Fe contents. (b) Perovskite $(Mg, Fe)SiO_3$ with 8 and 11 at.% Fe at 52 GPa. (After Peyronneau and Poirier, 1989.)

dependence on temperature (activation energy: 0.1–0.2 eV). Li *et al.* (1993) found that conductivity increases with pressure and measured a negative activation volume of $-0.12\,cm^3/mol$. Peyronneau and Poirier (1989), however, measured the conductivity of the same perovskite at 52 GPa, in a diamond-anvil cell heated by an external furnace up to about 400 °C; they found that the conductivity is already 0.01 S/m at 400 °C and that it increases with temperature and iron content in a way entirely consistent with a hopping mechanism (Fig 6.24(b)). Shankland *et al.* (1993) confirmed these results, finding an activation energy of 0.48 eV and an activation volume of $-0.26\,cm^3/mol$; the value of conductivity extrapolated to the lower-mantle conditions is of the order of 1 S/m. Katsura *et al.* (1998)

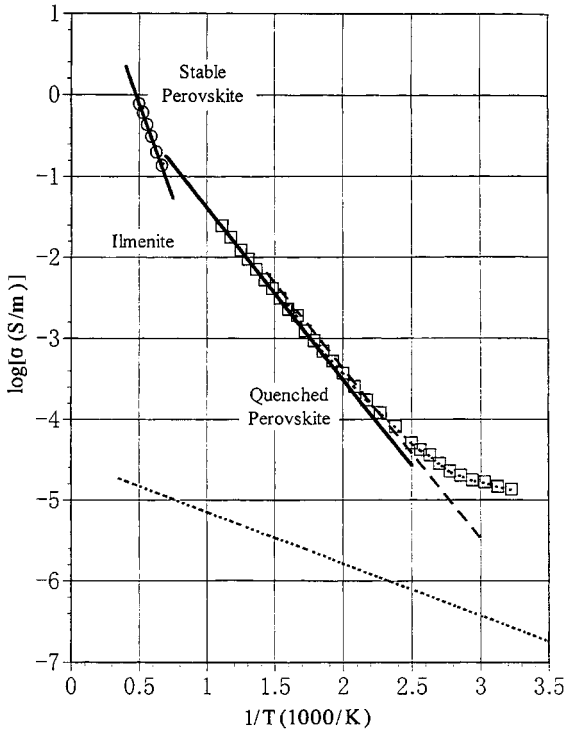

Figure 6.25 Electrical conductivity of perovskite, measured in a multi-anvil press at a pressure of 23 GPa. Enstatite was brought up to temperatures above 1500 K and transformed to stable perovskite. Measurements were then performed on quenched perovskite reheated up to 1500 K. The results of Shankland *et al.*, 1993 (dashed line) and of Li and Jeanloz, 1990a (dotted line) are shown for comparison (after Katsura *et al.*, 1998).

measured the conductivity of perovskite in a multi-anvil press, up to 23 GPa and 2000 K; they found an excellent agreement with the results of Shankland *et al.* (1993) up to about 1000 K (activation energy: 0.41 eV) (Fig. 6.25), but report another regime, close to 2000 K, with an activation energy of 0.92 eV.

Values of the conductivity of the order of 1 S/m at lower-mantle conditions, as extrapolated by Shankland *et al.* (1993) and Katsura *et al.* (1998), are in good agreement with geophysical determinations. It is probable that the discrepancy of more than four orders of magnitude between the results found by Li and Jeanloz using laser-heating and by other teams using external heating is due to the difference in experimental conditions.

Some other perovskites have been investigated and are generally

thought to be electronic extrinsic semi-conductors up to the highest temperatures investigated (generally about 1000 °C). This is, in particular, the case for $SrTiO_3$, with an activation energy of 0.4 eV above 1000 K (Stumpe *et al.*, 1983). The conductivity of $CaTiO_3$ has also been investigated up to 1100 °C; it exhibits several regimes of conduction depending on the oxygen partial pressure, which are interpreted in terms of small amounts of acceptor impurities (Balachandran *et al.*, 1982).

Fluoride perovskites $NaMgF_3$ (O'Keefe and Bovin, 1979) and $KZnF_3$ (Poirier *et al.*, 1983) were reported to exhibit a solid-electrolyte-like behavior close to the melting point, attributed to an abnormally high mobility of quasi-delocalized fluorine anions, which gives a very high electrical conductivity comparable to that of a liquid. Kapusta and Guillopé (1988) and Wall and Price (1989) performed molecular dynamics simulations on $MgSiO_3$ and found a very high mobility of the oxygen ions, which leads them to the conclusion that the silicate perovskite might also behave as a solid electrolyte at high temperatures. There is, however, no experimental support, so far, for this hypothesis.

(iv) Perovskite–magnesiowüstite assemblage

There is reasonably good evidence that a perovskite–magnesiowüstite assemblage is representative of the composition of the lower mantle. The electrical conductivity of this assemblage resulting from the disproportionation of olivine at high pressure was measured at Berkeley in a laser-heated diamond-anvil cell (Li and Jeanloz, 1987, 1991) and in Paris in an externally heated diamond-anvil cell (Peyronneau and Poirier, 1989 (see Fig. 6.24(a)); Poirier and Peyronneau, 1992; Shankland *et al.*, 1993; Poirier *et al.*, 1996). As in the case of pure silicate perovskite, there is a discrepancy of about four orders of magnitude between the results, which can be ascribed to differences in experimental conditions (Duba and Wanamaker, 1994). There is a reasonable agreement of the Paris extrapolated value of the conductivity at conditions of the lower mantle (of the order of 1 S/m) with geophysical determinations (Shankland *et al.*, 1993).

However, the experimental determination of the lower-mantle conductivity is fraught with many difficulties arising, in particular, from the presence of impurities in the minerals, which may alter the oxidation state and the conductivity. Thus, San Carlos olivine containing some nickel has a higher conductivity than nickel-free synthetic olivine (Duba *et al.*, 1997). More important, perhaps, is the fact that aluminum is present in the lower mantle, and it has been clearly shown that aluminum can not only dissolve in perovskite and extend its stability field (Kesson *et al.*, 1995), but it also

modifies the partition coefficient of iron between perovskite and magnesiowüstite (Wood and Rubie, 1996; Mao *et al.*, 1997). In the absence of aluminum, iron partitions mostly into magnesiowüstite, whereas it may partition equally between both phases when aluminum is present. Furthermore, in perovskite containing some aluminum a high proportion of the iron becomes ferric (McCammon, 1997). Xu *et al.* (1998) have found that the conductivity of perovskite containing 2.9 wt% Al_2O_3 is about 3.5 times greater than the conductivity of aluminum-free $(Mg_{0.915}, Fe_{0.085})SiO_3$ perovskite. It is, therefore, probable that the perovskite of the lower mantle is richer in Fe and in Fe^{3+} than the perovskite obtained in diamond-anvil cells from the disproportionation of aluminum-free olivine (McCammon *et al.*, 1997), and that it might contribute more to the conductivity of the assemblage (Poirier, 1997; Katsura *et al.*, 1998).

6.5.4 Electrical conductivity of the fluid core

The fluid core is a liquid alloy of iron and nickel with about 10 wt% light elements (see Poirier, 1994a) at temperatures close to the melting point and pressures above 1.3 Mbar.

Measurements of the electrical conductivity of pure liquid iron at atmospheric pressure yield a value of about 7×10^5 S/m (Iida and Guthrie, 1988). Conductivity decreases with increasing temperature, since electrons are scattered by thermal vibrations of the atoms. One can write (Mott, 1934):

$$\sigma \propto \frac{M\Theta_D^2}{T} \tag{6.148}$$

where Θ_D is Debye temperature and M, the mass of the atoms. Conductivity then must increase with pressure, as compression of the lattice restricts the thermal vibrations. From (6.148), one can derive:

$$\frac{\partial \ln \sigma}{\partial \ln \rho} = 2\frac{\partial \ln \Theta_D}{\partial \ln \rho} = 2\gamma_D \tag{6.149}$$

where γ_D is the Grüneisen parameter.

Conversely, impurities in solution scatter the electrons and cause a decrease in conductivity. Estimates (Gardiner and Stacey, 1971) and simple first-principle calculations (Jain and Evans, 1972) of the conductivity of the core fluid yielded values between 2×10^5 and 10^6 S/m.

Measurement, at atmospheric pressure and 1000 °C, of the conductivity of a "core mix" composed of liquid $(Fe_{0.9}Ni_{0.1})_3S_2$ alloyed with 2.6 wt%

carbon gave an average value $\sigma = 2.7 \times 10^5$ S/m (Johnston and Strens, 1973), while direct measurement of the conductivity of pure liquid iron close to the melting point gave $\sigma \approx 7 \times 10^5$ S/m (Van Zytveld, 1980). Shock-wave measurements of Fe–10 wt% Si alloys, at pressures between 50 and 150 GPa also yield a value of $\sigma \approx 7 \times 10^5$ S/m (Matassov, 1977). It seems that there is some compensation between the effects of temperature and impurities on the one hand and pressure on the other hand.

Secco and Schloessin (1989) have measured the electrical conductivity of pure iron in the solid and liquid state as a function of temperature and at pressures up to 7 GPa. Extrapolating their results to the P, T conditions of the outer core, they find it improbable that the conductivity of the impure outer core can differ much from that of pure liquid iron at pressures below 7 GPa and conclude that the most probable range of its value is 0.67–0.83×10^6 S/m.

6.6 Thermal conduction

(i) Generalities

Heat is transferred through solids by essentially two processes: lattice conduction (or phonon conduction) and electronic conduction. In the former case, the carriers are quantized lattice vibrations, i.e. phonons, and in the latter case, electrons. Both processes operate in some measure in all solids, but it is obvious that, in electrical insulators, phonons are responsible for almost all of the conductivity whereas, in metals, electronic conduction plays a predominant role. In both cases, the principal features of the mechanisms of conduction can be accounted for by the classical (or semi-classical) approach of the kinetic theory of gases, considering a gas of electrons or phonons. We will limit ourselves here to this elementary outlook, referring the reader to the book by Berman (1976) for a more rigorous treatment. Techniques of measurement are dealt with in Horai and Shankland (1987) and values of the thermal conductivities of many rock-forming minerals can be found in Horai (1971).

The geophysical literature usually lumps together thermal conduction and radiative heat transfer. This is somewhat misleading since thermal conduction refers to the transport of heat, the degraded form of energy, whereas radiative transfer concerns the propagation of energy, carried by electromagnetic waves (photons) through a more or less transparent (i.e. non-absorbing) medium. A justification can be found in the fact that, at high temperatures, most experimental methods for measuring the thermal

conductivity of solids yield an effective thermal conductivity, comprising a term corresponding to radiative transfer (Kanamori *et al.*, 1968). We will follow the common usage and briefly deal with radiative transfer at the end of this section.

(ii) Lattice conduction

The carriers of heat are phonons. In an anharmonic crystal, phonons interact (collide) and the thermal conductivity is controlled by the mean free path Λ between collisions: the more collisions there are, the shorter the mean free path and the smaller the conductivity. In a harmonic crystal, with no interactions between phonons, the mean free path, hence the conductivity, would be infinite.

Let us consider the thermal conduction in a material along direction x. The heat flux is given by:

$$J = -n(c\Lambda \operatorname{grad} T)v_x \tag{6.150}$$

where n is the number of carriers per unit volume, c, their specific heat ($c\Lambda \operatorname{grad} T$ is the amount of heat transferred over the length of the mean free path) and v_x is their average velocity in the x-direction. We can also write:

$$J = -\frac{1}{3}Cv\Lambda \operatorname{grad} T \tag{6.151}$$

where $C = cn$ is the lattice specific heat per unit volume and $v = 3v_x$ is the root mean square velocity of the phonon gas, i.e. the sound velocity. Comparison with (6.20) gives the lattice heat conductivity:

$$k_l = \frac{1}{3}Cv\Lambda \tag{6.152}$$

At low temperatures ($T < \Theta_D$) the lattice specific heat varies as T^3 and the mean free path Λ tends to become constant and controlled by defects, hence the thermal conductivity varies as T^3 (Fig. 6.26). At high temperatures ($T > \Theta_D$) the specific heat tends towards $3R$ (R is the gas constant) and it can be more or less empirically shown (Dugdale and McDonald, 1955) that the mean free path varies as $1/T$; thermal conductivity therefore decreases as $1/T$ at high temperatures (Fig. 6.26). Minerals of geophysical interest should not depart markedly from this behavior (Roufosse and Klemens, 1974).

As the lattice heat conductivity is linked to anharmonicity, it clearly must be possible to express it in terms of the Grüneisen parameter. Let us

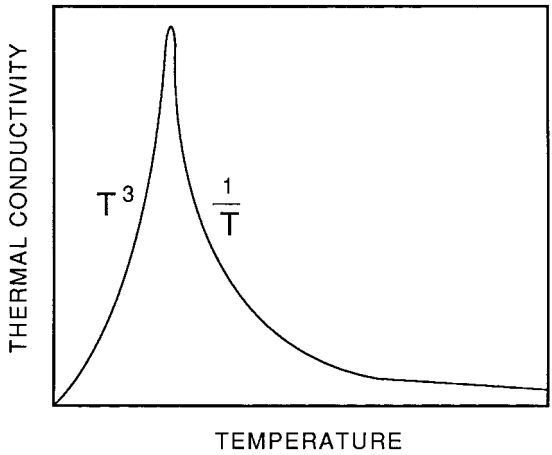

Figure 6.26 Temperature dependence of the lattice thermal conductivity.

start with (6.152) and with the expression of Dugdale and McDonald (1955) for the mean free path:

$$\Lambda = \frac{a}{\alpha\gamma T} \tag{6.153}$$

where a is an interatomic distance, α the thermal expansion coefficient and γ, the Grüneisen parameter. Taking for γ the thermodynamic gamma:

$$\gamma_{\text{th}} = \frac{\alpha K}{C} \tag{6.154}$$

where $C = \rho C_p$ is the specific heat per unit volume and K is the bulk modulus, we obtain:

$$k_1 = \frac{avK}{3\gamma_{\text{th}}^2 T} \tag{6.155}$$

Taking for the average phonon velocity: $v = v_\Phi = (K/\rho)^{1/2}$, we can write:

$$k_1 = \frac{av^3\rho}{3\gamma_{\text{th}}^2 T} \tag{6.156}$$

and obtain the expression first given by Lawson (1957):

$$k_1 = \frac{aK^{3/2}}{3\gamma_{\text{th}}^2 \rho^{1/2} T} \tag{6.157}$$

The thermal conductivity can also be expressed in terms of the Debye temperature Θ_D. Assuming the minimum wavelength of the vibrational modes to be equal to $2a$, the maximum frequency is:

$$\omega_{max} \approx \frac{\pi \hbar v}{a} = \frac{k_B \Theta_D}{\hbar} \tag{6.158}$$

Replacing v in (6.155) by its expression in terms of the Debye temperature and writing

$$K \propto v^2 M a^{-3}$$

where M is the average atomic weight, we obtain (Berman, 1976):

$$k_l \propto \frac{M a \Theta_D^3}{3\gamma_{th}^2 T} \tag{6.159}$$

Horai and Simmons (1969, 1970) found empirical relations between the thermal conductivity and the compressional (P-wave) and shear (S-wave) velocities:

$$v_P = 0.17 k_l + 5.93$$
$$v_S = 0.09 k_l + 3.31 \tag{6.160}$$

and between thermal conductivity and Debye temperature:

$$\Theta_D = 25.6 k_l + 385 \tag{6.161}$$

with k_l in mcal/cm s K, v_P and v_S in km/s and Θ_D in K (Fig. 6.27).

Using D. L. Anderson's (1967) seismic equation of state and introducing the concept of mean atomic specific heat, Maj (1978) derived a relation between the lattice thermal conductivity and the seismic parameter for silicate minerals:

$$k_l = 0.43 \Phi^{0.823} \tag{6.162}$$

where k_l is expressed in mcal/cm s K and Φ in km^2/s^2.

An order of magnitude value of the thermal conductivity of insulators can be found (Animalu, 1977) by setting in (6.152): $\Lambda = 3 \times 10^{-6}$ cm, $v = 10^5$ cm/s, $C = 3R$ cal/mol. One obtains:

$$k_l \approx \frac{0.3R}{V_{mol}}$$

with typical values of the molar volume V_{mol} of a few tens of cm^3, conduc-

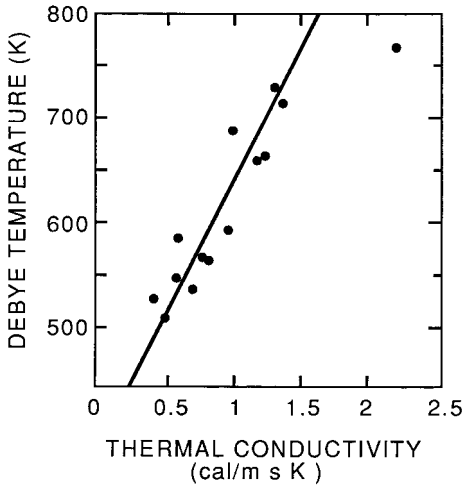

Figure 6.27 Correlation of Debye temperature and lattice thermal conductivity for silicates (after Horai and Simmons, 1970).

tivity values are found to lie in the range of about 5–30 mcal/cm s K (0.8–12.5 W/m).

The effect of pressure on thermal conductivity can be found through the theoretical or empirical relations between k_l and the sound velocity: k_l obviously increases with pressure. For typical mantle minerals, thermal conductivity can undergo a tenfold increase between ambient conditions and the pressure of the core–mantle boundary (Mao, 1972). From (6.157) we can also see that, along an adiabatic temperature gradient, we have:

$$\frac{d\ln k_l}{d\ln\rho} = -\frac{1}{3} + \frac{3}{2}\frac{d\ln K}{d\ln\rho} - \frac{1}{2} - \frac{d\ln T}{d\ln\rho} - 2\frac{d\ln\gamma}{d\ln\rho}$$

or, using $(d\ln T/d\ln\rho)_{ad} = \gamma$ and $\gamma\rho = \text{const}$:

$$\frac{d\ln k_l}{d\ln\rho} = 2\gamma + \frac{5}{3} \tag{6.163}$$

Using interatomic potentials, Roufosse and Jeanloz (1983) predicted the effect of phase transitions on the thermal conductivity of alkali halides; they suggested that the increase in coordination associated with a small volume change acts to reduce the thermal conductivity at high pressures.

The thermal diffusivity $\kappa = k_l/\rho C_p$ of rock-forming minerals at high temperatures and pressures have been measured by Kanamori *et al.* (1968) and Fujisawa *et al.* (1968) (Table 6.4). Chai *et al.* (1996) measured the

Table 6.4. *Thermal diffusivity of some minerals*

Mineral	T(K)	P(kbar)[a]	$\kappa(10^{-2}\,\mathrm{cm}^2/\mathrm{s})$	Reference
Quartz ∥ [001]	1100	0.001	1.64	Kanamori *et al.* (1968)
Quartz ∥ [010]	1100	0.001	1.28	Kanamori *et al.* (1968)
Olivine ∥ [001]	1100	0.001	1.35	Kanamori *et al.* (1968)
Forsterite	1100	30	0.94	Fujisawa *et al.* (1968)
	1100	50	1.10	Fujisawa *et al.* (1968)
NaCl	1000	29	1.20	Fujisawa *et al.* (1968)
Periclase	1100	0.001	3.23	Kanamori *et al.* (1968)
Jadeite	1100	0.001	0.96	Kanamori *et al.* (1968)
Garnet	1100	0.001	0.83	Kanamori *et al.* (1968)
Spinel	1100	0.001	2.13	Kanamori *et al.* (1968)

Note: [a]10 kbar = 1 GPa.

thermal diffusivity of olivine and orthopyroxene along the three directions a, b and c, at ambient pressure and temperature.

We see that for most minerals (and rocks) κ is of order $10^{-2}\,\mathrm{cm}^2/\mathrm{s}$. The pressure derivative $d\kappa/dP$ at 40 kbar (4 GPa) for Mg_2SiO_4 has been found to be $1.8 \times 10^{-4}\,\mathrm{cm}^2/\mathrm{s\,kbar}$ at 700 K and $0.8 \times 10^{-4}\,\mathrm{cm}^2/\mathrm{s\,kbar}$ at 1100 K (Fujisawa *et al.*, 1968). Using the volume dependence of the Grüneisen parameter, Kieffer (1976) built a model for the lattice thermal conductivity of the mantle: she found it to be minimal at the depth of the olivine–spinel transition and reach the value $k \approx 0.01$ cal/cm s at the core–mantle boundary.

(iii) Electronic conduction

The carriers are electrons instead of phonons but the same general formula (6.152) applies:

$$k_e = \tfrac{1}{3} C v_F \Lambda \tag{6.164}$$

where k_e is the electronic conductivity, $C = nc$ is the electronic specific heat per unit volume (n is the number of electrons per unit volume and c is the specific heat of an electron), v_F is the velocity of electrons at the Fermi level and Λ is their mean free path between collisions. The electrons in a metal are also the carriers of electric current and the electrical conductivity σ was given in the free-electron approximation by the Drude formula (6.118):

$$\sigma = \frac{ne^2\Lambda}{m_e v_F} \tag{6.165}$$

We therefore have:

$$\frac{k_e}{\sigma} = \frac{1}{3}\frac{m_e v_F^2 c}{e^2} \tag{6.166}$$

With $c = \frac{3}{2}k_B$, and $\frac{1}{2}m_e v_F^2 = \frac{3}{2}k_B T$, we have:

$$\frac{k_e}{\sigma T} = \frac{3}{2}\left(\frac{k_B}{e}\right)^2 \tag{6.167}$$

The rigorous quantum mechanical treatment (Ziman, 1965) would give:

$$\frac{k_e}{\sigma T} = \frac{\pi^2}{3}\left(\frac{k_B}{e}\right)^2 = L_0 = 2.45 \times 10^{-8}\,[\mathrm{W\Omega/K^2}] \tag{6.168}$$

This is the *Wiedemann–Franz* law. L_0 is known as the Lorentz number.

The Wiedemann–Franz law is generally well verified for metals, with values of the ratio in rather good agreement with the theoretical value of L_0 (2.47×10^{-8} for Fe and 2.23×10^{-8} for Cu at 0 °C).

At low temperatures, the mean free path of electrons is constant and determined by the distribution of defects and impurities; the electrical conductivity is constant and by the Wiedemann–Franz law, we see that the thermal conductivity varies linearly with T.

At high temperatures, the electrons are scattered by phonons and their mean free path is proportional to $1/T$, hence the electronic thermal conductivity varies as $1/T$.

The order of magnitude of k_e can be calculated (Animalu, 1977), taking typical values for $v_F \approx 10^8$ cm/s, $\Lambda \approx 10^{-5}$ cm and $C \approx 0.1R$ cal/mol. It is found to be two orders of magnitude larger than for lattice conductivity:

$$k_e = \frac{30R}{V_{mol}}$$

Metals are normally much better heat conductors than are electrical insulators; however, if the maximum of lattice conductivity occurs at relatively high temperature, the heat conductivity of an electrical insulator may be quite large. This is the case for diamond, whose heat conductivity at room temperature is about 2000 W/mK, compared to 400 W/mK for copper.

(iv) Radiative conductivity

In non-opaque media, a sizeable fraction of energy transfer at high temperatures may occur by thermal radiation (photon transfer). The *opacity* ε of a medium is defined by the decrease of the intensity, due to absorption and scattering, of a pencil of radiation passing through a thickness x of material:

$$I = I_0 \exp(-\varepsilon x) \tag{6.169}$$

The opacity is the reciprocal of the mean free path of radiation.

In the simplest case, in which the opacity is assumed to be independent of the wavelength of the radiation, the *radiative conductivity* k_r can be written (Clark, 1957):

$$k_r = \frac{16n^2ST^3}{3\varepsilon} \tag{6.170}$$

where n is the refractive index and S the Stefan–Boltzmann constant. With $n \approx 1.7$ (a typical value for ferromagnesian silicates), one gets:

$$k_r \approx 9.2 \times 10^{-9} \frac{T^3}{\varepsilon} \ [\mathrm{W/m\,K}] \tag{6.171}$$

One of the important mechanisms responsible for opacity in the ferromagnesian silicates is the absorption of photons causing the charge transfer from Fe^{2+} to Fe^{3+} (or, equivalently, the excitation of electrons from one narrow band to another). We have seen that the same charge-transfer process can be thermally activated and is then responsible for hopping electrical conduction. High pressure, favoring overlapping of the electronic orbitals of neighboring ions, increases the optical absorption due to charge transfer and causes the absorption edge to shift from the ultraviolet to the visible and infrared regions of the spectrum. It is then possible for energy transfer by radiation in the lower mantle to be effectively blocked, the increase of opacity with pressure overriding the T^3 dependence of the radiative conductivity (Mao, 1972, 1976).

7
Earth models

> Inferences about the interior of the Earth, so far from being all inferior to those in the 'exact' sciences, range from those which are indeed flimsily based to inferences that are now as well established as commonly accepted results in standard physics.
> *K. E. Bullen, The Earth's Density (1975)*

7.1 Generalities

All the information we have about the inaccessible interior of the Earth is embodied in Earth models which, if they are well constrained by observations and physical laws, are, at least in some respects, open to as little doubt as accepted tenets of, for instance, astronomy.

The previous chapters were devoted to laying the groundwork of the physics and thermodynamics that apply to the materials constituting the deep Earth, emphasizing the contribution of laboratory experimentation. We are now in a position to summarily present the recent view of the inner Earth that results from the conjunction of these physical constraints with a corpus of ever-improving geophysical observations.

We will follow the traditional, and convenient, habit of separately considering seismological, thermal and compositional (mineralogical) Earth models. It must, of course, be kept in mind that they strongly interact (Fig. 7.1).

The seismological models are based on velocity–depth profiles determined from the travel-time–distance curves for seismic waves and on periods of free oscillations (see Bullen and Bolt, 1985 and, for a clear elementary presentation, Bolt, 1982). Due to the development of worldwide networks of three-component broad-band seismographs, there are more and more data, of better and better quality. At the initiative of the

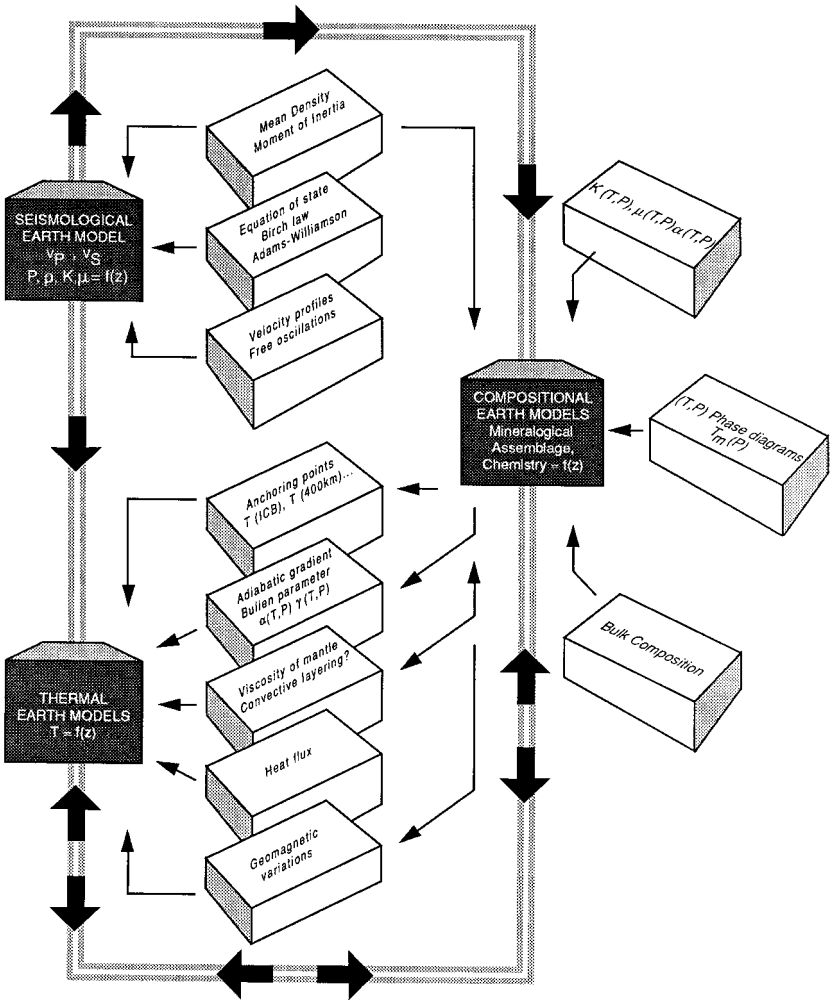

Figure 7.1 Interrelations between seismological, compositional, and thermal earth models.

International Association of Seismology and Physics of the Earth's Interior (IASPEI), a Preliminary Reference Earth Model (PREM) was set up (Dziewonski and Anderson, 1981). Although new global travel-time tables and velocity models (*iasp 91*) have since been generated (Kennett and Engdahl, 1991), PREM is still, in practice, the most currently used global seismological model.

Seismological models yield pressure, density and elastic moduli as functions of depth and, before introducing the PREM model, we will deal with

the fundamentals of density-profile determination. Bolt (1991) gave a critical analysis of the precision of density estimations from seismological models.

Thermal models necessarily depend on experimentally determined thermodynamic parameters, as well as observations of heat flux and geomagnetic variations. The temperature–depth profile (geotherm) has a strong influence on the compositional models since we need to know the temperature at a given pressure to infer from the experimentally determined phase diagrams which minerals are stable.

The compositional models, constrained by the density and velocity profiles from seismological models, in turn react on the thermal models by anchoring the geotherm and by allowing or forbidding convective layering, thus making the introduction of thermal boundary layers necessary or not.

7.2 Seismological models

7.2.1 Density distribution in the Earth

Knowing the mass of the Earth $M = 5.974 \times 10^{24}$ kg and its mean radius $R = 6371$ km, it is obvious that its mean density $\bar{\rho} = 5.515$ is higher than the average density (2.7 to 3.3) of the rocks found at the surface of the Earth. Besides, the moment of inertia of the Earth about its rotation axis, determined from flattening and precession measurements is $I = 0.33MR^2$, smaller than the value $0.4MR^2$ that would obtain for a homogeneous sphere of constant density, thus pointing to a concentration of mass near the center of the Earth. It could, of course, be entirely due to an increase in density with depth as the rocks are compressed. It is therefore necessary to examine the variation of density with depth, due to compression alone, of an isochemical material; it will turn out that it is insufficient to account for all of the mass concentration toward the center.

We assume that the compression is adiabatic, i.e. that there is no exchange of heat which could cause temperature variations and add a thermal expansion contribution to the density variations with pressure. We also assume that the Earth is in hydrostatic equilibrium and spherically symmetrical, hence:

$$dP = -\rho g dr \tag{7.1}$$

where P is the pressure at radius r or depth z (r[km] = 6371 − z) and ρ and g are the density and acceleration of gravity at radius r respectively, with:

$$g = Gmr^{-2} = 4\pi G r^{-2} \int_0^r \rho r^2 dr \tag{7.2}$$

where m is the mass of the sphere of radius r and density ρ and $G = 6.66 \times 10^{-8}$ SI is the gravitational constant. Hence:

$$\frac{dP}{dr} = -4\pi G\rho r^{-2} \int_0^r \rho r^2 dr \tag{7.3}$$

By definition of the (adiabatic) bulk modulus K and of the seismic parameter Φ, we have:

$$\frac{d\rho}{dP} = \frac{\rho}{K} = \Phi^{-1} \tag{7.4}$$

Hence, with (7.3):

$$\frac{d\rho}{dr} = -4\pi G K^{-1} \rho^2 r^{-2} \int_0^r \rho r^2 dr \tag{7.5}$$

or:

$$\frac{d}{dr}\left(r^2 K \rho^{-2} \frac{d\rho}{dr}\right) = -4\pi G r^2 \rho \tag{7.6}$$

N.B. Remembering that:

$$\frac{dU}{dr} = -g = \frac{dP}{dr}\rho^{-1}$$

where U is the gravitational potential, and with the definition of the Laplacian in spherical coordinates:

$$\nabla^2 U \equiv \frac{1}{r^2}\frac{d}{dr}\left(r^2 \frac{dU}{dr}\right)$$

we see that (7.6) is, in fact, Poisson's equation:

$$\nabla^2 U = 4\pi G\rho$$

Using an equation of state of the form:

$$K = C\rho^n \tag{7.7}$$

where C and n are constants, we obtain *Emden's equation* (first established to calculate the pressure inside stars):

$$\frac{d}{dr}\left(r^2 \rho^{n-2} \frac{d\rho}{dr}\right) = -A^2 r^2 \rho \tag{7.8}$$

with $A^2 = 4\pi G/C$.

We see, from (7.7), that:

$$n = \frac{d \ln K}{d \ln \rho} = \frac{dK}{dP} = K_0' \tag{7.9}$$

As we have seen before, $n \approx 4$ for the second-order Birch–Murnaghan equation.

Note that Laplace (1825), assuming that the derivative of the pressure with respect to the density was proportional to the density:

$$\frac{dP}{d\rho} = C\rho \tag{7.10}$$

had directly obtained equation (7.8) with $n = 2$, as immediately follows from (7.10). In this case Emden's equation (7.8) has a solution of the form: $\rho = \rho_0 (Ar)^{-1} \sin(Ar)$, but it has no simple solution in the general non-linear case.

Still assuming that the interior of the Earth is homogeneous and adiabatic, Williamson and Adams (1923) did not introduce an a-priori equation of state such as (7.7) into (7.5) to obtain a differential equation which turns out to be difficult to resolve for $\rho(r)$. They kept (7.5) under the form known as *Adams and Williamson's equation*:

$$\frac{d\rho}{dr} = -g\rho^2 K_S^{-1} = -g\rho\Phi_S^{-1} \tag{7.11}$$

or:

$$\ln\left(\frac{\rho}{\rho_0}\right) = -\int_{r_0}^{r} g\rho K_S^{-1} dr = -\int_{r_0}^{r} g\Phi_S^{-1} dr \tag{7.12}$$

where ρ_0 is the density at the surface of the Earth ($r = r_0$).

Equation (7.12) relating ρ and K for a given value of r is indeed an equation of state.

Using P- and S-wave velocity profiles determined from travel-time curves and starting from the surface with initial density 3 and 3.5, Williamson and Adams obtained a density–depth profile by approximation and repeated graphical integration, layer by layer. They find that the density variation due to compression alone accounts for the density profile in the lower mantle but that the density does not increase fast enough to make the mean density equal to 5.5. They conclude that: "It is therefore impossible to explain the high density of the Earth on the basis of compression alone. The dense interior cannot consist of ordinary rocks compressed to a small volume; we must therefore fall back on the only reasonable alternative,

namely, the presence of a heavier material, presumably some metal, which, to judge from its abundance in the Earth's crust, in meteorites and in the Sun, is probably iron."

The pressure–depth profile follows immediately by integration of (7.1). Williamson and Adams find the pressure at the center of the Earth $P_c = 318\,\text{GPa}$, which can be compared to the values $P_c = 308\,\text{GPa}$ found by Laplace and $P_c = 364\,\text{GPa}$ of the PREM model. Departure from the conditions of homogeneity and adiabaticity, hence from the conditions of validity of the Adams and Williamson equation can be expressed by the *Bullen parameter* η (Bullen, 1963), defined in the following fashion. The Adams–Williamson equation (7.11) can be written:

$$-\Phi_S \rho^{-1} g^{-1} \frac{d\rho}{dr} = 1 \tag{7.13}$$

If the conditions of adiabaticity or homogeneity are not fulfilled, the Bullen parameter is defined as being the value of the left-hand side member of (7.13), no longer equal to 1, since ρ then corresponds to a non-homogeneous or non-adiabatic region:

$$-\Phi_S \rho^{-1} g^{-1} \frac{d\rho}{dr} = \eta \tag{7.14}$$

The pressure derivative of the bulk modulus can be expressed in terms of the Bullen parameter; starting with the definition of the seismic parameter: $K = \rho\Phi$ and taking the derivative of K with respect to pressure, we obtain, with (7.14):

$$\frac{dK}{dP} = \left(\Phi \frac{d\rho}{dr} + \rho \frac{d\Phi}{dr}\right)\frac{dr}{dP} = \eta - \frac{1}{g}\frac{d\Phi}{dr} \tag{7.15}$$

which yields another expression for Bullen's parameter:

$$\eta = \frac{dK}{dP} + \frac{1}{g}\frac{d\Phi}{dr} \tag{7.16}$$

Another interesting expression for η immediately results from (7.14), if we write, on the model of (7.13):

$$\rho^{-1} g^{-1} \frac{d\rho}{dr} = -\Phi_S^{-1} \tag{7.17}$$

where ρ is the density of the non-homogeneous or non-adiabatic region; we then have:

$$\eta = \frac{\dfrac{d\rho}{dr}}{\left(\dfrac{d\rho}{dr}\right)_{\mathrm{AW}}} \tag{7.18}$$

The parameter η "gives the ratio of the actual density gradient to the gradient that would obtain if the composition remained uniform" (Bullen, 1963).

In the non-adiabatic, homogeneous, case, the Adams–Williamson equation can be corrected from the thermal expansion term, due to the superadiabatic gradient:

$$\frac{d\rho}{dr} = -g\Phi_S^{-1}\rho + \alpha\rho\left(\frac{dT}{dr} - \frac{g\alpha T}{C_P}\right) \tag{7.19}$$

With (7.18) and (7.17), we see that:

$$\eta = 1 - \frac{\alpha\rho\left(\dfrac{dT}{dr} - \dfrac{g\alpha T}{C_P}\right)}{\rho g\Phi_S^{-1}} < 1 \tag{7.20}$$

7.2.2 The PREM model

Seismological Earth models typically use the velocity–depth profiles and an equation of state relating ρ to K (or Φ or v_{P}) to obtain density, pressure and elastic moduli profiles. We will deal here only with the Preliminary Reference Earth Model PREM (Dziewonski and Anderson, 1981).

The Earth is divided into radially symmetrical shells separated by convenient seismological discontinuities, of which the principal are situated at depths of 400, 670, 2890 and 5150 km, corresponding to the seismic boundaries between uppermost mantle and transition zone, upper and lower mantle, mantle and core, and outer and inner core, respectively.

It is assumed that Adams and Williamson's equation is justified in each region from the center up to the 670 km discontinuity and that Birch's law $\rho = a + bv_{\mathrm{P}}$ can be applied in the upper mantle. The Earth's mass and its moment of inertia are given.

Starting values are assigned to the density below the crust ($\rho = 3.32$), at the base of the mantle ($\rho = 5.5$) and to the density jump between inner and outer core ($\Delta\rho = -0.5$).

The density at the center of the Earth and the jump in density at 670 km

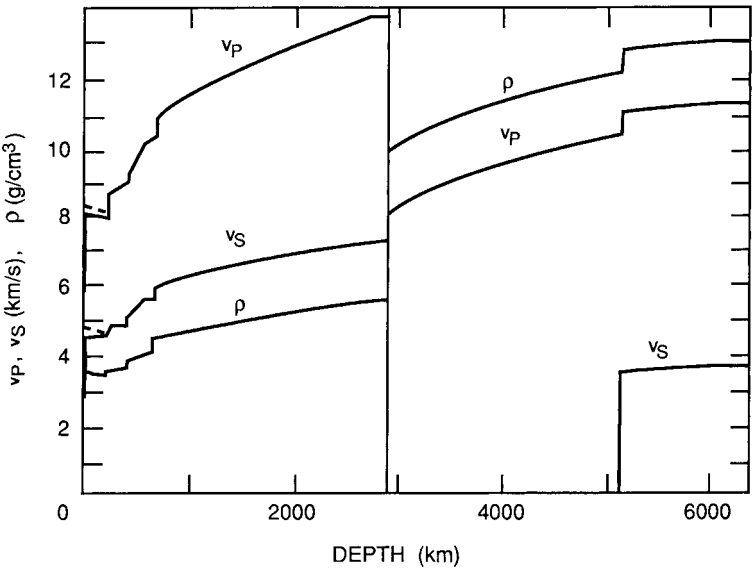

Figure 7.2 PREM model: Seismic velocities and density profile (after Dziewonski and Anderson, 1981).

are calculated and found to be $\rho_c = 12.97$ and $\Delta\rho = -0.35$ respectively. The starting density distribution is then known.

The observed values entering the model are the travel times of P and S body waves with a period of 1s and the periods of free oscillations, together with the attenuation factors. The starting model is defined by a set of five functions of radius: the velocities v_P and v_S; the density; and the attenuation factors in shear and compression. The inverse problem is solved simultaneously for elastic and anelastic parameters and perturbations are introduced into the starting model to satisfy the data. Elastic anisotropy is introduced in the uppermost 200 km of the upper mantle. The parameters of the final model are given as polynomials in r, or tabulated (see Appendix).

The velocity, density and pressure profiles of the PREM model are given in Figs. 7.2 and 7.3; the variation of the seismic parameter Φ and of Poisson's ratio with depth are given in Figs. 7.4 and 7.5.

Note that the Poisson's ratio of the outer core is equal to 0.5 as expected for a liquid, but the Poisson's ratio of the inner core is also quite high ($\nu = 0.44$). Various explanations have been given, including the possibility of liquid inclusions in the inner core. However, such conclusions are unnecessary, since a high Poisson's ratio does not necessarily imply the

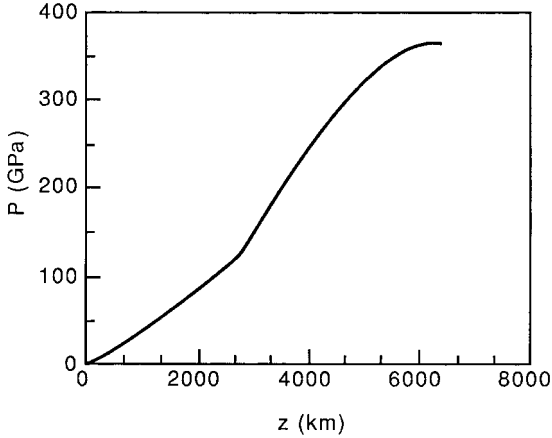

Figure 7.3 PREM model: Pressure profile.

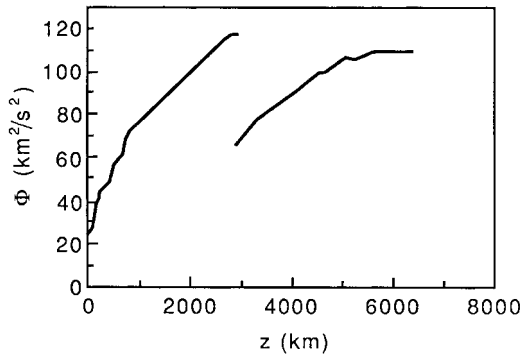

Figure 7.4 PREM model: Seismic parameter profile.

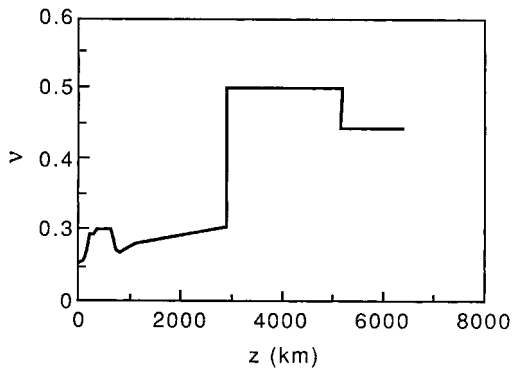

Figure 7.5 PREM model: Poisson's ratio profile.

presence of liquid: Some solid metals, for instance, have very high Poisson's ratios, e.g. $v = 0.42$ for gold and 0.45 for indium. Falzone and Stacey (1980) gave an explanation of the high Poisson's ratio at high pressure in terms of the second-order theory of elasticity.

7.3 Thermal models

7.3.1 Sources of heat

For a discussion of the sources of heat and temperatures in the Earth, the reader will profitably refer to Verhoogen's (1980) delightful and illuminating little book *Energetics of the Earth.*

The heat flux coming from inside the Earth can be measured at the surface; its mean value is about $80\,\mathrm{mW/m^2}$ or 4.2×10^{13} W (42 TW) for the whole Earth. This is, of course, a boundary condition for any thermal model but, to infer the temperature profile, one must also have some idea of the sources of the heat that is transported through the mantle and finally radiated out at the surface.

How much of the heat is original and how much is currently produced in the Earth? In other words, is the Earth still cooling from an original hot state, as was widely thought in the last century, or are there active sources of heat inside? We now know that radioactivity is the major heat source, but others may exist, and whether the Earth is still cooling is a matter of current debate. Let us briefly review the possible sources of heat.

(i) *The original heat*. This is the heat content of the Earth in the early stages of its history. It is essentially accretional heat, due to the dissipation of the gravitational energy when planetesimals bombarded the surface of the growing Earth, which eventually partly melted. There was also a contribution of short-lived, now extinct, radioactive elements such as ^{26}Al. During the differentiation stage that ensued, gravitational energy was again released when droplets of liquid iron or iron–sulfur eutectic trickled down to form the core. It is generally thought that the core was formed in a relatively short time, ending about 0.5 billion (0.5×10^9) years after the formation of the Earth, the corresponding heat therefore can be said to be "original". It is believed, although not universally, that the original heat contributes little to the thermal budget, with the exception of the heat stored in the liquid core.

(ii) *Radiogenic heat*. Decay of the radioactive elements present in the mantle is the main source of heat in the Earth. The principal radioactive

elements are: ^{235}U, ^{238}U, ^{232}Th whose decay eventually gives ^{207}Pb, ^{206}Pb, ^{208}Pb respectively, and ^{40}K whose decay gives ^{40}Ca and ^{40}Ar. The heat production per mass unit of each element is well known but their concentration in the Earth is much less certain. One estimate (Verhoogen, 1980) leads to the approximate lower bound of 2.4×10^{13} W for the total radiogenic production of heat in the mantle, i.e. about 60% at least of the total output of heat.

(iii) *Other sources of heat*. These include: tidal dissipation in the solid Earth, negligible at the present time, although it may have been important in the past, when the Moon was closer to the Earth; frictional dissipation in the convecting mantle; and latent heat released in exothermal phase transitions (e.g. olivine–spinel). All these contributions are unimportant when compared to that of radiogenic heat. However, in addition to the secular cooling of the core, a non-negligible contribution to the heat output of the core is made by the latent heat released during crystallization of the inner core and by the gravitational energy released as the fluid enriched in light elements by crystallization of the inner core rises.

N.B. The latent heat released during crystallization of the inner core is $L = T_m \Delta S_m$. With the values calculated by Poirier (1986) for the temperature of the inner core boundary ($T_m = 5000$ K) and the melting entropy ($\Delta S_m = 5.83$ J/mol K) and taking a molar volume at the pressure of the inner core boundary of 4.38 cm^3/mol and density of 12, we find: $L = 5.55 \times 10^5$ J/kg.

The heat flux from the core into the lower mantle is another boundary condition of the convective problem. It is not known, but lower and upper bounds of its value can be estimated to be 1 TW and 10 TW, corresponding to 6 mW/m^2 and 60 mW/m^2, respectively (see Buffett *et al.*, 1992 and Labrosse *et al.*, 1997). Verhoogen (1980) estimates that about 2.6 TW come from the cooling of the whole core, 0.34 TW come from the crystallization of the inner core and 0.66 TW correspond to the gravitational energy term. With these estimates, the total heat output of the core (input into the lower mantle) could be $Q_c \approx 3.6$ TW, about 10% of the total heat output of the Earth.

7.3.2 Heat transfer by convection

We have seen (Section 6.6) that, due to the opacity of the iron-bearing minerals under high pressure, radiative transfer of heat is most probably negligible in the Earth's mantle. The two remaining mechanisms for heat transfer are then conduction, consisting in heat transport by thermal

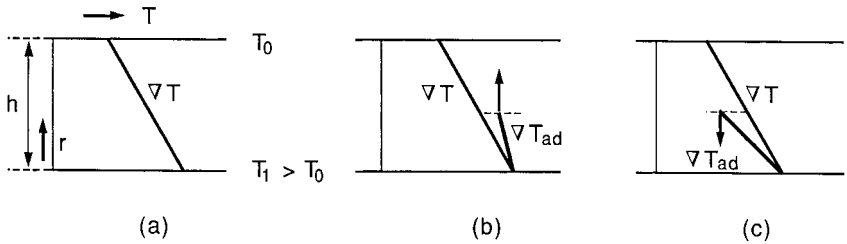

Figure 7.6 Convective instability in a sheet of fluid heated from below. (a) Temperature profile. (b) The temperature profile is superadiabatic: a parcel of fluid displaced upward is lighter than the surrounding fluid and keeps going up (convective instability). (c) The temperature profile is subadiabatic: a parcel of fluid displaced upward is heavier than the surrounding fluid and falls back (stable layering).

vibrations of the mineral lattices, and convection, in which the heat-containing matter is transported bodily in a fluid-like manner: On the time-scale of the geophysical phenomena (e.g. plate tectonics) the mantle can be considered as a fluid endowed with a very high viscosity (10^{21}–10^{22} Pa s).

It is completely beyond the scope of this book to deal with the fluid mechanics of convection. However, we will give the physical bases of the convective phenomenon in the simpler case of a fluid heated from below in a gravity field (Rayleigh–Bénard convection) (see Tritton, 1977; Turcotte and Schubert, 1982).

Let us consider a laterally infinite layer of fluid of density ρ in the gravitational field of the Earth, bounded by plane surfaces at $r = 0$ and $r = h$ (Fig. 7.6(a)). The upper surface is maintained at a fixed temperature T_0, while the lower surface is maintained at $T_1 > T_0$, thus establishing a temperature gradient $\nabla T = (T_1 - T_0)/h$ through the fluid. Let us now consider a small parcel of fluid at $r = 0$ and $T = T_1$ and let it rise rapidly by δr. It undergoes an adiabatic decompression and its temperature is lowered by:

$$\delta T = -\nabla T_{ad} \delta r \tag{7.21}$$

where ∇T_{ad} is the *adiabatic gradient*, given by (2.56). Since $dP = \rho g dz = -\rho g dr$, we have:

$$\nabla T_{ad} = \frac{dT}{dz} = \frac{g\alpha T}{C_P} \tag{7.22}$$

Note that we have:

$$\nabla T_{\mathrm{ad}} = \frac{g\gamma_{\mathrm{th}}}{\Phi} T \tag{7.23}$$

where γ_{th} is the thermodynamic Grüneisen parameter and Φ the seismic parameter; the adiabatic gradient in the lower mantle is about 0.3 K/km.

- If the temperature gradient in the fluid is subadiabatic, i.e. $|\nabla T| < |\nabla T_{\mathrm{ad}}|$ (Fig. 7.6(c)), the parcel of fluid is cooler, hence denser, than the surrounding fluid and sinks again. The fluid is stratified and stable with respect to convection. Heat is transported by conduction and the heat flux (per unit time and area) is:

$$H_{\mathrm{c}} = -k\nabla T = k\frac{T_1 - T_0}{h} \tag{7.24}$$

  where k is the thermal conductivity of the fluid.
- If the temperature gradient in the fluid is superadiabatic, i.e. $|\nabla T| > |\nabla T_{\mathrm{ad}}|$ (Fig. 7.6(b)), the parcel of fluid is warmer and lighter than the surrounding fluid, it is buoyant and will go on rising. The situation is unstable.

The criterion for the onset of convection is therefore that the temperature gradient be superadiabatic, or that the Bullen parameter be smaller than unity. The density of a fluid parcel displaced by δr upward is: $\rho + \delta r(d\rho/dr)_{\mathrm{ad}}$, while the density of the surrounding fluid is $\rho + \delta r(d\rho/dr)$, the gravitational force on the parcel is therefore: $-g\delta r[(d\rho/dr)_{\mathrm{ad}} - (d\rho/dr)]$ and the equation of motion of the parcel is:

$$\rho\frac{d^2\delta r}{dt^2} + g\delta r\left[\left(\frac{d\rho}{dr}\right)_{\mathrm{ad}} - \frac{d\rho}{dr}\right] = 0 \tag{7.25}$$

The fluid parcel oscillates about its original position with the *Brunt–Väisälä frequency N* (see Tritton, 1977):

$$N = \left\{\frac{g}{\rho}\left[\left(\frac{d\rho}{dr}\right)_{\mathrm{ad}} - \frac{d\rho}{dr}\right]\right\}^{1/2} \tag{7.26}$$

The Brunt–Väisälä frequency can be related to the Bullen parameter η, by writing (7.26) as:

$$\frac{N^2\Phi_S}{g^2} = \frac{\Phi_S}{\rho g}\left[\left(\frac{d\rho}{dr}\right)_{\mathrm{ad}} - \frac{d\rho}{dr}\right] = -1 + \eta$$

which yields:

$$N^2 = \frac{g^2}{\Phi_S}(\eta - 1) \tag{7.27}$$

We see that, if the gradient is superadiabatic ($\eta < 1$), the frequency is imaginary and a convective instability sets in and can grow exponentially if the physical properties of the fluid (essentially its viscosity) are such as to allow convection. The condition $\eta < 1$ is necessary but not sufficient for convection. A tighter criterion is given by the dimensionless *Rayleigh number* $\mathscr{R}a$, defined, in the case of a fluid heated from below, by:

$$\mathscr{R}a = \frac{g\alpha h^3 \Delta T}{\nu\kappa} \tag{7.28}$$

In (7.28), $\nu = \eta/\rho$ is the kinematic viscosity of the fluid, κ is its thermal diffusivity, α its thermal expansion coefficient and $\Delta T = T_1 - T_0$.

The Rayleigh number measures the relative importance of the buoyancy force $g\alpha\Delta T$, favoring convection, and the viscosity drag force $\nu\nabla^2 V$, hindering convection:

$$\mathscr{R}a = \frac{g\alpha\Delta T}{\nu\nabla^2 V} \tag{7.29}$$

If we scale velocity V to the value U, length to L and time to L/U, we have: $\nabla^2 V \approx UL^{-2}$ and $\kappa \approx L^2(L/U)^{-1} = UL$, hence $U \approx \kappa L^{-1}$ and $\nabla^2 V \approx \kappa L^{-3}$. Equation (7.29) is therefore equivalent to (7.28).

In the case of a fluid heated from within, the Rayleigh number is (see Turcotte and Schubert, 1982):

$$\mathscr{R}a = \frac{g\alpha\rho q h^5}{\nu\kappa k} \tag{7.30}$$

where k is the thermal conductivity of the fluid and q is the rate of internal heat production.

A linear stability analysis shows that perturbations can grow exponentially when the Rayleigh number is greater than the critical Rayleigh number $\mathscr{R}a_c$. For fluids heated from below as well as from within, $\mathscr{R}a_c \approx 2000$.

N.B. Let us calculate an order of magnitude value for the Rayleigh number of the internally heated Earth's whole mantle, using values of the various parameters:

$$\rho \approx 4 \times 10^3\,\mathrm{kg\,m^{-3}},\ \alpha \approx 3 \times 10^{-5}\,\mathrm{K^{-1}},\ \kappa \approx 0.01\,\mathrm{cm^2\,s^{-1}},\ \eta \approx 10^{21}\,\mathrm{Pa\,s},$$
$$g \approx 10\,\mathrm{ms^{-2}},\ \nu = \eta/\rho \approx 3 \times 10^{17}\,\mathrm{m^2\,s^{-1}},\ h \approx 3000\,\mathrm{km},$$
$$k \approx 4\,\mathrm{Wm^{-1}\,K^{-1}},\ q \approx 9 \times 10^{-12}\,\mathrm{Wkg^{-1}}.$$

We find a Rayleigh number of about 2×10^9, considerably above the critical value.

The *Nusselt number* $\mathcal{N}u$, measures the thermal efficiency of heat transfer. It is equal to the ratio of the total heat flux H to the heat flux that would be transported by conduction in the same conditions. With (7.24), we have:

$$\mathcal{N}u = \frac{Hh}{k\Delta T} \tag{7.31}$$

For $\mathcal{R}a > \mathcal{R}a_c$, we have $\mathcal{N}u > 1$.

In steady state, convection in a viscous fluid is controlled by the coupled differential equations for conservation of momentum and for transport of heat:

$$\rho \frac{D\mathbf{v}}{Dt} = \sum \mathbf{F} \tag{7.32}$$

$$\frac{DT}{Dt} = \kappa \nabla^2 T \tag{7.33}$$

N.B. The symbol D/Dt represents the material (or convective) derivative, which must be used when considering the variation with time of a quantity y in a fluid moving with a velocity $\mathbf{v}$.

$$\frac{Dy}{Dt} = \frac{\partial y}{\partial t} + \sum_i \frac{\partial y}{\partial x_i}\frac{\partial x_i}{\partial t} = \frac{\partial y}{\partial t} + \sum_i \frac{\partial y}{\partial x_i} v_i$$

x_i and v_i $(i = 1, 2, 3)$ are the components of the position and velocity vectors respectively. We can write:

$$\frac{Dy}{Dt} = \frac{\partial y}{\partial t} + \mathbf{v}\cdot\nabla y$$

The term $\mathbf{v}\cdot\nabla y$ is called the advective term.

In the equation of conservation of momentum for a viscous fluid, the forces $\mathbf{F}$ to be taken into account are the force resulting from a pressure gradient and the force needed to overcome viscosity (see equation (6.18)). We can write (7.32) under the form known as *Navier–Stokes equation*:

$$\frac{\partial \mathbf{v}}{\partial t} + (\mathbf{v}\cdot\nabla)\mathbf{v} = -\frac{1}{\rho}\nabla P + \mathbf{g} + \nu\nabla^2\mathbf{v} \tag{7.34}$$

The heat transport equation in a convecting compressible fluid is found by writing the continuity equation for heat:

$$\rho T \frac{dS}{dT} = \nabla\cdot(k\nabla T) + H \tag{7.35}$$

where S is the entropy and H the heat source.

Using Table 1.2, we find:

$$\frac{dS}{dT} = -\frac{\alpha}{\rho}\frac{dP}{\mathrm{dT}} + \frac{C_P}{T}\frac{dT}{dt} \tag{7.36}$$

and we can write:

$$\rho T\frac{dS}{dT} = -\alpha T\left(\frac{\partial P}{\partial t} + \mathbf{v}\cdot\nabla P\right) + \rho C_P\left(\frac{\partial T}{\partial t} + \mathbf{v}\cdot\nabla T\right) \tag{7.37}$$

Assuming $\partial P/\partial \mathrm{t} = 0$, we have:

$$\rho T\frac{dS}{dT} = \rho C_P\left[\frac{\partial T}{\partial t} + \mathbf{v}\cdot\left(\nabla T - \frac{\alpha T}{\rho C_P}\nabla P\right)\right] \tag{7.38}$$

and, with (7.35) and (7.22):

$$\rho C_P\left[\frac{\partial T}{\partial t} + \mathbf{v}\cdot(\nabla T - \nabla T_{\mathrm{ad}})\right] = \nabla\cdot(k\nabla T) + H \tag{7.39}$$

In the case of vigorous convection, the term corresponding to the diffusion of heat, $\kappa\nabla^2 T$, is negligible compared to the advective term, $\mathbf{v}\cdot(\nabla T - \nabla T_{\mathrm{ad}})$. The heat is transported with matter and has no time to diffuse far. In the steady state, the temperature profile in the convecting fluid tends toward an adiabat.

At the top and bottom of the convection cells, where heat is tranferred into the convecting fluid or out of it, or between thermally coupled but isolated convecting systems, there must exist a *thermal boundary layer* through which heat is transferred by conduction and where the gradient is highly superadiabatic.

7.3.3 Convection patterns in the mantle

Continental drift and plate tectonics are proof enough that the upper mantle convects. There is no direct evidence for convection in the lower mantle and it was thought for some time that the viscosity increase with pressure could be so high as to prevent convection (McKenzie, 1967). This view, which partly resulted from not taking into account the decrease of activation volume for creep with increasing pressure (see e.g. Poirier and Liebermann, 1984), is no longer currently entertained: The Rayleigh number for the lower mantle is supercritical and the Bullen parameter is close to 1 in most estimates. So, it is now generally agreed that the lower mantle is

convecting, even though its viscosity may be one or two orders of magnitude greater than that of the upper mantle.

The controversy now centers, not on whether the lower mantle convects or not, but on whether it convects together with the upper mantle (whole-mantle convection) or separately, with a thermal boundary layer at 670 km (two-layer convection).

The arguments presented by each school of thought for their favorite model and against the other one, are generally cogent and persuasive, which makes the question difficult to decide for an unprejudiced observer, all the more so since their proponents usually rely, perforce, on various unverifiable assumptions and on the feeling that the opposite view would lead, in their opinion, to improbable values of parameters which are, anyway, very little constrained by observational data. Note also that many of the arguments brought forward merely say that a given observation or calculation is consistent with one style of convection but generally do not prove that another style is excluded.

Reviewing the extant literature on convection, including the experimental and numerical models, could be the subject of a whole book. It will suffice here to briefly present the pro and con arguments for the main contending models and leave the reader to make up her or his own mind. Note that some authors use a temperature profile to defend a convection style, while others posit a convection style to derive a temperature profile. Indeed, the two problems are so intimately linked that it is only for the sake of convenience that we deal with them in different paragraphs.

(i) *Two-layer convection.* The principal arguments proposed are:

- The deepest earthquakes stop at 670 km and their focal mechanisms imply down-dip compression. It is therefore concluded that the subducting plates cannot penetrate the lower mantle.
- The 670 km discontinuity, in addition to being due to a phase transition, is also a compositional and/or chemical boundary (Liu, 1979). The density and seismic velocities agree with a lower mantle richer in silica (Anderson and Bass, 1986; Duffy and Anderson, 1989) and/or richer in iron (D. L. Anderson, 1989a) than the upper mantle (see Section 7.4).
- The 670 km discontinuity is a sharp seismic reflector that cannot be produced by a phase transition occurring over a wide depth interval, hence it must also be a chemical boundary (Lees *et al.*, 1983).
- The mantle has the same composition throughout but the convective systems of the upper and lower mantle are isolated by the subducted lithosphere trapped between 600 and 700 km (Ringwood and Irifune,

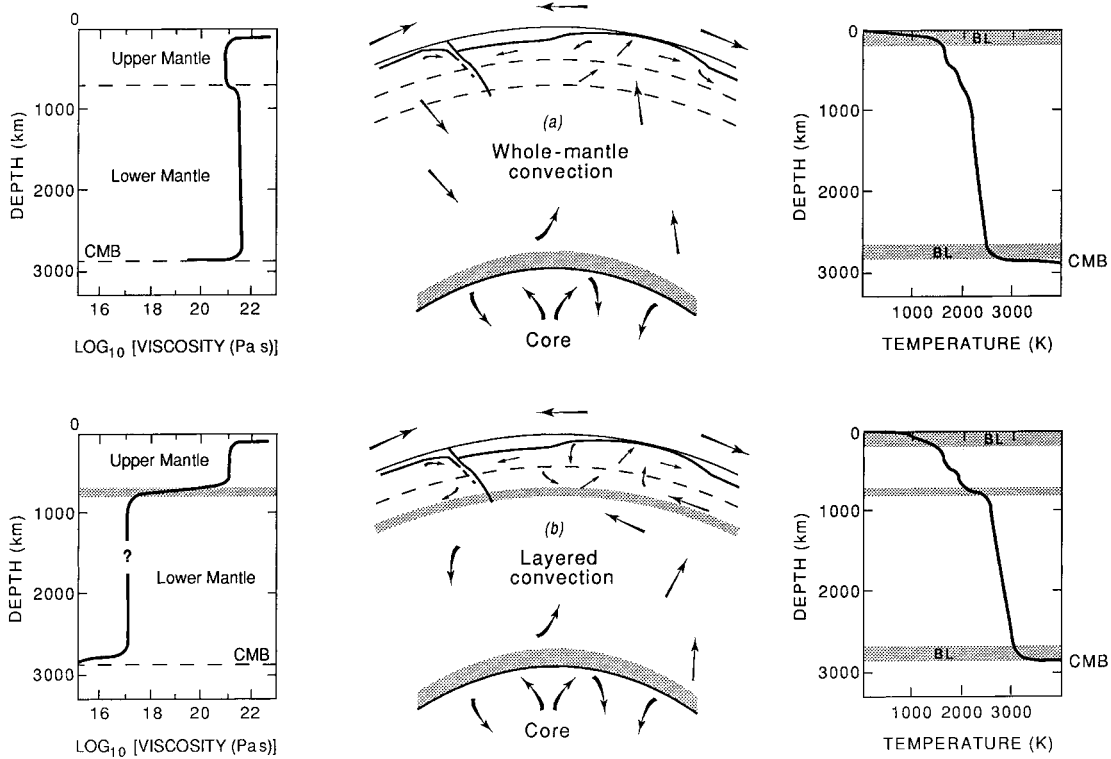

Figure 7.7 Schematic diagrams of (a) whole-mantle and (b) layered convection models, with corresponding temperature and viscosity profiles (after Peltier and Jarvis, 1982).

1988; Ringwood, 1994). A chemically heterogeneous "mesosphere boundary layer" between upper and lower mantle could be the source of the Ocean Island Basalts (Allègre and Turcotte, 1987).

- The upper and lower mantle are two different geochemical reservoirs that separately fractionated to produce the continental crust and the core, respectively (Allègre, 1982, 1987).
- A thermal boundary layer inside the mantle is required in the thermal model, in order to avoid using an unreasonably high value of the heat flux from the core into the mantle (Jeanloz and Richter, 1979).

(ii) *Whole-mantle convection.* A number of arguments in favor of this model are negative, i.e. against the two-layer model: They contend either that it is not required by the data (then, why not accept the simpler solution?) or that it would lead to unreasonable assumptions.

- A compositional difference between upper and lower mantle is not required (although not excluded) by the seismological data (Weidner, 1986; Jackson, 1998).
- The analysis of travel-times of deep earthquakes shows that there are fast (colder) regions below 670 km, in the prolongation of some subducting slabs which are therefore thought to penetrate into the lower mantle (Creager and Jordan, 1986; Fischer *et al.*, 1988). The seismically observed downward depressions of the 670 km discontinuity – "topography" of the discontinuity – (e.g. Wicks & Richards, 1993) can be interpreted as resulting from horizontal deflection of the subducting plates (Shearer and Masters, 1992), inhibiting convection across the boundary, but they are too small to prevent whole-mantle convection (Phipps Morgan and Shearer, 1993).
- The seismic constraints on the sharpness of the 670 km discontinuity are weak (Muirhead, 1985).
- The post-spinel phase transition at 670 km is sharp and could account for a good seismic reflectivity, a compositional difference between upper and lower mantle is not required (Ito and Takahashi, 1989).
- The existence of a thermal boundary layer at 670 km, where heat is transferred by conduction between the isolated convection cells, implies a high temperature gradient, hence a temperature in the lower mantle higher by about 800 °C than in the case of whole-mantle convection. As the lower-mantle viscosity is thermally activated, a higher temperature implies a viscosity of about 6×10^{16} Pa s for the lower mantle (Kenyon and Turcotte, 1983), whereas the viscosity deduced from post-glacial rebound is of the order of 10^{21} Pa s (Peltier and Jarvis, 1982) (Fig. 7.7).

Note, however, that in the absence of experimental data on the high-temperature creep of the lower-mantle material, any kind of extrapolated or otherwise calculated viscosity of the lower mantle is largely a matter of personal choice.

- Three-dimensional spherical models of whole-mantle convection (Bercovici *et al.*, 1989) predict upwelling plumes and downwelling sheets closely resembling the circum-Pacific subduction ring (but so would presumably 3-D models of two-layer mantle convection). Indeed, seismic tomography of the lower mantle shows a ring of high-velocity material, which projects to the surface as a circum-Pacific ring and might be the continuation of the subducting slabs (Olson *et al.*, 1990; Fukao, 1992; van der Hilst *et al.*, 1997).

Interesting observations of strong correlations between the geoid, the surface topography and the seismic velocity anomalies in the lower mantle have recently been presented (Hager *et al.*, 1985; Cazenave *et al.*, 1989); the geoid anomalies observed at the surface result from interior density contrasts (hot and cold matter) driving the convective flow and from the deformation of the boundaries caused by the flow. The magnitude and sign of the total effect depend on the viscosity profile and the style of convection. However, although the results of the analyses are compatible with one style of convection, they are not incompatible with the other.

- Finally, the study of the nature and composition of inclusions in some diamonds suggests a deep origin, possibly from the lower mantle (Kesson and Fitz Gerald, 1991; Kerr, 1993; McCammon *et al.*, 1997).

(iii) "*Middle of the road*" *convection.* Christensen (1984, 1995) modeled several types of convection and showed that "with the present uncertainties about the 670 km discontinuity a variety of convection styles are possible". He noted in particular that a phase-transition boundary alone could marginally produce a kind of leaky two-layer convection for current values of the Clapeyron slope, not significantly different from the most recent experimental value of -3 MPa/K (Ito and Takahashi, 1989). The influence of an endothermic phase transition at 670 km was further modeled by Machetel and Weber (1991) and Tackley *et al.* (1993), who found that downwelling cold material could accumulate above the discontinuity and be discharged at intervals, as avalanches into the lower mantle (see also Ringwood, 1991).

The seismic evidence that some plates penetrate into the lower mantle is now well accepted. Seismic tomography (see Montagner, 1994) provides a

rather convincing picture of the lower mantle (e.g. van der Hilst *et al.*, 1997), and improved 3-D computer modeling points to avalanches through the 670 km discontinuity. As a result, the style of convection of the mantle is now generally seen as intermediate between two-layer and whole-mantle convection: spatially non-uniform and temporally intermittent (Kerr, 1992, 1997). Some, but not all, plates, could sink down into the lower mantle through the 670 km discontinuity. Some cold material could accumulate above the discontinuity and intermittently go down in avalanches.

To reconcile the geochemical and seismological view points, Allègre (1997) proposes a time-dependent model of convection. Up to one billion years ago, two-layer convection would have taken place, with little exchange of matter between upper and lower mantle, then the convection pattern would have broken down, allowing some whole-mantle convection cells.

7.3.4 Geotherms

Temperature profiles (geotherms) are usually anchored at the depths of seismic discontinuities identified with phase transitions whose P, T boundaries are experimentally known or extrapolated. The principal discontinuities used are: the inner-core boundary (ICB), identified with the freezing of the liquid core iron alloy; and the 670 km discontinuity, identified with the post-spinel transition. Starting from these anchoring points, the geotherms follow an adiabat in the homogeneous regions where the Bullen parameter is close to 1 (lower mantle and outer core), the adiabatic gradient often being determined using a value of the acoustic Grüneisen parameter compatible with a seismological Earth model. The uncertainty is seldom claimed to be less than a few hundred degrees and often is of the order of 1000 K. The temperatures at various characteristic depths, determined in several studies, are given in Table 7.1 and the geotherms are shown in Fig. 7.8 (see also Duffy and Hemley, 1995).

In the lithosphere, the geotherm is often derived from pyroxene thermobarometry measurements made on peridotite xenoliths (e.g. Mercier, 1980).

In the transition zone, the most recent estimates using the phase diagram of the system Mg_2SiO_4–Fe_2SiO_4 (Ito and Katsura, 1989) give a temperature of 1400 °C at 350 km and of 1600 °C at 655 km.

In the lower mantle, Shankland and Brown (1985), starting from the temperature at 670 km (1600 °C) and using a seismological adiabatic gradient, arrive at a temperature of 3300 °C on the outer-core side of the

Table 7.1. *Temperatures inside the Earth* (*in Kelvin*)

z (km)	W72	V80	BS81	A82	SS84	BM86	P86	W87	IK89
100		1273		1450					
150		1473							
350									1400
371				1662					
655									1600
671 −			1873	1830	1970				
671 +				1980	2300				
1300	2800								
2571	3300			2814					
2885 −			2773	2937	3000				
2886 +			3573	3637	3800	3800	3800		
5156				4676	5000	5000		5000	6600
6371				4805			5000		6600

Source: W72: Wang (1972b). V80: Verhoogen (1980). BS81: Brown and Shankland (1981). A82: O. L. Anderson (1982). SS84: Spiliopoulos and Stacey (1984). BM: Brown and McQueen (1986). P86: Poirier (1986). W87: Williams *et al.* (1987a). IK89: Ito and Katsura (1989).

core–mantle boundary (CMB), in agreement with the temperature derived from their measurements of shock melting in iron, provided one assumes that the D" zone at the base of the mantle is a thermal boundary layer with $\Delta T = 800\,\mathrm{K}$. Under these conditions, they do not find it necessary to introduce a thermal boundary layer at 670 km.

Spiliopoulos and Stacey (1984) start upward from the temperature at the inner-core boundary, using $\Delta T = 800\,\mathrm{K}$ in the D" zone, and meet, at 670 km, a profile extrapolated down from the Mg_2SiO_4 phase transition. The temperature misfit of 300 K which they find is thought to be too small for a thermal boundary layer to be stable. They conclude that there is probably no boundary layer at 670 km, although it cannot be ruled out.

A temperature difference of 800 K across the D" zone corresponds to a gradient of 8 K/km over 100 km; this usually adopted value is derived from Fourier's law assuming a heat flux from the core of $0.032\,\mathrm{W/m^2}$ and a thermal conductivity of the lower mantle $k = 4\,\mathrm{W/m\,K}$. Brown (1986), taking into account the variation of k with temperature and pressure, finds that it could be three times larger than the currently adopted value at the core–mantle boundary, and that the need for a thermal boundary layer at the base of the mantle then disappears, unless one assumes an unrealistically high value for the heat flux from the core (higher than the heat flux at the surface of the Earth). Note, however, that there is a trade-off between

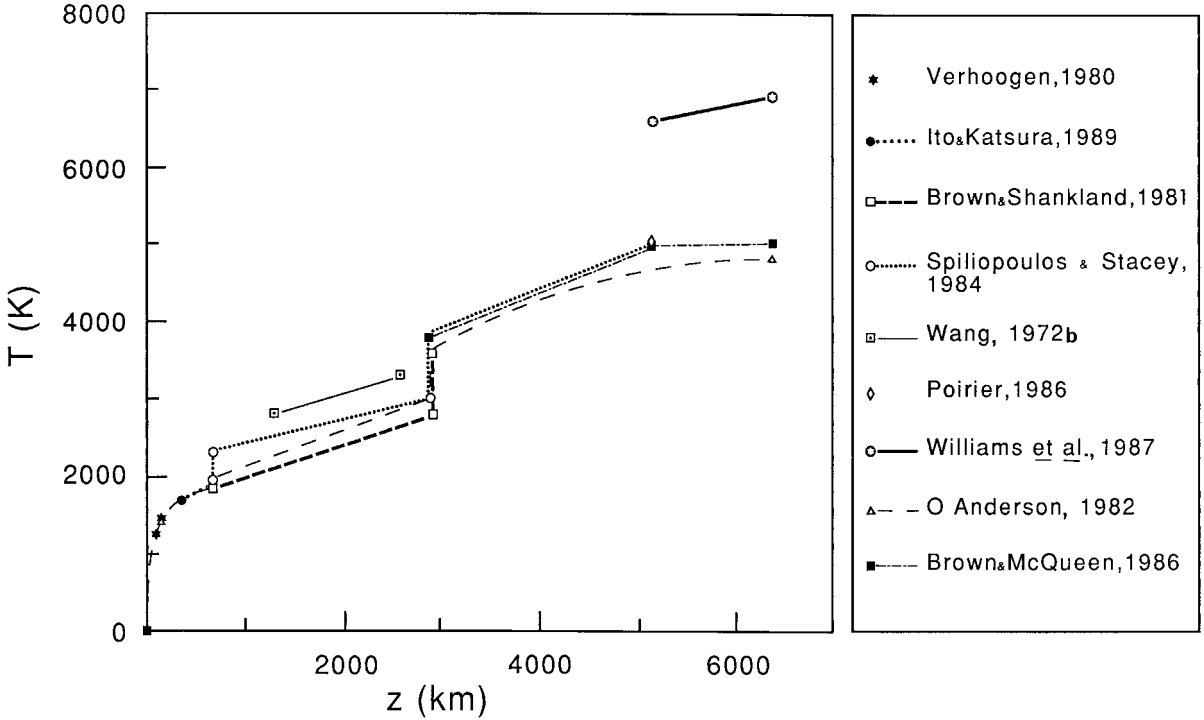

Figure 7.8 Geotherms. For all these temperature profiles, the error bar is about $\pm$ 800 K.

the thermal boundary layers at 670 km and at the core–mantle boundary and that the geotherms, estimated assuming a homogeneous mantle, cannot really be used as arguments for or against whole-mantle or two-layer convection.

Despite the large uncertainty on the temperatures, most models, whether based on theoretical calculations (Poirier, 1986; Poirier and Shankland, 1993) or extrapolations of the melting temperature of iron at the inner-core boundary (O. L. Anderson, 1982; Spiliopoulos and Stacey, 1984; Brown and McQueen, 1986; Anderson and Duba, 1997) generally agree on a temperature at the inner-core boundary between 5000 K and 6000 K (see Section 5.6).

7.4 Mineralogical models

7.4.1 Phase transitions of the mantle minerals

(i) Generalities on phase transitions

Nature's schemes for building up crystalline edifices from atoms are many, and compounds with a given crystal structure are generally stable only in a limited region of the temperature–pressure plane, where their Gibbs free energy is minimal. Even a simple element like iron has four known solid phases and the number of structures a polyatomic mineral can adopt at various pressures and temperatures can indeed be very large, especially if one considers the additional degree of freedom afforded by the possibility of partial replacement of one kind of atom by another (e.g. Mg by Fe, Si by Al, etc.). Descriptions of the atomic architecture of mineral structures can be found in the specialized volumes of the *Reviews in Mineralogy* or in such books as Wells (1984) or Muller and Roy (1974) for ternary oxides.

The number of thermodynamic degrees of freedom of a system (or *variance*) is the number of intensive parameters capable of independent variation. It is given by the Gibbs phase rule (see Callen, 1985):

$$\mathscr{V} = c + 2 - \phi \tag{7.40}$$

where $\mathscr{V}$ is the variance, c, the number of independent components, and ϕ, the number of phases in equilibrium.

In the simplest case of one-component systems, when the only intensive variables are temperature and pressure, the equilibrium between two phases is univariant and the domains of stability of two phases in the P–T plane are separated by a line boundary, i.e. the equilibrium pressure and temperature cannot be varied independently. The map of the stability

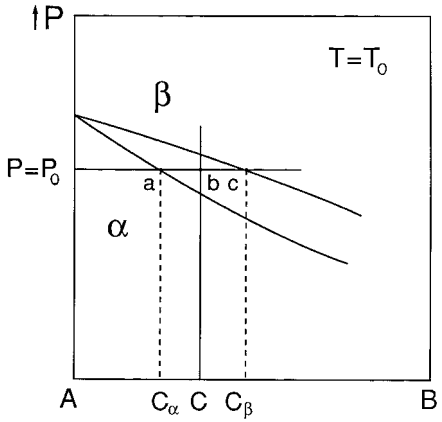

Figure 7.9 Lever rule: At $T = T_0$ and $P = P_0$ and for a composition C, for example x mol% of component B, the mole fraction x_β of high-pressure phase β, of composition C_β, and the mole fraction x_α of low-pressure phase α, of composition C_α, are in the proportion $x_\alpha/x_\beta = bc/ab$.

domains of the phases in the P–T plane is the *phase diagram*. For binary (two-component) systems, one usually considers sections of the three-dimensional phase diagram by planes of constant T or P. The phase-diagram boundaries are replaced by two-phase loops and at a given P (or T), for a given global composition, there are equilibrium mixtures of two phases. The proportion of the phases varies with T (or P) and is given by the "lever rule" (see Callen, 1985) (Fig. 7.9). The case of ternary systems is obviously more complicated and one often uses "pseudo-binary diagrams" (e.g. P, Fe % at constant T, between the compositions $MgSiO_3$ and $FeSiO_3$ in the ternary system MgO–FeO–SiO_2). One must of course beware not to reason on pseudo-binary diagrams as if they were binary diagrams.

Phase transitions can be usefully classified according to their *order* in Ehrenfest's sense (see Rao and Rao, 1978). For first-order transitions, there is a discontinuity in the first derivatives of the Gibbs free energy: entropy S and specific volume V. Hence, first-order transitions are accompanied by a volume change ΔV and latent heat $L = T\Delta S$ is absorbed (endothermal transition) or evolved (exothermal transition).

The slope of the phase boundary is given by the Clausius–Clapeyron relation (5.2):

$$\frac{dT_t}{dP} = \frac{\Delta V}{\Delta S} \tag{7.41}$$

already mentioned in the case of melting (melting is a first-order phase transition). Here, T_t is the temperature of transition at pressure P.

The specific volume of the high-pressure phase is always smaller than that of the low-pressure phase, and the high-temperature phase always has a higher entropy than the low-temperature phase. In many cases, the high-pressure phase has a lower entropy than the low-pressure phase and its stability field is wider at low temperatures, i.e. the slope of the Clapeyron is positive. However, at very high pressures, when the increase of the coordinance of the small cations (e.g. silicon going from 4 to 6 coordinance) is accompanied by an increase in the length of certain bonds, the transition toward the high-pressure phase may be accompanied by an increase in entropy. The slope of the Clapeyron is then negative. This was predicted by Navrotsky (1980) and verified in the case of the very-high-pressure phases of the mantle silicates (see below).

In a first-order phase transition, the phases are physically separated by a surface of discontinuity: the phase boundary. In many cases, the transformation operates by nucleation and growth of one phase at the expense of the other, growth being effected by diffusion-controlled displacement of the phase boundary.

Martensitic transformations are rapid, diffusionless transformations characterized by crystallographic orientation (topotactic) relations between parent and daughter phase and corresponding to a shear of the lattice.

For second-order phase transitions, the discontinuity in the derivatives of the Gibbs free energy affects only the second derivatives (e.g. specific heat, incompressibility) and there is no coexistence of phases on each side of a phase boundary. These transitions are often displacive transitions, the change in crystal structure corresponding to a mere distortion of the bonds, whereas in reconstructive first-order transitions atoms have to change places.

For more information on the mechanisms and kinetics of phase transitions in minerals, the reader is referred to Putnis and McConnell (1980) and Putnis (1992). The phase diagrams of elements, oxides and silicates have been reviewed by Liu and Bassett (1986).

In the following sections, we will summarize the state of the art concerning the experimental data on the principal isochemical phase transitions thought to occur in the Earth's mantle, particularly focusing on the polymorphic transitions of $MgSiO_3$ and Mg_2SiO_4. Most of the progress in recent years (see Akimoto, 1987) has been achieved using two high-pressure techniques: the multi-anvil apparatus, up to about 25 GPa and the laser-

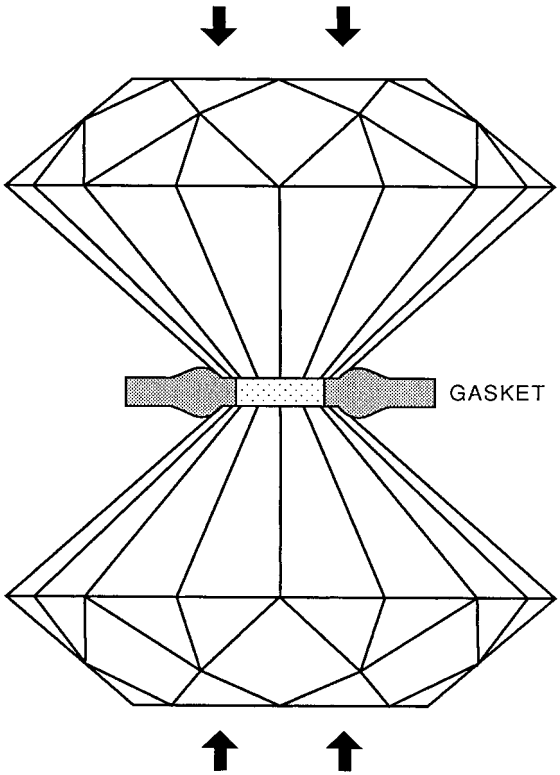

Figure 7.10 Principle of the diamond–anvil cell. The sample (stippled) is contained in a small hole (200–400 μm) drilled in a metal gasket, compressed by the diamonds. It can be heated by focusing a laser beam on it.

heated diamond-anvil cell (Fig. 7.10), up to 100 GPa (Ming and Bassett,1974; Bassett, 1977; Hemley *et al.*, 1987a).

(ii) The phase transitions of $MgSiO_3$

The phase diagram of $MgSiO_3$ has been investigated by Ringwood (1967), Liu (1976), Ito and Yamada (1982), Ito and Navrotsky (1985), Kato and Kumazawa (1985a), Sawamoto (1987), Irifune (1987), Akaogi *et al.* (1987) and Ito and Takahashi (1989) among others. The resulting phase diagram in the *P–T* plane (D. L. Anderson, 1987b) is shown in Fig. 7.11, and the pseudo-binary diagram at 1000 °C (Jeanloz and Thompson, 1983) is given in Fig. 7.12.

The low-pressure phase with composition $MgSiO_3$ is *enstatite*, an orthorhombic pyroxene with two formula units per unit cell ($Mg_2Si_2O_6$); its

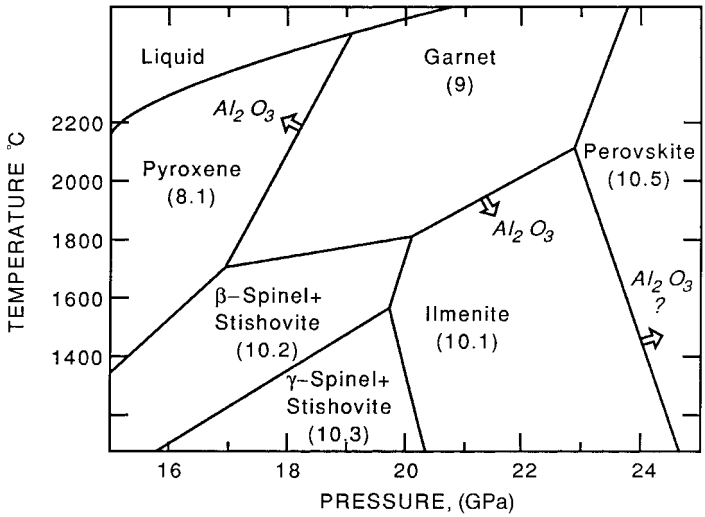

Figure 7.11 *P–T* phase diagram for $MgSiO_3$ composition. The approximate velocity of P-waves (in km/s) is indicated below the names of the mineral phases. The arrows show the direction in which the phase boundaries are expected to move when Al_2O_3 is added (after D. L. Anderson, 1987b).

structure can be described as consisting of chains of corner-sharing SiO_4 tetrahedra, with Mg^{2+} cations in the appropriate sites between the chains. Enstatite forms a continuous solid solution with the pyroxene *ferrosilite* $FeSiO_3$. The upper-mantle material, found in peridotite xenoliths or in ophiolites has a composition $Mg_{1-x}Fe_xSi_2O_6$, with $x \cong 0.1$ in most cases. At higher pressures, the orthorhombic enstatite changes to monoclinic clinoenstatite. At pressures between about 17 and 19 GPa and above about 2000 K, the pyroxene transforms into a phase with a garnet structure (isolated tetrahedra) and 4 formula units per unit cell ($Mg_4Si_4O_{12}$). The aluminous garnet *pyrope* has a formula ($Mg_3Al_2Si_3O_{12}$) resulting from the replacement of one Si^{4+} ion by one Al^{3+} ion and compensating the charge imbalance by replacing one Mg^{2+} by one Al^{3+}. At upper-mantle pressures, pyrope is soluble in the silicate garnet, giving the aluminous silicate garnet *majorite*, first identified in shocked meteorites and later synthesized by Ringwood and Major (1971). Alumina (Al_2O_3) widens the garnet stability field (Fig. 7.11). At pressures above about 20 GPa and temperatures lower than about 2000 K, $MgSiO_3$ garnet transforms into a phase with the *ilmenite* structure (Liu, 1976), that can be described as a corundum (Al_2O_3) structure with Mg^{2+} and Si^{4+} located in an ordered alternate fashion in the six-coordinated Al^{3+} sites. At lower-mantle pressures, the silicate

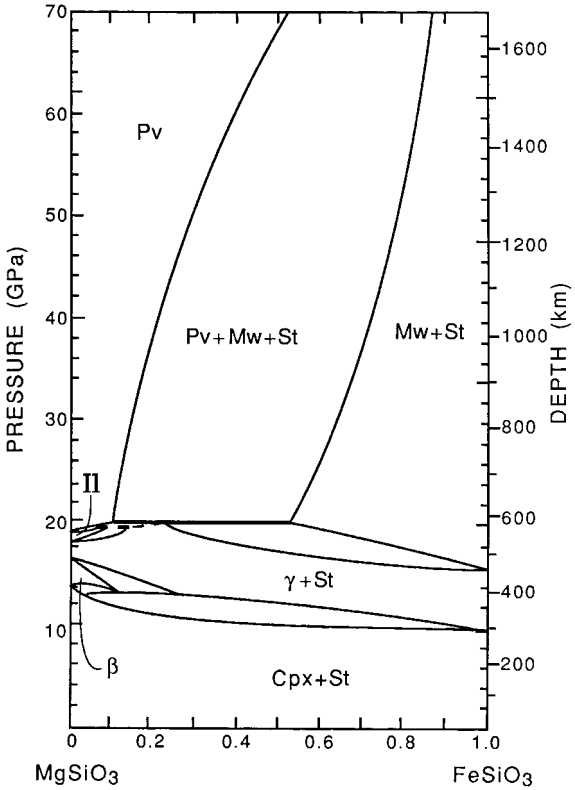

Figure 7.12 Isothermal ($T = 1000\,^{\circ}C$) phase diagram for the $MgSiO_3$–$FeSiO_3$ system. The crystalline structures are Cpx (clinopyroxene), β (β-phase), γ (γ-spinel), Mw (magnesiowüstite), St (stishovite), Pv (perovskite) (after Jeanloz and Thompson, 1983).

ilmenite transforms into a phase with the *perovskite* structure (Fig. 7.13), that can be described as a 3-D framework of corner-sharing SiO_6 octahedra, with Mg^{2+} in the dodecahedral sites. The slope of the Clapeyron, in the range 1000–1600 °C for the ilmenite–perovskite transition is negative, and is given (Ito and Takahashi, 1989) by: $P[\text{GPa}] = 26.8 - 0.0025T[^{\circ}\text{C}]$.

The existence of the perovskite phase was proved experimentally by Liu, who synthesized it in the diamond-anvil cell, first from pyrope (Liu, 1974), then by decomposition of Mg_2SiO_4 at high pressure (Liu, 1975a).

$(Mg, Fe)SiO_3$ perovskite is probably the most abundant mineral in the Earth, since it constitutes possibly more than 80 vol.% of the lower mantle. It is orthorhombic, at least up to 100 GPa at room temperature, with a structure derived from the ideal cubic perovskite by tilting of the octahedra

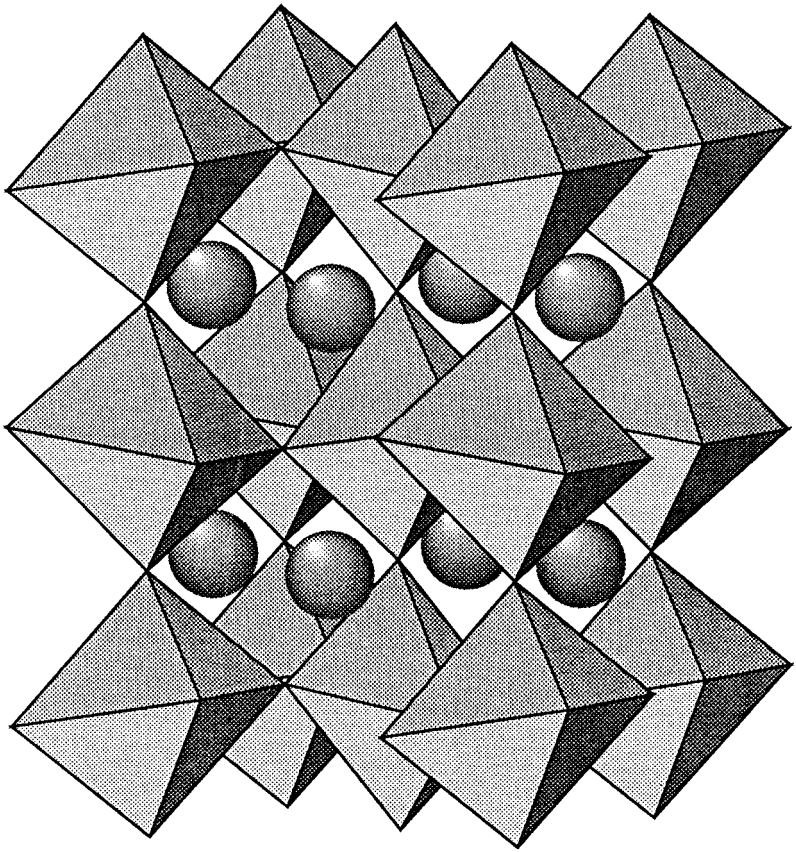

Figure 7.13 Structure of $MgSiO_3$ perovskite. The Mg cations are in dodecahedral sites between tilted corner-sharing SiO_6 octahedra. (The oxygen ions at the corners and the silicon ions at the centers of octahedra are not represented.)

(see Fig. 7.13) ($GdFeO_3$ distortion, see Muller and Roy, 1974). Measurement of the evolution of the distortion of the analog oxide perovskites $SrZrO_3$ led to the suggestion that $MgSiO_3$ perovskite might become cubic at mantle pressures (Andrault and Poirier, 1991). The high density of twins observed by electron microscopy in $(Mg, Fe)SiO_3$ perovskite quenched from high temperature might also point to the existence of a cubic phase at high temperature (Wang *et al.*, 1992). However, X-ray observation of $MgSiO_3$ perovskite at 36 GPa and 1900 K showed that it remained orthorhombic (Funamori and Yagi, 1993), in agreement with *ab-initio* electronic structure calculations (Stixrude and Cohen, 1993; Wentzcovitch *et al.*, 1995). Meade *et al.* (1995) found experimentally that $(Mg, Fe)SiO_3$ perov-

skite at 1850 K does indeed stay orthorhombic at 38 GPa, but becomes cubic at 64 and 70 GPa.

$FeSiO_3$ cannot take the perovskite structure, and above a certain concentration of iron, depending on temperature (see Fig. 7.12), $(Mg, Fe)SiO_3$ perovskite decomposes into stishovite SiO_2 and magnesiowüstite (Mg, Fe)O. Aluminum in solution in $(Mg, Fe)SiO_3$ perovskite expands its compositional stability field toward greater iron concentrations, up to 90 mol% of the ferrous end member for 25 mol% Al_2O_3 in solution (Kesson *et al.*, 1995).

The question arises whether perovskite remains stable in the lower mantle or decomposes to mixed oxides (which, incidentally, was the commonly accepted view before perovskite was identified as the high-pressure phase of enstatite). Indeed, $(Mg, Fe)SiO_3$ perovskite heated for more than one hour at 70 GPa decomposes into stishovite and magnesiowüstite (Meade *et al.*, 1995). Saxena *et al.* (1996) found that, at pressures from 58 to 85 GPa and temperatures from 1900 to 3200 K, even ironless $MgSiO_3$ perovskite breaks down to a mixture of periclase and stishovite. However the consensus is far from being reached, as other experiments up to 135 GPa and 3000 K show that $(Mg, Fe)SiO_3$ perovskite remains stable (Serghiou *et al.*, 1998; Kesson *et al.*, 1998).

The principal physical properties of silicate perovskite, insofar as they have been experimentally determined, are listed in Table 7.2. The density and the equation of state parameters K_0 and K_0' are reasonably well known, having been determined by several investigators. Values of the thermal expansion coefficient are given in Table 3.4. Melting of perovskite has been discussed in Section 5.5.1.

Phases with perovskite structure have also been found at high pressures for $CaSiO_3$ (Liu and Ringwood, 1975), diopside $CaMgSi_2O_6$, and diopside–jadeite solid solutions ($CaMgSi_2O_6$–$NaAlSi_2O_6$) (Liu, 1987). There is, however, no high-pressure phase with perovskite structure for the composition $FeSiO_3$, which decomposes into FeO and stishovite SiO_2 (Fig. 7.12).

(iii) The phase transitions of Mg_2SiO_4

Olivine $(Mg_{1-x}Fe_x)_2SiO_4$ is an important, possibly dominant, mineral of the upper mantle (with $x \approx 0.1$). The magnesian end member Mg_2SiO_4, *forsterite* forms a continuous series of solid solution with *fayalite* Fe_2SiO_4. The orthorhombic olivine structure can be described as a slightly distorted hexagonal close-packed (hcp) sublattice of oxygen ions, with the silicon ions occupying one-eighth of the tetrahedral sites and forming isolated SiO_4 tetrahedra, and the Mg or Fe ions occupying one-half of the octahed-

Table 7.2. *Physical properties (experimental) of $MgSiO_3$ perovskite*

Physical property	Experimental value	Reference
Cell dimensions (Å)	$a = 4.7787$	Ito & Matsui (1978)
	$b = 4.9313$	Ito & Matsui (1978)
	$c = 6.9083$	Ito & Matsui (1978)
Specific mass (g/cm^3)	4.108	Ito & Matsui (1978)
Mean atomic mass (g/atom)	20.08	Ito & Matsui (1978)
Molar volume (cm^3/mol)	24.4426	Ito & Matsui (1978)
K_0 (GPa) (Hill)	246.4	Yeganeh-Haeri *et al.* (1989)
K_0'	3.9	Knittle *et al.* (1987)
μ_0 (GPa) (Hill)	184.2	Yeganeh-Haeri *et al.* (1989)
v_P (km/s)	10.94	Yeganeh-Haeri *et al.* (1989)
v_S (km/s)	6.69	Yeganeh-Haeri *et al.* (1989)
γ_{th} (spectro)	1.9	Williams *et al.* (1987)
T_m (K) (at 22 GPa)	3000	Heinz & Jeanloz (1987)
α (K^{-1}) (298–840 K)	4×10^{-5}	Knittle & Jeanloz (1986)
(298–341 K)	2.2×10^{-5}	Ross & Hazen (1989)

ral sites. Alternatively, the structure can be considered as that of an intermetallic compound Mg_2Si (with the Ni_2In structure), stuffed with oxygen ions (O'Keefe and Hyde, 1981).

High-pressure phases of the ferromagnesian olivines were first synthesized by Ringwood and Major (1966, 1970) and Akimoto and Fujisawa (1966). Fayalite directly transforms into the spinel structure, still with isolated SiO_4 tetrahedra, but with a face-centered-cubic packing of oxygens. Forsterite and Mg-rich olivines first transform to an orthorhombic phase with face-centered-cubic (fcc) packing of oxygens, where the SiO_4 tetrahedra are linked in pairs by a corner. This phase is called β-phase (α is olivine and γ is spinel) or "modified spinel". The *P–T* phase diagram of the Mg_2SiO_4 polymorphs, constrained by thermochemical data (Akaogi *et al.*, 1984) is given in Fig. 7.14 and the pseudo-binary diagram of Mg_2SiO_4–Fe_2SiO_4 (Akaogi *et al.*, 1989) in Fig. 7.15 (see also Katsura and Ito, 1989).

Natural high-pressure spinel phase or *ringwoodite*, was found in shocked chondritic meteorites (Binns *et al.*, 1969) and unambiguously identified by transmission electron microscopy by Putnis and Price (1979) and Poirier and Madon (1979). The high-pressure β-phase (*wadsleyite*) was also found in shocked chondrites (Price *et al.*, 1983; Madon & Poirier, 1983).

The mechanism of the olivine–γ-spinel transformation in silicates and analog germanates has been much investigated in recent years. Since the oxygen sublattice goes from hexagonal close packed in olivine to face-centered cubic in spinel, Poirier (1981a,b) proposed that, by analogy with

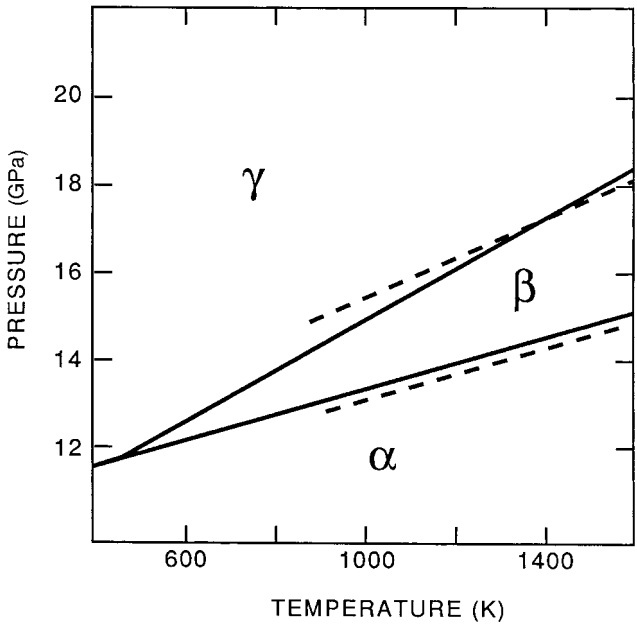

Figure 7.14 *P–T* phase diagram for the Mg_2SiO_4 polymorphs (α: olivine, β: modified spinel phase, γ: spinel). Solid lines from Akaogi *et al.* (1984), dashed lines from Suito (1977) (after Akaogi *et al.*, 1984).

other hcp–fcc transformations, olivine could transform to γ-spinel by shear restacking of oxygen ions due to invasion of the grains by stacking faults, the cations falling simultaneously into their new sites by "synchroshear". This "martensitic-like" mechanism was indeed found to be operative in experiments conducted in diamond-anvil cells (Lacam *et al.*, 1980; Furnish and Bassett, 1983; Boland and Liu, 1983), although there exists an intermediate stage, where the cations are disordered, thus ruling out synchroshear (Furnish and Bassett, 1983). However, in experiments conducted in large-volume apparatus, the transformation was found to take place by nucleation and growth (Boland and Liebermann, 1983; Vaughan *et al.*, 1982) with no cation disordering (Yagi *et al.*, 1987), although disordering was found in experiments conducted in a belt-type apparatus (Lauterjung and Will, 1986).

Using multi-anvil apparatus and transmission electron microscopy to study the olivine–β-phase transition in forsterite, Fujino and Irifune (1992) found that it occurred by nucleation and growth, and Guyot *et al.* (1991) observed an intermediate phase filled with stacking faults destroying the cation long-range order. Brearley *et al.* (1992) and Rubie and Brearley

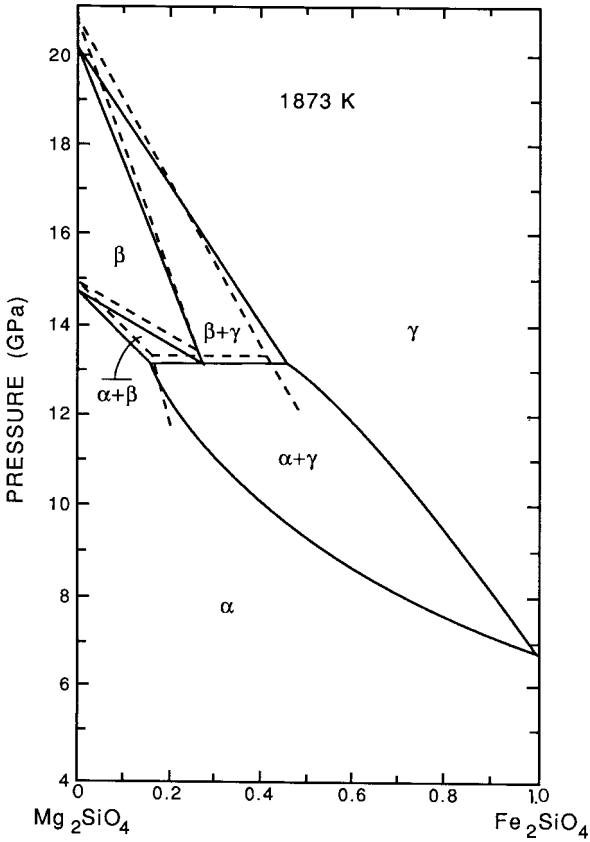

Figure 7.15 Isothermal ($T = 1600\,^{\circ}C$) calculated phase diagram for the Mg_2SiO_4–Fe_2SiO_4 system. The crystalline structures are α (olivine), β (β-phase), γ (γ-spinel). The boundaries determined experimentally by Katsura and Ito (1989) are shown by dashed curves (after Akaogi *et al.*, 1989).

(1994) showed that, although the β–γ transition occurs by nucleation and growth, the reverse tranformation occurs by a shear mechanism. Kubo *et al.* (1998) directly studied the kinetics of the transformation by X-ray diffraction using synchrotron radiation.

Kerschhofer *et al.* (1996) observed two competing mechanisms in the transformation of $(Mg_{1.8}Fe_{0.2})_2SiO_4$ olivine: incoherent nucleation on olivine grain boundaries and coherent intracrystalline nucleation of ringwoodite lamellas on shear-induced stacking faults on (100) planes (in agreement with Poirier, 1981b), followed by nucleation of wadsleyite on the ringwoodite.

Burnley and Green (1989) suggested that the "martensitic-like" mechan-

ism for the olivine–spinel transition occurs only for experiments conducted under large shear stresses, as is the case for the diamond-anvil cell. However, experiments conducted in a large-volume press on the analog $MgGeO_4$ showed that the transformation occurs by nucleation and growth near the Clapeyron and by "martensitic-like" shear restacking of the oxygen ions at high overpressures (Burnley, 1995). Indeed, the fact that the "martensitic-like" mechanism is observed in experiments conducted in diamond-anvil cells but usually not in a multi-anvil apparatus may be due to the fact that in the latter type of experiments, the pressure and temperature paths make it easy to perform runs close to the Clapeyron, whereas in the diamond-cell the high pressure must be applied before laser-heating, producing a very high overpressure and a high effective stress on the dislocations responsible for the shear of the lattice (Poirier, 1982).

The seismic discontinuity at 670 km has been, for a long time, attributed to the transformation of $(Mg, Fe)_2SiO_4$ to denser post-spinel phases. It was first believed that spinel transformed to a mixture of magnesiowüstite (Mg, Fe)O and stishovite, the high-pressure phase of quartz, where silicon is in SiO_6 octahedra ("mixed oxide" lower-mantle models). Ming and Bassett (1975) indeed found that the X-ray diffraction patterns of the disproportionated phase were consistent with the mixed-oxide models. Liu (1975a), however, conclusively showed that the post-spinel phases were a mixture of magnesiowüstite and the perovskite phase $(Mg, Fe)SiO_3$:

$$(Mg, Fe)_2SiO_4 \Rightarrow (Mg, Fe)O + (Mg, Fe)SiO_3$$

Observations by analytical electron microscopy (Guyot *et al.*, 1988b; Madon *et al.*, 1989b) give direct evidence of the validity of this disproportionation reaction. At high iron contents, however, (higher than those currently admitted for the lower mantle) the perovskite is not stable and the disproportionation indeed leads to a mixture of magnesiowüstite and stishovite.

The pressure interval within which the decomposition takes place ("sharpness" of the transition) has long been a subject of controversy, bearing on the problem of the composition of the lower mantle (e.g. Lees *et al.*, 1983). Ito and Takahashi (1989) found that magnesian spinel with less than 26 at.% Fe dissociates within a very narrow pressure interval (0.15 GPa at 1600 °C), thus buttressing the view that the transition is quite sharp (Fig. 7.16). The negative Clapeyron is given by: $P[\text{GPa}] = 27.6 - 0.0028T[^\circ\text{C}]$. Calculation of the phase boundaries using thermodynamic data by Akaogi *et al.* (1998) confirms the results of Ito and Takahashi (Figs. 7.17 and 7.18). However, a determination of the post-spinel phase boundary by synchrotron X-ray diffraction under pressure

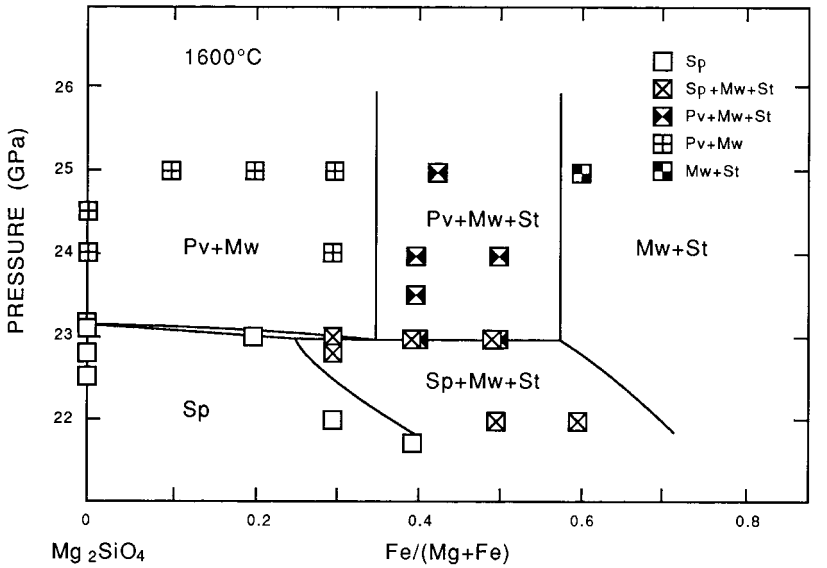

Figure 7.16 Isothermal ($T = 1600\,^{\circ}C$) phase diagram for the post-spinel transformation in the Mg_2SiO_4–Fe_2SiO_4 system. Note that the spinel (Sp) transforms to perovskite (Pv) and magnesiowüstite (Mw) over a narrow pressure interval; St indicates stishovite (after Ito and Takahashi, 1989).

and temperature (Irifune *et al.*, 1998) yields a boundary located at 21.1 GPa at 1600 °C, about 2 GPa lower than previous estimates.

Iron does not disproportionate equally between magnesiowüstite and perovskite and goes preferentially into magnesiowüstite (Bell *et al.*, 1979; Ito *et al.*, 1984). The partition coefficient of iron can be written:

$$K = \left(\frac{x_{Fe}}{x_{Mg}}\right)_{Mw} \Big/ \left(\frac{x_{Fe}}{x_{Mg}}\right)_{Pv}$$

where x is the Fe or Mg content of the phases, given in at.%. Guyot *et al.* (1988b) have measured the value of K as a function of pressure by analytical transmission electron microscopy and found that it decreases with increasing pressure and remains constant ($K \cong 3.5$) at pressures above 40 GPa (Fig. 7.19). For the starting material used, it corresponds to the reaction:

$$(Mg_{0.83}Fe_{0.17})_2SiO_4 \Rightarrow Mg_{0.91}Fe_{0.09}SiO_3 + Mg_{0.74}Fe_{0.26}O$$

More recent measurements by analytical transmission electron micro-

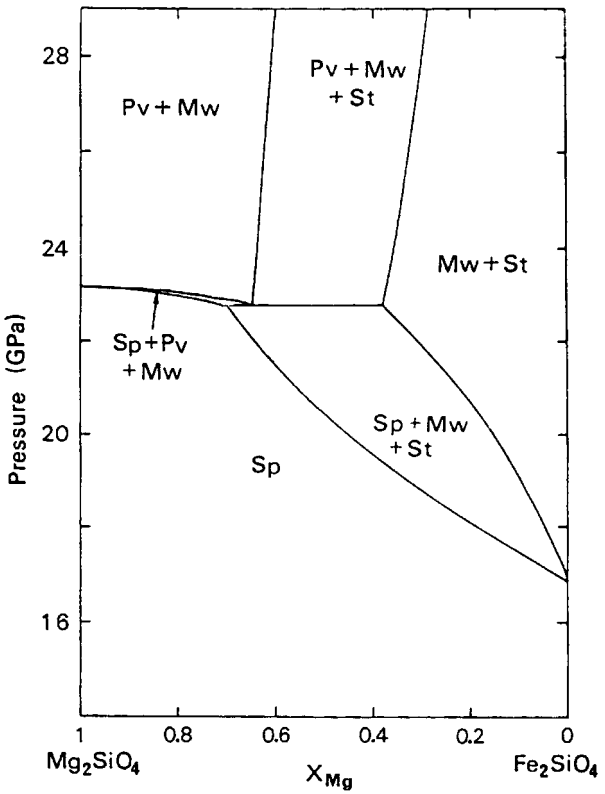

Figure 7.17 Isothermal ($T = 1600\,^{\circ}C$) phase diagram of system Mg_2SiO_4–Fe_2SiO_4 system. The phase boundaries were calculated from experimental data (after Akaogi *et al.*, 1998).

scopy (Martinez *et al.*, 1997) yielded a value of $K = 3.8 \pm 0.3$ at 26 GPa and 1300 °C and $K = 4.3 \pm 0.4$ at 26 GPa and 1600 °C.

The partitioning of iron between magnesiowüstite and perovskite depends on the alumina concentration in the perovskite. It as been shown that in presence of alumina, iron enters perovskite more readily (Wood and Rubie, 1996). As a result of the dissolution of aluminous garnet into perovskite, mantle perovskite can contain up to 9 wt% Al_2O_3. The measurements of Wood and Rubie suggest that, in the lower mantle, perovskite might contain as much iron as magnesiowüstite. The stability limit of Fe in perovskite increases as temperature and pressure increase (Mao *et al.*, 1997) and perovskite can accept Fe^{3+} in larger concentrations than Fe^{2+}. As a higher proportion of the iron in perovskite tends to become ferric in the presence of aluminum (McCammon, 1997), it seems

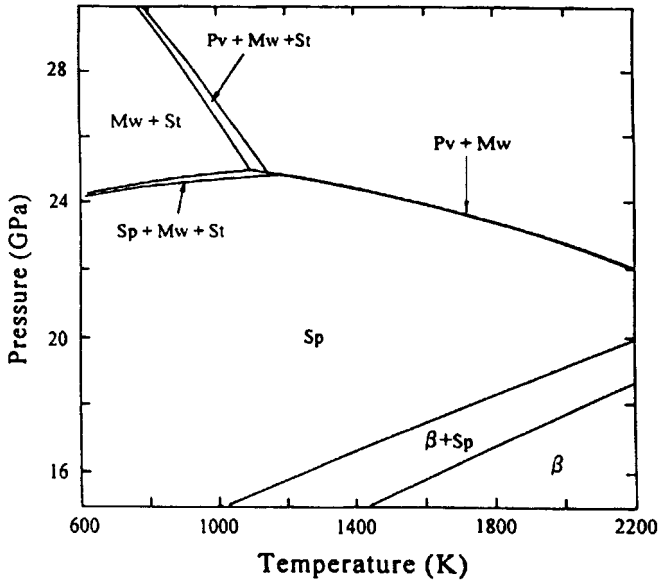

Figure 7.18 Calculated P–T phase diagram of $(Mg_{0.89}Fe_{0.11})_2SiO_4$ (after Akaogi *et al.*, 1998).

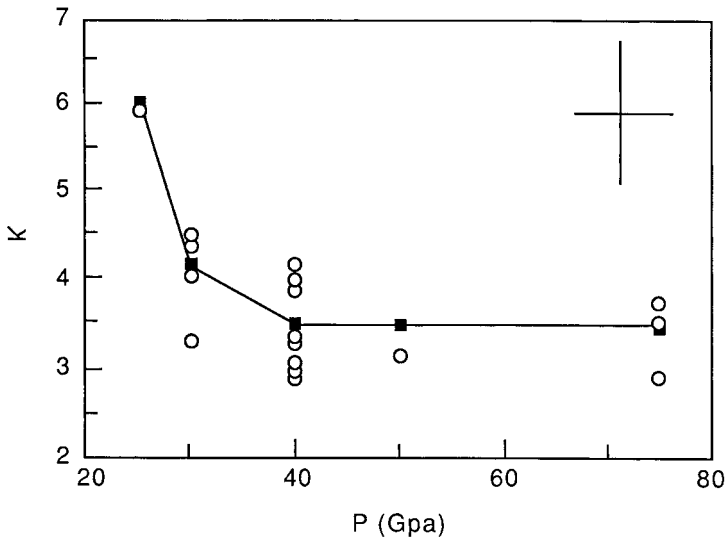

Figure 7.19 Variation with pressure P of the partition coefficient K of iron between magnesiowüstite and perovskite. The error bars on the measurements are shown in the upper right-hand corner (after Guyot *et al.*, 1988b).

reasonable to believe that the perovskite of the lower mantle is richer in iron than the perovskite prepared experimentally by disproportionation of olivine.

The structure of the disproportionated mixture of magnesiowüstite and perovskite was investigated as a function of T and P by transmission electron microscopy of metastable quenched samples recovered from the diamond-anvil cell (Guyot *et al.*, 1988b; Madon *et al.*, 1989b). Wang *et al.* (1997) and Martinez *et al.* (1997) also used transmission electron microscopy to observe the resulting product of disproportionation of olivine; their observations led them to suggest a two-step mechanism for the transformation, involving first the formation of ringwoodite by shear, followed by break-down to magnesiowüstite and perovskite.

7.4.2 Mantle and core models

(i) Constraints and trade-offs

The compositional Earth models are usually patterned after the description of rocks by petrographers: For each region of the mantle, one must know the "norm" i.e. the chemical composition expressed in weight % of oxides and the "mode" i.e. the proportions of the various constituent minerals.

Compositional models are bound by different types of constraints:

- They are required to agree as much as possible with the seismological models, i.e. they must account for the velocity and density profiles. This of course implies that the P–T phase diagrams for the candidate compositions are known and that the equations of state, elastic moduli and thermal expansion coefficients, as well as their temperature and pressure derivatives, are known for the relevant minerals. A geotherm must be chosen.
- The starting normative composition is usually chosen on the basis of assumptions about the primitive bulk Earth composition and the chemical evolution of the Earth.
- Compositional models are often more or less openly tailored to fit other geophysical requirements: e.g. whole-mantle convection (hence chemically homogeneous mantle) or two-layer convection (hence possibility for the upper and lower mantle to be chemically different). Note that this also conditions the choice of the geotherm.

The construction of a compositional model usually follows one of two lines:

(i) The actual density and elastic moduli (often only the bulk modulus) at depth are adiabatically extrapolated to zero pressure and brought down from the final temperature to room temperature. A mineral assemblage is devised so that its density and aggregate elastic properties fit the decompressed material.

(ii) A mineral assemblage at room temperature and ambient pressure is devised so that after heating and adiabatically compressing it, its density and seismic velocities (often only the bulk velocity) fit the seismological model.

In both cases, the elastic moduli of the high-pressure phases and their pressure and temperature derivatives, either have been measured at ambient pressure in the metastable state, or, at any rate, have been estimated from elastic systematics. The thermal expansion coefficients often are estimated.

Most of the discrepancies between contending compositional Earth models come from one of two sources.

(i) The models use different assumptions as to the primitive bulk Earth composition and its evolution. It is generally assumed that the primitive composition of the bulk Earth (and terrestrial planets) is that of the devolatilized solar nebula (Hart and Zindler, 1986). Now, the problem is to decide what was the composition of the original solar nebula and to what degree it has lost volatile elements. It is currently thought that the solar abundance of refractory elements is well reflected in the composition of the CI chondrites, meteorites that have not been differentiated and are considered as samples of the primitive nebular material (Anders and Grevesse, 1989). The composition of the primitive upper mantle, however, derived from the study of mantle peridotites, corresponds to a smaller Mg/Si ratio than that of the chondrites; it has been proposed that the Mg/Si ratio of the terrestrial planets is more representative of the solar nebula value than that of the CI chondrites (Ringwood, 1989).

If one believes that the bulk Earth is nevertheless chondritic, one is drawn to the conclusion that the missing silicon is hidden away in the lower mantle and/or core and the resulting compositional models are called *chondritic Earth models* (e.g. Liu, 1982; D. L. Anderson, 1984; Anderson and Bass, 1986). In these models, the lower mantle is more silica-rich than the upper mantle and can be composed almost entirely of $(Mg, Fe)SiO_3$ perovskite, thus leading to a two-layer convection pattern.

One can also solve the case of the missing silicon by assuming that this

element, less refractory than calcium and aluminum, was partly volatilized away. The mantle then need not be chemically heterogeneous and whole-mantle convection is not precluded (although not required). The most popular model of a homogeneous mantle is the *pyrolite model* (see Ringwood, 1979): The bulk composition of the mantle is that of "pyrolite", a non-specific olivine–pyroxene rock, capable of yielding a basaltic magma and a peridotite residue upon partial melting in the uppermost mantle. Pyrolite is a fictitious rock in that it is defined by its chemical composition (norm) only and not by its mineralogy (mode).

D. L. Anderson (1989a), using new estimates of the solar composition, proposed that the Sun should be richer in iron and calcium than the CI chondrites. If the bulk Earth composition is solar, it then should be richer in iron and calcium than the chondritic model. Javoy (1995) presented a model in which the Earth is essentially built from the material of enstatite chondrites (EH), resulting in a large difference in chemical composition between upper and lower mantle.

Allègre *et al.* (1995) did not a priori assume that the bulk Earth composition is that of any particular chondrite; they determined it from meteorite correlations and used the fact that the ratios of elements which do not enter the core (e.g. Al and Mg) are the same in the mantle (assumed to be homogeneous) and in the bulk Earth. By difference, they found that the core should contain silicon.

The composition of the mantle corresponding to the various hypotheses is given in Table 7.3.

(ii) The other source of discrepancy lies in the choice of the elastic and thermal parameters of the high-pressure candidate minerals. Most of them are, if not unknown, at least known with a high degree of uncertainty, stemming either from the inherent experimental errors and/or from the fact that we must often rely on only one measurement. Also, the elastic parameters are sensitive to the assumed iron content. As a consequence, many trade-offs are possible and various mineral assemblages may be fitted to the velocity and density profiles – themselves known within the resolution of the seismological methods only, see Bolt (1991) – by choosing an appropriate geotherm and not unlikely combinations of elastic moduli, thermal expansion coefficient and P–T derivatives (see Jackson, 1983, 1998).

In recent years considerable progress has been made due to the improvement of high-pressure apparatus and to the possibility of obtaining elastic

Table 7.3. *Composition models for the Earth's mantle, in wt%, for the five major oxides*

Oxide	Pyrolite[a]	Chondritic[b]	Chondritic[c]	Chondritic[d]	Solar[e]	[f]
SiO_2	45.0	50.8	49.52	45.96	45	46.12
MgO	38.8	36.6	35.68	37.78	32.7	37.77
FeO	7.6	6.08	7.14	7.54	15.7	7.49
Al_2O_3	4.4	3.67	3.56	4.06	3.2	4.09
CaO	3.4	2.89	2.82	3.21	3.4	3.23

[a]Jackson (1983); [b]Anderson & Bass (1986); [c]Hart & Zindler (1986); [d]Hart & Zindler (1986): devolatilized chondritic (LOSIMAG); [e]Anderson (1989a); [f]Allègre *et al.* (1995).

and thermal parameters of mantle phases, as well as their pressure and temperature derivatives, by simultaneous measurements at high temperature and high pressure, using synchrotron radiation. However, it still might be submitted that, at the present time, there is no compelling evidence in favor of any one of the contending models, such evidence as is usually presented for one model never really ruling out other models.

(ii) Mantle models

We have some direct knowledge of the composition of the uppermost mantle from the produce of its partial melting (basalts) and from the peridotites found in ophiolitic complexes, massifs, and in xenoliths brought up from as deep as 200 or 250 km by basalts or kimberlites. Ringwood (1979) drew the conclusion that the uppermost mantle is composed of residual peridotite strongly depleted in the low melting-point minerals that went into basalt during partial melting. A typical peridotite is composed of mostly olivine and orthopyroxene (enstatite) with some calcic clinopyroxene (diopside) and an aluminous phase (plagioclase, spinel or pyrope garnet, in that order with increasing depth). Below the lithosphere, there must exist a primitive source material: *pyrolite*, defined as we have seen above by its capacity to produce basalt and residual peridotite. The phase transitions of the relevant minerals, described above, are compatible with the following model (for a review, see Gillet, 1995):

At about 350 km, pyroxene and aluminous garnet enter into solid solution, giving majorite with garnet structure and, at 400 km, olivine goes to β-phase; then, in the transition zone, β-phase goes to γ-spinel, garnet goes to ilmenite, and the $CaSiO_3$ component goes to calcic perovskite. Finally, at 650 km, $(Mg, Fe)SiO_3$ disproportionates to perovskite and magnesiowüstite. Ringwood (1975) found that these transitions provided a

satisfactory explanation of the position and magnitude of the seismic discontinuities and density jumps and that there was no need for changes in chemical composition and, in particular, no need for an enrichment in iron of the lower mantle. The 670 km seismic discontinuity is then thought to be due only to phase transitions, but it is seismically marked by the thin subducted oceanic lithosphere trapped at the interface between upper and lower mantle (Ringwood and Irifune, 1988).

D. L. Anderson (1984), Anderson and Bass (1986) and Duffy and Anderson (1989) account for the seismic velocity profiles by mineralogical assemblages consistent with a chondritic mantle having melted (magma ocean) and differentiated at an early stage of the Earth's history: low-density olivine crystallizes first and concentrates into a peridotite uppermost mantle, the residual fluid freezes to a clinopyroxene garnet-rich assemblage with less than 50% olivine, termed *piclogite*, which would constitute the transition zone. The lower-mantle velocities are found to be consistent with a silica-rich composition of pure perovskite, as also proposed by Liu (1979). In a later (Anderson, 1989a) model, the lower mantle is also richer in iron and there is more diopside in the transition zone. Stixrude *et al.* (1992) find that the seismological data are consistent with a lower mantle consisting of nearly pure perovskite.

The two major classes of upper mantle models are (see Fig. 7.20 and Table 7.4):

- The "pyrolite" mantle models, with no chemical difference between upper and lower mantle.
- The "piclogite" mantle models, with a more silica- (and iron-) rich lower mantle.

Jackson (1983) showed that due to the trade-offs between composition, temperature and physical properties, pyrolite and chondritic models could be equally plausible. Experimental investigation of the phase relations of the $MgO–FeO–SiO_2$ system (Ito *et al.*, 1984) led the authors to the conclusion that a pyrolite lower mantle satisfied the density and bulk modulus constraints, although a pure perovskite composition or a composition close to that of E enstatite chondrites could not be ruled out. Poirier (1987) investigated the variation of Poisson's ratio of the perovskite–magnesiowüstite assemblage with various perovskite and iron contents and found that the Poisson's ratio and the seismic parameter of the lower mantle were satisfied both by a pyrolite and a chondritic model. Weidner (1986), investigating the agreement between the upper-mantle models and the seismological data, found that the phase transitions in the transition

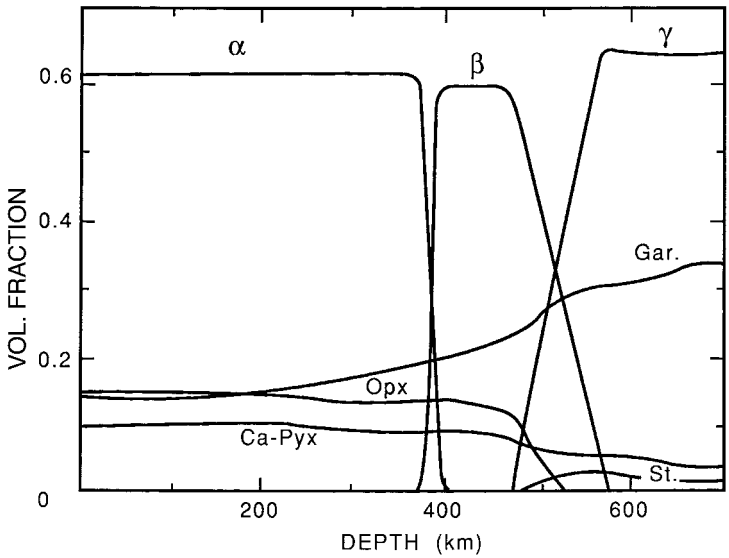

(a)

Figure 7.20(a) The calculated volume fraction of mineral phases for a pyrolite mantle composition as a function of depth (after Weidner, 1986).

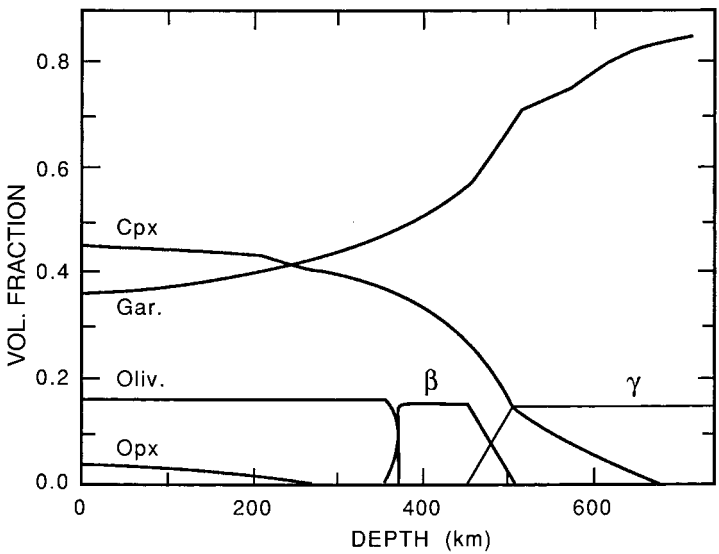

(b)

Figure 7.20(b) The calculated volume fraction of mineral phases for a piclogite mantle composition as a function of depth (after Weidner, 1986).

Table 7.4. *Upper mantle models*

Oxide	Pyrolite	Piclogite
Norm		
MgO	40.3	21.0
FeO	7.9	5.7
CaO	3.0	7.0
SiO_2	45.2	48.9
Al_2O_3	3.5	14.4
Na_2O	0.0	3.0
Mode		
Olivine	61	16
Orthopyroxene	15	3
Clinopyroxene	10	45
Garnet	14	36

Note: Norm in wt% oxides, mode in vol.% minerals.
Source: Weidner (1986).

zone alone could satisfy the data without resorting to mineralogical stratification as in "piclogite" models. The latter, however, cannot be categorically ruled out.

In conclusion, it is difficult to eliminate one of the models on the grounds that it does not fit the seismological data and it is possible to say with Weidner (1986) that "within the uncertainty of the current data-base, we need look no further than the pyrolite model to find a chemical composition compatible with the data for the upper mantle"; as for the lower mantle it is even less well constrained. Note again that a homogeneous mantle does *not* necessarily imply whole-mantle convection.

(iii) The core–mantle boundary and D" layer

The core–mantle boundary (CMB) is possibly the major discontinuity in the Earth, with a specific mass contrast of 4.4 g/cm^3 between the core and the mantle (compared to 2.7 g/cm^3 between the crust and the atmosphere) and a viscosity contrast of the order of 10^{21} poise. The CMB may be bumpy, with a "topography" of several kilometers amplitude at the scale of thousands of kilometers (Morelli and Dziewonski, 1987), while it may be sharp and flat in places (Vidale and Benz, 1992). The analysis of the correlations between the geoid and the surface topography show that the amplitude of the topography dynamically maintained by convection at the CMB should be of about 3 km (Hager *et al.*, 1985). The core–mantle boundary region is the seat of energetic exchanges and couplings between

core and mantle that may be of extreme geodynamic importance and it is becoming the object of a sustained interest. The progress in recent years can be assessed by reading the special issue of *Geophysical Research Letters* (volume **13**, no.13, 1986) and the successive reviews by Young and Lay (1987), Lay (1989), Loper and Lay (1995) and Lay *et al.* (1998).

Global seismological Earth models exhibit a zone of reduced or even negative velocity gradient (Lay, 1989, 1995), extending 200 to 300 km above the CMB, called the D" layer. As, from most estimates, there is a finite heat flux from the core into the mantle, it was natural to think of the D" zone as a thermal boundary layer. Numerical simulations lead to the picture of the D" zone as an unstable thermal boundary layer over the depth of which the temperature-dependent viscosity can decrease by several orders of magnitude, inducing the rise of convective instabilities, or plumes, (Loper, 1984; Zharkov *et al.*, 1985; Olson *et al.*, 1987). If, as convincingly argued by Stevenson (1981), the core is not in equilibrium with the mantle, the core–mantle boundary must indeed be a chemically active and heterogeneous zone.

Recent seismological investigations, using travel-time residuals of body waves reflected from the core, transmitted through it, or diffracted near the boundary show that the structure of the D" layer is rather complicated. There is evidence of lateral heterogeneities of velocity up to 4% for P- and S-waves (Wysession *et al.*, 1992; Vidale and Benz, 1993) and of seismic anisotropy (Kendall and Silver, 1993; Vinnik *et al.*, 1998). The heterogeneity and anisotropy can be interpreted as due to rafts of denser subducted plate material, unevenly distributed at the CMB, much like the continents at the top of the mantle (Dornboos *et al.*, 1986; Wysession, 1996).

Chemically denser material (dregs) may lie at the bottom of the mantle, in an uneven layer of variable thickness, interacting with the convection and modulating the heat flow from the core (Davies and Gurnis, 1986). The nature of the dense material is still as speculative as its existence: lithospheric plate material coming from above or core material coming from below. Indeed, there is good evidence that the molten iron alloy of the core can react with the silicate perovskite and magnesiowüstite (Williams *et al.*, 1987b; Urakawa *et al.*, 1987; Knittle and Jeanloz, 1989a; Goarant *et al.*, 1992; Song and Ahrens, 1994). It has been proposed that the accumulation of infiltrated liquid iron or reaction products between iron and silicates layer might make up an electrically conducting D" layer, possibly affecting the magnetic field (Jeanloz, 1990; Knittle and Jeanloz, 1991a). However, the infiltrated layer, likely to be extremely thin (a few hundred meters at most) and possibly re-equilibrated, cannot be identified with the D" layer; its

effects on the magnetic field must be negligible (Poirier and Le Mouël, 1992; Le Mouël *et al.*, 1997).

There is recent seismic evidence for a very thin ultra-low-velocity zone (ULVZ) lying near the CMB. Its laterally varying thickness is probably of the order of a few tens of kilometers (Wen and Helmberger, 1998; Garnero *et al.*, 1998). The ULVZ is unlikely to be caused by infiltration of iron from the core (Poirier *et al.*, 1998) and it is currently thought to be due to partial melting at the base of the mantle (Williams and Garnero, 1996; Vidale and Hedlin, 1998; Wen and Helmberger, 1998). This view is supported by experimental determinations of the solidus of the magnesiowüstite–perovskite assemblage of the lower mantle (Holland and Ahrens, 1997; Zerr *et al.*, 1998).

(iv) The outer core

The physical state and composition of the Earth's core have been a matter of considerable controversy up to recent times (see Brush, 1979, 1982) and there still is some debate as to exactly what elements it contains in addition to iron. That the core is made of iron is consistent with the large increase in density at the core–mantle boundary and with the idea that iron meteorites constitute the cores of small differentiated planetary bodies.

The view had been entertained (Ramsey, 1949) that the core, like the mantle, was composed of silicate phases, compressed to a very high density and having undergone a transition to the metallic state. Birch (1952, 1961b, 1963), using the bulk-velocity–density systematics he had established for a number of elements and the Hugoniot compression curves obtained experimentally for iron, conclusively showed that the core was indeed iron (see Section 4.6.2 and Fig. 4.6). His principal argument was that silicates, with a mean atomic mass close to 20, could never achieve the density of the core given by seismological models, unless under pressures much larger than the pressure at the center of the Earth (or that the bulk sound velocity of silicates at core pressure densities would be much too high); iron on the contrary, gave good agreement with the density and seismic velocities, if alloyed with a small quantity of light elements. Even though Ramsey's theory is revived from time to time, it is clearly not tenable (O. L. Anderson, 1985).

By analogy with iron meteorites and from cosmic abundances consideration, it is reasonable to assume that there is some nickel in the core. If the Earth is of cosmic composition, there should be about 4–5 wt% nickel in the Earth's core (Brett, 1976; Allègre *et al.*, 1995).

A core of pure iron (and *a fortiori* a core containing some nickel) would

have a density about 10% higher than that deduced from seismological observations (Birch, 1952). The density may be adjusted by assuming that iron–nickel is alloyed with some proportion of light elements. What the light elements are is an object of debate (for a review, see Poirier, 1994a). It must be noted that the arguments pro and con a given element often rely on assumptions about the bulk Earth composition and the mode of formation of the core.

- Silicon may be present in the core, although there are some difficulties regarding core formation processes. Indeed, the presence of silicon in the core was suggested a long time ago (MacDonald and Knopoff, 1958).
- Oxygen is little soluble in iron near its liquidus at atmospheric pressure, but its solubility increases with temperature and probably with pressure. Ringwood (1977, 1979) estimates the oxygen content of the core to be 10 ± 4 wt% (44 ± 16 wt% FeO). The probability for oxygen to be present in the core is enhanced by experimental results showing that FeO, immiscible with Fe at ambient pressure, becomes metallic above 70 GPa and can thus be incorporated in the iron core (Knittle and Jeanloz, 1986). The metallization may be due to a Mott transition (Sherman, 1989).
- Sulfur also remains a good candidate since it easily partitions into iron and can form a low melting-point eutectic with it (Rama Murthy and Hall, 1970); 8 to 10 wt% S would be enough to account for the core density (Stevenson, 1981).
- Hydrogen has been found to be highly soluble in iron at high pressure and to form hydrides (Badding *et al*., 1991). It has been suggested that hydrogen might be one of the light elements present in the core (Suzuki *et al*., 1984; Fukai and Suzuki, 1986).
- Carbon was suggested by Wood (1993).
- Potassium might be present in the core, especially if there is sulfur. The radioactive decay of ^{40}K might then contribute to the heat flow from the core (Stacey, 1972). Oversby and Ringwood (1972) found that potassium did not significantly partition into iron. However, later experimental and theoretical investigations pointed to the still little understood effects of pressure and oxygen partial pressure on the solubility of potassium in iron (Bukowinski, 1976; Ganguly and Kennedy, 1977; Murrell and Burnet, 1986; Sherman, 1990; Parker *et al*., 1996). The problem of whether there is potassium in the core is still not satisfactorily solved.

Of course, as pointed out by Stevenson (1981) there is no reason to believe that the core is a particularly "clean" system and that there is only

one light element present in it. Allègre *et al.* (1995) find about 7.3% Si, 2.3% S and 4% O (in wt%).

The light elements, whichever they are, partition into the liquid phase during crystallization of the iron alloy at the inner-core boundary, the lighter liquid can then rise and the ensuing "compositional convection" is thought to be essential to the generation of the magnetic field (Braginsky, 1964; Loper, 1978).

The physical, thermal and elastic properties of the core have been reviewed by Poirier (1994b) and Stacey (1995). Estimates of the dynamic viscosity of the outer core, from geodetic, seimological, and geomagnetic studies, as well as theoretical and experimental estimates are listed in Secco (1995). Extrapolations of experimental measurements of the viscosity of Fe–S liquids yield values or the order of 10^{-3} Pa s (LeBlanc and Secco, 1996; Secco *et al.*, 1998), consistent with estimates of Poirier (1988a) and *ab-initio* calculations of de Wijs *et al.* (1998).

(v) The inner core

The inner core is the most remote region of the Earth and its composition and structure have been (and sometimes still are) the object of unbridled and fanciful speculation, involving, for instance, the existence near its center of a subcore of uranium and thorium, seat of nuclear reactions (Nanda, 1989; Herndon, 1996).

There is, however, little doubt that inner core freezes out of the outer core (Jacobs, 1953). It is essentially iron, but the nature of the high-pressure phase of iron (perhaps ε-Fe) is still debated (see Section 5.6). Crystallization of a liquid alloy leads to a purer solid phase and a liquid enriched in light elements. However, pure liquid iron is 3–6% denser than the inner core (Anderson and Ahrens, 1994), implying that several percent of the light component must be present in the inner core, as proposed by Jephcoat and Olson (1987).

The inner core is seismically anisotropic. The velocity of seismic waves parallel to the Earth's rotation axis is 3–4% faster than that of waves traveling in the equatorial plane (Creager, 1992; Song, 1997). The attenuation is also anisotropic, the direction of strong attenuation coinciding with the fast direction (Souriau and Romanowicz, 1996).

The origin of the seismic anisotropy is debated. It has been assigned to lattice preferred orientation of crystals induced by plastic flow during convection of the inner core (Jeanloz and Wenk, 1988; Romanowicz *et al.*, 1996). This view rested on the assumption (Wenk *et al.*, 1988) that the ε-Fe inner core deformed primarily on prism planes, like titanium. Poirier and

Price (1999), however, contend that the primary slip planes of ε-Fe should be basal, and would not lead to the observed anisotropy. Other mechanisms were proposed: magnetic field-induced preferred orientation of iron crystals (Karato, 1993), solidification texturing (Bergman, 1997), alignment of crystals under the stress field produced by the flow resulting from isostatic adjustment of the inner core (Yoshida *et al.*, 1996).

Grain size and viscosity of the inner core are parameters entering some of the above models. Assuming the material of the inner core to be ε-Fe leads Stixrude and Cohen (1995b) to the conclusion that the observed anisotropy can be explained only if the alignment of the crystals is so perfect as to make the inner core equivalent to a single crystal. From the observed seismic attenuation anisotropy, Bergman (1998) estimates that the smallest grain dimension must be of the order of hundreds of meters. Buffett (1997) discusses the mechanisms for the production of seismic anisotropy according to viscosity estimates.

This Page Intentionally Left Blank

Appendix

Table A.1. *PREM model (1s) for the mantle and core*

z	r	P	ρ	v_P	v_S	Φ	K	μ	ν	g
24.4	6346	6	3.38	8.11	4.49	38.9	1315	682	0.28	984
40	6331	11.2	3.38	8.11	4.48	38.8	1311	680	0.28	984
60	6311	17.9	3.38	8.09	4.48	38.7	1307	677	0.28	985
80	6291	24.5	3.37	8.08	4.47	38.6	1303	674	0.28	986
115	6256	36.2	3.37	8.03	4.44	38.2	1287	665	0.28	988
185	6186	59.4	3.36	8.01	4.43	38.0	1278	660	0.28	989
220	6151	71.1	3.36	7.99	4.42	37.8	1270	656	0.28	990
220	6151	71.1	3.44	8.56	4.64	44.5	1529	741	0.29	990
265	6106	86.5	3.42	8.65	4.68	45.6	1579	757	0.29	992
310	6061	102	3.49	8.73	4.71	46.7	1630	773	0.30	994
355	6016	118	3.52	8.81	4.74	47.8	1682	790	0.30	995
400	5971	134	3.54	8.91	4.77	49.0	1735	806	0.30	997
400	5971	134	3.72	9.13	4.93	51.0	1899	906	0.29	997
450	5921	152	3.79	9.39	5.08	53.8	2037	977	0.29	998
500	5871	171	3.85	9.65	5.22	56.7	2181	1051	0.29	999
550	5821	191	3.91	9.90	5.37	59.6	2332	1128	0.29	1000
600	5771	210	3.98	10.16	5.51	62.6	2489	1210	0.29	1000
635	5736	224	3.98	10.21	5.54	63.3	2523	1224	0.29	1001
670	5701	238	3.99	10.27	5.57	64.0	2556	1239	0.29	1001
670	5701	238	4.38	10.75	5.95	68.5	2999	1548	0.28	1001
721	5650	261	4.41	10.91	6.09	69.5	3067	1639	0.27	1001
771	5600	283	4.44	11.07	6.24	70.5	3133	1730	0.27	1000
871	5500	328	4.50	11.24	6.31	73.3	3303	1794	0.27	999
971	5400	373	4.56	11.41	6.38	76.1	3471	1856	0.27	997
1071	5300	419	4.62	11.58	6.44	78.7	3638	1918	0.28	996
1171	5200	465	4.68	11.73	6.50	81.3	3803	1979	0.28	995
1271	5100	512	4.73	11.88	6.56	83.8	3966	2039	0.28	994
1371	5000	559	4.79	12.02	6.62	86.2	4128	2098	0.28	993
1471	4900	607	4.84	12.16	6.67	88.5	4288	2157	0.28	993
1571	4800	655	4.90	12.29	6.72	90.8	4448	2215	0.29	993
1671	4700	704	4.95	12.42	6.77	93.1	4607	2273	0.29	994
1771	4600	754	5.00	12.54	6.83	95.3	4766	2331	0.29	995
1871	4500	804	5.05	12.67	6.87	97.4	4925	2388	0.29	996
1971	4400	854	5.11	12.78	6.92	99.6	5085	2445	0.29	999
2071	4300	906	5.16	12.90	6.97	101.7	5246	2502	0.29	1002
2171	4200	958	5.21	13.02	7.01	103.9	5409	2559	0.30	1005
2271	4100	1010	5.26	13.13	7.06	106.0	5575	2617	0.30	1010
2371	4000	1064	5.31	13.25	7.10	108.2	5744	2675	0.30	1016
2471	3900	1118	5.36	13.36	7.14	110.5	5917	2734	0.30	1023

Table A.1 *(cont.)*

z	r	P	ρ	v_P	v_S	Φ	K	μ	v	g
2571	3800	1173	5.41	13.48	7.19	112.7	6095	2794	0.30	1031
2671	3700	1230	5.46	13.60	7.23	115.1	6279	2855	0.30	1041
2771	3600	1287	5.51	13.67	7.27	117.0	6440	2907	0.30	1052
2871	3500	1346	5.56	13.71	7.26	117.6	6537	2933	0.30	1065
2891	3480	1358	5.57	13.72	7.26	117.8	6556	2938	0.31	1068
2891	3480	1358	9.90	8.06	0	65.0	6441	0	0.5	1068
2971	3400	1442	10.02	8.19	0	67.2	6743	0	0.5	1051
3071	3300	1547	10.18	8.36	0	69.9	7116	0	0.5	1028
3171	3200	1651	10.33	8.51	0	72.5	7484	0	0.5	1005
3271	3100	1754	10.47	8.66	0	75.0	7846	0	0.5	981
3371	3000	1856	10.60	8.80	0	77.4	8202	0	0.5	956
3471	2900	1957	10.73	8.93	0	79.7	8550	0	0.5	930
3571	2800	2056	10.85	9.05	0	81.9	8889	0	0.5	904
3671	2700	2153	10.97	9.17	0	84.0	9220	0	0.5	877
3771	2600	2248	11.08	9.28	0	86.1	9542	0	0.5	850
3871	2500	2342	11.19	9.38	0	88.1	9855	0	0.5	822
3971	2400	2342	11.29	9.48	0	90.0	10158	0	0.5	794
4071	2300	2521	11.39	9.58	0	91.8	10451	0	0.5	766
4171	2200	2607	11.48	9.67	0	93.5	10735	0	0.5	736
4271	2100	2690	11.57	9.75	0	95.1	11009	0	0.5	707
4371	2000	2770	11.65	9.83	0	96.7	11273	0	0.5	677
4471	1900	2848	11.73	9.91	0	98.3	11529	0	0.5	647
4571	1800	2922	11.81	9.99	0	99.1	11775	0	0.5	617
4671	1700	2993	11.88	10.05	0	101.1	12013	0	0.5	586
4771	1600	3061	11.95	10.12	0	102.5	12242	0	0.5	555
4871	1500	3126	12.01	10.19	0	103.8	12464	0	0.5	524
4971	1400	3187	12.07	10.25	0	105.1	12679	0	0.5	494
5071	1300	3245	12.13	10.31	0	106.3	12888	0	0.5	464
5150	1221	3289	12.17	10.36	0	107.2	13047	0	0.5	440
5150	1221	3289	12.76	11.02	3.50	105.3	13434	1567	0.44	440
5171	1200	3300	12.77	11.03	3.51	105.4	13462	1574	0.44	432
5271	1100	3354	12.83	11.07	3.54	106.0	13586	1603	0.44	397
5371	1000	3402	12.87	11.11	3.56	106.5	13701	1630	0.44	362
5471	900	3447	12.91	11.14	3.58	106.9	13805	1654	0.44	326
5571	800	3487	12.95	11.16	3.60	107.3	13898	1676	0.44	291
5671	700	3522	12.98	11.18	3.61	107.7	13981	1696	0.44	255
5771	600	3553	13.01	11.21	3.63	108.2	14053	1713	0.44	217
5871	500	3579	13.03	11.22	3.64	108.3	14114	1727	0.44	182
5971	400	3600	13.05	11.24	3.65	108.5	14164	1739	0.44	146
6071	300	3617	13.07	11.25	3.66	108.7	14203	1749	0.44	110
6171	200	3629	13.08	11.26	3.66	108.8	14231	1755	0.44	73
6271	100	3636	13.09	11.26	3.67	108.9	14248	1759	0.44	37
6371	0	3639	13.09	11.26	3.67	108.9	14253	1761	0.44	0

Note: z: depth, in km; r: radius, in km; P: pressure, in kbar; ρ: specific mass, in g/cm^3; v_P: P-wave velocity, in km/s; v_S: S-wave velocity, in km/s; Φ: seismic parameter, in km^2/s^2; K: bulk modulus, in kbar; μ: shear modulus, in kbar; v: Poisson's ratio; g: acceleration of gravity, in cm/s^2. [10 kbar = 1 GPa.]

This Page Intentionally Left Blank

Bibliography

Abramson, E. H., Brown, J. M., Slutsky, L. J. & Zaug, J. (1997). The elastic constants of San Carlos olivine to 17 GPa. *J. Geophys. Res.*, **102**, 12 253–12 263.

Ahrens, T. J. (1971). Shock-wave equation of state of minerals. In *Scuola Int. di Fisica "E. Fermi": "Mantello e nucleo nella fisica planetaria"*, J. Coulomb & M. Caputo eds., Academic Press, New York, pp. 157–187.

Ahrens, T. J. (1980). Dynamic compression of Earth materials. *Science*, **207**, 1035–1041.

Ahrens, T. J. (1987). Shock wave techniques for geophysics and planetary physics. In *Methods of Experimental Physics*, C. G. Sammis & T. L. Henyey eds., Academic Press, **24 A**, 185–235.

Ahrens, T. J., Anderson, D. L. & Ringwood, A. E. (1969). Equations of state and crystal structures of high-pressure phases of shocked silicates and oxides. *Rev. Geophys.*, **7**, 667–707.

Akaogi, M., Ito, E. & Navrotsky, A. (1989). Olivine-modified spinel–spinel transitions in the system Mg_2SiO_4–Fe_2SiO_4: Calorimetric measurements, thermochemical calculation, and geophysical application. *J. Geophys. Res.*, **94**, 15 671–15 685.

Akaogi, M., Kojitani, H., Matsuzaka, K., Suzuki, T. & Ito, E. (1998). Post-spinel transformations in the system Mg_2SiO_4–Fe_2SiO_4: Element partitioning, calorimetry and thermodynamic calculation. In *Properties of Earth and Planetary Materials at High Pressure and Temperature*, M. H. Manghnani & T. Yagi eds., American Geophysical Union Monograph 101, AGU, Washington D.C., pp. 373–384.

Akaogi, M., Navrotsky, A., Yagi, T. & Akimoto, S. (1987). Pyroxene–garnet transformation: Thermochemistry and elasticity of garnet solid solutions and application to a pyrolite mantle. In *High-Pressure Research in Mineral Physics*, M. H. Manghnani & Y. Syono eds., American Geophysical Union, Washington, D.C., pp. 251–260.

Akaogi, M., Ross, N., McMillan, P. & Navrotsky, A. (1984). The Mg_2SiO_4 polymorphs (olivine, modified spinel and spinel) – Thermodynamic properties from oxide melt solution calorimetry, phase relations and models of lattice vibrations. *Amer. Mineral.*, **69**, 499–512.

Akimoto, S. (1987). High-pressure research in geophysics: Past, present and future. In *High-Pressure Research in Mineral Physics*, M. H. Manghnani & Y. Syono eds., American Geophysical Union, Washington, D.C., pp. 1–13.

Akimoto, S. & Fujisawa, H. (1965). Demonstration of the electrical conductivity jump produced by the olivine–spinel transition. *J. Geophys. Res.*, **70**, 443–449.

Akimoto, S. & Fujisawa, H. (1966). Olivine–spinel transition in the system Mg_2SiO_4–Fe_2SiO_4 at 800 °C. *Earth Planet. Sci. Lett.*, **1**, 237–240.

Akimoto, S., Suzuki, T., Yagi, T. & Shimomura, O. (1987). Phase diagram of iron determined by high pressure/temperature X-ray diffraction using synchrotron radiation. In *High Pressure Research in Mineral Physics*, M. H. Manghnani & Y. Syono eds., American Geophysical Union, Washington, D.C., pp. 149–154.

Alers, G. A. (1965). Use of sound velocity measurements in determining the Debye temperature of solids. In *Physical Acoustics*, *vol. III B*, W. P. Mason & R. N. Thurston eds., Academic Press, New York, pp. 1–42.

Allègre, C. J. (1982). Chemical geodynamics. *Tectonophysics*, **81**, 109–132.

Allègre, C. J. (1987). Isotope geodynamics. *Earth Planet. Sci. Lett.*, **86**, 175–203.

Allègre, C. J. (1997). Limitation on the mass exchange between the upper and lower mantle: The evolving convection regime of the Earth. *Earth Planet. Sci. Lett.*, **150**, 1–6.

Allègre, C. J. & Turcotte, D. L. (1987). Geodynamic mixing in the mesosphere layer and the origin of oceanic islands. *Geophys. Res. Lett.*, **12**, 207–210.

Allègre, C. J., Poirier, J. P., Humler, E. & Hofmann, A. W. (1995). The chemical composition of the Earth. *Earth Planet. Sci. Lett.*, **134**, 515–526.

Anders, E. & Grevesse, N. (1989). Abundance of the elements: Meteoritic and solar. *Geochim. Cosmochim. Acta*, **35**, 197–214.

Anderson, D. L. (1967). A seismic equation of state. *Geophys. J. R. astr. Soc.*, **13**, 9–30.

Anderson, D. L. (1984). The Earth as a planet: Paradigms and paradoxes. *Science*, **223**, 347–355.

Anderson, D. L. (1987a). A seismic equation of state, II. Shear properties and thermodynamics of the lower mantle. *Phys. Earth Planet. Interiors*, **45**, 307–323.

Anderson, D. L. (1987b). Thermally induced phase changes, lateral heterogeneity of the mantle, continental roots and deep slab anomalies. *J. Geophys. Res.*, **92**, 13 968–13 980.

Anderson, D. L. (1988). Temperature and pressure derivatives of elastic constants, with application to the mantle. *J. Geophys. Res.*, **93**, 4668–4700.

Anderson, D. L. (1989a). Composition of the Earth. *Science*, **243**, 367–370.

Anderson, D. L. (1989b). *Theory of the Earth*, Blackwell, Oxford.

Anderson, D. L. & Anderson, O. L. (1970). The bulk modulus–volume relationship for oxides. *J. Geophys. Res.*, **75**, 3494–3500.

Anderson, D. L. & Bass, J. D. (1986). Transition region of the Earth's upper mantle. *Nature*, **320**, 321–328.

Anderson, D. L. & Kanamori, H. (1968). Shock-wave equations of state for rocks and minerals. *J. Geophys. Res.*, **73**, 6477–6502.

Anderson, O. L. (1963). A simplified method for calculating the Debye temperature from elastic constants. *J. Phys. Chem. Solids*, **24**, 909–917.

Anderson, O. L. (1979). Evidence supporting the approximation $\gamma\rho = \text{const}$ for the Grüneisen parameter of the Earth lower mantle. *J. Geophys. Res.*, **84**, 3537–3542.

Anderson, O. L. (1980). An experimental high-temperature thermal equation of state bypassing the Grüneisen parameter. *Phys. Earth Planet. Interiors*, **22**,

173–183.
Anderson, O. L. (1982). The Earth's core and the phase diagram of iron. *Phil. Trans. Roy. Soc. Lond.*, **A306**, 21–35.
Anderson, O. L. (1984). A universal thermal equation of state. *J. Geodynamics* , **1**, 185–214.
Anderson, O. L. (1985). Ramsey's silicate core revisited. *Nature*, **314**, 407–408.
Anderson, O. L. (1986). Properties of iron at the Earth's core conditions. *Geophys. J. R. astr. Soc.*, **84**, 561–579.
Anderson, O. L. (1988). Simple solid-state equations for materials of terrestrial planet interiors. In *The Physics of Planets*. S. K. Runcorn ed., J. Wiley, London, pp. 27–60.
Anderson, O. L. (1995a). *Equations of State of Solids for Geophysics and Ceramic Science*. Oxford University Press, Oxford.
Anderson, O. L. (1995b). The volume dependence of thermal pressure in solids. *J. Phys. Chem. Solids*, **58**, 335–343.
Anderson, O. L. (1997). Iron: beta phase frays. *Science*, **278**, 821–822.
Anderson, O. L. (1998). Thermoelastic properties of $MgSiO_3$ perovskite using the Debye approach. *Amer. Mineralogist*, **83**, 23–35.
Anderson, O. L. & Duba, A. (1997). Experimental melting curve of iron revisited. *J. Geophys. Res.*, **102**, 22 659–22 669.
Anderson, O. L. & Isaak, D. G. (1995). Elastic constants of mantle minerals at high temperature. *Mineral Physics and Crystallography, A Handbook of Physical Constants*, T. J. Ahrens, ed., American Geophysical Union, Washington, D.C., pp. 64–97.
Anderson, O. L. & Nafe, J. E. (1965). The bulk modulus–volume relationship for oxide compounds and related geophysical problems. *J. Geophys. Res.*, **70**, 3951–3963.
Anderson, O. L. & Sumino, Y. (1980). The thermodynamic properties of the Earth's lower mantle. *Phys. Earth Planet. Interiors*, **23**, 314–331.
Anderson, O. L. & Suzuki, I. (1983). Anharmonicity of three minerals at high temperature: Forsterite, fayalite and periclase. *J. Geophys. Res.* , **88**, 3549–3556.
Anderson, O. L., Masuda, K. & Isaak, D. G. (1995). A new thermodynamic approach for high-pressure physics. *Phys. Earth Planet. Interiors*, **91**, 3–16.
Anderson, P. W. (1984). *Basic Notions of Condensed Matter Physics*. Benjamin, London, pp. 49–69.
Anderson, W. W. & Ahrens, T. J. (1994) An equation of state for liquid iron and implications for the Earth's core. *J. Geophys. Res.* , **99**, 4273–4284.
Andrade, E. N. da C. (1934). A theory of the viscosity of liquids. *Phil. Mag.*, **17**, 497–732.
Andrade, E. N. da C. (1952). Viscosity of liquids. *Proc. Roy. Soc. Lond.*, **215A**, 36–43.
Andrault, D. & Poirier, J. P. (1991) Evolution of the distortion of perovskites under pressure: An EXAFS study of $BaZrO_3$, $SrZrO_3$ and $CaGeO_3$. *Phys. Chem. Minerals*, **18**, 91–105.
Andrault, D., Fiquet, G., Kunz, M., Visocekas, F. & Haüsermann, D. (1997). The orthorhombic structure of iron: An *in-situ* study at high temperature and high pressure. *Science*, **278**, 831–834.
Angel, R. J. & Ross, N. L. (1996). Compression mechanisms and equations of state. *Phil. Trans. Roy. Soc. Lond.*, **A 354**, 1449–1459.
Animalu, A. O. E. (1977). *Intermediate Quantum Theory of Crystalline Solids*,

Prentice-Hall, New Jersey.
Appel, J. (1968). Polarons. *Sol. State Phys.*, **21**, 193–391.
Austin, I. G. & Mott, N. F. (1969). Polarons in crystalline and non-crystalline materials. *Adv. Phys.*, **18**, 41–102.
Babb, S. E. (1963a). Parameters in the Simon equation relating pressure and melting temperature. *Rev. Mod. Phys.*, **35**, 400–413.
Babb, S. E. (1963b). Values of the Simon constants. *J. Chem. Phys.*, **38**, 2743–2749.
Badding, J. V., Hemley, R. J. & Mao, H. K. (1991). High-pressure chemistry of hydrogen in metals: *In-situ* study of iron hydrides. *Science*, **253**, 421–424.
Badro, J., Gillet, P. & Barrat, J. L. (1998). Melting and pressure-induced amorphization of quartz. *Europhys. Lett.*, **42**, 643–648.
Bai, Q., Mackwell, S. J. & Kohlstedt, D. L. (1991). High-temperature creep of olivine single crystals. 1. Mechanical results for buffered samples. *J. Geophys. Res.*, **96**, 2441–2463.
Balachandran, U., Odekirk, B. & Eror, N. G. (1982). Electrical conductivity of calcium titanate. *J. Solid State Chem.*, **41**, 185–194.
Banks, B. E. C., Damjanovic, V. & Vernon, C. A. (1972). The so-called thermodynamic compensation law and thermal death. *Nature*, **240**, 147–148.
Barin, I. & Knacke, O. (1973) *Thermochemical properties of inorganic substances*, Springer.
Bassett, W. A. (1977). The diamond cell and the nature of the Earth's interior. *Ann. Rev. Earth Planet. Sci.*, **7**, 357–384.
Bassett, W. A. & Huang, E. (1987). Mechanism of the body-centered cubic–hexagonal close-packed phase transition in iron. *Science*, **238**, 780–783.
Bassett, W. A. & Weathers, M. S. (1990). Stability of the body-centered cubic phase of iron: A thermodynamic analysis. *J. Geophys. Res.*, **95**, 21709–21711.
Battezzati, L. & Greer, A. L. (1989). The viscosity of liquid metals and alloys. *Acta Metall.*, **37**, 1791–1802.
Béjina, F. & Jaoul, O. (1997). Silicon diffusion in silicate minerals. *Earth Planet. Sci. Lett.*, **153**, 229–238.
Béjina, F., Ratteron, P., Zhang, J., Jaoul, O. & Liebermann, R. C. (1997). Activation volume of silicon diffusion in San Carlos olivine. *Geophys. Res. Lett.*, **24**, 2597–2600.
Bell, P. M., Mao, H. K. & Xu, J. A. (1987). Error analysis in parameter-fitting in equations of state for mantle minerals. In *High-Pressure Research in Mineral Physics*, M. H. Manghnani & Y. Syono eds., American Geophysical Union, Washington, D.C., pp. 447–454.
Bell, P. M., Yagi, T. & Mao, H. K. (1979). Iron–magnesium distribution coefficients between spinel $(Mg, Fe)_2SiO_4$, magnesiowüstite (Mg, Fe)O and perovskite $(Mg, Fe)SiO_3$. *Carnegie Inst. Washington Yearbook*, **78**, 618–621.
Bercovici, D., Schubert, G. & Glatzmaier, G. A. (1989). Three-dimensional spherical models of convection in the Earth's mantle. *Science*, **244**, 950–955.
Berger, J. & Joigneau, S. (1959). Au sujet de la relation linéaire existant entre la vitesse matérielle et la vitesse de l'onde de choc se propageant dans un métal. *C. R. Acad. Sci. Paris*, **249**, 2506–2508.
Bergman, M. I. (1997). Measurements of elastic anisotropy due to solidification texturing and the implications for the Earth's inner core. *Nature*, **389**, 60–63.
Bergman, M. I. (1998). Estimates of the Earth's inner core grain size. *Geophys. Res. Lett.*, **25**, 1593–1596.
Berman, R. (1976). *Thermal Conduction in Solids*, Oxford University Press, Oxford.

Bester, H. & Lange, K. W. (1972). Abschätzung mittlerer Werte für die Diffusion von Kohlenstoff, Sauerstoff, Wasserstoff, Stickstoff und Schwefel in festem und flüssigen Eisen. *Archiv für das Eisenhüttenweisen*, **3**, 207–213.

Bina, C. R. (1995). Confidence limits for silicate perovskite equations of state. *Phys. Chem. Minerals*, **22**, 375–382.

Binns, R. A., Davis, R. J., & Reed, S. J. B. (1969). Ringwoodite, natural Mg_2SiO_4 spinel in the Tenham meteorite. *Nature*, **221**, 943–944.

Birch, F. (1938). The effect of pressure upon the elastic parameters of isotropic solids, according to Murnaghan's theory of finite strain. *J. Appl. Phys.*, **9**, 279–288.

Birch, F. (1947). Finite elastic strain of cubic crystals. *Phys. Rev.*, **71**, 809–924.

Birch, F. (1952). Elasticity and constitution of the Earth's interior. *J. Geophys. Res.*, **57**, 227–286.

Birch, F. (1961a). The velocity of compressional waves in rocks to 10 kilobars, Part 2. *J. Geophys. Res.*, **66**, 2199–2224.

Birch, F. (1961b). Composition of the Earth's mantle. *Geophys. J. R. astr. Soc.*, **4**, 295–311.

Birch, F. (1963). Some geophysical applications of high-pressure research. In *Solids under Pressure* , W. Paul & D. M. Warschauer eds., McGraw Hill, New York, pp. 137–162.

Birch, F. (1964). Density and composition of mantle and core. *J. Geophys. Res.*, **69**, 4377–4388.

Birch, F. (1968). Thermal expansion at high pressures. *J. Geophys. Res.*, **73**, 817–819.

Birch, F. (1972). The melting relations of iron and temperatures in the Earth's core. *Geophys. J. R. astr. Soc.*, **29**, 373–387.

Blackman, M. (1955). The specific heat of solids. In *Handbüch der Physik*, vol. VII. S. Flugge ed., Springer, pp. 325–382.

Bocquet, J. L., Brébec, G. & Limoge, Y. (1983). Diffusion in metals and alloys. In *Physical Metallurgy*, R. W. Cahn and P. Haasen eds., North-Holland, Amsterdam, pp. 386–475.

Boehler, R. (1982). Adiabats of quartz, coesite, olivine and magnesium oxide to 50 kbar and 100 K, and the adiabatic gradient in the Earth's mantle. *J. Geophys. Res.*, **87**, 5501–5506.

Boehler, R. (1986). The phase diagram of iron to 430 kbar. *Geophys. Res. Lett.*, **13**, 1153–1156.

Boehler, R. (1992). Melting of Fe–FeO and Fe–FeS systems at high pressure: Constraints on core temperatures. *Earth & Planet. Sci. Lett.*, **111**, 217–227.

Boehler, R. (1993). Temperatures in the Earth's core from melting point measurements of iron at high static pressures. *Nature*, **363**, 534–536.

Boehler, R. (1997). Melting curve of aluminum in a diamond anvil cell to 0.8 Mbar: Implications for iron. *Earth & Planet. Sci. Lett.*, **153**, 223–227.

Boehler, R. & Ramakrishnan, J. (1980). Experimental results on the pressure dependence of the Grüneisen parameter: A review. *J. Geophys. Res.*, **85**, 6996–7002.

Boehler, R., von Bargen, N. & Chopelas, A. (1990) Melting, thermal expansion and phase transitions of iron at high pressures. *J. Geophys. Res.*, **95**, 21 731–21 736.

Boehler, R. & Zerr, A. (1994). (Response to) High-pressure melting of $(Mg, Fe)SiO_3$ perovskite [by Heinz, D. L. *et al.*]. *Science*, **264**, 279–281.

Boland, J. N., & Liebermann, R. C. (1983). Mechanism of the olivine to spinel

phase transformation in Ni_2SiO_4. *Geophys. Res. Lett.*, **10**, 87–90.
Boland, J. N. & Liu, L. G. (1983). Olivine to spinel transformation in Mg_2SiO_4 via faulted structures. *Nature*, **303**, 233–235.
Bolt, B. A. (1982). *Inside the Earth*, W. H. Freeman & Co., San Francisco.
Bolt, B. A. (1991). The precision of density estimation deep in the Earth. *Q. J. R. astr. Soc.*, **32**, 367–388.
Boon, M. R. (1973). Thermodynamic compensation rule. *Nature*, **243**, 401.
Borg, R. J., & Dienes, G. J. (1988). *An Introduction to Solid State Diffusion*, Academic Press, New York.
Born, M. (1939). Thermodynamics of crystals and melting. *J. Chem. Phys.*, **7**, 591–603.
Boschi, E. & Caputo, M. (1969). Equations of state at high pressure and the Earth's interior. *Riv. Nuovo Cimento*, **1**, 441–513.
Bottinga, Y. (1985). On the isothermal compressibility of silicate liquids at high pressure. *Earth Planet. Sci. Lett.*, **74**, 350–360.
Bowen, H. K., Adler, D. & Auker, B. H. (1975). Electrical and optical properties of FeO. *J. Solid State Chem.*, **12**, 355–359.
Bradley, R. S., Jamil, A. K. & Munro, D. C. (1964). The electrical conductivity of olivine at high temperature and pressure. *Geochim. Cosmochim. Acta*, **28**, 1669–1678.
Bradley, R. S., Milnes, G. J. & Munro, D. C. (1973). The electrical conductivities at elevated temperatures and pressures of polycrystalline manganese, cobalt and nickel orthosilicates. *Geochim. Cosmochim. Acta*, **37**, 2379–2394.
Brady, J. B. (1995). Diffusion data for silicate minerals, glasses and liquids. In *Mineral Physics and Crystallography, A Handbook of Physical Constants*, T. J. Ahrens, ed., American Geophysical Union, Washington, D.C., pp. 269–290.
Braginsky, S. I. (1964). Magnetohydrodynamics of the Earth's core? *Geomagnetism & Aeronomy*, **4**, 698–712.
Brearley, A. J., Rubie, D. C. & Ito, E. (1992). Mechanisms of the transformations between the α, β and γ polymorphs of Mg_2SiO_4 at 15 GPa. *Phys. Chem. Minerals*, **18**, 343–358.
Brennan, B. J. & Stacey, F. D. (1979). A thermodynamically based equation of state for the lower mantle. *J. Geophys. Res.*, **84**, 5535–5539.
Brett, R. (1976). The current status of speculations on the composition of the core of the Earth. *Rev. Geophys. Space Phys.*, **14**, 375–383.
Brillouin, L. (1938). On the thermal dependence of elasticity in solids. *Phys. Rev.*, **54**, 916–917.
Brillouin, L. (1940). Influence de la température sur l'élasticité d'un solide. *Mémorial des Sciences Mathématiques*, **94**, 1–65.
Brillouin, L. (1960). *Les Tenseurs en Mécanique et en Elasticité*, Masson, Paris.
Brillouin, M. (1898). Théorie de la fusion complète et de la fusion pâteuse. *Ann. Chim. et Phys.*, **13**, 264–275.
Brown, J. M. (1986). Interpretation of the D″ zone at the base of the mantle: Dependence on assumed values of thermal conductivity. *Geophys. Res. Lett.*, **13**, 1509–1512.
Brown, J. M. & McQueen, R. G. (1980). Melting of iron under core conditions. *Geophys. Res. Lett.*, **7**, 533–536.
Brown, J. M. & McQueen, R. G. (1982). The equation of state for iron and the Earth's core. In *High Pressure Research in Geophysics* , S. Akimoto & M. H. Manghnani eds., D. Reidel, Dordrecht, pp. 611–623.
Brown, J. M. & McQueen, R. G. (1986). Phase transitions, Grüneisen parameter

and elasticity for shocked iron between 77 GPa and 400 GPa. *J. Geophys. Res.*, **91**, 7485–7494.
Brown, J. M. & Shankland, T. J. (1981). Thermodynamic parameters in the Earth as determined from seismic profiles. *Geophys. J. R. astr. Soc.*, **66**, 579–596.
Brush, S. G. (1962). Theories of liquid viscosity. *Chemical Reviews*, **62**, 513–548.
Brush, S. G. (1979). Nineteenth century debates about the inside of the Earth: Solid, liquid or gas? *Annals of Science*, **36**, 225–254.
Brush, S. G. (1982). Chemical history of the Earth's core. *EOS Trans. AGU*, **63**, 1185–1188.
Buffett, B. A. (1997). Geodynamic estimates of the viscosity of the Earth's inner core. *Nature*, **388**, 571–573.
Buffett, B. A., Huppert, H. E., Lister, J. R. & Woods, A. W. (1992). Analytical model for solidification of the Earth's core. *Nature*, **356**, 329–331.
Bukowinski, M. S. T. (1976). The effect of pressure on the physics and chemistry of potassium. *Geophys. Res. Lett.*, **3**, 491–494.
Bullen, K. E. (1963). An index of degree of chemical inhomogeneity in the Earth. *Geophys. J. R. astr. Soc.*, **7**, 584–592.
Bullen, K. E. (1975). *The Earth's Density*, Chapman & Hall, London.
Bullen, K. E. & Bolt, B. A. (1985). *An Introduction to the Theory of Seismology*, Cambridge University Press, Cambridge.
Bundy, F. P. (1965). Pressure–temperature phase diagram of iron to 200 kbar, 900 °C. *J. Appl. Phys.*, **36**, 616–620.
Burchfield, J. D. (1990). *Lord Kelvin and the Age of the Earth*. University of Chicago Press, Chicago.
Burnley, P. C. (1995). The fate of olivine in subducting slabs: A reconnaissance study. *Amer. Mineralogist*, **80**, 1293–1301.
Burnley, P. C. & Green, H. W. (1989). The olivine–spinel transformation: The dependence of the nucleation mechanism on the level of stress. *Nature*, **338**, 753–756.
Butler, R. & Anderson, D. L. (1978). Equation of state fits to the lower mantle and outer core. *Phys. Earth Planet. Interiors*, **17**, 147–162.
Callen, H. B. (1985). *Thermodynamics, an Introduction to Thermostatistics*, J. Wiley, New York.
Cannon, W. R. & Langdon, T. G. (1983). Creep of ceramics. *J. Mat. Sci.*, **18**, 1–50.
Carslaw, H. S. & Jaeger, J. C. (1959). *Conduction of Heat in Solids*. Oxford University Press, Oxford.
Cazenave, A., Souriau, A. & Dominh, K. (1989). Global coupling of Earth surface topography with hotspots, geoid and mantle heterogeneities. *Nature*, **340**, 54–57.
Cemic, L., Will, G. & Hinze, E. (1980). Electrical conductivity measurements on olivines Mg_2SiO_4–Fe_2SiO_4 under defined thermodynamic conditions. *Phys. Chem. Minerals*, **6**, 95–107.
Chai, M., Brown, J. M. & Slutsky, L. J. (1996). Thermal diffusivity of mantle minerals. *Phys. Chem. Minerals*, **23**, 470–475.
Chen, G. & Ahrens, T. J. (1995). Equations of state of α, ε and liquid iron and iron's melting curve – Thermodynamic calculations. *Geophys. Res. Lett.*, **22**, 21–24.
Chen, G., Liebermann, R. C. & Weidner, D. J. (1998). Elasticity of single-crystal MgO to 8 gigapascals and 1600 kelvin, *Science*, **280**, 1913–1916.
Chen, H. C., Gartstein, E. & Mason, T. O. (1982). Conduction mechanism analysis for $Fe_{1-\delta}O$ and $Co_{1-\delta}O$. *J. Phys. Chem. Solids*, **43**, 991–995.

Chen, W. K. & Peterson, N. L. (1980). Iron diffusion and electrical conductivity in magnesiowüstite solid solutions (Mg,Fe)O. *J. Phys. Chem. Solids*, **41**, 335–339.

Chopelas, A. & Boehler, R. (1989). Thermal expansion measurements at very high pressures, systematics and a case for a chemically homogeneous mantle. *Geophys. Res. Lett.*, **16**, 1347–1350.

Chopelas, A. & Boehler, R. (1992). Thermal expansivity in the lower mantle. *Geophys. Res. Lett.*, **19**, 1983–1986.

Christensen, U. (1984). Large-scale mantle dynamics and the 670 km discontinuity. *Terra Cognita*, **4**, 59–66.

Christensen, U. (1995). Effects of phase transitions on mantle convection. *Ann. Rev. Earth Planet. Sci.*, **23**, 65–87.

Chung, D. H. (1972). Birch's law: Why is it so good? *Science*, **177**, 261–263.

Clark, S. P. (1957). Radiative transfer in the Earth's mantle. *Trans. AGU*, **38**, 931–938.

Cohen, M. H. & Turnbull, D. S. (1959). Molecular transport in liquids and glasses. *J. Chem. Phys.*, **31**, 1164–1169.

Cohen, R. E. (1987). Elasticity and equation of state of $MgSiO_3$ perovskite. *Geophys. Res. Lett.*, **14**, 1053–1056.

Cohen, R. E. & Weitz, J. S. (1998). The melting curve and premelting of MgO. In *Properties of Earth and Planetary Materials at High Pressure and Temperature*, M. H. Manghnani & T. Yagi eds., American Geophysical Union Monograph 101, AGU, Washington D.C., pp. 185–196.

Cotterill, R. M. J. (1980). The physics of melting. *J. Crystal Growth*, **48**, 582–588.

Coey, J. M. D., Bakas, T., McDonagh, C. M. & Litterst, F. J. (1989). Electrical and magnetic properties of cronstedtite. *Phys. Chem. Minerals*, **16**, 394–400.

Creager, K. C. (1992). Anisotropy of the inner core from differential travel times of the phases PKP and PKIKP. *Nature*, **356**, 309–314.

Creager, K. C. & Jordan, T. H. (1986). Slab penetration into the lower mantle beneath the Mariana and other island orcs of the northwest Pacific. *J. Geophys. Res.*, **91**, 3573–3589.

Davies, G. F. (1976). The estimation of elastic properties from analogue compounds. *Geophys. J. R. astr. Soc.*, **44**, 625–647.

Davies, G. F. & Gurnis, M. (1986). Interaction of mantle dregs with convection: Lateral heterogeneity at the core–mantle boundary. *Geophys. Res. Lett.*, **13**, 1517–1520.

Dewaele, A. & Guyot, F. (1998). Thermal parameters of the Earth's lower mantle. *Phys. Earth Planet. Interiors*, **107**, 261–267.

de Wijs, G. A., Kresse, G., Vočadlo, L. *et al.* (1998). The viscosity of liquid iron at the physical conditions of the Earth's core. *Nature*, **392**, 805–807.

Dieckmann, R. (1984). Point defects and transport properties of binary and ternary oxides. In *Transport in Non-Stoichiometric Compounds*, G. Petot-Ervas, H. J. Matzke, C. Monty eds., North-Holland, Amsterdam, pp. 1–22.

Dobson, D. P., Richmond, N. C. & Brodholt, J. P. (1997). A high-temperature electrical conduction mechanism in the lower mantle phase $(Mg, Fe)_{1-x}O$. *Science*, **275**, 1779–1781.

Domb, C. (1951). The melting curve at high pressures. *Phil. Mag.*, **42**, 1316–1324.

Dornboos, D. J., Spiliopoulos, S. & Stacey, F. D. (1986). Seismological properties of D″ and the structure of a thermal boundary layer. *Phys. Earth Planet. Interiors*, **41**, 225–239.

Dosdale, T. & Brook, R. J. (1983). Comparison of diffusion data and of activation energies. *J. Amer. Ceram. Soc.*, **66**, 392–395.
Doukhan, J. C. (1995). The phenomenon of early partial melting. *C. R. Acad. Sci. Paris IIa*, **320**, 1–8.
Drickamer, H. G. (1963). The electronic structure of solids under pressure. In *Solids under Pressure*, W. Paul & D. Warschauer eds., McGraw-Hill, 357–384.
Duba, A. (1992). Earth's core not so hot. *Nature*, **359**, 197–198.
Duba, A. & Nicholls, I. A. (1973). The influence of the oxidation state on the electrical conductivity of olivine. *Earth Planet. Sci. Lett.*, **18**, 59–64.
Duba, A., Heard, H. C. & Schock, R. N. (1974). Electrical conductivity of olivine at high pressure and under controlled oxygen fugacity. *J. Geophys. Res.*, **79**, 1667–1673.
Duba, A., Ito, J. & Jamieson, J. C. (1973). The effect of ferric iron on the electrical conductivity of olivine. *Earth Planet. Sci. Lett.*, **18**, 279–284.
Duba, A., Peyronneau, J., Visocekas, F. & Poirier, J. P. (1997). Electrical conductivity of magnesiowüstite/perovskite produced by laser heating of synthetic olivine in the diamond anvil cell. *J. Geophys. Res.*, **102**, 27 723–27 728.
Duba, A. G. & Wanamaker, B. J. (1994). DAC measurement of perovskite conductivity and implications for the distribution of mineral phases in the lower mantle. *Geophys. Res. Lett.*, **21**, 1643–1646.
Dubrovinsky, L. S., Saxena, S. K. & Lazor, P. (1998a). High-pressure and high-temperature *in-situ* X-ray diffraction study of iron and corundum to 68 GPa using an internally heated diamond anvil cell. *Phys. Chem. Minerals*, **25**, 434–441.
Dubrovinsky, L. S., Saxena, S. K. & Lazor, P. (1998b). Stability of β-iron: a new synchrotron X-ray study of heated iron at high pressure. *Eur. J. Mineral*, **10**, 43–47.
Duffy, T. S. & Anderson, D. L. (1989). Seismic velocities in mantle minerals and the mineralogy of the upper mantle. *J. Geophys. Res.*, **94**, 1895–1912.
Duffy, T. S. & Hemley, R. J. (1995). Some like it hot: The temperature structure of the Earth. *Rev. Geophys., Supplement* (July), 5–9.
Dugdale, J. S. & MacDonald, D. K. C. (1953). The thermal expansion of solids. *Phys. Rev.*, **89**, 832–834.
Dugdale, J. S. & MacDonald, D. K. C. (1955). Lattice thermal conductivity. *Phys. Rev.*, **98**, 1751–1752.
Durand, M. A. (1936). The temperature variation of the elastic moduli of NaCl, KCl and MgO. *Phys. Rev.*, **50**, 449–455.
Dziewonski, A. M. & Anderson, D. L. (1981). Preliminary reference Earth model. *Phys. Earth Planet. Interiors*, **25**, 297–356.
Eddington, A. S. (1930). *The Internal Constitution of the Stars*, Cambridge University Press, Cambridge.
Eliezer, S., Ghatak, A. & Hora, H. (1986). *An Introduction to Equations of State. Theory and Applications*, Cambridge University Press, Cambridge.
Ellsworth, K., Schubert, G. & Sammis, C. G. (1985). Viscosity profile of the lower mantle. *Geophys. J. R. astr. Soc.*, **83**, 199–214.
Elsasser, W. M. (1951). Quantum-theoretical densities of solids at extreme compressions. *Science*, **113**, 105–107.
Emin, D. (1975). Transport properties of small polarons. *J. Sol. State Chem.*, **12**, 246–252.

Exner, O. (1964). Concerning the isokinetic relation. *Nature*, **201**, 488–490.
Eyring, H. (1936). Viscosity, plasticity and diffusion as examples of absolute reaction rates. *J. Chem. Phys.*, **4**, 283–291.
Falzone, A. J. & Stacey, F. D. (1980). Second-order elasticity theory: Explanation for the high Poisson's ratio of the inner core. *Phys. Earth Planet. Interiors*, **21**, 371–377.
Fei, Y. & Mao, H. K. (1994). *In-situ* determination of the NiAs phase of FeO at high pressure and temperature. *Science*, **266**, 1678–1680.
Fei, Y., Bertka, C. M. & Finger, L. W. (1997). High-pressure iron–sulfur compound Fe_3S_2 and melting relations in the Fe–FeS system. *Science*, **275**, 1621–1623.
Fei, Y., Mao, H. K., Shu, J. & Hu, J. (1992). P–V–T equation of state of magnesiowüstite $(Mg_{0.6}, Fe_{0.4})O$. *Phys. Chem. Minerals*, **18**, 416–422.
Feynman, R. P., Metropolis, N. & Teller, E. (1949). Equations of state of elements based on the generalized Fermi–Thomas theory. *Phys. Rev.*, **75**, 1561–1573.
Fiquet, G., Andrault, D., Dewaele, A., Charpin, T., Kunz, M. & Haüsermann, D. (1998). *P–V–T* equation of state of $MgSiO_3$ perovskite. *Phys. Earth Plant. Interiors*, **105**, 21–31.
Fischer, K. M., Jordan, T. H. & Creager, K. C. (1988). Seismic constraints on the morphology of deep slabs. *J. Geophys. Res.*, **93**, 4773–4783.
Frank, F. C. (1939). Melting as a disorder phenomenon. *Proc. Roy. Soc. Lond.*, **A 170**, 182–189.
Freer, R. (1980). Self-diffusion and impurity diffusion in oxides. *J. Mat. Sci.*, **15**, 803–824.
Freer, R. (1981). Diffusion in silicate minerals and glasses: A data digest and guide to the literature. *Contrib. Mineral. Petrol.*, **76**, 440–454.
Friedel, J. (1964). *Dislocations*. Pergamon Press, Oxford.
Frost, H. J. & Ashby, M. F. (1982). *Deformation-mechanism Maps*. Pergamon Press, Oxford.
Fujino, K. & Irifune, T. (1992). TEM studies on the olivine to modified spinel transformation in Mg_2SiO_4. In *High-Pressure Research*: *Applications to Earth and Planetary Sciences*, Y. Syono & M. H. Manghnani eds., Terra pub, Tokyo, pp. 237–243.
Fujisawa, H. (1998). Elastic wave velocities of forsterite and its β-spinel form and chemical boundary hypothesis for the 410-km discontinuity. *J. Geophys. Res.*, **103**, 9591–9608.
Fujisawa, H., Fujii, N., Mizutani, H., Kanamori, H. & Akimoto, S. (1968). Thermal diffusivity of Mg_2SiO_4, Fe_2SiO_4 and NaCl at high pressures and temperatures. *J. Geophys. Res.*, **73**, 4727–4733.
Fukai, Y. & Suzuki, T. (1986). Iron–water reaction under high pressure and its implications in the evolution of the Earth. *J. Geophys. Res.*, **91**, 9222–9230.
Fukao, Y. (1992). Seismic tomography of the Earth's mantle: Geodynamic implications. *Science*, **258**, 625–630.
Funamori, N. & Yagi, T. (1993) High pressure and high temperature *in-situ* X-ray observation of $MgSiO_3$ perovskite under lower mantle conditions. *Geophys. Res. Lett.*, **20**, 387–390.
Funamori, N., Yagi, T., Utsumi, W., Kondo, T., Uchida, T. & Funamori, M. (1996). Thermoelastic properties of $MgSiO_3$ perovskite determined by *in situ* X-ray observations up to 30 GPa and 2000 K. *J. Geophys. Res.*, **101**, 8257–8269.
Furnish, M. D. & Bassett, W. A. (1983). Investigation of the mechanism of the

olivine–spinel transition in fayalite by synchrotron radiation. *J. Geophys. Res.*, **88**, 10 333–10 341.
Ganguly, J. & Kennedy, G. C. (1977). Solubility of K in Fe–S liquid, silicate–K–$(Fe–S)^{liq}$ equilibria, and their planetary implications. *Earth Planet. Sci. Lett.*, **35**, 411–420.
Gardiner, R. B. & Stacey, F. D. (1971). Electrical resistivity of the core. *Phys. Earth Planet. Interiors*, **4**, 406–410.
Garnero, E. J., Revenaugh, J., Williams, Q., Lay, T. & Kellogg, L. H. (1998). Ultralow velocity zone at the core–mantle boundary. In *The Core–Mantle Boundary Region*, M. Gurnis *et al.* eds., American Geophysical Union, Washington, D.C., pp. 319–334.
Gérard, O. & Jaoul, O. (1989). Oxygen diffusion in San Carlos olivine. *J. Geophys. Res.*, **94**, 4119–4128.
Gillan, M. J. (1997). The virtual matter laboratory. *Contemp. Phys.*, **38**, 115–130.
Gillet, P. (1995). Mineral physics, mantle mineralogy and mantle dynamics. *C. R. Acad. Sci. Paris IIa*, **320**, 341–356.
Gillet, P., Guyot, F. & Malezieux, J. M. (1989). High pressure, high temperature Raman spectroscopy of Ca_2GeO_4 (olivine form): Some insights on anharmonicity. *Phys. Earth Planet. Interiors*, **58**, 141–154.
Gilvarry, J. J. (1956a). The Lindemann and Grüneisen laws. *Phys. Rev.*, **102**, 308–316.
Gilvarry, J. J. (1956b). Grüneisen's law and the fusion curve at high pressure. *Phys. Rev.*, **102**, 317–325.
Gilvarry, J. J. (1956c). Equation of the fusion curve. *Phys. Rev.*, **102**, 325–331.
Gilvarry, J. J. (1956d). Grüneisen parameter for a solid under finite strain. *Phys. Rev.*, **102**, 331–340.
Gilvarry, J. J. (1957a). Temperature dependent equations of state of solids. *J. Appl. Phys.*, **28**, 1253–1261.
Gilvarry, J. J. (1957b). Temperatures in the Earth's interior. *J. Atm. Terrestr. Phys.*, **10**, 84–95.
Gilvarry, J. J. (1966). Lindemann and Grüneisen laws and a melting law at high pressures. *Phys. Rev. Lett.*, **16**, 1089–1091.
Goarant, F., Guyot, F., Peyronneau, J. & Poirier, J. P. (1992). High-pressure and high-temperature reactions between silicates and liquid iron alloys, in the diamond anvil cell, studied by analytical electron microscopy. *J. Geophys. Res.*, **97**, 4477–4487.
Graham, E. K. & Barsch, G. R. (1969). Elastic constants of single-crystal forsterite as a function of temperature and pressure. *J. Geophys. Res.*, **74**, 5949–5960.
Graham, E. K. Schwab, J. A., Sopkin, S. M. & Takei, H. (1988). The pressure and temperature dependence of the elastic properties of single-crystal fayalite Fe_2SiO_4. *Phys. Chem. Minerals*, **16**, 186–198.
Grosse, A. V. (1963). The empirical relation between the activation energy of viscosity of liquid metals and their melting points. *J. Inorg. Nuclear Chem.*, **25**, 317–318.
Guillermet, A. F. & Gustafson, P. (1984). *An Assessment of the Thermodynamic Properties and Phase Diagram of Iron.* Report Trita-Mac-0229, Materials Centre, Roy. Inst. Technology, Stockholm. 38 pp.
Gurney, R. W. (1966). *Introduction to Statistical Mechanics.* Dover, New York.
Guyot, F., Gwanmesia, G. D. & Liebermann, R. C. (1991). An olivine to beta phase transformation mechanism in Mg_2SiO_4. *Geophys. Res. Lett.*, **18**, 89–92.
Guyot, F., Madon, M., Peyronneau, J. & Poirier, J. P. (1988a). X-ray micro-

analysis of high-pressure/high-temperature phases synthesized from natural olivine in a diamond anvil cell. *Earth Planet. Sci. Lett.*, **90**, 52–64.
Guyot, F., Peyronneau, J. & Poirier, J. P. (1988b). TEM study of high pressure reactions between iron and silicate perovskites. *Chemical Geology*, **70**, 61.
Hager, B. H., Clayton, R. W., Richards, M. A., Comer, R. P. & Dziewonski, A. (1985). Lower mantle heterogeneity, dynamic topography and the geoid. *Nature*, **313**, 541–545.
Hama, J. & Suito, K. (1996). The search for a universal equation of state correct up to very high pressures. *J. Phys.: Condens. Matter*, **8**, 67–81.
Hama, J. & Suito, K. (1998) Equation of state of $MgSiO_3$ perovskite and its thermoelastic properties under lower-mantle conditions, *J. Geophys. Res.*, **103**, 7443–7462.
Hamilton, R. M. (1965). Temperature variation at constant pressures of the electrical conductivity of periclase and olivine. *J. Geophys. Res.*, **70**, 5679–5692.
Hansen, K. W. & Cutler, I. B. (1966). Electrical conductivity in $Fe_{1-x}O$–MgO solid solutions. *J. Amer. Ceram. Soc.*, **49**, 100–102.
Harris, P. S. (1973). Compensation effect and experimental error. *Nature*, **243**, 401–402.
Hart, S. R. (1981). Diffusion compensation in natural silicates. *Geochim. Cosmochim. Acta*, **45**, 279–291.
Hart, S. R. & Zindler, A. (1986). In search of a bulk Earth composition. *Chemical Geology*, **57**, 247–267.
Hausleitner, C. & Hafner, J. (1989) A theoretical study of the melting curve of iron to very high pressure. *J. Phys.: Condens. Matter*, **1**, 5243–5252.
Heinz, D. L. & Jeanloz, R. (1987). Measurement of the melting curve of $Mg_{0.9}Fe_{0.1}SiO_3$ at lower-mantle conditions and its geophysical implications. *J. Geophys. Res.*, **92**, 11 437–11 444.
Heinz, D. L., Knittle, E., Sweeney, J. S., Williams, Q. & Jeanloz, R., and response by Boehler, R. & Zerr, A. (1994). High-pressure melting of $(Mg, Fe)SiO_3$ perovskite. *Science*, **264**, 279–281.
Hemley, R. J., Bell, P. M. & Mao, H. K. (1987a). Laser techniques in high-pressure geophysics. *Science*, **237**, 605–612.
Hemley, R. J., Jackson, M. D. & Gordon, R. G. (1985). First-principles theory for the equations of state of minerals at high pressures and temperatures: application to MgO. *Geophys. Res. Lett.*, **12**, 247–250.
Hemley, R. J., Jackson, M. D. & Gordon, R. G. (1987b). Theoretical study of the structure, lattice dynamics, and equation of state of perovskite-type $MgSiO_3$ and $CaSiO_3$. *Phys. Chem. Minerals*, **14**, 2–12.
Hemley, R. J., Jephcoat, A. P., Mao, H. K., Ming, L. C. & Manghnani, M. H. (1988). Pressure-induced amorphization of silica. *Nature*, **334**, 52–54.
Hemley, R. J., Mao, H. K., Finger, L. W., Jephcoat, A. P., Hazen, R. M. & Zha, C. S. (1990) Equation of state of solid hydrogen and deuterium from single crystal diffraction to 26.5 GPa. *Phys. Rev. B*, **42**, 6458–6470.
Herndon, J. M. (1996). Substructure of the inner core of the Earth. *Proc. Natl. Acad. Sci. USA*, **93**, 646–648.
Hirsch, L. M., Shankland, T. J. & Duba, A. G. (1993). Electrical conduction and polaron mobility in Fe-bearing olivine. *Geophys. J. Int.*, **114**, 36–44.
Holland, K. G. & Ahrens, T. J. (1997) Melting of $(Mg, Fe)_2SiO_4$ at the core–mantle boundary of the Earth. *Science*, **275,** 1623–1625.
Honig, J. M. (1970). Band and transport theories in solids. In *Modern Aspects of*

Solid State Chemistry, C. N. R. Rao ed., Plenum Press, New York, pp. 497–566.
Horai, K. (1971). Thermal conductivity of rock-forming minerals. *J. Geophys. Res.*, **76**, 1278–1308.
Horai, K. & Shankland, T. (1987). Thermal conductivity of rocks and minerals. In *Methods of Experimental Physics, Geophysics*, C. G. Sammis & T. L. Henyey eds., Academic, New York, **24 A**, pp. 271–302.
Horai, K. & Simmons, G. (1969). Thermal conductivity of rock-forming minerals. *Earth Planet. Sci. Lett.*, **6**, 359–368.
Horai, K. & Simmons, G. (1970). An empirical relationship between thermal conductivity and Debye temperature for silicates. *J. Geophys. Res.*, **75**, 978–982.
Houlier, B., Cheraghmakani, M. & Jaoul, O. (1990). Silicon diffusion in San Carlos olivine. *Phys. Earth Planet. Interiors*, **62**, 329–340.
Iida, T. & Guthrie, R. I. L. (1988). *The Physical Properties of Liquid Metals*, Oxford University Press, Oxford.
Irifune, T. (1987). An experimental investigation of the pyroxene–garnet transformation in a pyrolite composition and its bearing on the composition of the mantle. *Phys. Earth Planet. Interiors.*, **45**, 324–336.
Irifune, T., Nishiyama, N., Kuroda, K. *et al.* (1998). The postspinel phase boundary in Mg_2SiO_4 determined by *in-situ* X-ray diffraction. *Science*, **279**, 1698–1700.
Irvine, R. D. & Stacey, F. D. (1975). Pressure dependence of the thermal Grüneisen parameter, with application to the lower mantle and outer core. *Phys. Earth Planet. Interiors*, **11**, 157–165.
Isaak D. G. (1992). High-temperature elasticity of iron-bearing olivines. *J. Geophys. Res.*, **97**, 1871–1885.
Isaak, D. G., Anderson, O. L., Goto, T. & Suzuki, I. (1989). Elasticity of single crystal forsterite measured to 1700 K. *J. Geophys. Res.*, **94**, 5895–5906.
Ito, E. & Katsura, T. (1989). A temperature profile of the mantle transition zone. *Geophys. Res. Lett.*, **16**, 425–428.
Ito, E. & Katsura, T. (1992). Melting of ferromagnesian silicates under the lower mantle conditions. In *High-Pressure Research: Applications to Earth and Planetary Sciences*, Y. Syono & M. H. Manghnani eds., Terra pub., Tokyo, pp. 315–322.
Ito, E. & Matsui, Y. (1978). Synthesis and crystal-chemical characterization of $MgSiO_3$ perovskite. *Earth Planet. Sci. Lett.*, **38**, 443–450.
Ito, E. & Navrotsky, A. (1985). $MgSiO_3$ ilmenite: Calorimetry, phase equilibria, and decomposition at atmospheric pressure. *Amer. Mineral.*, **70**, 1020–1026.
Ito, E. & Takahashi, E. (1987a). Ultra-high pressure phase transformations and the constitution of the deep mantle. In *High Pressure Research in Mineral Physics*, M. H. Manghnani & Y. Syono eds., American Geophysical Union, Washington, pp. 221–229.
Ito, E. & Takahashi, E. (1987b). Melting of peridotite at uppermost lower mantle conditions. *Nature*, **328**, 514–517.
Ito, E. & Takahashi, E. (1989). Post-spinel transformations in the system Mg_2SiO_4–Fe_2SiO_4 and some geophysical implications. *J. Geophys. Res.*, **94**, 10 637–10 646.
Ito, E., Takahashi, E. & Matsui, Y. (1984). The mineralogy and chemistry of the lower mantle: An implication of the ultra-high pressure phase relations in the system MgO–FeO–SiO_2. *Earth Planet. Sci. Lett.*, **67**, 238–248.

Ito, E. & Yamada, H. (1982). Stability relations of silicate spinels, ilmenites and perovskites. In *High-Pressure Research in Geophysics*, S. Akimoto & M. H. Manghnani, eds., D. Reidel, Dordrecht, pp. 405–419.

Iyengar, G. N. K. & Alcock, C. B. (1970). A study of semiconduction in dilute magnesiowüstites. *Phil. Mag.*, **21**, 293–304.

Jackson, I. (1977). Melting of some alkaline-earth and transition-metal fluorides and alkali fluoroberyllates at elevated pressures: a search for melting systematics. *Phys. Earth Planet. Interiors*, **14**, 143–164.

Jackson, I. (1983). Some geophysical constraints on the chemical constitution of the Earth's lower mantle. *Earth Planet. Sci. Lett.*, **62**, 91–103.

Jackson, I. (1998). Elasticity, composition and temperature of the Earth's lower mantle: A reappraisal. *Geophys. J. Int.*, **134**, 291–311.

Jackson, I. N. S. & Liebermann, R. C. (1974). Melting and elastic shear instability of alkali halides. *J. Phys. Chem. Solids*, **35**, 115–119.

Jackson, I. & Niesler, H. (1982). The elasticity of periclase to 3 GPa and some geophysical implications. *Advances in Earth & Planet. Sci.*, **12**, 93–113.

Jackson, I. & Rigden, S. M. (1996). Analysis of P–V–T data: constraints on the thermoelastic properties of high-pressure minerals. *Phys. Earth Planet. Interiors*, **96**, 85–112.

Jacobs, J. A. (1953). The Earth's inner core. *Nature*, **172**, 297–298.

Jacobs, J. A. (1986). *The Earth's Core*, Academic Press, London.

Jain, A. & Evans, R. (1972). Calculation of the electrical resistivity of liquid iron and the Earth's core. *Nature* (*Phys. Sci.*), **235**, 165–167.

Jaoul, O. (1990). Multicomponent diffusion and creep in olivine. *J. Geophys. Res.*, **95**, 17 631–17 642.

Jaoul, O., Houlier, B. & Abel, F. (1983). Study of ^{18}O diffusion in magnesium orthosilicate by nuclear microanalysis. *J. Geophys. Res.*, **88**, 613–624.

Jaoul, O., Béjina, F., Elie, F. & Abel, F. (1995). Silicon self-diffusion in quartz. *Phys. Rev. Lett.*, **74**, 2038–2041.

Jaoul, O., Poumellec, M., Froidevaux, C. & Havette, A. (1981). Silicon diffusion in forsterite: A new constraint for understanding mantle deformation. In *Anelasticity in the Earth*, F. D. Stacey, M. S. Paterson & A. Nicolas, eds., American Geophysical Union, pp. 95–100.

Javoy, M. (1995). The integral enstatite chondrite model of the Earth. *Geophys. Res. Lett.*, **22**, 2219–2222.

Jeanloz, R. (1981). Majorite:Vibrational and compressional properties of a high-pressure phase. *J. Geophys. Res.*, **86**, 6171–6179.

Jeanloz, R. (1990). The nature of the Earth's core. *Ann. Rev. Earth Planet. Sci.*, **18**, 357–386.

Jeanloz, R. & Grover, R. (1988). Birch–Murnaghan and U_s–u_p equations of state. In *Shock Waves in Condensed Matter 1987*, S. C. Schmitt & N. C. Holmes eds., Elsevier, Amsterdam.

Jeanloz, R. & Hemley, R. J. (1994). Thermoelasticity of perovskite: an emerging consensus. *EOS Trans. AGU.*, **75**, October 11, 476–477.

Jeanloz, R. & Richter, F. M. (1979). Convection, composition and the thermal state of the lower mantle. *J. Geophys. Res.*, **84**, 5497–5503.

Jeanloz, R. & Thompson, A. B. (1983). Phase transitions and mantle discontinuities. *Rev. Geophys. Space Phys.*, **21**, 51–74.

Jeanloz, R. & Wenk, H. R. (1988). Convection and anisotropy of the inner core. *Geophys. Res. Lett.*, **15**, 72–75.

Jephcoat, A. & Olson, P. (1987). Is the inner core of the Earth pure iron? *Nature*,

325, 332–335.
Johnston, M. J. S. & Strens, R. G. J. (1973). Electrical conductivity of molten Fe–Ni–S–C core mix. *Phys. Earth Planet. Interiors*, **7**, 217–218.
Jones, L. E. A. & Liebermann, R. C. (1974). Elastic and thermal properties of fluoride and oxide analogues in the rocksalt, fluorite, rutile and perovskite structures. *Phys. Earth Planet. Interiors*, **9**, 101–107.
Joos, B. (1996). The role of dislocations in melting. In *Dislocations in Solids*, F. R. N. Nabarro & M. S. Duesberry eds., Elsevier, Amsterdam, pp. 505–587.
Kanamori, H., Fujii, N. & Mizutani, H. (1968). Thermal diffusivity measurement of rock-forming minerals from 300 to 1100 K. *J. Geophys. Res.*, **73**, 595–605.
Kapusta, B. & Guillopé, M. (1988). High ionic diffusivity in the perovskite $MgSiO_3$: A molecular dynamics study. *Phil. Mag.*, **58**, 809–816.
Karato, S. (1981a). Rheology of the lower mantle. *Phys. Earth Planet. Interiors*, **24**, 1–14.
Karato, S. (1981b). Pressure dependence of diffusion in ionic solids. *Phys. Earth Planet. Interiors*, **25**, 38–51.
Karato, S. (1993). Inner core anisotropy due to the magnetic field-induced preferred orientation of iron. *Science*, **262**, 1708–1711.
Karki, B. B., Stixrude, L., Clark, S. J., Warren, M. C., Ackland, G. J. & Crain, J. (1997). Elastic properties of orthorhombic $MgSiO_3$ perovskite at lower-mantle pressures. *American Mineralogist*, **82**, 635–638.
Kato, T. & Kumazawa, M. (1985a). Garnet phase of $MgSiO_3$ filling the pyroxene ilmenite gap at very high temperature. *Nature*, **316**, 803–805.
Kato, T. & Kumazawa, M. (1985b). Effect of high pressure on the melting relation in the system Mg_2SiO_4–$MgSiO_3$. *J. Phys. Earth*, **33**, 513–524.
Kato, T., Ohtani, E., Morishima, H., *et al.* (1995). *In-situ* X-ray observation of high-pressure phase transitions of $MgSiO_3$ and thermal expansion of $MgSiO_3$ perovskite at 25 GPa by double-stage multianvil system. *J. Geophys. Res.*, **100**, 20 475–20 481.
Katsura, T. & Ito, E. (1989). The system Mg_2SiO_4–Fe_2SiO_4 at high pressures and temperatures: Precise determination of stabilities of olivine, modified spinel and spinel. *J. Geophys. Res.*, **94**, 15 663–15 670.
Katsura, T., Sato, K. & Ito, E. (1998). Electrical conductivity of silicate perovskite at lower mantle conditions. *Nature*, **395**, 493–495.
Kawai, N. & Inokuti, Y. (1968). Low-temperature melting of elements under high pressure and its progression in the periodic table. *Jap. J. Appl. Phys.*, **7**, 989–1004.
Kemeny, G. & Rosenberg, B. (1973). Compensation law in thermodynamics and thermal death. *Nature*, **243**, 400.
Kendall, J. M. & Silver, P. G. (1996). Constraints from seismic anisotropy on the nature of the lowermost mantle. *Nature*, **381**, 409–412.
Kennedy, G. C. & Vaidya, S. N. (1970). The effect of pressure on the melting temperature of solids. *J. Geophys. Res.*, **75**, 1019–1022.
Kennett, B. L. N. & Engdahl, E. R. (1991). Traveltimes for global earthquake location and phase identification. *Geophys. J. Int.*, **105**, 429–465.
Kenyon, P. M. & Turcotte, D. L. (1983). Convection in a two-layer mantle with a strongly temperature-dependent viscosity. *J. Geophys. Res.*, **88**, 6403–6414.
Kerr, R. A. (1992). Having it both ways in the mantle. *Science*, **258**, 1576–1578.
Kerr, R. A. (1993). Bits of the lower mantle found in Brazilian diamonds. *Science*, **261**, 1391.
Kerr, R. A. (1997). Deep-sinking slabs stir the mantle. *Science*, **275**, 613–615.

Kerschhofer, L., Sharp, T. G. & Rubie, D. C. (1996). Intracrystalline transformation of olivine to wadsleyite and ringwoodite under subduction zone conditions. *Science*, **274**, 79–81.

Kesson, S. E. & Fitz Gerald, J. D. (1991). Partitioning of MgO, NiO, MnO and Cr_2O_3 between magnesian silicate perovskite and magnesiowüstite: Implications for the origin of inclusions in diamond and the composition of the lower mantle. *Earth Planet. Sci. Lett.*, **111**, 229–240.

Kesson, S. E., Fitz Gerald, J. D., Shelley, J. M. G. & Withers, R. L. (1995). Phase relations, structure and crystal chemistry of some aluminous silicate perovskites. *Earth Planet. Sci. Lett.*, **134**, 187–201.

Kesson, S. E., Fitz Gerald, J. D. & Shelley, J. M. G. (1998). Mineralogy and dynamics of a pyrolite lower mantle. *Nature*, **393**, 252–255.

Keyes, R. W. (1958). Volumes of activation for diffusion in solids. *J. Chem. Phys.*, **29**, 467–475.

Keyes, R. W. (1960). Volumes of activation. II. Pressure dependence of activation parameters. *J. Chem. Phys.*, **32**, 1066–1067.

Keyes, R. W. (1963). Continuum model of the effect of pressure on activated processes. In *Solids under Pressure*, W. Paul & D. Warschauer eds., McGraw-Hill, New York, pp. 71–91.

Kieffer, S. W. (1976). Lattice thermal conductivity within the Earth and considerations of a relationship between the pressure dependence of the thermal diffusivity and the volume dependence of the Grüneisen parameter. *J. Geophys. Res.*, **81**, 3025–3030.

Kieffer, S. W. (1979a). Thermodynamics and lattice vibrations of minerals: 1. Mineral heat capacities and their relationships to simple lattice vibrational models. *Rev. Geophys. Space Phys.*, **17**, 1–19.

Kieffer, S. W. (1979b). Thermodynamics and lattice vibrations of minerals: 2. Vibrational characteristics of silicates. *Ibid.*, **17**, 20–34.

Kieffer, S. W. (1979c). Thermodynamics and lattice vibrations of minerals: 3. Lattice dynamics and an approximation for minerals with application to simple substances and framework silicates. *Ibid.*, **17**, 35–59.

Kieffer, S. W. (1985). Heat capacity and entropy: Systematic relations to lattice vibrations. In *Microscopic to Macroscopic* , S. W. Kieffer & A. Navrotsky eds., Mineral. Soc. America, Washington, D.C., pp. 65–126.

Kirchheim, R. & Huang, X. Y. (1987). A relationship between prefactor and activation energy for diffusion. *Phys. stat. sol.* (*b*), **144**, 253–257.

Kittel, C. (1967). *Introduction to Solid State Physics*, J. Wiley, New York.

Knittle, E. (1995). Static compression measurements of equations of state. In *Mineral Physics and Crystallography, A Handbook of Physical Constants*, T. J. Ahrens ed., American Geophysical Union, Washington, D.C., pp. 98–142.

Knittle, E. & Jeanloz, R. (1986). High-pressure metallization of FeO and implications for the Earth's core. *Geophys. Res. Lett.*, **13**, 1541–1544.

Knittle, E. & Jeanloz, R. (1987). Synthesis and equation of state of $(Mg, Fe)SiO_3$ perovskite to over 100 gigapascals. *Science*, **235**, 668–670.

Knittle, E. & Jeanloz, R. (1989a). Simulating the core–mantle boundary: An experimental study of high-pressure reactions between silicate and liquid iron. *Geophys. Res. Lett.*, **16**, 609–612.

Knittle, E. & Jeanloz, R. (1989b). Melting curve of $(Mg, Fe)SiO_3$ perovskite to 96 GPa: Evidence for a structural transition in lower-mantle melts. *Geophys. Res. Lett.*, **16**, 421–424.

Knittle, E. & Jeanloz, R. (1991a). Earth's core–mantle boundary: Results of

experiments at high pressures and temperatures. *Science*, **251**, 1438–1443.
Knittle, E. & Jeanloz, R. (1991b). The high-pressure phase diagram of $Fe_{0.94}O$: A possible constituent if the Earth's core. *J. Geophys. Res.*, **96**, 16 169–16 180.
Knittle, E. Jeanloz, R. & Smith, G. L. (1987). Thermal expansion of silicate perovskite and stratification of the Earth's mantle. *Nature*, **319**, 214–216.
Knopoff, L. & Shapiro, J. N. (1969). Comments on the interrelationships between Grüneisen's parameter and shock and isothermal equations of state. *J. Geophys. Res.*, **74**, 1439–1450.
Kobayashi, Y. & Maruyama, H. (1971). Electrical conductivity of olivine single crystals at high temperature. *Earth Planet. Sci. Lett.*, **11**, 415–419.
Kofstad, P. (1983). *Nonstoichiometry, Diffusion and Electrical Conductivity in Binary Metal Oxides*, R. E. Krieger Publ. Co., Malabar, Florida.
Kraut, E. A. & Kennedy, G. C. (1966a). New melting law at high pressures. *Phys. Rev. Lett.*, **16**, 608–609.
Kraut, E. A. & Kennedy, G. C. (1966b). New melting law at high pressures. *Phys. Rev.*, **151**, 668–675.
Kubo, T., Ohtani, E., Kato, T., *et al.* (1998). An *in-situ* X-ray diffraction study of the $\alpha-\beta$ transformation kinetics of Mg_2SiO_4. *Geophys. Res. Lett.*, **25**, 695–698.
Kuhlmann-Wilsdorf, D. (1965). Theory of melting. *Phys. Rev.*, **A 140**, 1599–1610.
Kumazawa, M. & Anderson, O. L. (1969). Elastic moduli, pressure derivatives, and temperature derivatives of single-crystal olivine and single-crystal forsterite. *J. Geophys. Res.*, **74**, 5961–5972.
Kündig, W. & Hargrove, R. S. (1969). Electron hopping in magnetite. *Solid State Comm.*, **7**, 223–227.
Labrosse, S., Poirier, J. P. & Le Mouël, J. L. (1997). On cooling of the Earth's core. *Phys. Earth Planet. Interiors*, **99**, 1–17.
Lacam, A., Madon, M. & Poirier, J. P. (1980). Olivine glass and spinel formed in a laser-heated, diamond-anvil high pressure cell. *Nature*, **288**, 155–157.
Laplace, M. le Marquis de (1825). *Traité de Mécanique Céleste*, V, Bachelier, Paris, pp. 48–50.
Lasaga, A. C. (1979). Multicomponent exchange and diffusion in silicates. *Geochim. Cosmochim. Acta*, **43**, 455–469.
Lasocka, M. (1975). On the entropy of melting. *Physics Lett.*, **51A**, 137–138.
Lauterjung, J. & Will, G. (1986). The kinetics of the olivine–spinel transformation in Mg_2GeO_4 under high pressure and temperature. *Physica*, **139–140B**, 343–346.
Lawson, A. W. (1957). On the high temperature heat conductivity of insulators. *Phys. Chem. Solids*, **3**, 155.
Lay, T. (1989). Structure of the core–mantle transition zone: A chemical and thermal boundary layer. *EOS Trans. AGU*, **70**, 49–59.
Lay, T. (1995). Seismology of the lower mantle and core–mantle boundary. *Rev. Geophys. Supplement*, (July), 325–328.
Lay, T., Williams, Q. & Garnero, E. J. (1998). The core–mantle boundary layer and deep Earth dynamics. *Nature*, **392**, 461–468.
LeBlanc, G. E. & Secco, A. R. (1996) Viscosity of an Fe–S liquid up to 1300 °C and 5 GPa. *Geophys. Res. Lett.*, **23**, 213–216.
Lees, A. C., Bukowinski, M. S. T. & Jeanloz, R. (1983). Reflection properties of phase transition and compositional change models of the 670 km discontinuity. *J. Geophys. Res.*, **88**, 8145–8159.
Le Mouël, J. L., Hulot, G. & Poirier, J. P. (1997). Core–mantle interactions. In

Earth's Deep Interior (*The Doornbos Memorial Volume*), D. J. Crossley, ed., Gordon & Breach, New York, pp. 197–221.

Lennard-Jones, J. E. & Devonshire, A. F. (1937). Critical phenomena in gases – I. *Proc. Roy. Soc. Lond.*, **A 163**, 53–70.

Lennard-Jones, J. E. & Devonshire, A. F. (1939). Critical and cooperative phenomena. (a) III A theory of melting and the structure of liquids. *Proc. Roy. Soc. Lond.*, **A 169**, 317–338. (b) IV A theory of disorder in solids and liquids and the process of melting. *Proc. Roy. Soc. Lond.*, **A 170**, 464–484.

Levin, E. M., Robbins, C. R. & McMurdie, H. F. (1964). *Phase Diagrams for Ceramicists*, American Ceramic Society.

Li, B., Chen, G., Gwanmesia, G. D. & Liebermann, R. C. (1998). Sound velocity measurements at mantle transition zone conditions of pressure and temperature using ultrasonic interferometry in a multi anvil apparatus. In *Properties of Earth and Planetary Materials at High Pressure and Temperature*, M. H. Manghnani & T. Yagi eds., American Geophysical Union Monograph 101, AGU, Washington D.C., pp. 41–61.

Li, B., Gwanmesia, G. D. & Liebermann, R. C. (1996). Sound velocities of olivine and beta polymorphs of Mg_2SiO_4 at Earth's transition zone pressures, *Geophys. Res. Lett.*, **23**, 2259–2262.

Li, X. & Jeanloz, R. (1987). Measurement of the electrical conductivity of $(Mg, Fe)SiO_3$ perovskite and a perovskite-dominated assemblage at lower mantle conditions. *Geophys. Res. Lett.*, **14**, 1075–1078.

Li, X. & Jeanloz, R. (1990a). Laboratory study of the electrical conductivity of silicate perovskites at high pressures and temperatures. *J. Geophys. Res.*, **95**, 5067–5078.

Li, X. & Jeanloz, R. (1990b). High-pressure–temperature electrical conductivity of magnesiowüstite as a function of iron oxide concentration. *J. Geophys. Res.*, **95**, 21 609–21 612.

Li, X. & Jeanloz, R. (1991). Effect of iron content on the electrical conductivity of perovskite and magnesiowüstite assemblages at lower mantle conditions. *J. Geophys. Res.*, **96**, 6113–6120.

Li, X., Ming, L. C., Manghnani, M. H., Wang, Y. & Jeanloz, R. (1993). Pressure dependence of the electrical conductivity of $(Mg_{0.9}, Fe_{0.1})SiO_3$ perovskite. *J. Geophys. Res.*, **98**, 501–508.

Libby, W. F. (1966). Melting points at high compressions from zero compression properties through the Kennedy relation. *Phys. Rev. Lett.*, **17**, 423–424.

Liebermann, R. C. (1973). On velocity–density systematics, polymorphic phase transformations and the transition zone of the Earth's mantle. *Comments on Earth Sciences*: *Geophysics*, **3**, 127–133.

Liebermann, R. C. (1982). Elasticity of minerals at high pressure and temperature. In *High Pressure Researches in Geosciences*, W. Schreyer ed., Schweizerbart'sche Verlag, Stuttgart, pp. 1–14.

Liebermann, R. C. & Ringwood, A. E. (1973). Birch's law and polymorphic phase transformations. *J. Geophys. Res.*, **78**, 6926–6932.

Liebermann, R. C., Jones, L. E. A. & Ringwood, A. E. (1977). Elasticity of aluminate, titanate, stannate and germanate compounds with the perovskite structure. *Phys. Earth Planet. Interiors*, **14**, 165–178.

Limoge, Y. & Grandjean, A. (1996). On the correlations between activation enthalpies and entropies of activated processes in the solid state. *Proc. DIMAT* 96, H. Mehrer *et al.* eds., Nordkirchen, Scitec Pub. pp. 747–752.

Lindemann, F. A. (1910). Über die Berechnung molekularer Eigenfrequenzen.

Physikalisches Zeitsch., **11**, 609–612.
Liu, L. G. (1974). Silicate perovskite from phase transformations of pyrope garnet at high pressure and temperature. *Geophys. Res. Lett.*, **1**, 277–280.
Liu, L. G. (1975a). Post-oxide phases of forsterite and enstatite. *Geophys. Res. Lett.*, **2**, 417–419.
Liu, L. G. (1975b). On the (γ, ε, l) triple point of iron and the Earth's core. *Geophys. J. R. astr. Soc.*, **43**, 697–705.
Liu, L. G. (1976). The high-pressure phases of $MgSiO_3$. *Earth Planet. Sci. Lett.*, **31**, 200–208.
Liu, L. G. (1979). On the 650 km seismic discontinuity. *Earth Planet. Sci. Lett.*, **42**, 202–208.
Liu, L. G. (1982). Chemical inhomogeneity of the mantle: Geochemical considerations. *Geophys. Res. Lett.*, **9**, 124–126.
Liu, L. G. (1987). New silicate perovskites. *Geophys. Res. Lett.*, **14**, 1077–1082.
Liu, L. G. & Bassett, W. A. (1975). The melting of iron up to 200 kbar. *J. Geophys. Res.*, **80**, 3777–3782.
Liu, L. G. & Bassett, W. A. (1986). *Elements, Oxides, Silicates*, Oxford University Press, Oxford.
Liu, L. G. & Ringwood, A. E. (1975). Synthesis of a perovskite-type polymorph of $CaSiO_3$. *Earth Planet. Sci. Lett.*, **28**, 209–211.
Loper, D. E. (1978). The gravitationally powered dynamo. *Geophys. J. R. astr. Soc.*, **54**, 389–404.
Loper, D. E. (1984). The dynamical structure of D″ and deep plumes in a non-Newtonian mantle. *Phys. Earth Planet. Interiors*, **34**, 57–67.
Loper, D. E. & Lay, T. (1995). The core–mantle boundary region. *J. Geophys. Res.*, **100**, 6397–6420.
Love, A. E. H. (1944). *A Treatise on the Mathematical Theory of Elasticity*. Dover, New York.
Machetel, P. & Weber, P. (1991). Intermittent layered convection in a model mantle with an endothermic phase change at 670 km. *Nature*, **350**, 55–57.
MacDonald, G. F. J. & Knopoff, L. (1958). On the chemical composition of the outer core. *Geophys. J. R. astr. Soc.*, **1**, 284–297.
Madon, M. & Poirier, J. P. (1983). Transmission electron microscope observations of α, β and γ $(MgFe)_2SiO_4$ in shocked meteorites: Planar defects and polymorphic transitions. *Phys. Earth Planet. Interiors*, **33**, 31–44.
Madon, M., Castex, J. & Peyronneau, J. (1989a). A new hollandite-type structure as a possible host for calcium and aluminium in the lower mantle. *Nature*, **342**, 422–424.
Madon, M., Guyot, F., Peyronneau, J. & Poirier, J. P. (1989b). Electron microscopy of high-pressure phases synthesized from natural olivine in diamond anvil cell. *Phys. Chem. Minerals*, **16**, 320–330.
Maj, S. (1978). A relationship between phonon conductivity and seismic parameter for silicate minerals. *Pageoph*, **116**, 1225–1230.
Mao, H. K. (1972). Observations of optical absorption and electrical conductivity in magnesiowüstite at high pressures. In *Carnegie Institution of Washington Annual Report*, pp. 554–557.
Mao, H. K. (1976). Charge transfer processes at high pressure. In *The Physics and Chemistry of Minerals and Rocks*, R. G. J. Strens ed., J. Wiley, London, pp. 573–581.
Mao, H. K. & Bell, P. M. (1979). Equations of state of MgO and ε Fe under static pressure conditions. *J. Geophys. Res.*, **84**, 4533–4536.

Mao, H. K., Bell, P. M. & Hadidiacos, C. (1987). Experimental phase relations of iron to 360 kbar, 1400 °C, determined in an internally heated diamond-anvil apparatus. In *High Pressure Research in Mineral Physics*, M. H. Manghnani & Y. Syono eds., AGU, Washington, 135–138.

Mao, H. K., Shen, G. & Hemley, R. J. (1997). Multivariable dependence of Fe–Mg partitioning in the lower mantle. *Science*, **278**, 2098–2100.

Mao, H. K., Shen, G., Hemley, R. J. & Duffy, T. S. (1998). X-ray diffraction with a double hot-plate laser-heated diamond cell. In *Properties of Earth and Planetary Materials at High Pressure and Temperature*, M. H. Manghnani & T. Yagi eds., American Geophysical Union Monograph 101, AGU, Washington D.C., pp. 27–33.

Martin, C. J. & O'Connor, D. A. (1977). An experimental test of Lindemann law. *J. Phys. C.*, **10**, 3521–3526.

Martinez, I., Wang, Y., Guyot, F., Liebermann, R. C. & Doukhan, J. C. (1997). Microstructures and iron partitioning in $(Mg, Fe)SiO_3$ perovskite–(Mg, Fe)O magnesiowüstite assemblages: An analytical transmission electron microscopy study. *J. Geophys. Res.*, **102**, 5265–5280.

Mashimo, T., Kondo, K., Sawaoka, A., Syono, Y., Takei, H. & Ahrens, T. J. (1980). Electrical conductivity measurement of fayalite under shock compression up to 56 GPa. *J. Geophys. Res.*, **85**, 1876–1881.

Masters, G. (1979). Observational constraints on the chemical and thermal structure of the Earth's deep interior. *Geophys. J. R. astr. Soc.*, **57**, 507–534.

Matassov, G. (1977). *The Electrical Conductivity of Iron–Silicon Alloys at High Pressures and the Earth's Core*, Lawrence Livermore Laboratory Report UCRL-52322, 180 pp.

May, A. N. (1970). Extrapolation of the shear elastic moduli of face-centred cubic solids to the molten state. *Nature*, **228**, 990–991.

McCammon, C. A. (1997). Perovskite as a possible sink for ferric iron in the lower mantle. *Nature*, **387**, 694–696.

McCammon, C. A., Brown, T. H. & Meagher, E. P. (1991). Calculation of the equation of state and elastic moduli of MgO using molecular orbital theory, *Phys. Chem. Minerals*, **17**, 622–628.

McCammon, C. A., Hutchison, M. & Harris, J. (1997). Ferric iron content in mineral inclusions in diamonds from São Luis: A view into the lower mantle. *Science*, **278**, 434–436.

McKenzie, D. P. (1967). The viscosity of the mantle. *Geophys. J. R. astr. Soc.*, **14**, 297–305.

McQueen, R. G., Fritz, J. N. & Marsh, S. P. (1963). On the equation of state of stishovite. *J. Geophys. Res.*, **68**, 2319–2322.

McQueen, R. G., Fritz, J. N. & Marsh, S. P. (1964). On the composition of the Earth's interior. *J. Geophys. Res.*, **69**, 2947–2965.

Meade, C., Mao, H. K. & Hu, J. (1995). High-temperature phase transition and dissociation of $(MgFe)SiO_3$ perovskite at lower mantle pressures. *Science*, **268**, 1743–1745.

Means, W. D. (1976). *Stress and Strain*. Springer, New York.

Mercier, J. C. C. (1980). Single pyroxene thermobarometry. *Tectonophysics*, **70**, 1–37.

Ming, L. C. & Bassett, W. A. (1974). Laser heating in the diamond anvil press up to 2000 °C sustained and 3000 °C pulsed at pressures up to 260 kilobars. *Rev. Sci. Instr.*, **45**, 1115–1118.

Ming, L. C. & Bassett, W. A. (1975). The post-spinel phases in the

Mg_2SiO_4–Fe_2SiO_4 system. *Science*, **187**, 66–68.
Mishima, O. (1996). Relationship between melting and amorphization of ice. *Nature*, **384**, 546–549.
Mishima, O., Calvert, L. D. & Whalley, E. (1984). "Melting ice" at 77 K and 10 kbar: a new method of making amorphous solids. *Nature*, **310**, 393–395.
Mitoff, S. P. (1962). Electronic and ionic conductivity in single crystals of MgO. *J. Chem. Phys.*, **36**, 1383–1389.
Mizushima, S. (1960). Dislocation models of liquid structure. *J. Phys. Soc. Japan*, **15**, 70–77.
Mizutani, H. & Kanamori, H. (1967). Electrical conductivities of rock-forming minerals at high temperatures. *J. Phys. Earth*, **15**, 25–31.
Montagner, J. P. (1994). Can seismology tell us anything about convection in the mantle? *Rev. Geophys.*, **32**, 115–137.
Morelli, A. & Dziewonski, A. M. (1987). Topography of the core–mantle boundary and lateral homogeneity of the liquid core. *Nature*, **325**, 678–683.
Morin, F. J., Oliver, J. R. & Housley, R. M. (1977). Electrical properties of forsterite, Mg_2SiO_4, I. *Phys. Rev.*, **B16**, 4434–4445.
Morin, F. J., Oliver, J. R. & Housley, R. M. (1979). Electrical properties of forsterite, Mg_2SiO_4, II. *Phys. Rev.*, **B19**, 2886–2894.
Morishima, H., Ohtani, E., Kato, T., Shimomura, O. & Kikegawa, T. (1994). Thermal expansion of $MgSiO_3$ perovskite at 20.5 GPa. *Geophys. Res. Lett.*, **21**, 899–902.
Mott, N. F. (1934). The resistance of liquid metals. *Proc. Roy. Soc. Lond.*, **A 146**, 465–472.
Mott, N. F. & Jones, H. (1958). *The Theory of the Properties of Metals and Alloys*, Dover, New York.
Mott, N. F. (1961). The transition to the metallic state. *Phil. Mag.*, **6**, 287–309.
Muirhead, K. (1985). Comments on "Reflection properties of phase transition and compositional change models of the 670 km discontinuity" by Lees, Bukowinski and Jeanloz. *J. Geophys. Res.*, **90**, 2057–2059.
Mukherjee, K. (1966). Clapeyron's equation and melting under high pressures. *Phys. Rev. Lett.*, **17**, 1252–1254.
Mulargia, F. (1986). The physics of melting and the temperatures in the Earth's outer core. *Q. J. R. astr. Soc.*, **27**, 383–402.
Mulargia, F. & Quareni, F. (1988). Validity of the Sutherland–Lindemann law and melting temperatures in the Earth's interior. *Geophys. J.*, **92**, 269–282.
Muller, O. & Roy, R. (1974). *The Major Ternary Structural Families*, Springer–Verlag, Berlin.
Murnaghan, F. D. (1967). *Finite Deformation of an Elastic Solid*, Dover, New York.
Murrell, M. T. & Burnet, D. S. (1986). Partitioning of K, U, and Th between sulfide and silicate liquid: Implications for radioactive heating of planetary cores. *J. Geophys. Res.*, **91**, 8126–8136.
Nabarro, F. R. N. (1967). *Theory of Crystal Dislocations*, Oxford University Press, Oxford.
Nachtrieb, N. H. (1967). Self-diffusion in liquid metals. *Adv. in Phys.*, **16**, 309–323.
Nachtrieb, N. H. (1977). Atomic transport properties in liquid metals. In *The Properties of Liquid Metals*, S. Takeuchi, ed., Taylor & Francis, London, pp. 521–535.
Nanda, J. N. (1989). The Earth's inner core. *Proc. Indian natn. Sci. Acad.*, **55**, 101–109.

Navrotsky, A. (1980). Lower mantle phase transitions may generally have negative pressure–temperature slopes. *Geophys. Res. Lett.*, **7**, 709–711.
Ninomiya, T. (1978). Theory of melting, dislocation model. *J. Phys. Soc. Japan*, **44**, 263–271.
Nye, J. F. (1957). *Physical Properties of Crystals*, Oxford University Press, Oxford.
O'Connell, R. J. (1977). On the scale of mantle convection. *Tectonophysics*, **38**, 119–136.
Oishi, Y. & Ando, K. (1984). Oxygen self-diffusion coefficient in single crystal forsterite. In *Materials Science of the Earth's Interior*, I. Sunagawa ed., Terra pub., Tokyo, pp. 271–280.
O'Keefe, M. & Bovin, J. O. (1979). Solid electrolyte behaviour of $NaMgF_3$: Geophysical implications. *Science*, **206**, 599–600.
O'Keeffe, M. & Hyde, B. G. (1981). Why olivine transforms to spinel at high pressure. *Nature*, **293**, 727–728.
Olson, P., Schubert, G. & Anderson, C. (1987). Plume formation in the D″ layer and the roughness of the core–mantle boundary. *Nature*, **327**, 409–413.
Olson, P., Silver, P. G. & Carlson, R. W. (1990). The large-scale structure of convection in the Earth's mantle. *Nature*, **344**, 209–215.
Oriani, R. A. (1951). The entropies of melting of metals. *J. Chem. Phys.*, **19**, 93–97.
Oversby, V. M. & Ringwood, A. E. (1972). Potassium distribution between metal and silicate and its bearing on the occurrence of potassium in the Earth's core. *Earth Planet. Sci. Lett.*, **14**, 345–347.
Parker, L. J., Atou, T. & Badding, J. V. (1996). Transition element-like chemistry for potassium under pressure. *Science*, **273**, 95–97.
Parkhomenko, E. I. (1982). Electrical resistivity of minerals and rocks at high temperature and pressure. *Rev. Geophys. Space Phys.*, **20**, 193–218.
Patel, A., Price, G. D., Matsui, M., Brodholt, J. P. & Howarth, R. J. (1996). A computer simulation approach to the high pressure thermoelasticity of $MgSiO_3$ perovskite. *Phys. Earth Planet. Interiors*, **98**, 55–63.
Paul, W. & Warschauer, D. M. (1963). The role of pressure in semiconductor research. In *Solids under Pressure*, W. Paul & D. Warschauer eds., McGraw-Hill, 179–249.
Peltier, W. R. & Jarvis, G. T. (1982). Whole mantle convection and the thermal evolution of the Earth. *Phys. Earth Planet. Interiors*, **29**, 281–304.
Perry, J. (1895). On the age of the Earth. *Nature*, **51**, 224–227.
Peyronneau, J. & Poirier, J. P. (1989). Electrical conductivity of the material of the Earth's lower mantle. *Nature*, **342**, 537–539.
Phipps Morgan, J. & Shearer, P. M. (1993). Seismic constraints on mantle flow and topography of the 660-km discontinuity: evidence for whole-mantle convection. *Nature*, **365**, 506–511.
Poirier, J. P. (1978). Is power-law creep diffusion controlled? *Acta Metall.*, **26**, 629–637.
Poirier, J. P. (1981a). Martensitic olivine–spinel transformation and plasticity of the mantle transition zone. In *Anelastic Properties and Related Processes in the Earth's Mantle*, F. D. Stacey, M. S. Paterson & A. Nicolas eds., American Geophysical Union Monograph, AGU, pp. 113–117.
Poirier, J. P. (1981b). On the kinetics of the olivine spinel transition. *Phys. Earth Planet. Interiors*, **26**, 179–187.
Poirier, J. P. (1982). The kinetics of martensitic olivine γ-spinel transition and its dependence on material and experimental parameters. In *High Pressure Research in Geophysics*, S. Akimoto & M. H. Manghnani eds., D. Reidel,

Dordrecht, pp. 361–371.
Poirier, J. P. (1985). *Creep of Crystals*, Cambridge University Press, Cambridge.
Poirier, J. P. (1986). Dislocation-mediated melting of iron and the temperature of the Earth's core. *Geophys. J. R. astr. Soc.*, **85**, 315–328.
Poirier, J. P. (1987). On Poisson's ratio and the composition of the Earth's lower mantle. *Phys. Earth Planet. Interiors*, **46**, 357–368.
Poirier, J. P. (1988a). Transport properties of liquid metals and viscosity of the Earth's core. *Geophys. J.*, **92**, 99–105.
Poirier, J. P. (1988b). The rheological approach to the viscosity of planetary mantles: A critical assessment. In *The Physics of Planets*, S. K. Runcorn ed., J. Wiley & Sons, Chichester, pp. 161–171.
Poirier, J. P. (1989). Lindemann law and the melting temperature of perovskites. *Phys. Earth Planet. Interiors*, **54**, 364–369.
Poirier, J. P. (1994a). Light elements in the Earth's outer core: A critical review. *Phys. Earth Planet. Interiors*, **85**, 319–337.
Poirier, J. P. (1994b). Physical properties of the Earth's core. *C. R. Acad. Sci. Paris, série II*, **318**, 341–350.
Poirier, J. P. (1995). Plastic rheology of crystals. In *Mineral Physics and Crystallography, A Handbook of Physical Constants*, T. J. Ahrens, ed., American Geophysical Union, Washington, D.C., pp. 237–247.
Poirier, J. P. (1997). Aluminium under the spotlight. *Nature*, **387**, 653–654.
Poirier, J. P. (1999). Equations of state. *NATO ASI Summer School, Il Ciocco, Sept.* 1998.
Poirier, J. P. & Le Mouël, J. L. (1992). Does infiltration of core material into the lower mantle affect the observed magnetic field? *Phys. Earth Planet. Interiors*, **73**, 29–37.
Poirier, J. P. & Liebermann, R. C. (1984). On the activation volume for creep and its variation with depth in the Earth's lower mantle. *Phys. Earth Planet. Interiors*, **35**, 283–293.
Poirier, J. P. & Madon, M. (1979). Transmission electron microscopy of natural $Mg_{0.74}Fe_{0.26}SiO_4$ spinel. *EOS Trans. AGU*, **60**, 370.
Poirier, J. P. & Peyronneau, J. (1992). Experimental determination of the electrical conductivity of the material of the Earth's lower mantle. In *High-Pressure Research: Applications to Earth and Planetary Sciences*, Y. Syono & M. H. Manghnani eds., Terra pub, Tokyo, pp. 77–87.
Poirier, J. P. & Price, G. D. (1992). Dislocation melting of metals. *Phys. Earth Planet. Interiors*, **69**, 153–162.
Poirier, J. P. & Price, G. D. (1999). Primary slip system of ε iron and anisotropy of the Earth's inner core. *Phys. Earth Planet. Interiors*, **110**, 147–156.
Poirier, J. P. & Shankland, T. J. (1993). Dislocation melting of iron and the temperature of the inner core, revisited. *Geophys. J. Int.*, **115**, 147–151.
Poirier, J. P. & Tarantola, A. (1998). A logarithmic equation of state. *Phys. Earth Planet. Interiors*, **109**, 1–8.
Poirier, J. P., Goddat, A. & Peyronneau, J. (1996). Ferric iron dependence of the electrical conductivity of the Earth's lower mantle material. *Phil. Trans. Roy. Soc. Lond.*, **A 354**, 1361–1369.
Poirier, J. P., Malavergne, V. & Le Mouël, J. L. (1998). Is there a thin electrically conducting layer at the base of the mantle? In *The Core–Mantle Boundary Region*, American Geophysical Union, Washington, D.C., pp. 131–137.
Poirier, J. P., Peyronneau, J., Madan, M., Guyot, F. & Revcoleschi, A. (1983). Viscosity and conductivity of the lower mantle; an experimental study on a

$MgSiO_3$ perovskite analogue, $KZnF_3$. *Phys. Earth Planet. Interiors*, **32**, 273–287.
Price, G. D. & Vočadlo, L. (1996). Computational mineralogy, *C. R. Acad. Sci. Paris*, **323** IIa, 357–371.
Price, G. D., Putnis, A., Agrell, S. O. & Smith, D. G. W. (1983). Wadsleyite, natural β-$(MgFe)_2SiO_4$ from the Peace River meteorite. *Can. Mineralogist*, **21**, 29–35.
Prigogine, I. (1962). *Introduction to Thermodynamics of Irreversible Processes*, J. Wiley, London.
Putnis, A. (1992). *Introduction to Mineral Sciences*, Cambridge University Press, Cambridge.
Putnis, A. & McConnell, J. D. C. (1980). *Principles of Mineral Behaviour*, Elsevier, New York.
Putnis, A. & Price, G. D. (1979). High-pressure Mg_2SiO_4 phases in the Tenham chondrite meteorite. *Nature*, **280**, 217–218.
Quareni, F. & Mulargia, F. (1988). The validity of the common approximate expressions for the Grüneisen parameter. *Geophys. J.*, **93**, 505–519.
Ramakrishnan, J., Boehler, R., Higgins, G. & Kennedy, G. (1978). Behavior of Grüneisen's parameter of some metals at high pressure. *J. Geophys. Res.*, **83**, 3535–3538.
Rama Murthy, V. & Hall, H. T. (1970). The chemical composition of the Earth's core: Possibility of sulfur in the core. *Phys. Earth Planet. Interiors*, **2**, 276–282.
Ramsey, W. H. (1949). On the nature of the Earth's core. *Mon. not. R. astr. Soc. Geophys. Suppl.*, **5**, 409–426.
Rao, C. N. R. & Rao, K. J. (1978). *Phase Transitions in Solids*, McGraw-Hill, New York.
Reddy, K. P. R., Oh, S. M., Major Jr, L. D. & Cooper, A. R. (1980). Oxygen diffusion in forsterite. *J. Geophys. Res.*, **85**, 322–326.
Reiner, M. (1969). *Deformation, Strain and Flow*. H. K. Lewis, London.
Richet, P. (1988). Superheating, melting and vitrification through decompression of high pressure minerals. *Nature*, **331**, 56–58.
Richet, P. & Bottinga, Y. (1986). Thermochemical properties of silicate glasses and liquids. *Rev. Geophys.*, **24**, 1–25.
Richet, P. & Gillet, P. (1997). Pressure-induced amorphization of minerals: A review. *Eur. J. Mineral.*, **9**, 907–933.
Richet, P., Ingrin, J., Mysen, B. O., Courtial, P. & Gillet, P. (1994). Premelting effects in minerals. *Earth Planet. Sci. Lett.*, **121**, 589–600.
Richet, P., Mao, H. K. & Bell, P. M., (1988). Static compression and equation of state of CaO to 1.35 Mbar. *J. Geophys. Res.*, **93**, 15 279–15 288.
Richter, F. M. (1986). Kelvin and the age of the Earth. *J. of Geology*, **94**, 395–401.
Rigden, S. M., Jackson, I., Niesler, H., Ringwood, A. E. & Liebermann, R. C. (1988). Pressure dependence of the elastic wave velocities for Mg_2GeO_4 spinel. *Geophys. Res. Lett.*, **15**, 605–608.
Ringwood, A. E. (1967). The pyroxene–garnet transformation in the Earth's mantle. *Earth Planet. Sci. Lett.*, **2**, 255–263.
Ringwood, A. E. (1970). Phase transformations and the constitution of the mantle. *Phys. Earth Planet. Interiors*, **3**, 109–155.
Ringwood, A. E. (1975). *Composition and Petrology of the Earth's Mantle*, McGraw-Hill, New York.
Ringwood, A. E. (1977). Composition of the core and implications for origin of

the Earth. *Geochemical J*., **11**, 111–135.
Ringwood, A. E. (1979). Composition and origin of the Earth. In *The Earth, its Origin, Structure and Evolution*, M. W. McElhinny ed., Academic Press, New York, pp. 1–58.
Ringwood, A. E. (1989). Significance of the Mg/Si terrestrial ratio. *Earth Planet Sci. Lett*., **95**, 1–7.
Ringwood, A. E. (1991). Phase transformations and their bearing on the constitution and dynamics of the mantle. *Geochim. Cosmochim. Acta*, **55**, 2083–2110.
Ringwood, A. E. (1994). Role of the transition zone and 660 km discontinuity in mantle dynamics. *Earth Planet. Sci. Lett*., **86**, 5–24.
Ringwood, A. E. & Irifune, T. (1988). Nature of the 650-km seismic discontinuity: Implications for mantle dynamics and differentiation. *Nature*, **331**, 131–136.
Ringwood, A. E. & Major, A. (1966). Synthesis of Mg_2SiO_4–Fe_2SiO_4 spinel solid solutions. *Earth Planet Sci. Lett*., **1**, 241–245.
Ringwood, A. E. & Major, A. (1970). The system Mg_2SiO_4–Fe_2SiO_4 at high pressures and temperatures. *Phys. Earth Planet. Interiors*, **3**, 89–108.
Ringwood, A. E. & Major, A. (1971). Synthesis of majorite and other high pressure garnets and perovskites. *Earth Planet. Sci. Lett*., **12**, 411–418.
Rivier, N. & Duffy, D. M. (1982). On the topological entropy of atomic liquids and the latent heat of fusion. *J. Phys. C*, **15**, 2867–2874.
Robie, R. A. & Edwards, J. L. (1966). Some Debye temperatures from single-crystal elastic constant data. *J. Appl. Phys*., **37**, 2569–2663.
Romanowicz, B., Li, X. & Durek, J. (1996). Anisotropy in the inner core: Could it be due to low-order convection? *Science*, **274**, 963–966.
Ross, M. (1969). Generalized Lindemann melting law. *Phys. Rev*., **184**, 233–242.
Ross, M., Young, D. A. & Grover, R. (1990). Theory of the iron phase diagram at Earth core conditions. *J. Geophys. Res*., **95**, 21 713–21 716.
Ross, N. L. & Hazen, R. M. (1989). Single crystal X-ray diffraction study of $MgSiO_3$ perovskite from 77 to 400 K. *Phys. Chem. Minerals*, **16**, 415–420.
Roufosse, M. C. & Jeanloz, R. (1983). Thermal conductivity of minerals at high pressure: The effect of phase transitions. *J. Geophys. Res*., **88**, 7399–7409.
Roufosse, M. C. & Klemens, P. G. (1974). Lattice thermal conductivity of minerals at high temperatures. *J. Geophys. Res*., **79**, 703–705.
Rubie, D. C. & Brearley, A. J. (1994). Phase transitions between β and γ $(Mg, Fe)_2SiO_4$ in the Earth's mantle: Mechanisms and rheological implications. *Science*, **264**, 1445–1448.
Ruoff, A. L. (1965). Mass transfer problems in ionic crystals with charge neutrality. *J. Appl. Phys*., **36**, 2903–2907.
Ruoff, A. L. (1967). Linear shock-velocity–particle-velocity relationship. *J. Appl. Phys*., **38**, 4976–4980.
Ryerson, F. J. (1987). Diffusion measurements: experimental methods. *Methods of Experimental Physics, Geophysics*, C. G. Sammis & T. L. Henyey eds., **24 A**, 89–130.
Salter, L. (1954). The Simon melting equation. *Phil. Mag*., **54**, 369–378.
Samara, G. A. (1967). Insulator to metal transition at high pressure. *J. Geophys. Res*., **72**, 671–678.
Sammis, C. G., Smith, J. C. & Schubert, G. (1981). A critical assessment of estimation methods for activation volume. *J. Geophys. Res*., **86**, 10 707–10 718.
Sawamoto, H. (1987). Phase diagram of $MgSiO_3$ at pressures up to 24 GPa and

temperatures up to 2200 °C: Phase stability and properties of tetragonal garnet. In *High-Pressure Research in Mineral Physics*, M. H. Manghnani & Y. Syono eds., American Geophysical Union, Washington, pp. 209–219.
Sawamoto, H., Weidner, D. J., Sasaki, S. & Kumazawa, M. (1984). Single crystal elastic properties of modified spinel (Beta) phase of magnesium orthosilicate. *Science*, **224**, 749–751.
Saxena, S. K. & Dubrovinsky, L. S. (1997). Detecting phases of iron. *Science*, **275**, 94–96.
Saxena, S. K. & Dubrovinsky, L. S. (1998). Thermodynamics of iron phases at high pressures and temperatures. In *Properties of Earth and Planetary Materials at High Pressure and Temperature*, M. H. Manghnani & T. Yagi eds., American Geophysical Union Monograph 101, AGU, Washington D.C., pp. 271–279.
Saxena, S. K., Dubrovinsky, L. S., Häggkvist, P., Cerenius, Y., Shen, G. & Mao, H. K. (1995). Synchrotron X-ray study of iron at high pressure and high temperature. *Science*, **269**, 1703–1704.
Saxena, S. K., Dubrovinsky, L. S., Lazor, P., *et al.* (1996). Stability of perovskite ($MgSiO_3$) in the Earth's mantle. *Science*, **274**, 1357–1359.
Saxena, S. K., Shen, G. & Lazor, P. (1993). Experimental evidence for a new iron phase and implications for the Earth's core. *Science*, **260**, 1312–1314.
Saxena, S. K., Shen, G. & Lazor, P. (1994). Temperatures in the Earth's core based on melting and phase transformation experiments on iron. *Science*, **264**, 405–407.
Saxton, H. J., & Sherby, O. D. (1962). Viscosity and atomic mobility in liquid metals. *Trans. ASM*, **55**, 826–843.
Schock, R. N., Duba, A. G. & Shankland, T. J. (1989). Electrical conduction in olivine. *J. Geophys. Res.*, **94**, 5829–5839.
Schreiber, E. & Anderson, O. L. (1970). Properties and composition of lunar materials: Earth analogies. *Science*, **168**, 1579–1580.
Secco, A. R. (1995) Viscosity of the outer core. In *Mineral Physics and Crystallography, A Handbook of Physical Constants*, T. J. Ahrens, ed., American Geophysical Union, Washington, D.C., pp. 218–226.
Secco, R. A. & Schloessin, H. H. (1989). The electrical resistivity of solid and liquid Fe at pressures up to 7 GPa. *J. Geophys. Res.*, **94**, 5887–5894.
Secco, A. R., LeBlanc, G. E., Yang, H. & Seibel, J. N. (1998) High-pressure viscosity of an Fe–S liquid: Experimentally derived estimate of the viscosity of Earth's outer core. In *Properties of Earth and Planetary Materials at High Pressure and Temperature*, M. H. Manghnani & T. Yagi eds., American Geophysical Union Monograph 101, AGU, Washington D.C., pp. 495–505.
Serghiou, G., Zerr, A. & Boehler, R. (1998). $(MgFe)SiO_3$ perovskite stability under lower mantle conditions. *Science*, **280**, 2093–2095.
Shankland, T. J. (1972). Velocity–density systematics: Derivation from Debye theory and the effect of ionic size. *J. Geophys. Res.*, **77**, 3750–3758.
Shankland, T. J. (1977). Elastic properties, chemical composition and crystal structure of minerals. *Geophys. Surveys*, **3**, 69–100.
Shankland, T. J. & Brown, J. M. (1985). Homogeneity and temperatures in the lower mantle. *Phys. Earth Planet. Interiors*, **38**, 51–58.
Shankland, T. J., Nitsan, U. & Duba, A. G. (1979). Optical absorption and radiative heat transport in olivine at high temperature. *J. Geophys. Res.*, **84**, 1603–1610.
Shankland, T. J., Peyronneau, J. & Poirier, J. P. (1993). Electrical conductivity of

the lower mantle. *Nature*, **366**, 453–455.
Shapiro, J. N. & Knopoff, L. (1969). Reduction of shock-wave equations of state to isothermal equations of state. *J. Geophys. Res.*, **74**, 1435–1438.
Sharma, S. M. & Sikka, S. K. (1996). Pressure-induced amorphization of materials. *Progress in Materials Science*, **40**, 1–77.
Shearer, P. M. & Masters, T. G. (1992). Global mapping of topography on the 660-km discontinuity. *Nature*, **355**, 791–796.
Shen, G. & Lazor, P. (1995). Measurement of melting temperatures of some minerals under lower-mantle pressure. *J. Geophys. Res.*, **100**, 17 699–17 713.
Shen, G., Lazor, P. & Saxena, S. K. (1993). Melting of wüstite and iron up to pressures of 600 kbar. *Phys. Chem. Minerals*, **20**, 91–96.
Shen, G., Mao, H. K., Hemley, R. F., Duffy, T. S. & Rivers, M. L. (1998). Melting and crystal structure of iron at high pressures and temperatures. *Geophys. Res. Lett.*, **25**, 373–376.
Sherman, D. M. (1989). The nature of the pressure-induced metallization of FeO and its implication to the core–mantle boundary. *Geophys. Res. Lett.*, **17**, 693–696.
Sherman, D. M. (1990). Chemical bonding and the incorporation of potassium into the Earth's core. *Geophys. Res. Lett.*, **16**, 515–518.
Shimoji, M. & Itami, T. (1986). *Atomic Transport in Liquid Metals*, TransTech Publications, Switzerland.
Shockley, W. (1952). Dislocation models of grain boundaries. *L'Etat Solide*. 9ème Conseil de Physique Solvay, Brussels.
Simon, F. & Glatzel, G. (1929). Bemerkungen zur Schmelzdruckkurve. *Z. Anorg. Allg. Chem.*, **178**, 309–316.
Simmons, G. & Wang, H. (1971). *Single Crystal Elastic Constants and Calculated Aggregate Properties: A Handbook*, MIT Press, Cambridge, MA.
Slater, J. C. (1939). *Introduction to Chemical Physics*, McGraw-Hill, New York.
Song, X. (1997). Anisotropy of the Earth's inner core. *Rev. Geophys.*, **35**, 297–313.
Song, X. & Ahrens, T. J. (1994). Pressure–temperature range of reactions between the liquid iron in the outer core and mantle silicates. *Geophys. Res. Lett.*, **21**, 153–156.
Souriau, A. & Romanowicz, B. (1996). Anisotropy in inner core attenuation: A new type of data to constrain the nature of the inner core. *Geophys. Res. Lett.*, **23**, 1–4.
Spiliopoulos, S. & Stacey, F. D. (1984). The Earth's thermal profile: Is there a mid-mantle thermal boundary layer? *J. Geodynamics*, **1**, 61–77.
Stacey, F. D. (1972). Physical properties of the Earth's core. *Geophys. Surveys*, **1**, 99–119.
Stacey, F. D. (1977a). A thermal model of the Earth. *Phys. Earth Planet. Interiors*, **15**, 341–348.
Stacey, F. D. (1977b). Applications of thermodynamics to fundamental Earth physics. *Geophys. Surveys*, **3**, 175–204.
Stacey, F. D. (1993a) Properties of a harmonic lattic. *Phys. Earth Planet. Interiors*, **78**, 19–22.
Stacey, F. D. (1993b). Thermodynamic relationships and the properties of iron at Earth's core conditions. In *High-Pressure Science and Technology – 1993*, S. C. Schmidt, J. W. Shaner, G. A. Samara & M. Ross, eds., American Institute of Physics, New York, pp. 899–902.
Stacey, F. D. (1995). Theory of thermal and elastic properties of the lower mantle and core. *Phys. Earth Planet. Interiors*, **89**, 219–245.

Stacey, F. D. & Irvine, R. D. (1977a). Theory of melting: Thermodynamic basis of Lindemann law. *Aust. J. Phys.*, **30**, 631–640.
Stacey, F. D. & Irvine, R. D. (1977b). A simple dislocation theory of melting. *Aust. J. Phys.*, **30**, 641–646.
Stacey, F. D., Brennan, B. J. & Irvine, R. D. (1981). Finite strain theories and comparison with seismological data. *Geophys. Surveys*, **4**, 189–232.
Stebbins, J. F., Carmichael, I. S. E. & Moret, L. K. (1984). Heat capacities and entropies of silicate liquids and glasses. *Contrib. Min. Petrol.*, **86**, 131–148.
Steinberg, D. J. (1981). The temperature independence of Grüneisen's gamma at high temperature. *J. Appl. Phys.*, **52**, 6415–6417.
Stern, E. A. & Zhang, K. (1988). Local premelting about impurities. *Phys. Rev. Lett.*, **60**, 1872–1875.
Stevenson, D. J. (1981). Models of the Earth's core. *Science*, **214**, 611–619.
Stishov, S. M., Makarenko, I. N., Ivanov, V. A. & Nikolaenko, A. M. (1973). On the entropy of melting. *Physics Lett.*, **45A**, 18.
Stixrude, L. & Cohen, R. E. (1993). Stability of orthorhombic $MgSiO_3$ perovskite in the Earth's lower mantle. *Nature*, **364**, 613–616.
Stixrude, L. & Cohen, R. E. (1995a). Constraints on the crystalline structure of the inner core: Mechanical instability of BCC iron at high pressure. *Geophys. Res. Lett.*, **22**, 125–128.
Stixrude, L. & Cohen, R. E. (1995b). High-pressure elasticity of iron and anisotropy of Earth's inner core, *Science*, **267**, 1972–1975.
Stixrude, L., Hemley, R. J., Fei, Y. & Mao, H. K. (1992). Thermoelasticity of silicate perovskite and magnesiowüstite and stratification of the Earth's mantle. *Science*, **257**, 1099–1101.
Strong, H. M., Tuft, R. E. & Hanneman, R. E. (1973). The iron fusion curve and the γ–δ–l triple point. *Metallurgical Trans.*, **4**, 2657–2661.
Stumpe, R., Wagner, D. & Bäuerle, D. (1983). Influence of bulk and interface properties on the electric transport in ABO3 perovskites. *Phys. Stat. Sol.*, **75**, 143–154.
Suito, K. (1977). Phase relations of pure Mg_2SiO_4 up to 200 kilobars. In *High Pressure Research*, M. H. Manghnani & S. Akimoto, eds., Academic Press, New York, pp. 255–266.
Sumino, Y. & Anderson, O. L. (1984). Elastic constants of minerals. In *Handbook of Physical Properties of Rocks*, CRC press, Boca Raton, pp. 39–138.
Sumino, Y., Anderson, O. L. & Suzuki, I. (1983). Temperature coefficients of elastic constants of single crystal MgO between 80 and 1300 K. *Phys. Chem. Minerals* , **9**, 38–47.
Sutherland, W. (1890). A new periodic property of the elements. *Phil. Mag.*, **30**, 318–323.
Sutherland, W. (1891). A kinetic theory of solids, with an experimental introduction. *Phil. Mag.*, **32**, 31–43.
Suzuki, H. (1983). Dislocation models of liquids. Basic concepts and phenomena related to atomic motions. In *Topological Disorder in Condensed Matter*, F. Yonegawa & T. Ninomiya, eds., Springer–Verlag, Berlin, pp. 222–233.
Suzuki, I. (1975). Thermal expansion of periclase and olivine and their anharmonic properties. *J. Phys. Earth*, **23**, 145–159.
Suzuki, I., Ohtani, E. & Kumazawa, M. (1979). Thermal expansion of γ Mg_2SiO_4. *J. Phys. Earth*, **27**, 53–61.
Suzuki, T., Akimoto, S. & Fukai, Y. (1984). The system iron–enstatite–water at high pressures and temperatures – formation of iron hydride and some

geophysical implications. *Phys. Earth Planet. Interiors*, **36**, 135–144.
Swalin, R. (1959). On the theory of self-diffusion in liquid metals. *Acta Metall.*, **7**, 736–740.
Sweeney, J. S. & Heinz, D. L. (1993). Melting of iron–magnesium silicate perovskite. *Geophys. Res. Lett.*, **20**, 855–858.
Sweeney, J. S. & Heinz, D. L. (1998). Laser-heating through a diamond-anvil cell: Melting at high pressures. In *Properties of Earth and Planetary Materials at High Pressure and Temperature*, M. H. Manghnani & T. Yagi eds., American Geophysical Union Monograph 101, AGU, Washington D.C., pp. 197–213.
Tackley, P. J., Stevenson, D. J., Glatzmaier, G. A. & Schubert, G. (1993). Effects of an endothermic phase transition in a spherical model of convection in the Earth's mantle. *Nature*, **361**, 699–704.
Takahashi, E. (1986). Melting of dry peridotite KLB-1 up to 14 GPa: Implications on the origin of the peridotitic upper mantle. *J. Geophys. Res.*, **91**, 9367–9382.
Takeuchi, H. & Kanamori, H. (1966). Equations of state of matter from shock wave experiments. *J. Geophys. Res.*, **71**, 3985–3994.
Tallon, J. L. (1980). The entropy change on melting of simple substances. *Physics Lett.*, **76A**, 139–142.
Tallon, J. L., & Robinson, W. H. (1977). A mechanical instability hypothesis for melting in the alkali halides. *Phil. Mag.*, **36**, 741–751.
Tallon, J. L., Robinson, W. H. & Smedley, S. I. (1977). A melting criterion based on the dilatation dependence of shear moduli. *Nature*, **266**, 337–338.
Tannhauser, D. S. (1962). Conductivity in iron oxides. *J. Phys. Chem. Solids*, **23**, 25–34.
Tritton, D. J. (1977). *Physical Fluid Dynamics*, van Nostrand–Reinhold, New York.
Tuller, H. L. & Nowick, A. S. (1977). Small polaron electron transport in reduced CeO_2 single crystals. *J. Phys. Chem. Solids*, **38**, 859–867.
Turcotte, D. L. & Schubert, G. (1982). *Geodynamics*, J. Wiley & Sons, New York.
Ubbelohde, A. R. (1978). *The Molten State of Matter*, Wiley, London.
Urakawa, S., Kato, M. & Kumazawa, M. (1987). Experimental study on the phase relations in the system Fe–Ni–O–S up to 15 GPa. In *High Pressure Research in Mineral Physics*, M. H. Manghnani & Y. Syono eds., American Geophysical Union, Washington, D.C., pp. 95–111.
Utsumi, W., Funamori, N., Yagi, T., Ito, E., Kikegawa, T. & Shimomura, O. (1995). Thermal expansivity of $MgSiO_3$ perovskite under high pressures up to 20 GPa. *Geophys. Res. Lett.*, **22**, 1005–1008.
Utsumi, W., Weidner, D. J. & Liebermann, R. C. (1998). Volume measurement of MgO at high pressures and high temperatures. In *Properties of Earth and Planetary Materials at High Pressure and Temperature*, M. H. Manghnani & T. Yagi eds., American Geophysical Union Monograph 101, AGU, Washington D.C., pp. 327–333.
Vaidya, S. N., & Gopal, E. S. R. (1966). Melting law at high pressures. *Phys. Rev. Lett.*, **17**, 635–636.
van der Hilst, R. D., Widiyantoro, S. & Engdahl, E. R. (1997). Evidence for deep mantle circulation from global tomography. *Nature*, **386**, 578–584.
van Liempt, J. (1935). Die Berechnung der Auflockerunswärme der Metalle aus Rekristallisationsdaten. *Z. Phys.*, **96**, 534–541.
Van Zytveld, J. B. (1980). Electrical resistivity of liquid transition metals. *J. Physique*, **41**, C8-504–C8-506).
Vashchenko, V. Ya. & Zubarev, V. N. (1963). Concerning the Grüneisen constant.

Soviet Phys. Solid State, **5**, 653–655.
Vaughan, P. J., Green, H. W. & Coe, R. S (1982). Is the olivine–spinel phase transformation martensitic? *Nature*, **298**, 357–358.
Verhoogen, J. (1980). *Energetics of the Earth*, Nat. Acad. Sci., Washington, D.C.
Vidale, J. E. & Benz, H. M. (1992). A sharp and flat section of the core–mantle boundary. *Nature*, **359**, 627–629.
Vidale, J. E. & Benz, H. M. (1993). Seismological mapping of fine structure near the base of the Earth's mantle. *Nature*, **361**, 529–532.
Vidale, J. E. & Hedlin, M. A. (1998). Evidence for partial melt at the core–mantle boundary north of Tonga from the strong scattering of seismic waves. *Nature*, **391**, 682–685.
Vinet, P., Ferrante, J., Rose, J. H. & Smith, J. R. (1987). Compressibility of solids. *J. Geophys. Res.*, **92**, 9319–9325.
Vinet, P., Rose, J. H., Ferrante, J. & Smith, J. R. (1989). Universal features of the equation of state of solids. *J. Phys.:Condens. Matter*, **1**, 1941–1963.
Vinnik, L., Breger, L. & Romanowicz, B. (1998). Anisotropic structures at the base of the Earth's mantle. *Nature*, **393**, 564–567.
Vočadlo, L. & Price, G. D. (1994). The Grüneisen parameter – computer calculations via lattice dynamics. *Phys. Earth Planet. Interiors* , **82**, 261–270.
Vočadlo, L. & Price, G. D. (1996). The melting of MgO – computer calculations via molecular dynamics. *Phys. Chem. Minerals*, **23**, 42–49.
Vočadlo, L., Patel, A. & Price, G. D. (1995). Molecular dynamics: some recent developments in classical and quantum mechanical simulation of minerals. *Mineralogical Magazine*, **59**, 597–605.
Vočadlo, L., de Wijs, G. A., Kresse, G., Gillan, M. J. & Price, G. D. (1997). First principle calculations of crystalline and liquid iron at Earth's core conditions. In *Solid State Chemistry – New Opportunities for Computer Simulation*, W. Mackrodt & R. Catlow eds., Faraday Discussion No. 106, Royal Society of Chemistry, London, pp.
Wall, A., & Price, G. D. (1989). Electrical conductivity of the lower mantle; a molecular dynamics simulation of $MgSiO_3$. *Phys. Earth Planet. Interiors*, **58**, 192–204.
Wallace, D. C. (1991). Melting of elements. *Proc. Roy. Soc. Lond.*, **A 433**, 631–661.
Wanamaker, B. J. & Duba, A. G. (1993). Electrical conductivity of San Carlos olivine along [100] under oxygen- and pyroxene-buffered conditions and implications for defect equilibria. *J. Geophys. Res.*, **98**, 489–500.
Wang, C. Y. (1968a). Equation of state of periclase and Birch's relationship between velocity and density. *Nature.*, **218**, 74–76.
Wang, C. Y. (1968b). Constitution of the lower mantle as evidenced from shock-wave data for some rocks. *J. Geophys. Res.*, **73**, 6459–6476.
Wang, C. Y. (1970). Density and constitution of the mantle. *J. Geophys. Res.*, **75**, 3264–3284.
Wang, C. Y. (1978). Elastic constants systematics. *Phys. Chem. Minerals*, **3**, 251–261.
Wang, Y., Guyot, F. & Liebermann, R. C. (1992). Electron microscopy of $(Mg, Fe)SiO_3$ perovskite: Evidence for structural phase transitions and implications for the lower mantle. *J. Geophys. Res.*, **97**, 12 327–12 347.
Wang, Y., Martinez, I., Guyot, F. & Liebermann, R. C. (1997). The breakdown of olivine to perovskite and magnesiowüstite. *Science*, **275**, 510–513.
Wang, Y., Weidner, D. J., Liebermann, R. C. & Zhao, Y. (1994). P–V–T equation of state of $(Mg, Fe)SiO_3$ perovskite: Constraints on composition of the lower

mantle. *Phys. Earth Planet. Interiors*, **83**, 13–40.
Wasserman, E., Stixrude, L. & Cohen, R. E. (1996). Thermal properties of iron at high pressures and temperatures. *Phys. Rev. B*, **53**, 8296–8309.
Watt, J. P. (1988). Elastic properties of polycrystalline minerals: Comparison of theory and experiment. *Phys. Chem. Minerals*, **15**, 579–587.
Watt, J. P., Davies, G. F. & O'Connell, R. J. (1976). The elastic properties of composite materials. *Rev. Geophys. Space Phys.*, **14**, 541–563.
Weertman, J. (1970). The creep strength of the Earth's mantle. *Rev. Geophys. Space Phys.*, **8**, 145–168.
Weertman, J. (1978). Creep laws for the mantle of the Earth. *Phil. Trans. Roy. Soc. Lond.*, **A288**, 9–26.
Weidner, D. J. (1986). Mantle models based on measured physical properties of minerals. In *Chemistry and Physics of Terrestrial Planets*, S. K. Saxena ed., Springer, New York, pp. 251–274.
Weidner, D. J. (1987). Elastic properties of rocks and minerals. *Methods of Experimental Physics, Geophysics*. C. G. Sammis, T. L. Henyey eds, **24 A**, 1–30.
Weidner, D. J. & Ito, E. (1985). Elasticity of $MgSiO_3$ in the ilmenite phase. *Phys. Earth Planet. Interiors*, **40**, 65–70.
Weidner, D. J., Sawamoto, H., Sasaki, S. & Kumazawa, M. (1984). Single crystal elastic properties of the spinel phase of Mg_2SiO_4. *J. Geophys. Res.*, **89**, 7852–7860.
Wells, A. F. (1984). *Structural Inorganic Chemistry*, 5th edn, Oxford University Press, Oxford.
Wen, L. & Helmberger, D. V. (1998). Ultra-low velocity zones near the core–mantle boundary from broadband PKP precursors. *Science*, **279**, 1701–1703.
Wenk, H. R., Takeshita, T., Jeanloz, R. & Johnson, G. C. (1988). Development of texture and elastic anisotropy during deformation of hcp metals. *Geophys. Res. Lett.*, **15**, 76–79.
Wentzcovitch, R. M., Ross, N. L. & Price, G. D. (1995) Ab-initio study of $MgSiO_3$ and $CaSiO_3$ perovskites at lower mantle pressures. *Phys. Earth Planet. Interiors*, **90**, 101–112.
White, G. K. & Anderson, O. L. (1966). Grüneisen parameter of magnesium oxide. *J. Appl. Phys.*, **37**, 430–432.
Wicks, C. W. & Richards, M. A. (1993). A detailed map of the 660 kilometer discontinuity beneath the Izu-Bonin subduction zone. *Science*, **261**, 1424–1427.
Will, G., Cemic, L., Hinze, E., Seifert, K. F. & Voigt, R. (1979). Electrical conductivity measurements on olivines and pyroxenes under defined thermodynamic activities as a function of temperature and pressure. *Phys. Chem. Minerals*, **4**, 189–197.
Will, G., Hoffbauer, W., Hinze, E. & Lauterjung, J. (1986). The compressibility of forsterite up to 300 kbar measured with synchrotron radiation. *Physica*, **139–140B**, 193–197.
Williams, Q. & Garnero, E. J. (1996). Seismic evidence for partial melt at the base of the Earth's mantle, *Science*, **273**, 1528–1530.
Williams, Q. & Jeanloz, R. (1990). Melting relations in the iron–sulfur system at ultra-high pressures: Implications for the thermal state of the Earth. *J. Geophys. Res.*, **95**, 19 299–19 310.
Williams, Q., Jeanloz, R., Bass, J., Svendsen, B. & Ahrens, T. J. (1987a). The

melting curve of iron to 250 Gigapascals: A constraint on the temperature at the Earth's center. *Science*, **236**, 181–182.
Williams, Q., Jeanloz, R. & McMillan, P. (1987b). Vibrational spectrum of $MgSiO_3$ perovskite: Zero-pressure Raman and mid-infrared spectra to 27 GPa. *J. Geophys. Res.*, **92**, 8116–8128.
Williams, Q., Knittle, E. & Jeanloz, R. (1987c). High temperature experiments on liquid iron alloys: Applications to the Earth's core. *EOS Trans. AGU*, **68**, 1493.
Williams, Q., Knittle, E. & Jeanloz, R. (1991). The high-pressure melting curve of iron: A technical discussion. *J. Geophys. Res.*, **96**, 2171–2184.
Williamson, E. D. & Adams, L. H. (1923). Density distribution in the Earth. *J. Washington Acad. Sci.*, **13**, 413–428.
Wolf, G. H. & Bukowinski, M. S. T. (1985). Ab initio structural and thermoelastic properties of orthorhombic $MgSiO_3$. *Geophys. Res. Lett.*, **12**, 809–812.
Wolf, G. H. & Bukowinski, M. S. T. (1987). Theoretical study of the structural properties and equation of state of $MgSiO_3$ and $CaSiO_3$ perovskites: implications for lower-mantle composition. In *High-Pressure Research in Mineral Physics*, M. H. Manghnani & Y. Syono eds., American Geophysical Union, Washington, D.C., pp. 313–331.
Wolf, G. H. & Jeanloz, R. (1984). Lindemann melting law: Anharmonic correction and test of its validity for minerals. *J. Geophys. Res.*, **89**, 7821–7835.
Wood, B. J. (1993). Carbon in the core. *Earth Planet. Sci. Lett.*, **117**, 593–607.
Wood, B. J. & Nell, J. (1991). High-temperature electrical conductivity of the lower-mantle phase (Mg, Fe)O. *Nature*, **351**, 309–311.
Wood, B. J. & Rubie, D. C. (1996). The effect of alumina on phase transformations at the 660 kilometer discontinuity from Fe–Mg partitioning experiments. *Science*, **273**, 1522–1524.
Wysession, M. E. (1996). Continents of the core. *Nature*, **381**, 373–375
Wysession, M. E., Okal, E. A. & Bina, C. R. (1992). The structure of the core–mantle boundary from diffracted waves. *J. Geophys. Res.*, **97**, 8749–8764.
Xu, J. A., Mao, H. K. & Bell, P. M. (1986). High-pressure ruby and diamond fluorescence: observations at 0.21 to 0.55 terapascal. *Science*, **232**, 1404–1406.
Xu, Y., McCammon, C. & Poe, B. T. (1998a). Effect of alumina on the electrical conductivity of silicate perovskite. *Science*, **282**, 922–924.
Xu, Y., Poe, B. T., Shankland, T. J. & Rubie, D. C. (1998b). Electrical conductivity of olivine, wadsleyite and ringwoodite under upper-mantle conditions. *Science*, **280**, 1415–1418.
Yagi, T. & Akimoto, S. (1974). Electrical conductivity jump produced by the α–β–δ transformations in Mn_2GeO_4. *Phys. Earth Planet. Interiors*, **8**, 235–240.
Yagi, T, Akaogi, M., Shimomura, O., Suzuki, T. & Akimoto, S. (1987). *In-situ* observation of the olivine–spinel transformation in Fe_2SiO_4 using synchrotron radiation. *J. Geophys. Res.*, **92**, 6207–6213.
Yagi, T., Mao, H. K. & Bell, P. M. (1982). Hydrostatic compression of perovskite-type $MgSiO_3$. In *Advances in Physical Geochemistry*, S. K. Saxena ed., Springer–Verlag, **2**, 317–325.
Yamashita, J. & Kurosawa, T. (1958). On electronic current in NiO. *J. Phys. Chem. Solids*, **5**, 34–43.
Yeganeh-Haeri, A., Weidner, D. J. & Ito, E. (1989). Elasticity of $MgSiO_3$ in the perovskite structure. *Science*, **243**, 787–789.

Yoo, C. S., Akella, J., Campbell, A. J., Mao, H. K. & Hemley, R. J. (1995). Phase diagram of iron by *in-situ* X-ray diffraction: Implications for the Earth's core. *Science*, **270**, 1473–1475.

Yoo, C. S., Akella, J., Campbell, A. J., Mao, H. K. & Hemley, R. J. (1997). Detecting phases of iron. *Science*, **275**, 96.

Yoo, C. S., Holmes, N. C., Ross, M., Webb, D. J. & Pike, C. (1993). Shock temperatures and melting of iron at Earth core conditions. *Phys. Rev. Lett.*, **70**, 3931–3934.

Young, C. J., & Lay, T. (1987). The core–mantle boundary. *Ann. Rev. Earth Planet. Sci.*, **15**, 25–46.

Yoshida, S., Sumita, I. & Kumazawa, M. (1996). Growth model of the inner core coupled with the outer core dynamics and the resulting elastic anisotropy. *J. Geophys. Res.*, **101**, 28 085–28 103.

Zerr, A. & Boehler, R. (1993). Melting of $(Mg, Fe)SiO_3$ perovskite to 625 kilobars: Indication of a high melting temperature in the lower mantle. *Science*, **262**, 553–555.

Zerr, A. & Boehler, R. (1994). Constraints on the melting temperature of the lower mantle from high-pressure experiments on MgO and magnesiowüstite. *Nature*, **371**, 506–508.

Zerr, A., Diegeler, A. & Boehler, R. (1998). Solidus of Earth's deep mantle. *Science*, **281**, 243–246.

Zerr, A., Reichmann, H., Euler, H., & Boehler, R. (1993). Hydrostatic compression of γ Mg_2SiO_4 to 50.0 GPa. *Phys. Chem. Minerals*, **19**, 507–509.

Zha, C. S., Duffy, T. S., Downs, R. T., Mao, H. K. & Hemley, R. J. (1998a). Brillouin scattering and X-ray diffraction of San Carlos olivine: direct pressure determination to 32 GPa. *Earth Planet. Sci. Lett.*, **159**, 25–33.

Zha, C. S., Duffy, T. S., Downs, R. T., Mao, H. K., Hemley, R. J. & Weidner, D. J. (1998b). Single-crystal elasticity of the α and β Mg_2SiO_4 polymorphs at high pressure. In *Properties of Earth and Planetary Materials at High Pressure and Temperature*, M. H. Manghnani & T. Yagi eds., American Geophysical Union Monograph 101, AGU, Washington D.C., pp. 9–16.

Zharkov, V. N. & Kalinin, V. A. (1971). *Equations of State for Solids at High Pressures and Temperatures*, Consultants Bureau, New York.

Zharkov, V. N., Karpov, P. B. & Leontjeff, V. V. (1985). On the thermal regime of the boundary layer at the bottom of the mantle. *Phys. Earth Planet. Interiors*, **41**, 138–142.

Ziman, J. M. (1965). *Principles of the Theory of Solids*, Cambridge University Press, Cambridge.

Zwanzig, R. (1983). On the relation between self-diffusion and viscosity of liquids. *J. Chem. Phys.*, **79**, 4507–4508.

Zwikker, C. (1954). *Physical Properties of Solid Materials*, Pergamon Press, Oxford.

This Page Intentionally Left Blank

Index